

University of Warwick institutional repository: <http://go.warwick.ac.uk/wrap>

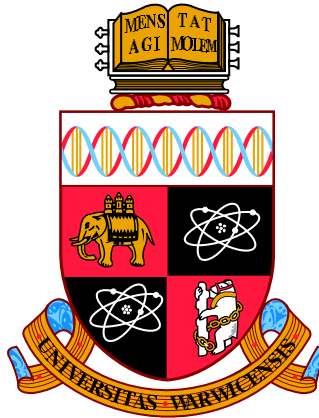
A Thesis Submitted for the Degree of PhD at the University of Warwick

<http://go.warwick.ac.uk/wrap/75554>

This thesis is made available online and is protected by original copyright.

Please scroll down to view the document itself.

Please refer to the repository record for this item for information to help you to cite it. Our policy information is available from the repository home page.



Orbital Parameters Estimation for Compact Binary Stars

by

Penélope Alejandra Longa-Peña, MSc

Thesis

Submitted to the University of Warwick
for the degree of
Doctor of Philosophy

Department of Physics

December 2015

THE UNIVERSITY OF
WARWICK

Contents

Contents	i
List of Figures	iv
List of Tables	viii
Acknowledgements	ix
Declaration and Published Work	xi
Abbreviations	xiii
Abstract	xv
1 Introduction	1
1.1 Compact Binary Stars	1
1.1.1 Binary Geometry	2
1.1.2 Evolution: Common Envelope and Stable Mass Transfer	4
1.1.3 Accretion Disc	5
1.1.4 Angular Momentum Loss	6
1.1.5 Compact Binaries Classification	8
1.1.6 Orbital Parameters	15
1.2 Spectral Line Formation	18
1.2.1 Spectral Features in CBs	20
1.3 Ca II and the Bowen blend	23
1.4 Summary and Outline	26
2 Methods	27
2.1 Spectroscopy	27
2.1.1 Long Slit Spectroscopy	28
2.1.2 Echelle spectroscopy	29

2.1.3	Data Reduction	32
2.2	Radial Velocity Analysis	37
2.2.1	Diagnostic Diagram	38
2.3	Bootstrap	40
2.3.1	The bootstrap estimate of standard error	40
2.4	Indirect Imaging: Doppler Tomography	40
2.4.1	Profile Formation by Projection	41
2.4.2	Understanding Doppler maps	43
2.4.3	Maximum Entropy Inversion	44
2.4.4	The effect of the systemic velocity γ in Doppler maps	45
2.4.5	Axioms of Doppler Tomography	46
2.4.6	Doppler tomography and Bootstrapping	47
2.4.7	Orbital Parameters with Doppler Tomography	47
2.4.8	Secondary star and Phase zero from K_{em}	51
2.5	Summary	63
3	Emission line tomography of CC Scl and V2051 Oph	65
3.1	Introduction	65
3.2	Observations and Reduction	67
3.3	Results	67
3.3.1	Spectrum	67
3.3.2	Radial velocities analysis	68
3.3.3	Doppler tomography	73
3.4	Discussion and Conclusions	83
3.4.1	CC Scl	84
3.4.2	V2051 Oph	85
3.5	Summary	86
4	The Low Mass Black Hole Candidate 4U 1957+111	89
4.1	Introduction	89
4.2	4U 1957+111	89
4.3	Instrument Performance on the Bowen blend	91
4.4	Observation and Data Reduction	92
4.5	Results	94
4.5.1	Averaged Spectrum	94
4.5.2	Radial Velocities	96
4.5.3	Spectroscopic Period	96

4.5.4	Doppler Tomography	99
4.6	Discussions and Conclusions	104
4.7	Summary	105
5	Orbital Parameters of four Superhumping CVs	107
5.1	Introduction	107
5.2	Observations and Data Reduction	108
5.3	Average Spectra	109
5.4	Radial Velocities	116
5.5	Doppler Tomography	117
5.5.1	Secondary Star and Phase Zero	123
5.5.2	Systemic Velocity γ	124
5.5.3	Radial Velocity of the Primary Star	125
5.5.4	Mass Ratio	126
5.6	Discussions and Conclusions	129
5.7	Summary	132
6	Discussions and Conclusions	135
6.1	Dynamic constraints with Doppler tomography	135
6.2	Ca II emission	136
6.3	4U 1957 and the Bowen blend	136
6.4	Implications for the $\epsilon - q$ relation	136
6.5	Conclusions	138
6.6	Future Research	138
6.6.1	Ca II	138
6.6.2	Short Period CVs	138
6.6.3	Extending the method	139
	Bibliography	141

List of Figures

1.1	Roche Potential	3
1.2	Schematic representation of the accretion disc formation.	7
1.3	Schematic of CV evolution. Based on figure from Postnov & Yungelson (2014). Figure not to scale.	9
1.4	Orbital period distribution	11
1.5	Mass transfer versus orbital period of CVs	12
1.6	Superhump excess versus mass ratio.	14
1.7	Evolution of NS binaries	16
1.8	Orbital phases	18
1.9	Stars of masses M_1 and M_2 orbiting around their centre of mass.	18
1.10	Sodium spectra	20
1.11	Blackbody radiation curves. Image created for educational purposes, courtesy of “Darth Kule”.	21
1.12	Disc’s double peaked profile formation	22
1.13	Cataclysmic variable spectrum	23
1.14	X-ray binary spectrum	24
1.15	Trailed spectra of Sco X-1 from Steeghs & Casares (2002)	25
2.1	Schematic of the essential components of a spectrograph	29
2.2	MagE spectra of the X-ray binary Sco X-1.	30
2.3	Photograph of MagE installed on the Magellan II telescope.	31
2.4	MagE optical design.	31
2.5	MagE bias frame	32
2.6	MagE flat field frame.	34
2.7	MagE ThAr lamp frame	34
2.8	MagE spectra of V4140 Sgr	36
2.9	Diagnostic diagram for CC Scl	39
2.10	Schematic of the bootstrap process.	41
2.11	S-wave.	42

2.12	Representation of the line profile formation process.	43
2.13	Schematic view of a CV in velocity coordinates.	44
2.14	Simulated data for 3 values of γ	46
2.15	Histograms of FWHM for two values of γ	49
2.16	FWHM and STD of the donor versus systemic velocity	50
2.17	Residuals level against K_1	51
2.18	Doppler map of CaII 8662 Å of CC Scl.	52
2.19	K_1 - q plane	53
2.20	Location of different velocities on the donor surface	53
2.21	Dependence of K_{em} and K-correction upon the inclination angle assumed in the model.	55
2.22	K_1 - q plane for two inclination angles	56
2.23	Dependence of K_{em} and K-correction upon the disc height.	57
2.24	K_1 - q plane for two values of K_1	58
2.25	Synthetic data Doppler maps.	58
2.26	Gaussian spot of FWHM=40 km/s, S/N=2.	59
2.27	Gaussian spot of FWHM=40 km/s, S/N=25	60
2.28	Gaussian spot of FWHM=80 km/s, S/N=2	60
2.29	Gaussian spot of FWHM=40 km/s, accretion disc at the same intensity level, S/N=2.	61
2.30	Gaussian spot of FWHM=40 km/s, accretion disc at the same intensity level, S/N=25	61
2.31	Gaussian spot of FWHM=40 km/s, accretion disc, intensity 5 times lower than the spot, S/N=25	61
2.32	Gaussian spot of FWHM=40 km/s, accretion disc, intensity 5 times lower than the spot, S/N=2	62
3.1	Average spectrum of CC Scl.	69
3.2	Average spectrum of V2051 Oph.	70
3.3	Diagnostic diagram of $H\beta$ for V2051 Oph and CC Scl	71
3.4	Radial velocity curves of $H\alpha$, $H\beta$ and CaII. CC Scl.	72
3.5	Radial velocity curves of $H\alpha$, $H\beta$ and CaII	72
3.6	Two Doppler maps of $H\beta$ for CC Scl generated with the same value of χ^2 but with two different periods	73
3.7	Doppler maps for CC Scl	74
3.8	Doppler maps for V2051 Oph	75
3.9	Histograms for two values of γ	76
3.10	FWHM of the secondary star and STD versus systemic velocity for CC Scl	77
3.11	FWHM of the secondary star and STD versus systemic velocity for V2051 Oph.	77
3.12	Scheme of boxes location	79

3.13	K_1 velocity for five different boxes and six different lines	80
3.14	K_{em} histogram for CC Scl	81
3.15	K_1 - q plane for CC Scl.	82
3.16	K_1 - q plane for V2051 Oph.	83
3.17	Doppler maps of the most prominent Balmer lines of V2051 Oph.	86
4.1	Two light curves of 4U1957	90
4.2	Comparison of the Bowen blend with different instruments	93
4.3	Comparison of the Bowen blend with different instruments	93
4.4	Average normalised spectrum of 4U 1957's MagE data	94
4.5	Diagnostic diagram of He II (top). Average spectrum of He II (bottom).	97
4.6	Periodogram for 4U 1957	98
4.7	Doppler maps of 4U 1957	100
4.8	Example Doppler maps of the Bowen blend, sub-set combinations	101
4.9	Average, STD and average/STD from 500 bootstrap samples of the Doppler map of the Bowen blend	101
4.10	FWHM and STD of the donor versus systemic velocity for 4U 1957	102
4.11	K_1 - q plane for 4U 1957	103
4.12	$M_1 - M_2$ plane for 4U 1957	105
5.1	Average Spectrum of AQ Eri UVB arm	110
5.2	Average Spectrum of QZ Vir UVB arm	110
5.3	Average spectrum of SDSS0137, UVB arm.	111
5.4	Average of 21 spectra of RZ Leo, UVB arm.	111
5.5	Average Spectrum of AQ Eri visual arm	112
5.6	Average Spectrum of QZ Vir visual arm	112
5.7	Average spectrum of SDSS0137, visual arm	113
5.8	Average of 21 spectra of RZ Leo, visual arm.	113
5.9	Average Spectrum of AQ Eri NIR arm	114
5.10	Average Spectrum of QZ Vir NIR arm	114
5.11	Average spectrum of SDSS 0137, NIR arm	115
5.12	Average spectrum of RZ Leo, NIR arm	115
5.13	Diagnostic diagrams of AQ Eri	118
5.14	Diagnostic diagrams of RZ Leo	119
5.15	Doppler maps of AQ Eri	121
5.16	Doppler maps of QZ Vir.	122
5.17	Doppler maps of SDSS0137	123
5.18	Doppler maps of RZ Leo	124

5.19	FWHM of the secondary star and STD versus systemic velocity for AQ Eri	125
5.20	FWHM of the secondary star and STD versus systemic velocity for QZ Vir	125
5.21	FWHM of the secondary star and STD versus systemic velocity for SDSS0137 using $H\gamma$	126
5.22	FWHM of the secondary star and STD versus systemic velocity for SDSS0137 using CaII II 3933Å	126
5.23	K_1 histograms	127
5.24	K_1 - q plane for Aq Eri.	128
5.25	K_1 - q plane for QZ Vir	129
5.26	K_1 - q plane for SDSS0137	130
6.1	$\epsilon - q$ plane with Knigge solution and our solution	137
6.2	Observed period distribution of CNe.	140

List of Tables

1.1	Types of compact remnants of single stars.	8
3.1	Orbital parameters derived from the diagnostic diagrams of CC Scl and V2051 Oph .	69
3.2	Orbital parameters summary	87
4.1	Instruments performance comparison for the Bowen lines range.	91
4.2	4U 1957 MagE observations. n is the number of spectra taken during the given date.	92
4.3	4U 1957 IMACS observations. n is the number of spectra taken during the given date.	94
4.4	4U 1957 average equivalent width per night. MagE data	95
4.5	4U 1957 average equivalent width per night. IMACS data.	95
4.6	4U 1957 orbital parameters derived from the diagnostic diagram of He II with MagE and IMACS data.	96
5.1	X-shooter observation dates.	109
5.2	Orbital parameters derived from the diagnostic diagrams of AQ Eri, QZ Vir, SDSS0137 and RZ Leo. Φ_0 is relative to our ephemeris (Section 5.5).	116
5.3	Ephemeris and K_{em} of the systems with a visible donor.	123
5.4	Primary velocity of the four systems calculated using the centre of symmetry technique.	128

Acknowledgements

*There they stood, ranged along the hillsides, met
To view the last of me, a living frame
For one more picture! In a sheet of flame
I saw them and I knew them all. And yet
Dauntless the slug-horn to my lips I set,
And blew. 'Childe Roland to the Dark Tower came.'*

-Robert Browning, Childe Roland to the Dark Tower came.

And on an epic quest of my own I blow the slug-horn at the end of an epic journey. For all the things I've lost on my way here, some I'll miss but I'll never regret: To my friends lost in one way or another and the sacrifices of many people that helped me to be writing here today, I acknowledge. But I found many things in this journey, the most important one, my family: my husband and son that stood along through wind and rain and made it sunshine and spring. New friends that supplied me with support, coffee, spelling checks, CRISPS and non scientific palaver (yes, my PhD student's party) and that made my life much easier with their youth of soul. And for these I'm grateful.

For the most important part of this journey, my journey to knowledge, I owe special gratitude to my supervisor Danny Steeghs for his valuable scientific advice, and for always been willing to share his ideas, a cup of coffee and a good laugh. I also would like to thanks to all the academics from the Astronomy group at the University of Warwick for the stimulating environment and additional supervision. A special mention to my former supervisor and friend Eduardo who always stood strong and showed me that I could fight harder than I believed that I was capable of my self.

I would like to thank Chris Copperwheat for the reducing the data used in Chapter 5.

Also, a HUGE thank you to my thesis correctors Boris and Chris for their very useful and thorough comments. I still like you =)

I stand today facing my destiny at the end of my quest. What awaits for me now that I've arrived, is to be revealed. The trip is always more important than the destiny. And what a trip it was!

Think first, fight afterwards' ... Stand and be true, I will be a knight¹.

¹Well, a Doctor. But that is epic enough ;)

Declaration and Published Work

I, Penelope Alejandra Longa-Peña, hereby declare that the work presented in this thesis is my own except where references stated otherwise. This thesis has not been submitted either wholly or in part in any previous application for a higher degree in this or any other academic institution. The following Chapters are based on published refereed publications:

Chapter two, Section 2.4.7, & Chapter three:

“Emission line tomography of the short period cataclysmic variables CC Scl and V2051 Oph”

P. Longa-Pena; D. Steeghs; T. Marsh

Monthly Notices of the Royal Astronomical Society 2014 447 (3): 149-159

Chapter four:

“Dynamical Constraints for the Low Mass Black Hole Candidate 4U 1957+111”

P. Longa-Pena; D. Steeghs; R. Cornelisse; J.M. Miller; J. Casares, P.A. Charles

In Preparation.

Some of the MagE data reduced as described in Chapter 2 has been published in:

“The unseen population of F- to K-type companions to hot subdwarf star”

Girven, J.; Steeghs, D.; Heber, U.; Gänsicke, B. T.; Marsh, T. R.; Breed, E.; Copperwheat, C. M.;

Pyrzas, S.; Longa-Peña, P. Monthly Notices of the Royal Astronomical Society 2012 425 (2): 1013-1041

“A Dynamical Study of the Black Hole X-ray Binary Nova Muscae 1991”

Jianfeng, W.; Orosz, J.A. ; McClintock, J. E.; Steeghs, D.; Longa-Peña, P.; Callanan, P.J. ;Gou, L.; Ho, L. C.; Jonker, P.; Reynolds, M.; Torres, M.

Accepted in The Astrophysical Journal.

Abbreviations

BH:	Black hole
Ca:	Calcium
CB:	Compact binary
CN:	Classical Nova
CCD:	Charge-Coupled Device
C/O:	Carbon/Oxygen
CRTS:	Catalina Realtime Transient Survey
CV:	Cataclysmic Variable
ESO:	European Southern Observatory
FWHM:	Full-Width at Half Maximum
H:	Hydrogen
He:	Helium
HST:	Hubble Space Telescope
INT :	Isaac Newton Telescope
LMXB:	Low mass x-ray binary
MagE:	Magellan Echellette
NIR:	near-infrared
SDSS:	Sloan Digital Sky Survey
S/N:	Signal to noise ratio
STD:	Standard Deviation
VIS:	visible
VLT:	Very Large Telescope
WD:	White Dwarf
WHT:	William Herschel Telescope

Abstract

Most stars in the Galaxy are found in multiple systems of two or more stars orbiting together. Two stars orbiting around their centre of mass are called binary stars. In close binary stars, the evolution of one star affects its companion and evolutionary expansion of one star allows for mass exchange between the components. In most cases, the material from the less massive star forms an accretion disc around the heavier companion that has evolved into a compact stellar remnant, the final state of stellar evolution. We call these systems compact binary stars (CBs). The study of CBs is key to the development of two fundamental phenomena: accretion and evolution of binary stars.

Statistical information on CBs can be deduced by extracting common properties and characteristic system parameter distributions from observed data. But, despite being fundamental for a wide range of astronomical phenomena, our comprehension of their formation and evolution is still poor, mainly because of the limited knowledge of crucial orbital parameters. This lack of reliable orbital parameters estimation is mainly due to observational handicaps, namely, the accretion disc outshines the system components. Astronomers have developed different techniques to overcome this, but are often very dependant of the signal to noise ratio of the data or are only able to obtain via target of opportunity programs (wait until the target is brighter).

The focus of this work is to test and develop techniques, based on indirect imaging methods, that can overcome the main observational handicaps to estimate orbital parameters of CBs. We combine these techniques with the exploitation of more “exotic” emission lines that trace the irradiated face of the donor star, namely Ca II NIR triplet and the Bowen blend. We made use of empirical properties of Doppler tomography to estimate the values of the phase zero ϕ_0 and the velocity of the irradiated face of the secondary star (K_{em}). We then used synthetic models accounting for an irradiated secondary to fit our measured K_{em} and perform a K-correction to derive the radial velocity of the secondary K_2 . To derive K_1 , we used the centre of symmetry technique, testing its validity among several emission lines and the stability of the results depending on the selected area. Having strong constraints for K_1 and K_2 , we find estimates for the mass ratio q . Furthermore, we developed a variation from the Doppler tomography secondary emission method to constrain the value of the systemic velocity γ . We derive meaningful uncertainties of

these parameters with the bootstrap technique.

Using these techniques, we have successfully set dynamical constraints on the radial velocities of the binary components of CBs and derived fundamental orbital parameters, including the mass ratio, using basic properties of Doppler tomography.

Only around half of the stars that we see when we look to the sky are single stars. The rest are multiple systems, consisting of two or more stars orbiting around each other due to their gravitational attraction. Two stars orbiting each other are called binary stars. Measurements of the dynamical interaction of the components in eclipsing binary stars provide the most accurately determined parameters of stars.

This work will focus on a particular class of binary: compact binary stars (CBs), consisting of a main sequence star and a stellar remnant- white dwarf (WD), neutron star (NS) or black hole (BH). These are considered primary targets for the forthcoming field of gravitational wave astronomy, since their orbital evolution is partially controlled by the emission of gravitational waves and ultimate leads to merging and possible explosive disruption of the components (for a review, see Thorne et al. 1987).

In Section 1.1 I will review the basics of binary geometry, evolution, classification and parameters. In Section 1.2 I will present some basics of spectral line formation and common features of CBs. Finally, in Section 1.3 I will present the advantages of the Bowen blend and the Ca II triplet to trace the secondary star in CB systems.

1.1 Compact Binary Stars

As the time scale of evolution of a star is largely dependant on its mass, the more massive the star the faster it evolves from the main sequence hydrogen burning phase to a stellar remnant. The initial (main sequence) mass of a star will determine how it will end its life: $\sim 1M_{\odot}$ stars will end their lives as a WD, stars of more than $\sim 8M_{\odot}$ will end up as either NSs or BHs. In close binary stars, the evolution of one star affects its companion. Evolutionary expansion of stars allows for mass exchange between the components. In most cases, the material from the less massive star feeds an accretion disc around the heavier companion that has evolved faster to a compact stellar remnant, the collapsed end state of stellar evolution. We call these systems compact binary stars (CBs).

The study of the structure of CBs is key to the development of three fundamental phenomena: accretion flow, discs and the evolution of binary stars. The theory of accretion is im-

portant for the study of quasars, active galactic nuclei and even for planet formation. Due to the shorter timescales and distances with respect to these sources, observational research of the accretion process can be studied more effectively in compact systems such as CBs (see Frank & Raine 2002).

CBs are also the key to a wide variety of astrophysical phenomena from short gamma - ray bursts (Paczynski 1986, Berger et al. 2005, Gehrels et al. 2005), pulses of gravitational-waves emitted by stellar black holes (Casares et al. 1992), to the basis of the 2011 Nobel Price in physics (Riess et al. 1998, Schmidt et al. 1998, Perlmutter et al. 1999): Type Ia supernovae, whose progenitors are WD binaries (Whelan & Iben 1973, Woosley et al. 1986, Ruiz-Lapuente et al. 2004).

Statistical information on CBs can be deduced by extracting common properties and characteristic system parameter distributions from observed data. Unfortunately, our understanding of their formation and evolution is still poor, mainly because of the limited quantity of statistically significant CBs parameter samples. In recent years, surveys such as the Sloan Digital Sky Survey and Chandra have helped to fill this gap. Nevertheless, as we will show in the following sections, to test population models and understand properties of many CVs, we still lack crucial orbital parameters for a large enough sample.

1.1.1 Binary Geometry

Given the potential function, $\Phi(\mathbf{r})$, we can draw a surface on which the potential is constant ($\Phi(\mathbf{r}) = C$, with $C = \text{constant}$). Such a surface is called an equipotential surface (see Figure 1.1).

Any flow of gas between two stars will be governed by the Euler equation (Frank & Raine, 2002):

$$\rho \frac{\partial \mathbf{v}}{\partial t} + \rho \mathbf{v} \cdot \nabla \mathbf{v} = -\nabla P + \mathbf{f} \quad (1.1)$$

where ρ is the density, \mathbf{v} is the velocity, P is pressure and \mathbf{f} is the external force. In our case, f are the centrifugal and Coriolis forces if we consider a frame of reference that rotates with the binary with an angular velocity ω with respect to an inertial frame:

$$\frac{\partial \mathbf{v}}{\partial t} + (\mathbf{v} \cdot \nabla) \mathbf{v} = -\nabla \Phi_R - 2\omega \times \mathbf{v} - \frac{1}{\rho} \nabla P \quad (1.2)$$

where $-2\omega \times \mathbf{v}$ is the Coriolis force per unit mass and $-\nabla \Phi_R$ includes the effect of the centrifugal and gravitational forces.

For a binary system with masses M_1 and M_2 , Φ_R is known as the Roche potential and is given by:

$$\Phi_R(\mathbf{r}) = \frac{-GM_1}{|\mathbf{r} - \mathbf{r}_1|} - \frac{-GM_2}{|\mathbf{r} - \mathbf{r}_2|} - \frac{1}{2}(\omega \times \mathbf{r})^2, \quad (1.3)$$

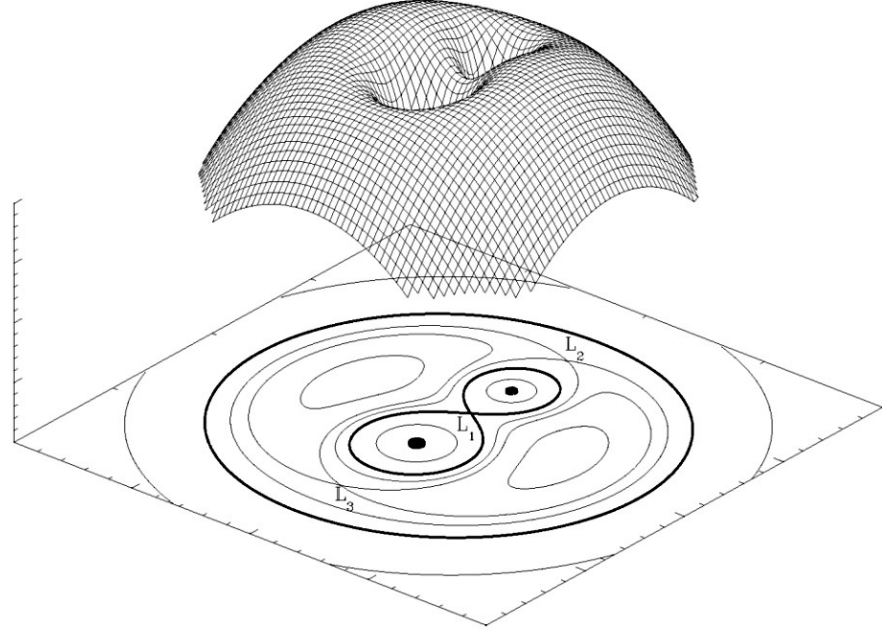


Figure 1.1: 3-D representation of the Roche potential for $q = 2$. The equipotential surfaces are outlined in black in the lower plane. Figure from Postnov & Yungelson (2014).

where G is the universal gravitational constant and $\mathbf{r}_1 = \sqrt{x^2 + y^2 + z^2}$ and $\mathbf{r}_2 = \sqrt{(x-1)^2 + y^2 + z^2}$ are the position vectors of each star with respect to the centre of mass (Frank & Raine, 2002).

The mass ratio q determines the shapes of the Roche equipotential and is given by:

$$q = \frac{M_2}{M_1} = \frac{K_1}{K_2} \quad (1.4)$$

where M_1 , M_2 , K_1 and K_2 are the masses and radial velocity semiamplitudes of the primary (compact) and secondary (donor) star, respectively. The binary separation a is given by Kepler's law as:

$$P_{orb}^2 = \frac{4\pi^2 a^3}{G[M_1 + M_2]} \quad (1.5)$$

where P_{orb} is the orbital period of the system.

From equations 1.3 and 1.5, the normalised Roche potential is then:

$$\phi_n = \frac{-2\phi}{G(M_1 + M_2)} = \frac{2}{r_1(1+q)} + \frac{2q}{r_2(1+q)} + \left(x - \frac{q}{1+q}\right)^2 + y^2, \quad (1.6)$$

showing explicitly the direct relation of the Roche potential and the mass ratio.

In a CB, the equipotential surface at which the donor star will start mass transfer to its compact companion is called the Roche lobe, the innermost level surface that encloses both components. Figure 1.1 shows the Roche lobe as darker black eight-shaped central line. At the

point marked L_1 , the inner Lagrangian point, the force exerted on a test particle co-rotating with the binary vanishes, so the particle can escape from the surface of one star and be captured by the companion. In a CB, the matter escapes through L_1 , and in the case of non magnetic CBs, as the matter comes with a given angular momentum it forms a disc orbiting the companion. We call this process Roche-lobe overflow (RLOF) and it begins when the radius of an initially more massive (and hence faster evolving) star, becomes equal to the radius of the Roche lobe.

1.1.2 Evolution: Common Envelope and Stable Mass Transfer

Despite being a key stage for the formation of a CB, the common envelope stage remains poorly understood. One theory proposes that when the mass transfer rate from the donor star is too high for the companion to accommodate all the accreting material, the overflowing material becomes an envelope that engulfs the whole system (e.g. Benson (1970), Neo et al. (1977), Webbink (1977) and Pringle & Livio (1985)). Another possibility is the formation of an extended envelope formed over the system due to unstable nuclear burning of an accreting WD in the compact binary (e.g. Starrfield et al. (1974), Paczynski & Zytlow (1978) and Nomoto et al. (1979)). A third scenario is when the donor star cannot keep synchronous rotation with the compact companion, forcing the compact object to spiral into the envelope of a giant donor (Sparks & Stecher, 1974). Despite of all these uncertainties, the dramatic decrease of angular momentum experienced in the course of a CB's evolution is compelling evidence of the existence of the common envelope stage.

Stable mass transfer depends on the balance between the response of the donor to mass loss, changes of separation and loss of angular momentum. Three time scales are important to regulate this process: the dynamical, thermal and nuclear time scales of the secondary. The dynamical time scale, on which the star reacts to departures from hydrostatic equilibrium is :

$$t_{\text{dyn}} = \sqrt{\frac{2R^3}{GM}}. \quad (1.7)$$

For the Sun this is $\sim 1600\text{s}$, meaning that if the internal pressure of the Sun were removed, it would take this time to collapse. This time is roughly the time that a sound wave requires to cross the Sun.

The thermal timescale, on which the star reacts to departures from thermal equilibrium is defined as:

$$t_{\text{th}} = \frac{GM}{RL}, \quad (1.8)$$

where L is the luminosity of the star. For the Sun, this is $\sim 3 \times 10^7 \text{yr}$. This is the timescale on which the Sun would contract if its nuclear energy sources were turned off.

The third timescale, the nuclear time scale, is the main-sequence lifetime of a star and can be defined as:

$$t_{\text{nuc}} = (7 \times 10^9) \frac{M}{M_{\odot}} \frac{L_{\odot}}{L} \text{ years.} \quad (1.9)$$

For the Sun this is $\sim 10^9$ yr, the time required to exhaust all the Sun's hydrogen at its current luminosity.

Neglecting the orbit's eccentricity the angular momentum J is given by (Landau & Lifshitz, 1969):

$$J = \frac{M_1 M_2}{M} a^2 \Omega_{\text{orb}} \quad (1.10)$$

where M is the total mass of the system, M_1 is the primary star, M_2 is the mass donor, a is the orbital separation and $\Omega_{\text{orb}}(r) = \left[\frac{GM}{r^3} \right]^{1/2}$ is the Keplerian orbital velocity. The rate of change in the orbital separation a is:

$$\frac{\dot{a}}{a} = 2 \frac{\dot{J}}{J} - 2 \frac{\dot{M}_1}{M_1} - 2 \frac{\dot{M}_2}{M_2} = \frac{2\dot{J}}{J} - \frac{2\dot{M}_2}{M_2} \left(1 - \frac{M_2}{M_1} \right). \quad (1.11)$$

If we conserve the angular momentum, $\dot{J} = 0$, when $M_2 < M_1$: $\frac{\dot{a}}{a} > 0$ and the orbit expands.

As the most massive star evolves first, mass transfer will always begin with $M_2 > M_1$ (note that the definition of M_1 and M_2 will reverse temporarily). As M_1 is unable to adjust its structure rapidly enough to maintain itself in the Roche lobe, mass transfer proceeds on the dynamical time scale, saturating and growing to form a common envelope around the stellar components. Inside the common envelope, the stars will spiral toward each other until enough orbital energy has been released to expel the envelope, delivering a barely detached system. Now, while the secondary evolves and eventually fills its Roche lobe, $M_2 < M_1$ and stable mass transfer on the nuclear time scale, will occur. As the mass ratio changes, the Roche geometry adjusts accordingly to the new system parameters. The response of the secondary to these changes will determine the nature of the mass transfer. If the secondary outer layers are radiative, the donor has to expand to maintain the mass transfer, having enough time to restore thermal equilibrium. On the other hand, if the secondary's outer layers are convective, the Roche lobe can expand sufficiently to remain comparable in size to the stellar radius and the mass transfer will occur on the nuclear timescale (de Loore, 1992).

1.1.3 Accretion Disc

A direct consequence of mass transfer via RLOF is that the stream of material has angular momentum and cannot directly accrete on the relatively small surface of the compact object. The material then tends to settle in the lowest energy orbit: a circular orbit. As a result, the first material that flows from L_1 will start orbiting the orbital plane of the binary with a radius R_{circ} , given

that R_{circ} has the same angular momentum as L_1 . R_{circ} is called the circularization radius and is defined as (Frank & Raine, 2002):

$$\frac{R_{\text{circ}}}{a} = (1 + q)[0.0500 - 0.227 \log q]^4 \quad (1.12)$$

Figure 1.2 summarises the disc formation process by RLOF (see Verbunt 1982 and references therein). The matter does not hit the star directly, but flows around it until it hits the stream again (Figure 1.2a). The shock changes the flow of the stream into a circular shape (Figure 1.2b). The stream spreads into a disc due to viscosity, transporting matter inwards and outwards to preserve angular momentum (Figure 1.2c). The expansion of the disc continues until the outward disc is stopped by tidal interactions with the donor and the inner edge of the disc reaches the surface or magnetosphere of the compact object and starts to accrete (Figure 1.2d). Figure 1.2e is a side view of the accretion disc.

1.1.4 Angular Momentum Loss

The angular momentum term of Equation 1.11 accounts for the total loss in angular momentum from magnetic braking and gravitational radiation. Here, we will show the classic mathematical treatment of these two mechanisms. However, Knigge et al. (2011) have suggested that a better description of the evolution of CVs was reached by scaling the classical equations (that we will show below), by numerical factors, see the paper for details.

Magnetic Braking

The rotation of the secondary star is tidally locked to the orbital period, forcing it to rotate faster than a similar type single star. This fast rotation leads to highly magnetic secondaries. Charged particles flow through the field lines and are forced to co-rotate with the secondary, accelerating them. When these particles are released, they take with them substantial angular momentum in proportion to the orbital velocity of the system Ω_{orb} (Verbunt & Zwaan, 1981)

$$\frac{j_{MB}}{J} \propto -f_{MB}^{-2} \frac{k^2 R_2^4}{a^2} \frac{M}{M_1} \Omega_{\text{orb}}^2 \quad (1.13)$$

where k is the radius of gyration of the part of the star coupled to the magnetic wind and $k^2 = 0.01$ (Verbunt & Zwaan, 1981). f_{MB} is an empirically determined factor varying between $f_{MB} = 0.73$ (Skumanich, 1972) and $f_{MB} = 1.78$ (Smith, 1979).

The standard theory predicts that magnetic braking is the main mechanism for angular momentum loss in systems with orbital periods above three hours, before the secondary becomes fully convective, disrupting the magnetic activity and the mass transfer. For shorter period systems (below two hours), mass transfer will resume when the secondary star makes con-

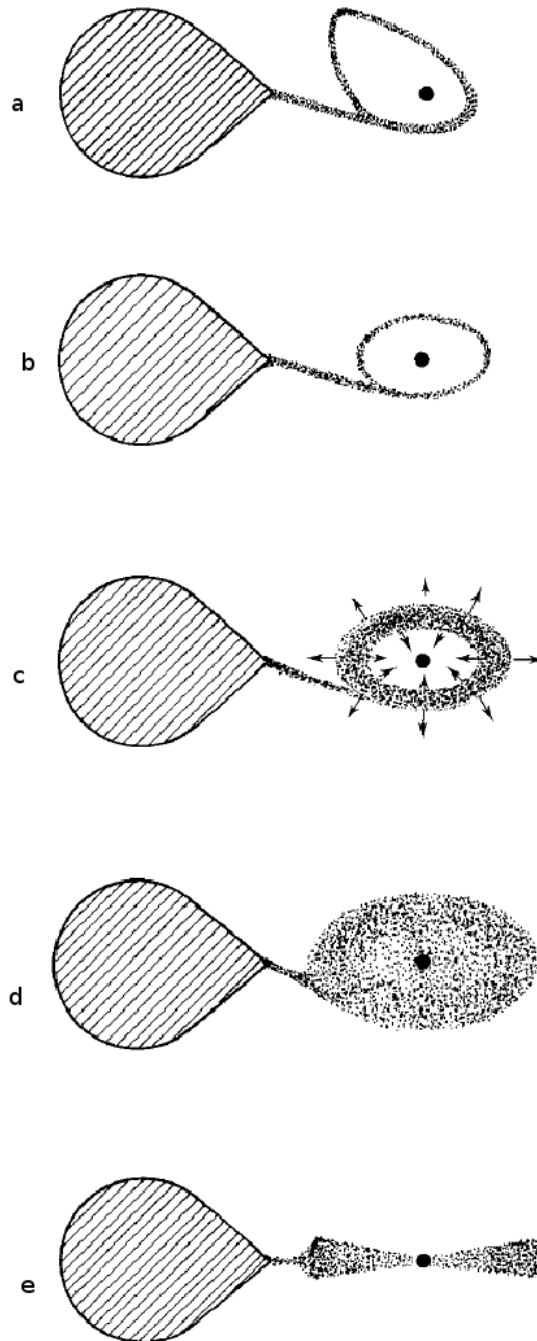


Figure 1.2: Schematic representation of accretion disc formation. Figure from Verbunt (1982).

Initial mass [M_{\odot}]	remnant type	typical remnant mass [M_{\odot}]
$0.95 < M < 8 - 12$	WD	0.6
$8 - 11 < M < 25 - 30$	NS	1.35
$20 < M < 150$	BH	~ 10

Table 1.1: Types of compact remnants of single stars. Table reproduced from Postnov & Yungelson 2014.

tact with its Roche lobe and the main angular momentum loss mechanism will be gravitational radiation.

Gravitational Radiation

General relativity predicts that matter curves space and that the acceleration of a binary system causes ripples in the fabric of space, moving outwards in a periodic wave, a gravitational wave. The energy and angular momentum carried by these ripples is extracted from the binary orbit, causing the system to spiral inwards. The rate of angular momentum loss due to gravitational radiation is given by (Landau & Lifshitz, 1969):

$$\frac{\dot{J}_{GR}}{J} = -\frac{32}{5} \frac{G^4}{c^5} \frac{M_1^2 M_2^2 M}{a^4} \quad (1.14)$$

For wide compact binaries with WD primaries, relativistic effects are weak, but as the stars orbit closer and faster, gravitational radiation dominates, becoming the main angular momentum loss mechanism (Warner, 1995).

1.1.5 Compact Binaries Classification

Compact binaries (CBs) are the end product of the evolution of stellar binaries. They typically consist of a lower mass main-sequence star and a compact object, but there are also double degenerate binaries, with two compact objects. The resulting CB depends on the initial mass of the compact object progenitor, M_0 . If M_0 is lower than the minimum mass required to ignite carbon in the core, then after the hydrogen and helium have burnt the star becomes a WD. If M_0 exceeds a certain mass, the star produces an iron core, which collapses into a NS or a BH. The boundaries between the masses of the progenitors are fairly uncertain, being usually accepted, for solar composition single stars, as the ones shown in Table 1.1.

Cataclysmic Variables

Cataclysmic variable stars (CVs) are compact binaries consisting of a mass-accreting WD primary star and a main sequence secondary star that fills its Roche lobe (Warner 1995). They owe

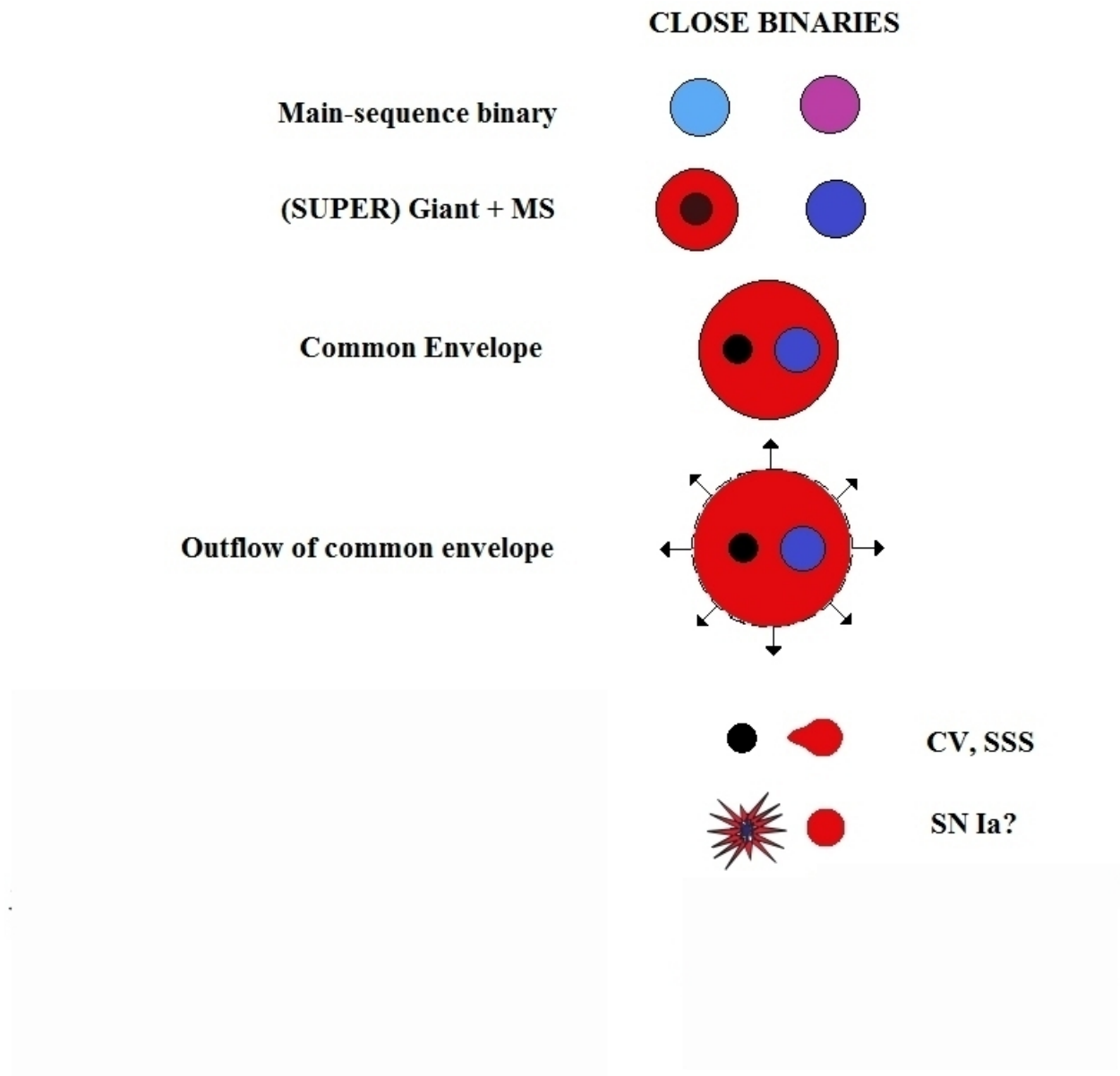


Figure 1.3: Schematic of CV evolution. Based on figure from Postnov & Yungelson (2014). Figure not to scale.

the name “cataclysmic” to their outbursts, observed as modulations in the light curve of the systems. Their prevalence makes CV populations particularly useful for improving our understanding of accretion and compact binary evolution. Figure 1.3 shows a schematic of the evolution of CVs.

Classification The classification of CVs is based on their light curves and refined with spectroscopy. For non-magnetic CVs:

- Dwarf Novae: These systems present outbursts that temporarily increases their brightness by 2-5 magnitudes (see Section 1.1.5). These outbursts last $\sim 2 - 20$ days, recurring on periods ranging from days to several decades. Outbursts are understood as instabilities that take place in the accretion disc, enhancing the accretion on to the surface of the primary star which as a consequence increases the system's brightness. The accretion disc, which in outburst is hot and large, shrinks between outbursts, reaching a cool state called quiescence. The dwarf novae group is further subdivided into three categories:
 - SU UMa: These systems exhibit super outbursts, which are about 5 times longer and brighter than regular outbursts (see Section 1.1.5).
 - Z Cam: These systems exhibit a mixture of outbursts and standstills, remaining for long periods at ~ 0.7 magnitudes below their maximum brightness.
 - U Gem: All the other dwarf novae that are neither SU UMa nor Z Cam.
- Classical novae: These systems have only been observed to have one eruption. We call this a nova eruption as they are thermonuclear runaways originated in the WD surface.
- Recurrent novae: These are systems which originally were classified as classical novae but then a new eruption was observed. Ejection of a shell from the primary stars's surface is observed in spectroscopic data from recurrent novae, separating them from the dwarf novae category.
- Nova-likes: These are all of the non-eruptive CVs with high accretion rates (\dot{M})

Magnetic CVs are classified into two groups, based on the effect the magnetic field of the WD has on the formation of the accretion disc:

- Polars: The WD's magnetic field is so strong that no disc is formed, so the material donated by the secondary accretes onto the poles of the white dwarf, following the magnetic field lines.
- Intermediate polars: These systems have discs that are truncated at the inner edge, where the WD's magnetic field is strong enough to completely disrupt the accretion disc.

Our research will focus on SU UMa type CVs that typically dominate at short orbital periods (shorter than 2 h).

Orbital Period Distribution The orbital period is the time in which the stellar components make a full orbit around the centre of mass. Population analysis of CVs are mainly based on their orbital period distribution, as this parameter is relatively easy to measure. Figure 1.4 presents

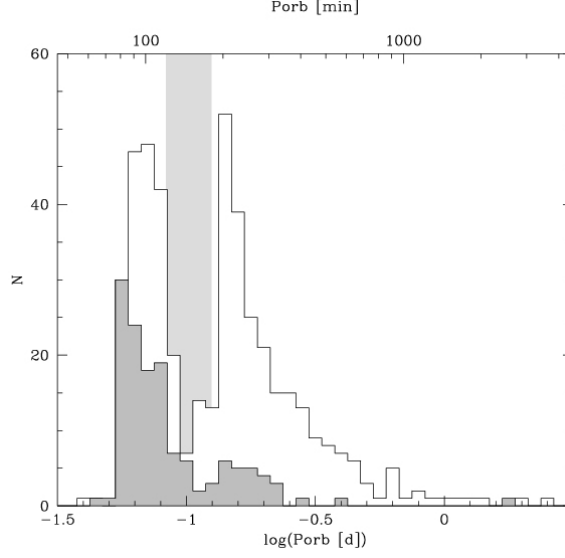


Figure 1.4: Orbital period distribution of 454 CVs from Ritter & Kolb (2003) which have no spectroscopic observation in SDSS DR6 (white) and the distribution of 137 SDSS CVs from Gänsicke et al. (2009) (gray). The gray shaded area represents the 2–3 h orbital period gap. Figure from Gänsicke et al. (2009).

the orbital period distribution from Gänsicke et al. (2009). There are 3 pronounced features that can be explained by the CV evolution models. These are: a sharp cut-off at short orbital periods, known as the period minimum, a deficit of systems in the 2–3 hours regime (grey shaded area), known as the period gap, and a diminishing number of CVs at long orbital periods.

First, notice that for orbital periods above ~ 12 hours ($-0.3 \log(d)$ in the figure) the number of systems considerably decreases. This is a result of the requirement that the secondary be less massive than the WD for stable mass transfer. The systems are then limited by the Chandrasekhar limit of a WD being $\leq 1.4M_{\odot}$; the mass of the secondary is also constrained by this limit. As the size of the binary increases with orbital period, so does the size of the secondary's Roche lobe. Larger Roche lobes require larger secondaries to fill them, setting the ~ 12 hours limit on the orbital period.

The grey shaded area in Figure 1.4 marks the abrupt drop of systems between 2–3 hours, commonly called the “period gap”. The period gap is produced when the main sequence donor becomes fully convective and magnetic braking becomes inefficient, dramatically reducing the angular momentum loss rate. The secondary responds to mass loss by contracting. During magnetic braking this happens on a long time scale, the secondary being slightly too large for its mass. When magnetic braking ceases at the higher end of the gap, the secondary contracts to its right size and the mass transfer stops. Gravitational radiation decreases the period until at the lower edge of the gap, mass transfer resumes.

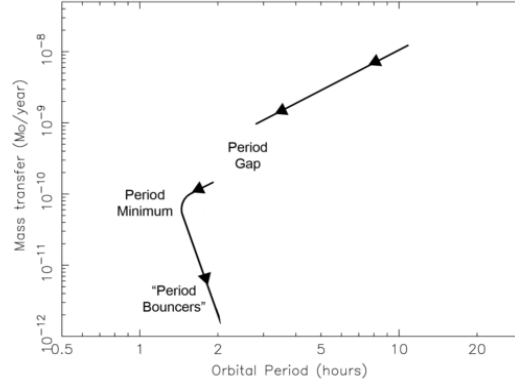


Figure 1.5: Mass transfer versus orbital period of CVs. Evolution proceeds from magnetic braking (MB) above the gap, and then by gravitational radiation (GR) below the gap (from Hellier (2001))

Angular momentum loss by magnetic braking (Rappaport et al. 1983) and gravitational radiation (Paczynski & Sienkiewicz 1981) drives CVs to shorter periods while the donor is transferring mass (see Figure 1.5). When the mass of the donor becomes too low to sustain hydrogen burning, it becomes degenerate, causing the orbital period to increase and hence we have a minimum orbital period (see Section 1.1.2 and 1.1.4).

It is believed that a large percentage of CVs should have evolved towards short orbital periods (~ 80 min). At this so-called period minimum, when the donor becomes degenerate, it no longer shrinks, but it expands in response to mass loss, and the period evolution reverses sign, leading to a period increase. Thus a CV is expected to spend a significant fraction of its time with an orbital period near the period minimum. Because of this, a significant accumulation of CVs at the minimum period is expected. This accumulation is often called the ‘period minimum spike’ (e.g. Kolb & Baraffe 1999). Two families of CVs are expected to coexist near the period minimum, one evolving from longer periods down towards the period minimum and the other one that has reached the minimum and is evolving out to longer periods (see Figure 1.5). The key difference between both families lies in the mass of the donor star. The first family is expected to have low mass main sequence stars, while on the second one, the donor has evolved towards much lower masses and resembles a brown dwarf.

The optical spectra of systems with periods close to the minimum period are dominated by the WD without showing a discernible signature of the faint donor star. This spectral signature has often made the orbital period the only measurable system parameter. Unfortunately this translates into having very few solid mass constraints in the non-eclipsing short orbital period regime and it is not trivial to determine which systems near the period minimum are pre or post bounce. In order to validate the theory and position the CVs on the correct evolutionary track (evolving towards or from the period minimum), more information about the parameters

of individual systems is needed, particularly, the masses of the components. The measurement of the superhump period (read further along this Section for the definition) could potentially provide an indication of the mass ratio of the systems via the empirical relation between the two observables (Pearson, 2006), but is poorly constrained at the short orbital periods end (see above).

While the standard CV evolution model can explain the bulk features of the CV period distribution, more quantitative comparisons between evolutionary models and the CV population are desired, in particular for those systems where more than just the binary period is known. Theoretical models of the evolution of CVs predict the distribution of their orbital parameters: orbital periods, mass ratio $q = M_2/M_1$ and the individual masses of the two stars, $M_1 + M_2$. Regrettably, too often the only reliable physical parameter that can be measured for most CVs is their orbital period, since the faint donor stars and cool WDs are difficult to find. In order to validate the theory and pinpoint the evolutionary track of CVs – evolving towards (pre-bounce) or from the period minimum (post-bounce) – more information about the parameters of individual systems is needed. Particularly, the mass of the secondary star can differentiate a pre- from a post-bouncer as the evolution of CVs is controlled by the properties of their secondaries (Knigge et al., 2011).

Dwarf Nova Outbursts The standard theory to explain the disc outbursts is a thermal-viscous instability that occurs in the accretion disc, called the disc instability model (Osaki, 1974). The viscosity is given by the so called α -prescription, where the viscosity is given by (Shakura & Sunyaev, 1973):

$$\nu = \alpha c_s H \quad (1.15)$$

where α is a number less than one, H is the vertical height of the disc and c_s is the sound speed in the gas. The instability arises when hydrogen becomes partially ionised and the disc opacity varies with temperature. A number of characteristics of many light curves are reproduced by the disc instability model if we assume that the viscosity parameter α is different in quiescence and in outburst.

Superoutburst and Superhumps During superoutburst, SU UMa stars show large amplitude variations in their light curves, with a periodicity that is slightly longer than their orbital period. These are called superhumps and are believed to be produced by the precession of an eccentric disc (Whitehurst 1988, Hirose & Osaki 1990 and Lubow 1991). In the inner disc, orbits are circular, but towards the edge of the disc, the presence of the secondary distorts the orbits, making them non-circular and forming a small bulge in the disc that is closest to the secondary. The disc orbits faster than the secondary, so the bulge tries to move ahead of it. The gravitational pull

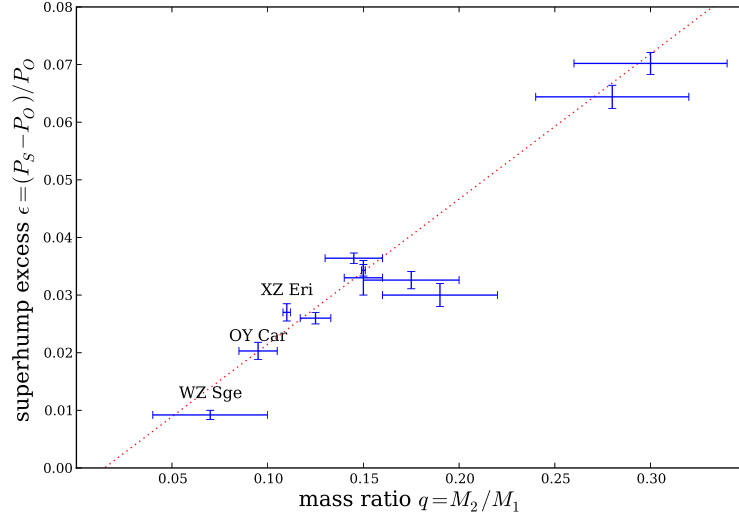


Figure 1.6: A CV superhump period is slightly in excess with respect to its orbital period. The figure shows that the fractional period excess appears to be correlated with the mass ratio “ q ” for the small number of systems with independent mass ratio estimates. This has potentially led to the use of the superhump period excess as an estimator of the mass ratio of many CVs. However, the low mass ratio end ($q < 0.12$) is poorly calibrated. The dashed line indicates the currently employed empirical conversion from superhump excess to “ q ”.

of the secondary slows the bulge, reducing its angular momentum thus helping the material to flow inwards in the disc. In equilibrium, this bulge would orbit slightly ahead of the secondary. However, if the secondary’s tidal interaction resonates with the radial motion of the disc, it will enhance the radial component of the motion, driving the outer disc elliptical. The most common resonance excited is 3:1, but in more extreme mass ratio systems, 2:1 can also be excited. As the elliptical orbits are no longer parallel to the circular inner orbits, these now intersect and cause collisions that result in energy dissipation and an enhanced emission in the system’s light curve. This emission appears as a hump-shaped modulation when the system reaches the peak of the super-outburst. Superhumps are commonly seen in CVs, and are discussed in more detail by Warner (1995), and can also occur in low mass X-ray binaries (LMXBs, Section 1.1.5).

When the mass ratio q is small enough, observations have revealed a correlation between the orbital period and the superhump period (Patterson et al. 2005, Pearson 2006, Knigge et al. 2011, see Figure 1.6). A CV superhump period is slightly in excess with respect to its orbital period. Figure 1.6 shows that the fractional period excess appears to be correlated with the mass ratio “ q ” for a number of systems with independent mass ratio estimates. This has led to the use of superhump period excess as an estimator of the mass ratio of many CVs. However, the low mass ratio end is poorly calibrated. In the short period / small q regime, the relation hinges upon only two systems, OY Car and WZ Sge. In the case of WZ Sge, published values of the mass

ratio vary by more than a factor of two and thus its use as a calibrator may be questioned. The dashed line indicates the currently employed empirical conversion from Knigge (2006). One of the aims of this work is to identify new calibrators for this empirical relation, especially in the low mass ratio end, and test the validity of the relationship.

X-ray Binaries

X-ray binaries come in a diverse range of systems, the most common division made between binaries with low or high mass secondary stars: low mass X-ray binaries (LMXB) and high mass X-ray binaries. This work will only concern LMXBs as these share the geometry of CVs but with a NS or BH as the compact object. Observationally, we can differentiate LMXB, into persistent and transient sources. In quiescent transient sources, the light usually becomes dominated by the secondary, allowing radial velocity studies to measure the system parameters, particularly the compact object mass. This is not possible in persistent sources.

Yet another important distinction is made between systems containing NSs or BHs. This classification is important, since many similarities can be found in the behaviour of low mass and high mass X-ray binaries. Both NS and BH binaries are descendants of initially massive binaries (Postnov & Yungelson, 2014). Figure 1.7 presents the standard evolutionary scenario for the formation of NS or BH binaries, from main sequence to potential merging of the components; see text in the Figure for details.

As we mention in Section 1.1.5, LMXBs can also exhibit superhumps. The most likely LMXBs to exhibit superhumps are BH systems since they have more extreme mass ratios than most NS LMXBs. The superhump mechanism in LMXBs is different than the one operating in CVs. As the optical light in a LMXB is not dominated by viscous dissipation, but by irradiation by X-rays, the superhumps arise from coupling of irradiation to tidal distortion of the disc (e.g. Haswell et al. 2001).

1.1.6 Orbital Parameters

In this section, we will present some of the physical parameters of CBs.

Orbital Period

Observing a binary system long enough with either photometry or spectroscopy will provide us with periodicities in the data that will allow us to determine the orbital period. The most commonly used technique to find such a periodicity is Scargle's periodogram (Scargle, 1982). It consists of a period dependant trigonometric function, P_x , that weights the data producing an indicator of how good a certain period describes the data. The periodogram allows inspection of

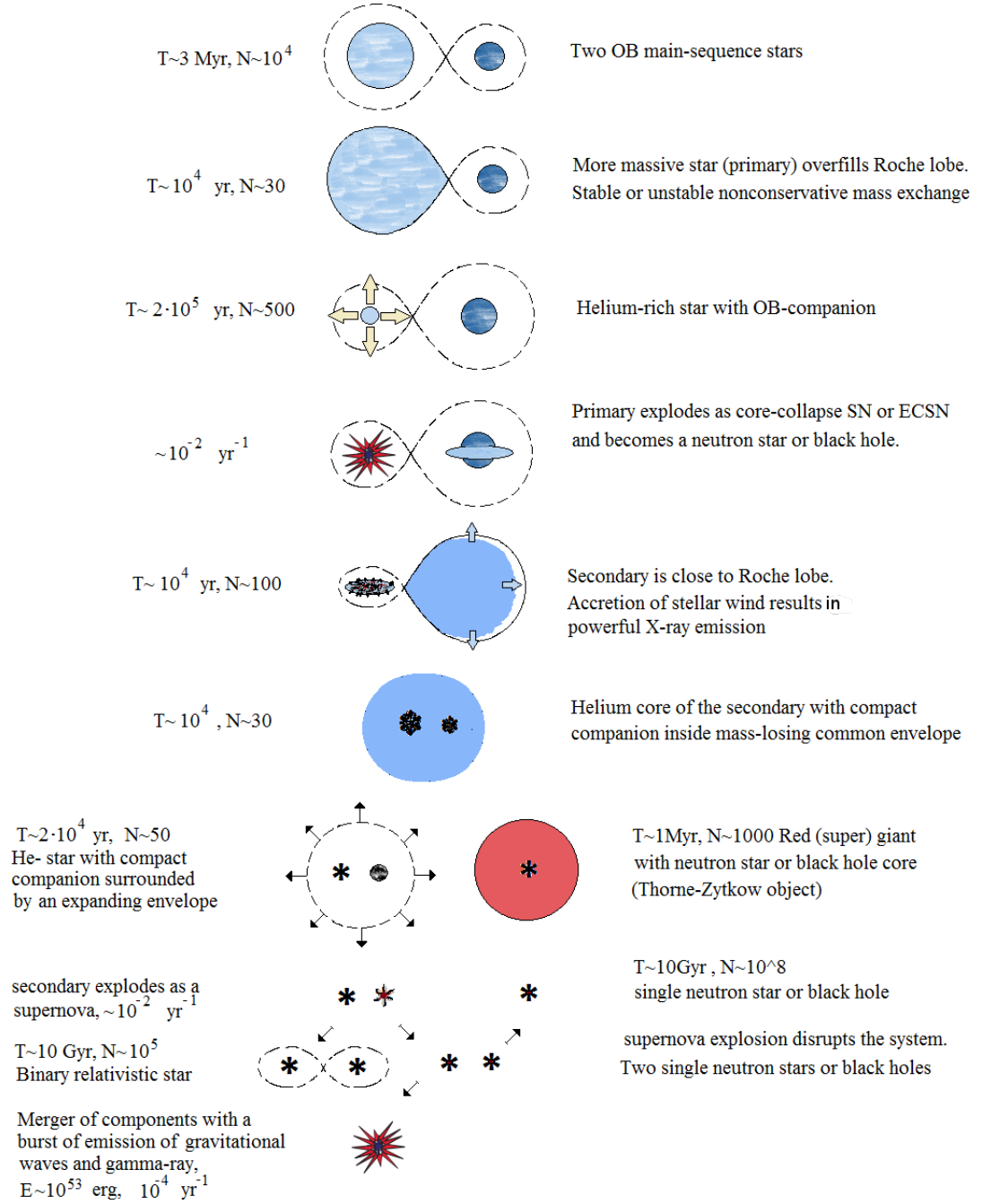


Figure 1.7: Evolution of NS binaries. Based on figure from Postnov & Yungelson (2014). Figure not to scale.

a given range of periods simultaneously, allowing for random contributions to disappear (except for the ones generated by the data collection itself). The test function is defined as:

$$P_x(\omega) = \frac{1}{2} \frac{\left[\sum_j X_j \cos(\omega)(t_j - \tau) \right]^2}{\sum_j \cos^2(\omega)(t_j - \tau)} + \frac{\left[\sum_j X_j \sin(\omega)(t_j - \tau) \right]^2}{\sum_j \sin^2(\omega)(t_j - \tau)} \quad (1.16)$$

where t_j are the sample times, X_j are the time series data, τ is the time delay and is given by:

$$\tan(2\omega\tau) = \frac{\sum_j \sin(2\omega t_j)}{\sum_j \cos(2\omega t_j)}$$

and ω is the candidate frequency, the inverse of the candidate period.

In practise, aliases and some orbital dependant variations (e.g. pulsations, elliptical discs), complicate the task of finding an accurate orbital period. Despite this, often enough, the orbital period is the only well determined orbital parameter for many CBs.

The plot of the candidate periods versus the test function is called a “periodogram”, hence the name of the technique.

Phase Zero

When the binary star orbits around its centre of mass, depending on its relative position with respect to the observer, it goes through different phases. When the primary star is aligned with the centre of mass and the secondary is between it and the observer, we call it phase zero or conjunction, as shown in Figure 1.8. Orbital phases go from 0 to 1. In Figure 1.8, we marked phases 0.25, 0.5, and 0.75, increasing anticlockwise. When the primary reaches phase zero again, this will now be phase 1 from the current orbital cycle and phase zero of the next cycle.

Inclination and Masses

Figure 1.9 shows the orbit of two masses M_1 and M_2 with an orbital period P_{orb} and a centre of mass separation of $a = a_1 + a_2$, where $a_1 M_1 = a_2 M_2$. The inclination angle is usually measured between the orbital plane of the system and the plane of the observer (ecliptic), perpendicular to the line of sight. If we observe the system with an inclination i , then the orbital velocity projected along the line of sight will be:

$$K_1 = \frac{2\pi a_1}{P_{orb}} \sin i \text{ and } K_2 = \frac{2\pi a_2}{P_{orb}} \sin i \quad (1.17)$$

for the primary and secondary, respectively. We will discuss how to measure these velocities in Chapter 2.

Combining 1.17 with Kepler’s third law, Eq. 1.5, we obtain:

$$\frac{(M_2 \sin i)^3}{(M_1 + M_2)^2} = \frac{P_{orb} K_1^3}{2\pi G} \quad (1.18)$$

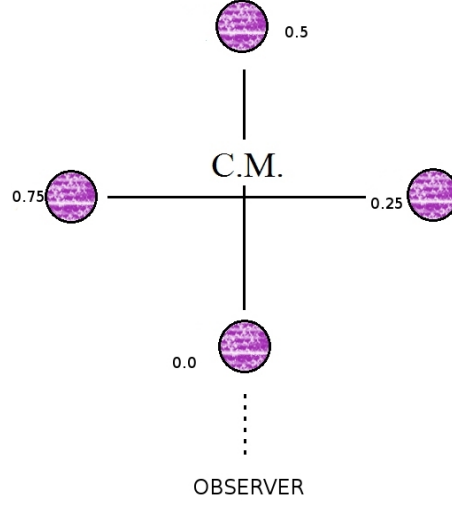


Figure 1.8: Orbital phases. The centre of mass is marked as C.M.

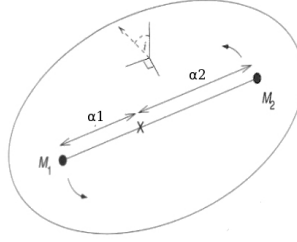


Figure 1.9: Two stars of masses M_1 and M_2 orbiting in a plane around their common centre of mass. The arrow points towards the observer, defining the inclination angle i .

and

$$\frac{(M_1 \sin i)^3}{(M_1 + M_2)^2} = \frac{P_{orb} K_2^3}{2\pi G} \quad (1.19)$$

where $a = a_1 \left(\frac{M_1 + M_2}{M_2} \right)$. Dividing these two equations, we obtain the mass ratio as in Eq. 1.4.

If the orbital period is known, we still would need the system inclination i to determine the mass ratio. The standard method to estimate the masses of a binary with a known orbital period is to measure K_1 , K_2 and i or to measure two of these three and another restriction (e.g. q).

1.2 Spectral Line Formation

A spectral line is a dark or bright line over a continuum spectrum. Each chemical element produces its own unique pattern of spectral lines, a unique set of wavelengths characteristic of that

element alone, allowing us to study the composition of celestial objects with spectral analysis. Figure 1.10 shows the spectra of Sodium in emission and absorption. To understand the differences between these two spectra, we must remember some basic quantum mechanics: given the Planck-Einstein relation:

$$E = \frac{hc}{\lambda} \quad (1.20)$$

where h is the Planck's constant $h = 6.62606876 \times 10^{-34}$ J s (Carrol & Ostlie, 2007). This relation shows that the energy of a photon E is inversely proportional to its wavelength λ . The wavelength is related to the frequency (ν) as $\lambda = c/\nu$. Given Bohr's frequency condition:

$$\Delta E = h\nu \quad (1.21)$$

where ΔE is the energy difference between two energy levels involved in an electronic transition.

When the electron jumps from one level to another, the atom emits or absorbs a photon of energy equal to the difference in energy between the two levels. From Equation 1.20, if two photons have the same energy, they must also have the same wavelength λ . Hence, if an atom can emit photons of a certain wavelength, it can also absorb photons of precisely the same wavelength, explaining what we see in Figure 1.10; a hot, dense gas or solid object produces a featureless continuous spectrum, a blackbody. A hot, diffuse gas produces bright emission lines. These are produced when an electron jumps from a higher to a lower orbit. The energy lost is carried away by a single photon that has two ways to decay: to ground state or to cascade one orbital at a time. A cool, diffuse gas in front of a source of continuous spectrum produces dark absorption lines in the continuous spectrum. These are produced when an electron jumps from a lower to a higher energy level, absorbing a photon that carries exactly the amount of energy equal to the difference in energy between the higher orbit and the electron's initial orbit.

These observations are summarised in Kirchhoff's laws (Kirchhoff, 1860):

1. A hot opaque body, such as a perfect blackbody, or a hot dense gas produces a continuous spectrum.
2. A hot transparent gas produces an emission line spectrum.
3. A cool, transparent gas in front of a source of a continuous spectrum produces an absorption line spectrum.

These results are used for the identification of chemical elements found in the stars (Figure 1.10), and also to study their velocities. The motion of a light source also affects wavelengths,

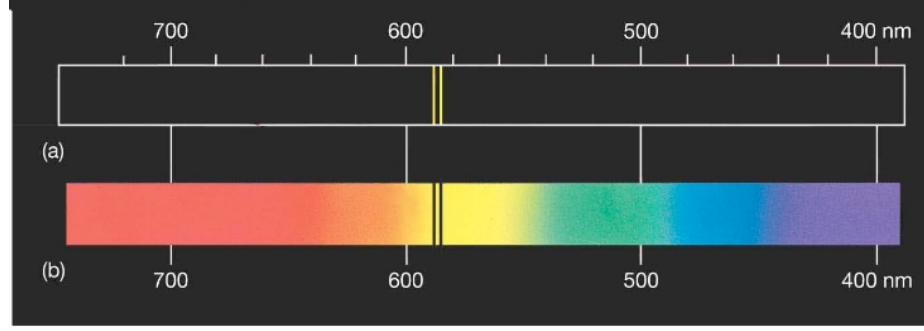


Figure 1.10: Emission and absorption spectra of Sodium.

permitting us to deduce how fast stars and other objects are approaching or receding. Measuring the non-relativistic Doppler shift of spectral lines can be used to determine the star's radial velocity (v_r):

$$\frac{\lambda_{\text{obs}} - \lambda_{\text{rest}}}{\lambda_{\text{rest}}} = \frac{\Delta\lambda}{\lambda_{\text{rest}}} = \frac{v_r}{c} \quad (1.22)$$

where λ_{obs} is the observed wavelength, λ_{rest} is the rest wavelength and c is the speed of light.

An ideal surface that absorbs all wavelengths of electromagnetic radiation that are incident upon its surface, will also emit at all possible wavelengths. This ideal surface is called a blackbody, and the continuous spectrum radiation that is emitted is known as blackbody radiation, which at absolute temperature T is given by

$$B_\nu(\nu, T) = \frac{2h\nu^3}{c^2} \frac{1}{e^{\frac{h\nu}{k_B T}} - 1} \quad (1.23)$$

where B_ν is the energy per unit time radiated per unit area of emitting surface by a blackbody of temperature T , h is the Planck constant, c is the speed of light, k_B is the Boltzmann constant ($1.3806488(13) \times 10^{-23} \text{ J K}^{-1}$) and ν is the frequency. This is the greatest amount of radiation that any body at thermal equilibrium can emit from its surface. Figure 1.11 shows blackbody curves for different temperatures T , we can see that blackbodies with different temperatures will peak in different colours of the visible spectrum.

Bearing these ideas in mind, it is possible to have a physical understanding of the nature of light in astronomical sources.

1.2.1 Spectral Features in CBs

In the following Sections, we will describe some of the characteristic spectral features of both CVs and LMXB.

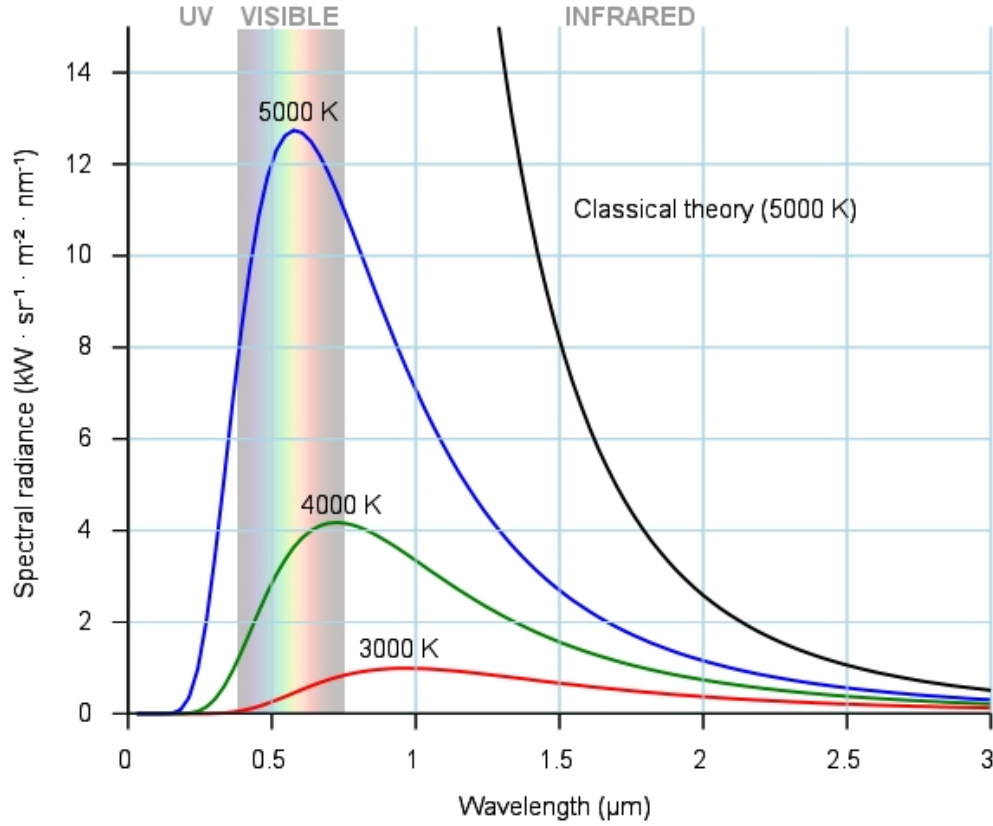


Figure 1.11: Blackbody radiation curves. Image created for educational purposes, courtesy of “Darth Kule”.

Spectral Features of CVs

CVs spectra originate from a range of individual components with different temperatures. If we remember equation 1.23, different temperatures will peak in different regions of the spectrum, making CVs suitable to study from the X-ray to the infra-red (Hellier, 2001). In optical wavelengths, the spectrum is usually dominated by bright accretion disc lines from low ionisation states of hydrogen, helium, iron, calcium and oxygen: H I, He I, He II, Fe II, Ca II and O I. Sometimes, the Bowen blend and other heavier elements are also present.

White Dwarf: The WD has typical temperatures of $T \sim 10000\text{K}$ and peaks near the ultra-violet. The high atmospheric pressure of WDs causes broadening of its spectral lines, most of which are absorption lines of hydrogen. In accreting WDs, some narrow metal lines can also be seen in absorption, due to accreted gas. Detecting any WD absorption line in a CV spectrum can allow us to directly determine K_1 . Unfortunately, these are only visible when they outshine the accretion disc, which usually happens only in low accretion rate systems.

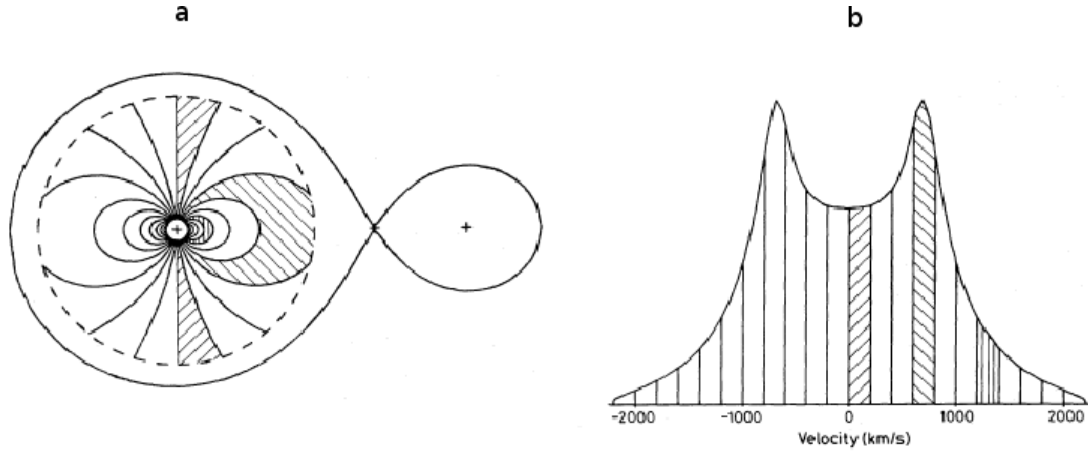


Figure 1.12: Accretion disc's double peaked profile formation. The hatched areas are regions of constant velocity. The corresponding radial velocities of the disc hatched on the left (a) are indicated by the same hatched pattern on the double peaked profiles on the right (b). From Horne & Marsh (1986).

Donor Star: As the donor star is a cool body ($T \sim 3000 - 6000K$), the spectrum is often significant only at red and infrared wavelengths. Spectral absorption features caused by titanium oxide (TiO) molecules can be present in M dwarf type secondaries. If enough energy is available to excite the atoms on the irradiated face of the donor, we may also see emission lines.

Accretion Disc: The accretion disc is often the dominant feature in a CV and it is normally modelled as the sum of a series of blackbodies with temperatures appropriate for each radius of the disc (hotter on the inside and cooler on the outside of the disc), although this is a quite simple approximation. It can show either emission or absorption lines, depending on its temperature. In a quiescent CV, it is optically thin, showing double peaked emission lines due to the radial velocities of the rotating disc projected along our line of sight, as shown in Figure 1.12. During outburst, the disc becomes optically thick and the spectral features become often dominated by strong, single peaked absorption lines. As the disc is centred on the WD, it follows its motion about the common centre of mass. When no WD feature is present in the spectrum, we use this fact to indirectly trace K_1 through the radial velocity of the disc.

Total Spectrum: The total spectrum of a CV will be a superposition of the individual spectra of the WD, the mass donor and the accretion regions. The extent to which each component will be visible depends on the accretion rate. In high accretion rate systems, the disc will dominate. In low accretion rate systems, we may see the WD and donor features on top of the disc's spectrum, allowing direct measurement of their radial velocities. Figure 1.13 shows an example of CV spectra over a wide range of wavelengths. Overlapped in grey are the models of a WD and a late type

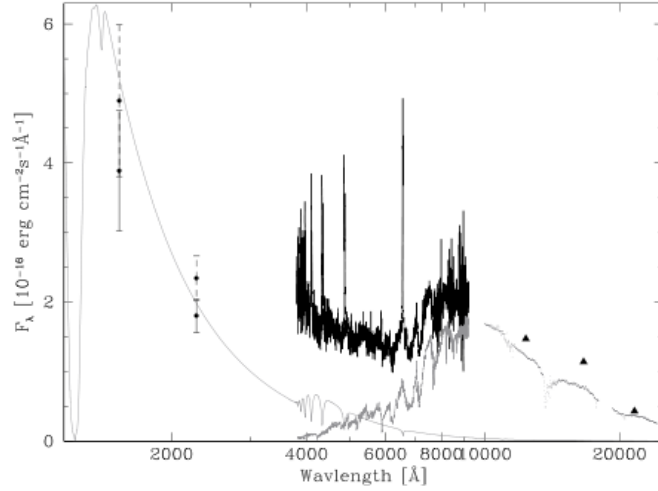


Figure 1.13: Multiwavelength spectrum of the cataclysmic variable SDSSJ10658.40+233724.4 from Southworth et al. (2009). The solid black line is the SDSS optical spectrum, the error bars are the GALEX UV fluxes and the black triangles are the 2MASS near infrared flux of the system. In grey are models of a M3.2 star (right) and a WD spectrum (left).

star.

Low Mass X-ray Binaries Spectra

Quiescent LMXBs present emission line profiles quite similar to CVs: double-peaked hydrogen and helium lines, consistent with an accretion disc dominated profile. Luminous systems can show a range of different lines, the main ones being carbon, nitrogen, oxygen and silicon. In the optical, the strongest of these metal features is the Bowen blend (see McClintock et al. 1975, and Section 1.3), lines generated on the secondary surface via fluorescence. Figure 1.14 shows an example of a LMXB spectrum indicating the position of the Bowen blend. In quiescence, higher excitation lines of He II are absent, and only weak He I and H I are present in emission. If the disc is dim enough, the companion star spectrum emerges, facilitating radial velocity constraints and hence, the derivation of the system parameters.

1.3 Ca II and the Bowen blend

Marsh & Dhillon (1997) found that the double peaked profile in a set of CVs was clearer in the fainter Ca II triplet (8498.03 Å, 8542.09 Å and 8662.14 Å) than in the Balmer lines. They suggested that the Ca II suffered less broadening than the Balmer lines, and although they couldn't determine the exact broadening mechanism that smoothed the peaks in the Balmer lines, it was clear that the Balmer lines are intrinsically broad, broad enough to smooth the structure contained in the profile. Despite this, nearly all the constraints on orbital parameters of non-eclipsing sys-

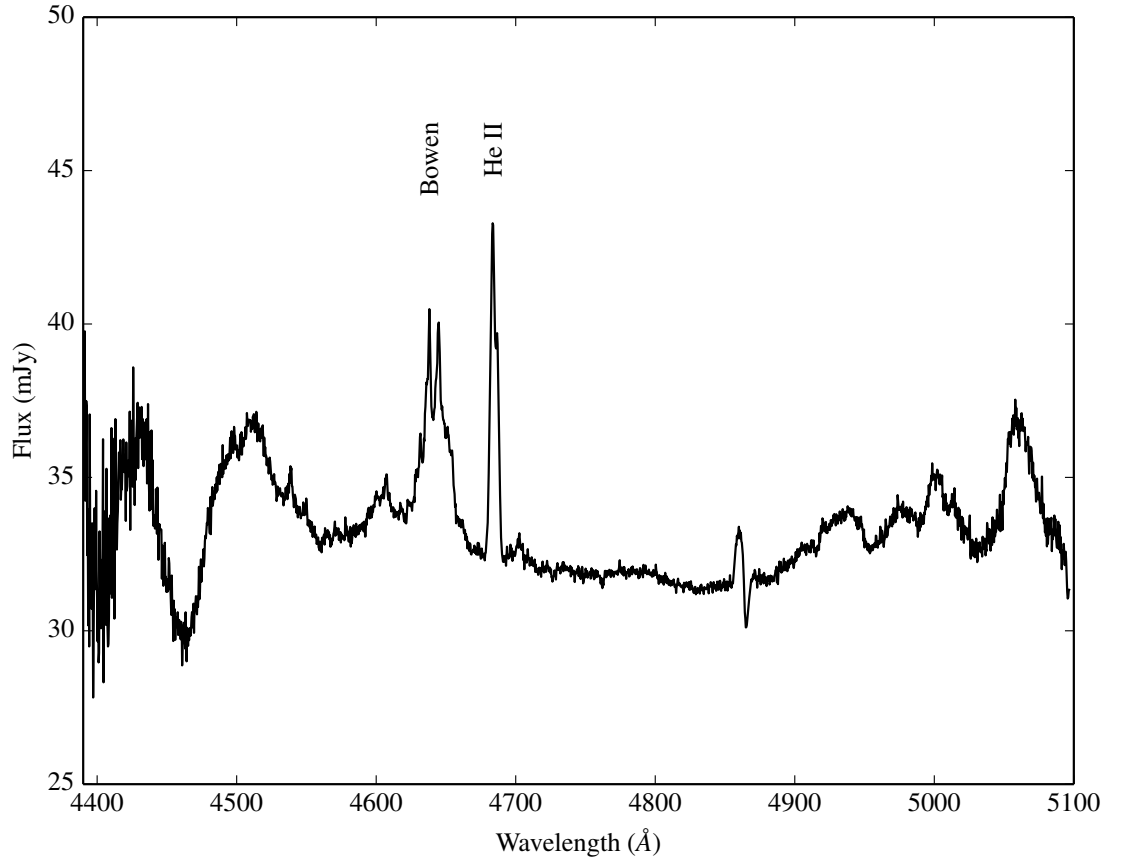


Figure 1.14: Section of the MagE spectrum of the LMXB Sco-X1 showing the position of the Bowen blend and He II 4685.78Å.

tems are limited to the study of the Balmer emission lines (e.g. Southworth et al. (2007), Neilsen et al. (2008), Mennickent et al. (2006)). Only recently, van Spaandonk et al. (2010) introduced the superior feature resolution of the Ca II triplet over the Balmer lines. Doppler tomography of the triplet showed that these lines also traced the movement of the irradiated face of the secondary star better than the Balmer, proving to be an auspicious candidate for orbital parameter constraints. Despite the relative weakness of the Ca II triplet with respect to the Balmer lines, it is commonly found in short period CVs and has a lower ionisation energy than H and He, thus is capable of being excited even by cool sources of radiation. Its thermal width and pressure broadening are smaller than H leading to sharper and more easily detected emission lines (Marsh & Dhillon, 1997). It is no surprise then that it can trace the movement of the donor star better than the Balmer lines, but the remaining question was: is it as common as the Balmer lines? In a survey of 18 short period CVs performed by Steeghs et al. (in preparation), disc emission features were found in the Ca II triplet lines in 90% of the surveyed quiescent systems and donor emission

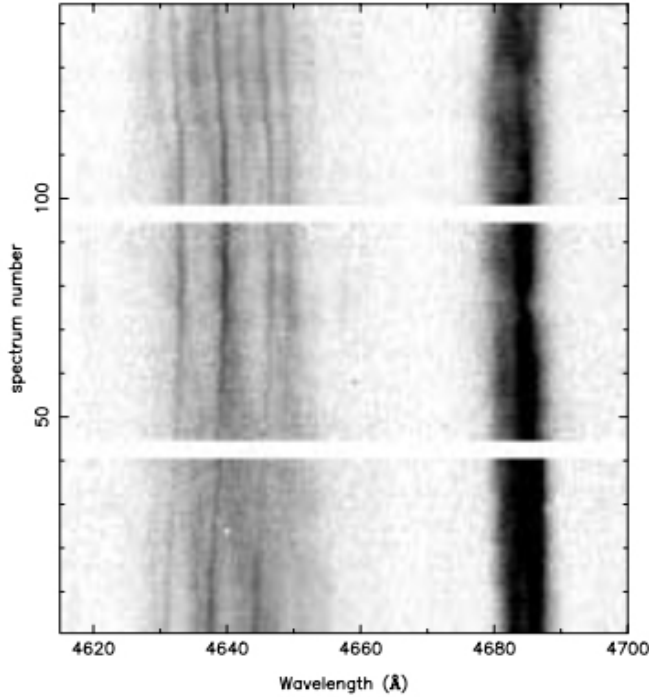


Figure 1.15: Trailed spectra of the Bowen blend and He II of Sco X-1 from Steeghs & Casares (2002).

features in 75% of these systems.

In the case of persistent LMXB systems, where no quiescent state is observed, as the spectra is dominated by the disc, we must look for a different source of radial velocity information. Steeghs & Casares (2002) proposed a new approach after finding narrow emission components, moving in anti phase with the disc components, in the Bowen blend (a mixture of mainly C III 4647.42/4650.25Å - N III 4640.64/4634.12Å lines). The idea that this feature was generated by the Bowen fluorescence process was proposed by McClintock et al. (1975), naming Sco X-1 and Her X-1 as good LMXB candidates to search for these lines. Looking at the trailed spectra of Sco X-1 by Steeghs & Casares shown in figure 1.15, we can see these narrow components trace the velocity of the secondary star. The major caveat here is that these emission lines originate from the irradiated inner face of the donor star, and so their centre of light would not coincide with the centre of mass of the secondary, thus the K_{em} value derived from this method is a lower limit to the true value of K_2 and must be corrected to derive the true value. We will discuss this technique in Chapter 2.

1.4 Summary and Outline

We have presented a short review on the formation of spectral lines, mentioning the main features of CB classes. We have set the scene of CBs by showing their geometry, parameters, classification and evolution. We have also explained the importance of constraining orbital parameters other than just the orbital period to test evolution theories and determine the nature of CBs. We showed some of the main problems in constraining the dynamical parameters of persistent LMWBs and short period CVs. Finally, we introduced the Ca II triplet and the Bowen blend as suitable alternatives to constrain these parameters

In the following Chapters we will study methods to dynamically constrain orbital parameters of CBs, particularly, the mass ratio q . In Chapter 2, we will discuss both classic and new methods necessary to constrain these parameters. In Chapter 3 we will apply these methods to constrain the mass ratio of the LMXB 4U 1957+11. Finally, in Chapters 4 and 5, we will compare our new methods against classic ones and constrain the orbital parameters of two sets of short period CVs.

Two

Methods

‘Understanding the light is a prerequisite to understanding the Universe’.

The Doppler tomography methods presented in this Section were published in:

“Emission line tomography of the short period cataclysmic variables CC Scl and V2051 Oph”

P. Longa-Pena; D. Steeghs; T. Marsh

Monthly Notices of the Royal Astronomical Society 2014, 447 (3): p 149-159

In this thesis, our main observational input has been time resolved spectroscopic data. Most of this time was spent developing and testing indirect imaging dependant methods to obtain a good estimate of the mass ratio of short period CVs with reliable uncertainties. The functionality of the methods was extensively tested in several different lines of several systems, proving to be reliable in the cases where there were known parameters. In practise, for non-eclipsing systems, obtaining a reliable estimate of any orbital parameter (except the orbital period) is not trivial, hence the importance of these new methods.

This chapter covers the basics of spectroscopy, CCD reduction and analysis of spectroscopic data. We will describe the different methods used to analyse these data and the techniques used to constrain the system parameters for our CBs sample.

2.1 Spectroscopy

In astronomy, spectroscopy is the study of the electromagnetic radiation as a function of wavelength of a celestial body. It detects the absorption or emission of radiation within a continuum at certain energies, and relates these with the energy levels implied for a given quantum transition. It is one of the most important tools for an astronomer to study the Universe. By means of studying the continuum and the emission and absorption lines, we can determine physical and chemical properties of distant celestial bodies.

In this Section we will discuss long-slit and Echelle spectroscopy, with special emphasis in the Magellan Echellette (MagE) spectrograph, with which most of the data in this thesis was obtained. In Section 2.1.3 we will discuss some basics of CCD reduction with special focus on MagE's reduction pipeline.

2.1.1 Long Slit Spectroscopy

Although modern spectrographs are more diverse and complex than the original prism used to disperse light from the Sun, the basic elements are still the same for every astronomical spectrograph. Every functional spectrograph should contain four essential elements (Carrol & Ostlie, 2007):

- a slit, to focus the light from the telescope and control the resolution.
- a collimator, to parallelize the light beam.
- a disperser, to disperse incoming light from an astronomical source.
- a camera, to focus the spectrum onto the detector.

As shown in Figure 2.1 the slit is placed in the focal plane of the telescope and the light from the star is focused onto the slit. Light then passes through a collimator, that forces the light to travel in a parallel direction and directs the beam towards the disperser, in most cases a grating with a number of grooves per millimetre. The dispersion of the grating depends directly upon the projected number of grooves per millimetre and is governed by the grating equation (Massey & Hanson, 2013):

$$m\lambda = \sigma(\sin(i) + \sin(\theta)), \quad (2.1)$$

where i is the incidence angle, θ is the refraction angle (see Figure 2.1), and m is an integer representing the order in which the grating is being used. Due to constructive interference, light from more than one order is simultaneously observed. The dispersion of an order m , also known as the angular spread, can be found by differentiating:

$$\frac{d\theta}{d\lambda} = \frac{m}{\sigma \cos(\theta)}, \quad (2.2)$$

for a given incidence angle i . If $i = \theta$ (called the Littrow condition):

$$\frac{d\theta}{d\lambda} = \left(\frac{2}{\lambda}\right) \tan(\theta) \quad (2.3)$$

A conventional spectroscope must be used in low orders ($m = 1$ or 2) to reduce the overlapping of different orders. Blocking filters can also be used to exclude unwanted orders.

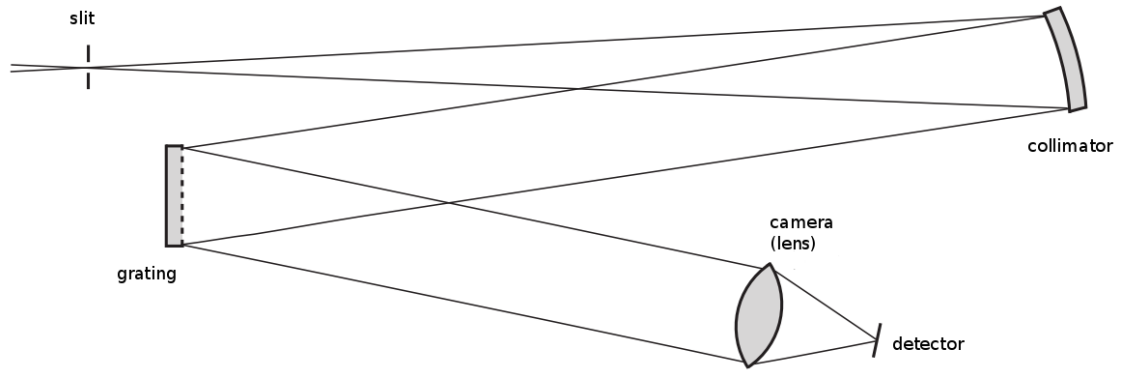


Figure 2.1: Schematic of the essential components of a spectrograph. Based on Figure 1 of Massey & Hanson (2013).

The spectral resolution is defined as:

$$R = \frac{\lambda}{\Delta\lambda}, \quad (2.4)$$

where $\Delta\lambda$ is the difference between two, equally strong, lines than can be resolved (the width of one resolution element). This is called the resolution element. $R \sim 1000$ is considered a moderate resolution, while a resolution on the order of $R \sim 10000$ is considered high. Most of our data is obtained at $R \sim 4100$.

2.1.2 Echelle spectroscopy

In the case of Echelle spectroscopes, a second dispersion element is inserted into the beam after the diffraction grating to provide cross-dispersion of the light, spreading the various orders across the detector. An example of this is shown in Figure 2.2, a spectrum taken with the Magellan Echellette spectrograph, where the detector shows multiple orders next to each other, maximising the use of the CCD detector.

For a given incidence angle θ , the free spectral range $\delta\lambda$ is the difference between two wavelengths λ_m and $\lambda_{(m+1)}$ in successive orders:

$$\delta\lambda = \lambda_m - \lambda_{(m+1)} = \frac{\lambda_{(m+1)}}{m}$$

The angular spread, $\delta\theta$, of a single echelle order will therefore be $\frac{\delta\lambda d\theta}{d\lambda}$. Using equation 2.3 for the angular dispersion:

$$\frac{\lambda}{\sigma \cos\theta} = \delta\lambda(2/\lambda) \tan\theta, \quad (2.5)$$

so the wavelength coverage of a single order will be:

$$\delta\lambda = \frac{\lambda^2}{2\sigma \sin\theta}. \quad (2.6)$$

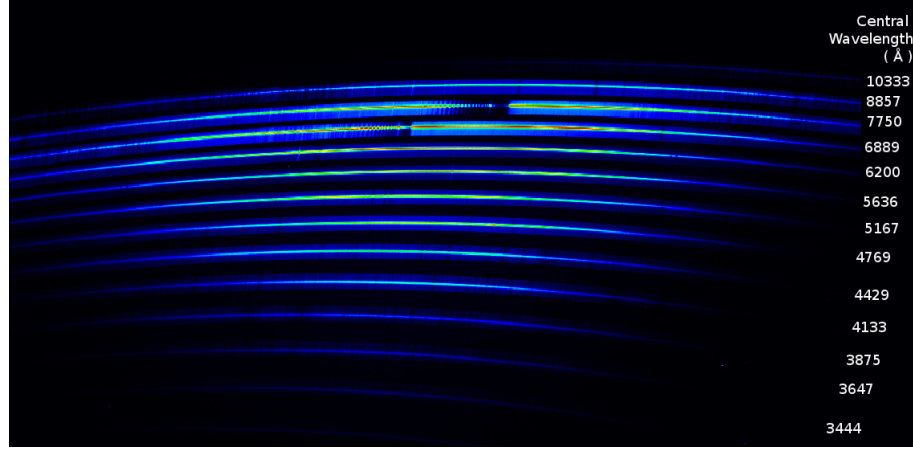


Figure 2.2: MagE spectra of the X-ray binary Sco X-1. The order numbers observed are 6 to 19 from top to bottom of the image, respectively, while the wavelength increases from bottom to top as shown in the figure.

The angular spread of a single order will be:

$$\Delta\theta = \frac{\lambda}{\sigma \cos\theta}. \quad (2.7)$$

The above implies that the number of angstroms covered in a single order increases with the square of the wavelength (Equation 2.6), while the spatial length of each order increases linearly with each order (Equation 2.7). In Figure 2.2 we can see this effect, as the shorter wavelengths span less of the chip and viceversa.

MagE Spectrograph

The Magellan Echellette (MagE) is located on the Magellan II (Clay) telescope at Las Campanas Observatory, Chile. MagE is a single object optical Echellette spectrograph. It provides spectral coverage from 3200 Å to 10000 Å in a single exposure, with a moderate resolution ($R \sim 1000$ to $R \sim 8000$), achieving $R = 4100$ (22 km/s pixel) with a 1" slit (Marshall et al., 2008).

Figure 2.4 shows the optical design of the instrument. Some elements are easily identified from the schematic of Figure 2.1 (the slit, collimator, prism, grating, camera and the detector). The light is focused onto a slit and then collimated by a mirror. There are also two cross dispersing prisms. The first one is used in double pass mode and the second one in a single pass. The grating has 175 lines/mm and is used in a quasi-Littrow configuration.

From Equation 2.1.2 we can deduce that the free spectral range scales inversely with the order number, so for low order numbers the free spectral range should be larger. This is not the case shown in Figure 2.2, since MagE spectrograph uses prisms and gratings for cross-dispersion, and the dispersion of a prism is greater in the blue than in the red, explaining the opposite behaviour to that predicted by Equation 2.1.2.



Figure 2.3: Photograph of MagE installed on the Magellan II telescope.

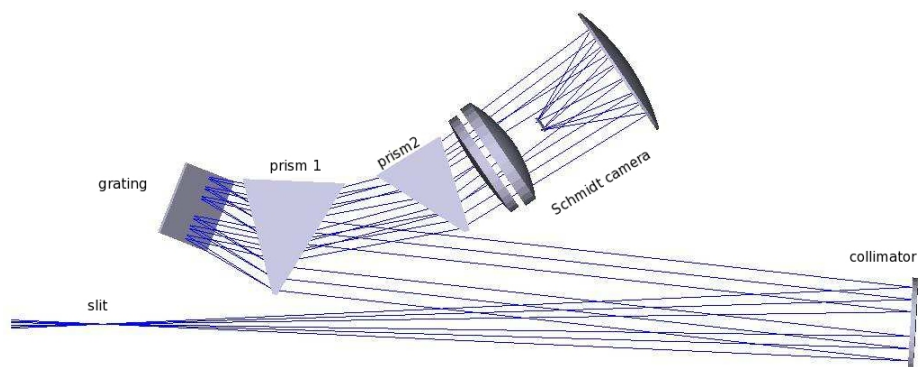


Figure 2.4: MagE optical design. Figure adapted from Marshall et al. (2008).

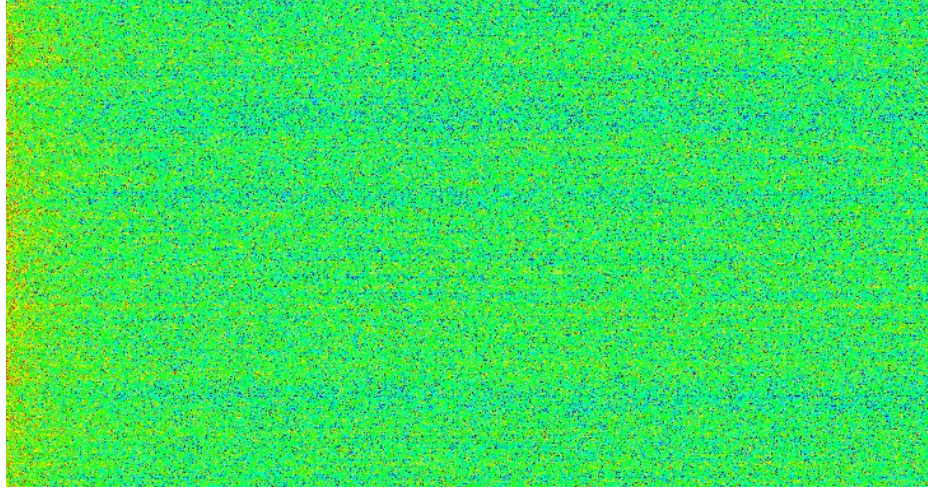


Figure 2.5: MagE bias frame. We can see some structure under the noise. A bias correction will remove this underlying structure from the final frames.

The detector is a 2048x1024 pixels CCD with 13.5μ pixels, placed at the prime focus of a vacuum Schmidt camera.

The instrument itself is easy to operate, but presents challenges in the data reduction. To overcome the difficulties of flat-fielding over a very large wavelength range, a combination of focused and de-focused xenon (Xe) lamps are utilised to provide enough flux in the near ultra-violet, and quartz lamps are used for the red. Another remarkable challenge is the curving of the orders on the detector, as can be seen from Figure 2.2. This means that the spectral features are also tilted, with a different inclination along each order. This makes the sky subtraction particularly difficult, since when the order is flattened, the sky line may be not perpendicular to the continuum, hence is not removed from the final spectra. We will discuss in more detail the data reduction of MagE spectra in the following section.

2.1.3 Data Reduction

A large portion of this work was carried out with MagE observations. The data were reduced with the Python based pipeline created by Dan Kelson (from the Carnegie Observatories Software Repository). Here we will discuss the basic reduction steps applicable to general spectrographs and remark upon the MagE pipeline specifics.

CCD Reduction

A charge-coupled device (CCD) is a light-sensitive integrated circuit that stores and displays the data for an image in such a way that each pixel in the image is converted into an electrical charge.

Given their high quantum efficiencies, linearity of their outputs and ease of use compared to photographic plates, CCDs are used in astronomy for nearly all applications.

The CCD data requires a set of calibrations to reduce the 2-D images (Top panel of Figure 2.8) into 1-D spectra (Bottom panel of Figure 2.8) (Marshall et al., 2008):

Bias Correction: The read out noise is an intrinsic property of the device used. To avoid any negative value pixels after the read out, a bias level of hundreds of electrons is added to each pixel. To subtract this level, we take zero exposure time frames with the shutter closed to have only the read out noise left, we call these frames bias frames. To avoid any bias structure, the bias frames are averaged and subtracted from each science target. Figure 2.5 is an example of a bias frame of the MagE spectrograph.

Dark Correction: The noise generated by thermal excitation of electrons is called dark current. If there is significant dark current, it needs to be corrected with frames that must be of the same length as the target, but obtained with a closed shutter. We called these dark frames. Most modern detectors have negligible dark current when cooled with liquid nitrogen. MagE's CCD is one of these, thus it does not need to be corrected by dark.

Flat field Correction: As the pixels of a CCD are not equally sensitive there are (small) variations in their response to the incident photons. This needs to be corrected by using the so called flat field exposures. These are uniform exposures of a featureless continuum. Exposures of the sky during twilight or/and exposures of a tungsten lamp build into the spectrograph are used as flat fields. A series of these exposures are averaged to find a master flat. In spectroscopy, the flat fields are not "flat" as the spectral shape of any flat field source is dependent on the wavelength. The master flat is then created by fitting the flat field shape along the wavelength axis with a low order polynomial and dividing the flat field average by this fit. The result is a normalised 2-D image with variations of up to a few percent which all science frames are divided by Figure 2.6 shows an example of the two types of flats necessary to reduce MagE data.

Wavelength Calibration: We use arc spectra to convert the x-axis from a pixel scale to a wavelength scale. Arcs are usually exposures of lamps of thorium and argon (ThAr) as in the case of MagE, or another combination of gasses rich in lines to apply wavelength calibration over the entire wavelength range. These are taken with the same setup as the science frames, they are then extracted in the same way than the target spectra. The pixel position of each identified arc line is then compared to its known reference wavelength, and a polynomial is fitted to determine the conversion between pixels and wavelength. This transformation is then applied to the target spectra. Figure 2.7 shows a ThAr lamp exposure of the MagE spectrograph. In every order it can be seen that multiple lines are available for calibration.

The MagE spectrograph requires some extra calibration data for the pipeline to run, as well as two kind of flat field frames:

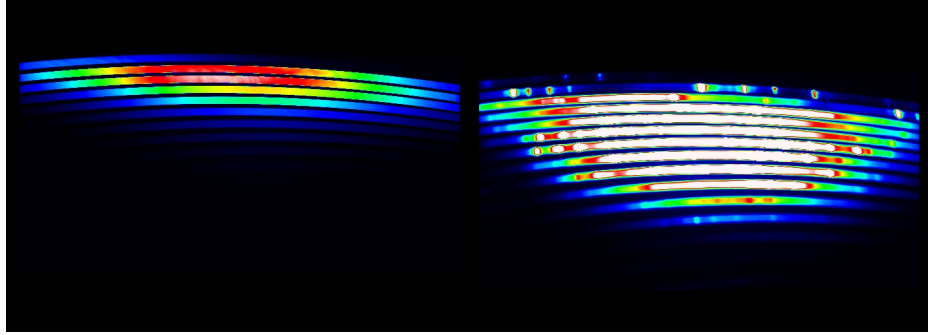


Figure 2.6: MagE flat field frame. Left: Quartz flat, to calibrate the red side of the spectra. Right: Xe-Flash frame, it saturates in all but the bluest orders to calibrate the blue end of the spectra.

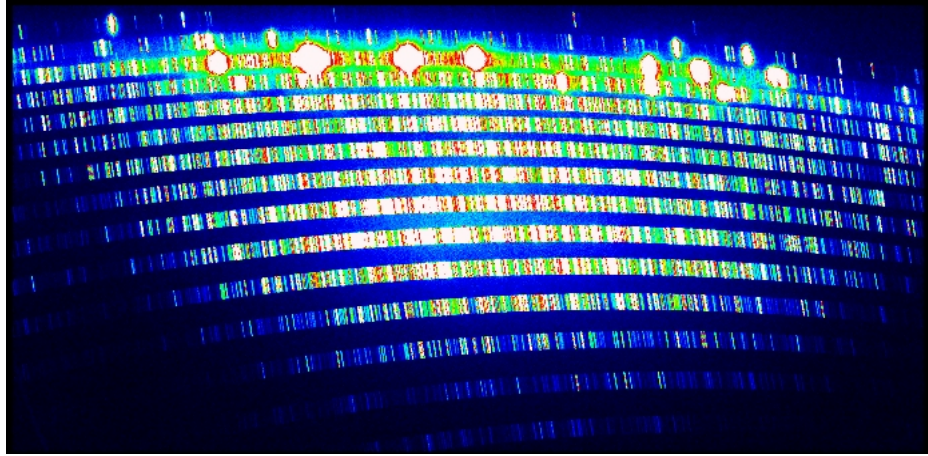


Figure 2.7: MagE ThAr lamp frame. Saturated at 80% to enhance the features of the fainter orders.

- Xe-Flash frames, to locate the order edges.
- De-focused Xe-Flash frames, for flat fielding the blue end of the spectrum.
- Dome flats, to construct the flat field at the red end of the spectrum.

MagE pipeline reduction

The MagE pipeline performs the following steps:

1. **Image Reorientation:** Rotates the image to have the wavelength in the horizontal plane.
2. **Fit and subtract over-scan:** the over-scan is a strip of 20-40 columns on the right side of the chip. It can be fitted with a low order polynomial after averaging the columns row by row.
3. **Trim:** trim the blank areas of the chip and the over-scan regions.

4. **Flattening:** Fits polynomials to straighten the curved orders and corrects for flat. The MagE pipeline constructs two sets of master flats, one for the blue end of the spectrum with frames taken with Xe-Flash lamp and a dome flat with exposures taken with an array of incandescent light mounted on the secondary cage.
5. **Construct and use illumination function correction:** The “slit illumination function” is the non-uniformity in the spatial direction of the spectra. The previous steps should in theory have removed any unevenness in the spatial direction, but as a precaution, this correction is also applied. The MagE pipeline can be used with or without the slit correction function, we use it with the slit correction.
6. **Wavelength calibration:** In this step, the comparison arcs spectrum needs to be extracted in exactly the same manner as the identified object spectrum (with the same trace). The various lines are identified and a fit to the wavelength as a function of the pixel number along the trace is performed.
7. **Identify object and sky:** This stage determines the width of the window used to extract the object spectra, and selects where the sky regions are relative to the target’s spectrum. The MagE pipeline uses the on-focus Xe-flash frames to extract information on the position of the stellar spectrum (trace). After this stage, the pipeline interpolates over bad pixels.
8. **Interpolate over bad pixels:** to get rid of CCD bad columns and non-linear pixels. The MagE pipeline does this after step above.
9. **Extraction:** Knowing the location of the spectrum and the wavelength calibration, one needs to add up all the data along the spatial profile, subtract the sky and apply the wavelength solution. The MagE spectrograph uses the “optimal extraction” algorithm as described in Horne (1986). Optimal extraction weights the contribution of each pixel, i , across the spectrum. The sky signal is then subtracted and the optimal weights of each pixel, W_i , are used to extract the target spectrum $S(\lambda)$ given by the equation:

$$S(\lambda) = \sum_i W_i(\lambda)(C_i(\lambda) - B_i(\lambda)) \quad (2.8)$$

where C_i are the counts and B_i the sky background from the pixel i at a given wavelength λ . The weights W_i are:

$$W_i(\lambda) = \frac{P_i(\lambda)/V_i(\lambda)}{\sum_i P_i^2(\lambda)/V_i(\lambda)} \quad (2.9)$$

where P_i is the flux and V_i the variance of the pixel i (Horne, 1986).

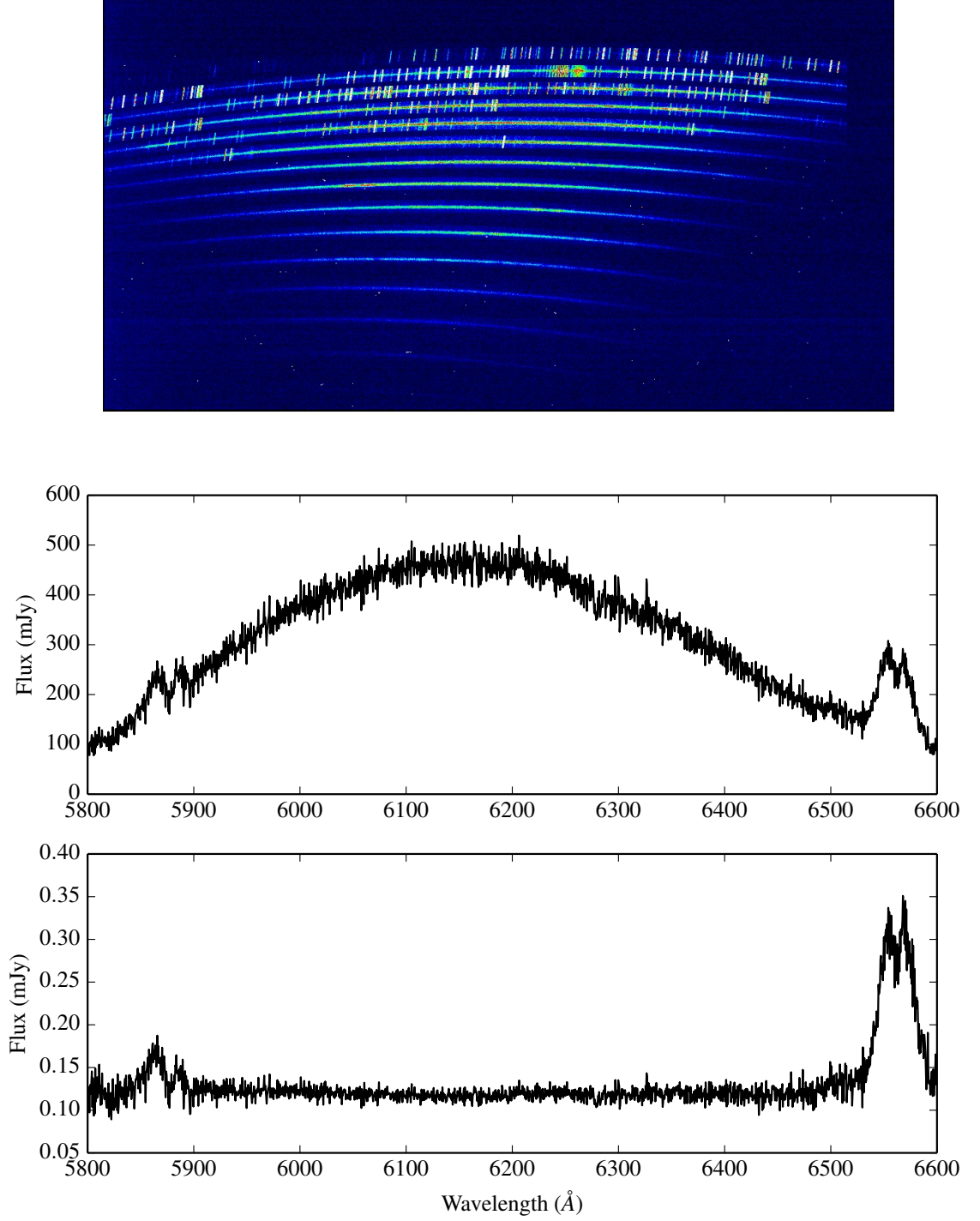


Figure 2.8: MagE spectra of V4140 Sgr. Top: raw spectrum (90% of saturation). Middle: reduced spectrum of order 10. Bottom: Flux calibrated final spectrum of order 10.

I had to modify the original pipeline to extract all the orders (the red orders were particularly challenging) and to not average all the spectra of each science target. At the end of running the MagE pipeline script, one is left with a "multispec" FITS file, in which is contained, for every order of each spectrum: Sum of the sky over the extraction aperture, sum of the object over the extraction aperture, expected noise from sum of object and sky plus the read noise, signal-to-noise spectrum (per pixel) and the sum of the lamp spectrum over the extraction aperture. The multi.fits files are not very user friendly, so I generated a series of scripts to store the results of each order of a single target in "molly"¹ files. Figure 2.8 shows an example of data before and after the reduction process. This is the spectrum of the CV V4041 Sgr. The two visible lines are He I and H α . The Figure shows a raw image at the top, followed by the 10th order spectrum before and after flux calibration. Flux calibration may be considered as the final step of spectral reduction, but depending on the kind of analysis that will be performed on the spectra, one might want to normalise instead. To flux calibrate the spectrum of the target, we need to observe a spectro photometric standard star during the observation night, using the same instrumental configuration than used for the target. The spectrum of the standard star is reduced and extracted in the same way than the science target spectra and compared to a known flux data (usually in the form of a flux table and available from the observatories web page). The ratio between the standard star and the flux table is calculated by fitting splines to determine flux to count ratio for each pixel. Finally, this conversion is applied to the science spectra to calibrate it by flux. The flux calibration or normalisation of the science spectra were made manually with "molly".

2.2 Radial Velocity Analysis

The most common analysis of the overall radial velocity measurements of a binary components is performed with a Gaussian fit to the line profiles. Radial velocity measurements of the primary and secondary stars can be used to determine the masses in a CB (see Equations 1.4 and 1.5).

To estimate K_1 , as the primary star is rarely visible, we rely on the emission lines from the accretion disc (K_{disc}) since it shares the motion of the primary in orbit. One of the problems with this assumption are the asymmetries among the disc. The standard methods rely on the assumption that the asymmetries will be confined to the outer region of the disc and try to obtain radial velocity curves from the wings of the emission lines which are created closer to the primary. One such method that is commonly used for CBs is the double Gaussian fit, developed by Schneider & Young (1980). This method consist of convolving the data with a Gaussian template. Having a spectrum $S(\Lambda)$, we can find the mean position of the emission line by solving the equation:

$$\int_{-\infty}^{+\infty} f(\Lambda) K(\Lambda - \lambda) d\Lambda = 0 \quad (2.10)$$

¹Tom Marsh's software <http://deneb.astro.warwick.ac.uk/phsaap/software/molly/html/INDEX.html>

To calculate the wavelength at any position of the line, with K usually of the form:

$$K(x) = \exp\left[-\frac{(x-a)^2}{2\sigma^2}\right] - \exp\left[-\frac{(x+a)^2}{2\sigma^2}\right] \quad (2.11)$$

where the Gaussians separation, a , and width, σ , can be adjusted to measure the velocity at the base of the emission line. These radial velocities are then fitted with an equation of the form of equation 2.15 to obtain an estimate of the orbital parameters of the system.

2.2.1 Diagnostic Diagram

The width and separations of the Gaussians used in the method described above can be adjusted to measure the velocity at any position in the line profile. The measured radial velocities then, will depend on the choice of a and σ . As the asymmetries of the disc may persist out to the emission line wings, a way to investigate the extent of these was developed by Shafter et al. (1986). The idea behind this technique is to map the line profile in radial velocity space, by using different Gaussian separations to measure the lines. These results are then plotted in what is called a diagnostic diagram, Figure 2.9. The diagnostic diagram shows the variation of K_1 , its associated error, σ_K/K , the systemic velocity γ and the phase zero Φ_0 as functions of the Gaussian separation a . The expectation is that the solution for K_1 should asymptotically approach the correct value when a is large enough and then diverge when the Gaussians hit the continuum noise instead of the spectral profile. Similarly, when a reaches the extreme wings and the signal is lost, the error should rise sharply. In practise, diagnostic diagrams do not always behave this way since in many systems asymmetries occur throughout the whole disc. In the case of Figure 2.9, we had more than one line available to perform this technique, allowing us to compare the results for three different lines. In this case, the diagnostic diagrams reach convergence between $a=2000$ and 2500 km/s. So, even though the value of K_1 is consistent among these three lines, the value of γ shows a dispersion of over 100 km/s from one line to the other. Discrepancies on the value of γ between the emission lines is commonly observed among CVs and it is often associated with blending with neighbouring lines (as is potentially the case of CaII, blended with Paschen in our example), wing asymmetries or even deviations from the flatness of the continuum. So, even when the simultaneous study of more than one emission line with diagnostic diagrams could lead to better constrained values of K_1 , the constraints on γ are still rather poor.

In the next Section, we will study alternative methods to constrain the system parameters based on Doppler tomography and compare these with the results delivered by the diagnostic diagram.

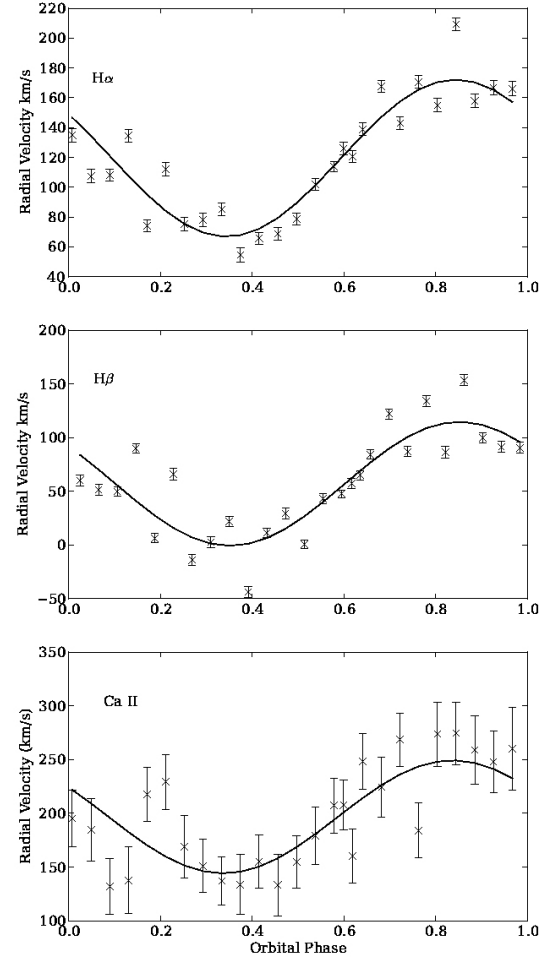
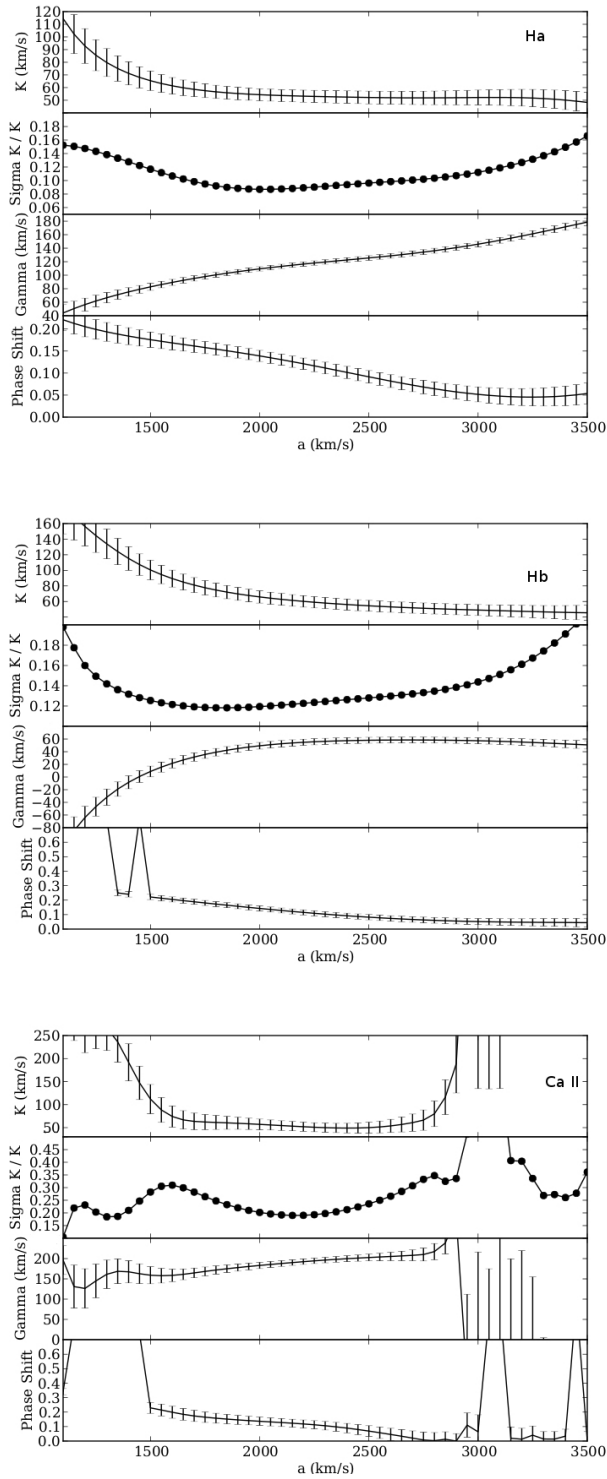


Figure 2.9: Diagnostic diagram for CC Scl with their respective radial velocity curve for the Gaussian separation a in the convergence zone. For emission lines from top to bottom: H α , H β and Ca II 8662 Å

2.3 Bootstrap

Bootstrapping is a computer based method for assigning measures of accuracy to statistical estimates invented by Efron (1979). It enjoys the advantage of being completely automatic, requires no theoretical calculations, and is available no matter how mathematically complicated the desired estimator may be. We used bootstrapping to estimate a large number of the errors in this thesis work.

2.3.1 The bootstrap estimate of standard error

Lets assume a data-set of n points $X = (x_1, x_2, \dots, x_n)$. A bootstrap sample is obtained by randomly sampling with replacement from the original data points. The bootstrap sample, $X^* = (x_1^*, x_2^*, \dots, x_n^*)$, consists then of members of the original data set appearing in the sample any value between zero and n with probability of $1/n$ times. We denote the bootstrap sample as “star” to remark that X^* is not the actual data set X , but a randomised version of it. If we wanted to obtain a certain parameter of interest from our sample X , lets say a statistical estimate $s(X)$, we would want to know how accurate this estimate is; enter the bootstrap algorithm.

The bootstrap algorithm works by drawing B number of independent bootstrap samples $X^{*1}, X^{*2}, \dots, X^{*B}$ each of size n . Corresponding to a bootstrap data set X^* is a bootstrap replication of the statistical estimator, $s(X^*)$, the result of applying the same function s to X^* as was applied to X . The bootstrap estimate of standard error, se_{boot} is the standard deviation (STD) of the bootstrap replications:

$$\hat{se}_{boot} = \left\{ \frac{\sum_{b=1}^B [s(X^{*b}) - s(\cdot)]^2}{(B-1)} \right\}^{\frac{1}{2}} \quad (2.12)$$

where $s(\cdot) = \sum_{b=1}^B \frac{s(X^{*b})}{B}$.

Bootstrap can assess more complicated accuracy measures like biases, prediction error and confidence intervals, (e.g. Efron & Tibshirani (1993)).

To summarise, Figure 2.10 shows an schematic view of the bootstrap process; it begins by generating a large number of independent bootstrap samples from the original data-set. Typical values for B range from 50 to 2000 and from 50 to 200 for standard error estimation. Bootstrap replicates are obtained by calculating the value of the statistic on each bootstrap sample. Finally, the standard deviation of the values $s(X^{*1}, X^{*2}, \dots, X^{*B})$ is our estimate of the standard error $s(X)$.

2.4 Indirect Imaging: Doppler Tomography

As the spectrum that we observe in CBs is actually a combination of the emission emitted by different sources, the interpretation of it can be ambiguous. The most effective way to overcome

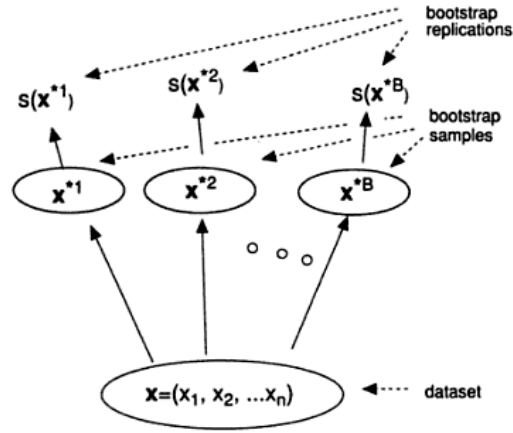


Figure 2.10: Schematic of the bootstrap process for estimating the standard error of a statistic $s(X)$. Figure from Efron & Tibshirani (1993).

this ambiguity are spatially resolved data, but our current technological capacity has made this impossible for CBs: these systems' separation is around $1R_{\odot}$ and are far away. The second best way is indirect imaging.

In the 1980's two indirect imaging techniques were developed that allowed effective spatial resolution over the accretion discs in angular scales of microseconds. One of these is Eclipse Mapping, developed by Horne (1985). This technique uses the eclipse's shape information contained in the light curve to construct a map of the surface brightness contribution of the accretion disc. The other technique is Doppler tomography, developed by Marsh & Horne (1988). Doppler tomography uses the variation of emission lines in spectroscopic profiles associated to the Doppler effect. These profiles are "slices" taken around the orbital phase of an object to reconstruct a two dimensional image of the object. Doppler tomography is applicable to a wide range of orbital inclinations and it will be key for the research presented in this work.

2.4.1 Profile Formation by Projection

Doppler tomography was initially developed as a tool to interpret the double-peaked emission line profiles of accretion discs, that are formed through the Doppler shifts of rotating gas (2.12). However, the presence of a disc is not necessary for Doppler tomography to work. Consider a single point-like source emitting in a binary. If we assume that this point-like source has a movement parallel to the binary orbital plane, then the emission line from the source will trace a sinusoid around the system's centre of mass velocity. We can see such a sinusoid in Figure 2.11. These are called S-waves. We can associate a S-wave with a particular velocity vector in the binary, depending on its phase and amplitude. Doppler tomography is able to cope with any number of S-waves even if they overlap or blend with each other. This makes Doppler tomography a unique

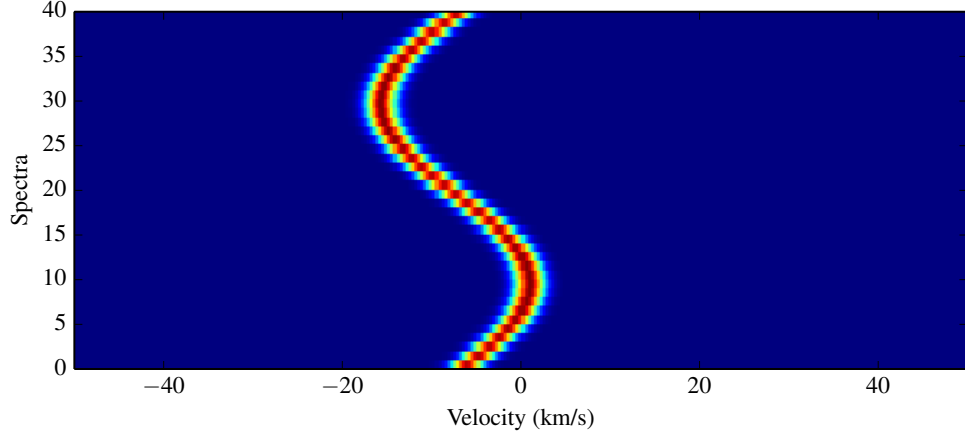


Figure 2.11: S-wave. These are an effect of the movement of a point-like source around the binary centre of mass. Doppler tomography can cope with a number of these S waves, even if they are overlapped and not visible to the human eye.

tool to deal with complex systems.

In a CB, a given point can be defined by its spatial position (X, Y) , but also by its velocity (V_x, V_y) (Marsh & Horne, 1988). Since the emission lines in the spectra could arise from sources other than the accretion disc, one cannot assume that they come from a Keplerian velocity frame. It is not trivial then to translate from velocity space to position space. For this reason Doppler maps give the distribution of the emission sources in velocity space. Inertial frame velocities change with the rotation of the binary, so, in order to define unique values of V_x and V_y , these should be measured in a particular orbital frame. If we define the x-axis to point from the white dwarf to the mass donor and the y-axis to point in the direction of motion of the donor and defining orbital phase zero as when the donor is the closest to the observer, the radial velocity of a given point is:

$$V_R(\phi) = \gamma - V_x \cos 2\pi\phi + V_y \sin 2\pi\phi, \quad (2.13)$$

where V_R is the observed inertial velocity, V_x and V_y are the velocities in the binary frame, ϕ is the phase and γ is the centre of mass (or systemic) velocity. Thus tracing an emission feature as a function of the binary phase provides a unique location in the velocity plane defined by V_x and V_y .

The observed line profile flux can be expressed as a function of radial velocity and orbital phase as:

$$f(V, \phi) = \int_{-\infty}^{\infty} \int_{-\infty}^{\infty} I(V_x, V_y) g(V - V_R) dV_x dV_y \quad (2.14)$$

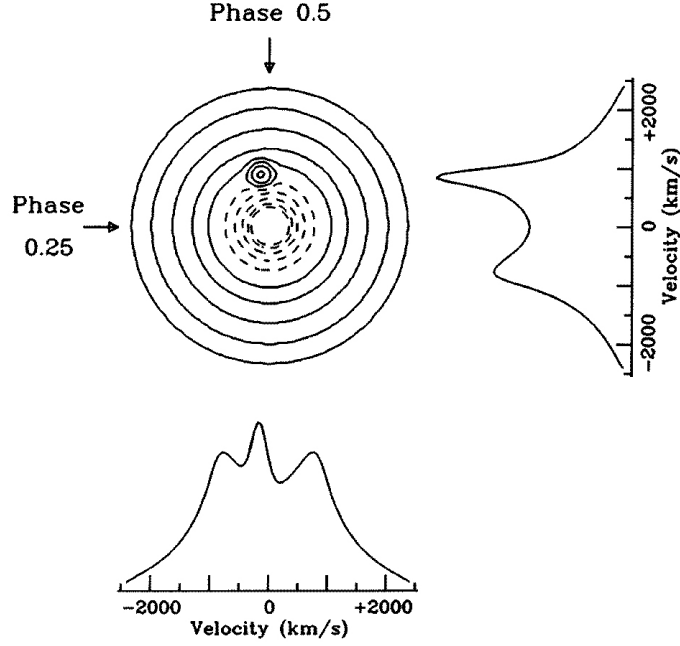


Figure 2.12: Representation of the line profile formation process from an artificial image for two projection angles at phase 0.5 (left profile) and 0.25 (right profile). From Marsh (2001).

where $I(V_x, V_y)$ is a system's image (as a function of velocity) and g is a narrow function that represents the line profile from any point in the image. In velocity coordinates, lines of equal radial velocity are always straight, we can just collapse the disc down to one dimension along the direction determined by the phase. Provided g is narrow, equation 2.14 picks out all regions of the image close to the straight line:

$$V = V_R = \gamma - V_x \cos 2\pi\phi + V_y \sin 2\pi\phi, \quad (2.15)$$

Different values of V will define straight lines across the image with their direction depending on the orbital phase. So orbital phase 0 will be a projection in the positive V_y direction, phase 0.25 corresponds to the positive V_x , 0.5 will be the negative V_y and so on. A series of line profiles at different orbital phases are then a set of projections of the same image at different angles, as shown in Figure 2.12. An image can then be decomposed into a set of projections at different angles or line profiles. The inverse process of reconstructing an image from its projections is called tomography, in analogy with medical CAT scanning, and hence the name of the technique.

2.4.2 Understanding Doppler maps

Figure 2.13 is a schematic view of a CB in velocity (or Doppler) coordinates (left) and in position coordinates (right). The right panel shows a CV containing a Roche lobe filling donor star,

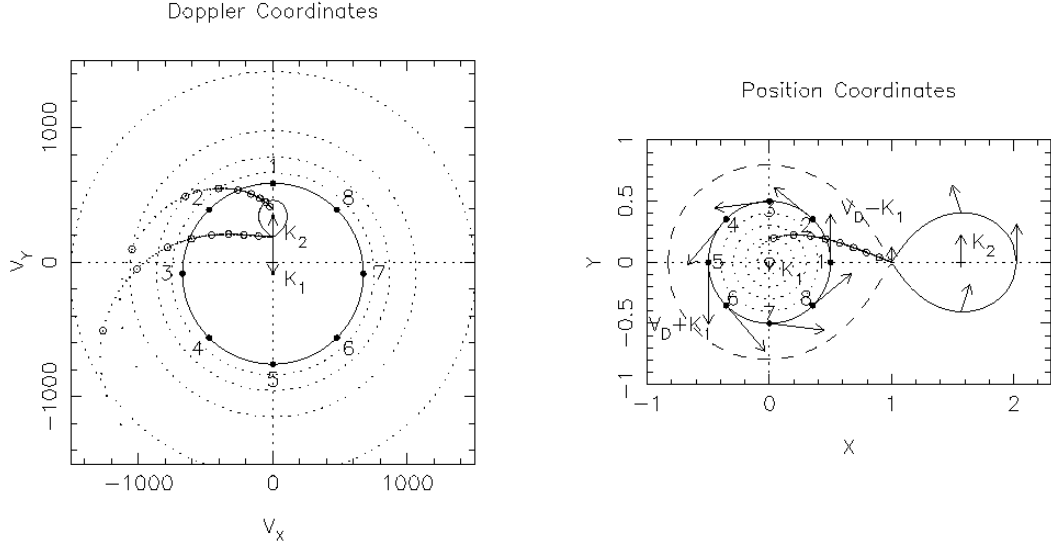


Figure 2.13: Schematic view of a CV in velocity coordinates. From Horne's lecture notes: <http://star-www.st-and.ac.uk/kdh1/pub0/doptom/doptom.html>

the mass transfer stream, the accretion disc and the WD. Indicated are also the velocity vectors of the primary star, K_1 and the secondary star, K_2 . We measure the projection of these velocities along our line of sight as a function of the binary phase, $I(v, \phi)$. To reconstruct the image plane in position coordinates, $I(x, y)$, more information is needed so we leave the map in velocity coordinates. To interpret a Doppler map, which is in velocity coordinates, left hand of Figure 2.13, we should consider the following: first, the centre of mass will be at the centre of the velocity coordinates. We must also consider that the largest Keplerian velocities occur in the inner part of the accretion disc in position coordinates, hence in velocity space these should be at the outer rim. The accretion disc appears then inside out in velocity space. We should also note the position of the donor star (with radial velocity K_2) at $(V_x, V_y) = (0, +K_2)$ and the primary (K_1) at $(V_x, V_y) = (0, -K_1)$. As $K_2 < K_{disc}$, the emission spot of the donor always lies within the disc ring in velocity space, unless the outer disc is significantly sub-Keplerian. The mass transfer stream is marked in both sides with white circles. We will make use of these geometric properties of Doppler maps in the next Chapter to develop techniques to derive fundamental parameters of CBs.

2.4.3 Maximum Entropy Inversion

To generate a Doppler map, for any image we predict data at given orbital phases and compare these with the observed data by a χ^2 goodness of fit. χ^2 is reduced until the predicted data is consistent with the observed data, a criterion that is in general satisfied by more than one image.

Here is where the Maximum Entropy Method (MEM), selects the image of maximum entropy as the preferred solution.

The entropy of an image I , for i alternatives, each with probability p_i is defined as (Narayan & Nityananda, 1986):

$$S = - \sum_i p_i \ln p_i \quad (2.16)$$

where $p_i = \frac{I_i}{\sum_j I_j}$. This form of entropy ensures that from all the possible images, the most uniform is selected. This can be a problem in the case of emission lines that are usually not uniform. Hence using this definition of entropy would be too restrictive and suppress small scale features. Instead of that, Doppler tomography uses a refined form of entropy that allows it to find the most axi-symmetric distribution that is consistent with a default image and allows the radial dependence to be determined by the data (Marsh & Horne 1988):

$$S = - \sum_{i=1}^M p_i \ln \frac{p_i}{q_i}, \quad (2.17)$$

where

$$q_i = \frac{D_i}{\sum_{j=1}^M D_j},$$

D is the called the default image, which can be radial, smoothed, etc., but is usually a blurred version of the original image. This form of entropy measures departures from the default image and allows a unique solution to be found.

2.4.4 The effect of the systemic velocity γ in Doppler maps

The centre of mass or systemic velocity, γ , represents the displacement of the position of the emission lines from their rest wavelength values. In a Doppler map, when γ is unknown, the model cannot fit the data properly. As it tries to do so, artifacts will arise. The main effect of an error in the value of γ will be a blurring of the features by $\approx \Delta\gamma$ (Marsh & Horne 1988). Casares et al. (2003) make use of this fact to constrain the value of γ reconstructing a Doppler map with different values of γ and using the FWHM of the signal of the secondary star as an indicator of the correct value: the sharper the signal (lowest FWHM) the closer to the correct value of γ . We show this effect in Figure 2.14. To plot this Figure, we generated a set of synthetic spectra with a Gaussian spot, assuming a given value of systemic velocity, $\gamma = 0$ km/s (see Section 2.4.7) and reconstructed assuming different values of γ . The left hand image was reconstructed with the right value of γ , the centre image was reconstructed with $\gamma = 50$ km/s and the right hand image was reconstructed using $\gamma = 100$ km/s. At first sight there is no difference between the left hand and centre images. The broadening of the feature is evident in the right hand image. We fitted 2-D Gaussians to the spots to determine their FWHM, obtaining FWHM=72 km/s, FWHM=73

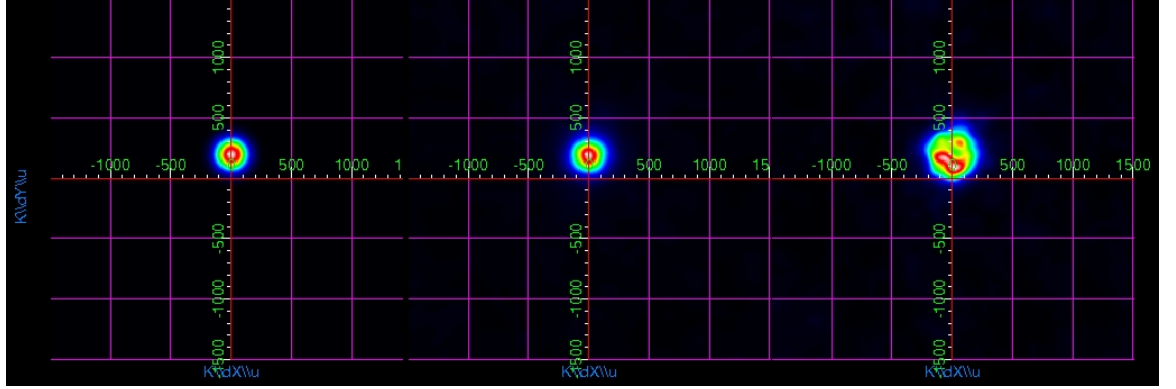


Figure 2.14: Same simulated data set reconstructed for 3 values of γ . The left Doppler map was made with the correct value of γ . The centre map was made with a γ shifted by 50 km/s. Right side map was made with γ shifted by 100 km/s from the actual value.

km/s and FWHM=300 km/s, respectively. These results indicate that with this method it is not possible to differentiate the correct value of γ to a certainty of less than 50 km/s.

2.4.5 Axioms of Doppler Tomography

There are some assumptions necessary when constructing a Doppler map:

1. All points are equally visible at all times.
2. The flux from any point fixed in the rotating frame is constant.
3. All motion is parallel to the orbital plane.
4. All velocity vectors rotate with the binary star.
5. The intrinsic width of the profile from any point is negligible.

Exceptions exist to each of these. For instance (1) is violated by the emission on the mass donor, (2) is violated during a system's outburst, (3) does not account for the real motion of the material and (5) does not account for the effects of orbital smearing. So it is important to be aware of Doppler tomography's limitations when interpreting the resulting map (Marsh 2001, Steeghs 2003).

The ultimate limit on Doppler tomography resolution is set, however, by thermal broadening. The maximum exposure time, t , that can be used to maximise signal to noise is given by:

$$\frac{t}{P_{\text{orb}}} \sim \frac{1}{2\pi} \frac{\Delta V}{K} \quad (2.18)$$

where P_{orb} is the orbital period, ΔV is the spectral resolution and K is the velocity amplitude of the component (Marsh 2001). The goal is that the orbital smearing remains less than the spectral resolution of the instrument, which for shorter period binaries will require bigger telescopes.

2.4.6 Doppler tomography and Bootstrapping

The advantage of using bootstrapping as an uncertainty propagator on Doppler tomography is that it automatically accounts for the true statistics of the data without adding extra noise as it would happen with the more usual Monte Carlo approach.

To avoid potential problems with the sampling methods (e.g. the algorithm selects the same point all the time, all the selected points are in the continuum, etc.), a sufficiently large bootstrap sample must be generated. Marsh (2001) suggests using 1000 bootstrap samples. Given that the MEM is computationally demanding, optimising the number of bootstrap samples, and hence the number of generated MEM Doppler maps is important and we decided to explore this number. We performed our statistics using 5000 bootstrap samples, decreased the number of samples for the same data set by 500 each time, calculated the same statistic for less bootstrap samples and compare the results. Our conclusion was that there was no significant difference between the results calculated from 5000 or 500 bootstrap samples, hence we used 500 bootstrap samples to generate the uncertainties of all the Doppler tomography-based calculations in this thesis.

2.4.7 Orbital Parameters with Doppler Tomography

In some cases, the weakness of an emission line makes it impossible to use a Gaussian fit on each spectrum to calculate the component's radial velocities. As Doppler tomography makes use of all data at once, some features that are too weak to be separated in individual spectra can be detected. Doppler tomography can also provide an excellent tool for identifying the kinematics and the origin of the various emission components.

Synthetic data generation

We constructed synthetic data using a tool in the code *Doppler* provided by Tom Marsh. This code mainly performs NDF-based routines for carrying out maximum entropy based Doppler tomography. It can also be used to construct Doppler maps given a series of parameters, allowing to add a Gaussian spot, a spiral pattern and a power law in radius. If constructing data, the code allows for the following parameters:

XCEN – X centre of Gaussian spot (km/s)

YCEN – Y centre of Gaussian spot (km/s)

WIDTH – FWHM of Gaussian spot (km/s)
 PGAUSS – Peak intensity of Gaussian
 XSP – X centre of spiral pattern and power law disc (km/s)
 YSP – Y centre of spiral pattern and power law disc (km/s)
 VLOW – Lowest disc velocity (outer disc) (km/s)
 VHIGH – Highest disk velocity (inner disc) (km/s)
 EXPON – exponent between them (intensity scales as $V^{**}EXPON$)
 ANGLE – Opening angle of two armed spiral pattern (degrees)
 CURVE – Difference in angle between outer and inner velocities
 PPOWER – Peak intensity of power law background
 PSPIRAL – Peak intensity of spiral shock

We only made use of the Gaussian spot tools to simulate the secondary star, fixing the position but varying the FWHM and the peak intensity of the spot, and disc tool, varying the intensity scale of the disc relative to the Gaussian spot. We did not add spiral patterns to our simulated data. The resolution of our simulated data was set to the resolution of MagE spectrograph at ~ 80 km/s at 300 pixels per side.

The synthetic data set used to test the capabilities of our methods in the following sections were made with a Gaussian spot of FWHM=40 km/s plus accretion disc at intensity 5 times lower than the spot with S/N=25.

Systemic Velocity γ

We make use of the dependence of MEM maps on the assumed systemic velocity (Section 2.4.4): The correct value of γ will generate maps with optimal sharpness, while reconstructions at considerable different values will broaden the features. The best features to assess this with, would be localised, sharp emission regions in the map, such as those caused by an S-wave. We generate a series of Doppler maps with systemic velocities varying over a wide range around 0 km/s in steps of 10 km/s, looking for the value that minimised the width of a two dimensional Gaussian fitted to the secondary star emission in each Doppler map (Casares et al., 2003).

Our initial search was used to determine an approximate estimate for γ . We then performed a search for γ spanning ± 50 km/s around this estimate in steps of 10 km/s. Furthermore, instead of reconstructing one map per assumed γ , we bootstrapped our data to generate 500 independent data-sets, and reconstructed Doppler maps for these data while aiming for the same χ^2 as the original map. We used a python script that fits a 2D Gaussian and calculates the FWHM of the secondary star in each bootstrapped sample. We kept record of the FWHM of each bootstrap for each value of γ . For each γ , we displayed histograms of the FWHM, as the ones showed

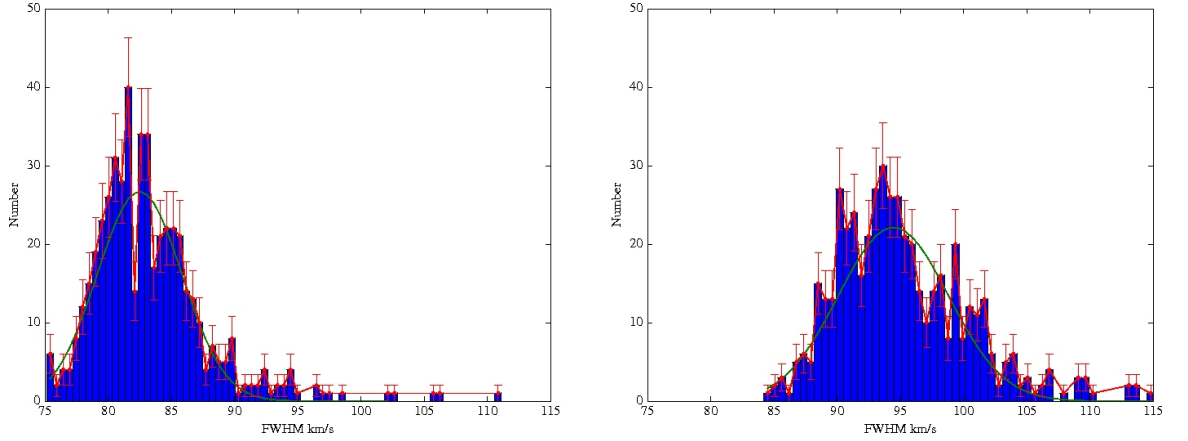


Figure 2.15: Histograms of FWHM for $\gamma = 0$ km/s (left) and $\gamma = 50$ km/s (right). The blue bars are the histogram's bins, the red error bars marks the bin centres and the green line is the Gaussian fit on the histograms.

in Figure 2.15. Since these histograms are well represented with a normal distribution, we fitted a Gaussian to these and determined the mean and STD of these distributions. To estimate an uncertainty on this optimal γ , we consider the uncertainties on the STD of the distributions and consider all γ 's whose STD uncertainties are less than three σ away from the optimal STD (horizontal line cutting the lower panel of Figure 2.16). We present the dependence of γ against the FWHM and the STD visually in Figure 2.16. We recovered the value of the systemic velocity for our synthetic data set with a Gaussian spot of FWHM=40 km/s and S/N=25. The plot shows that both, the lowest FWHM and STD are found for $\gamma = 0^{+35}_{-30}$ km/s. The synthetic data was in deed generated with $\gamma = 0$ km/s. Our method is thus able to pick the right value of γ , and also offers an estimate of its uncertainties. We can see in Figure 2.15 that the optimal value of γ (left) will show both a narrower distribution and lower values of the FWHM in comparison with a value of $\gamma = 50$ km/s away from the optimal value. Given that a departure of γ of less than 50 km/s is often not detectable by eye, we are confident that the implementation of the method is useful and we will apply it to real data in the following Chapters.

Our best γ indicator is therefore a combination between the smallest value of the STD and the sharpest secondary feature, reflected on a small FWHM value. In systems with unstable accretion discs, this method offers an advantage over traditional radial velocity methods, affected by disc variations and contamination by blended lines. Focusing on the secondary star signature rather than the disc to constrain the systemic velocity leads to a unique and reliable value of γ , eliminating the uncertainties of the radial velocity methods.

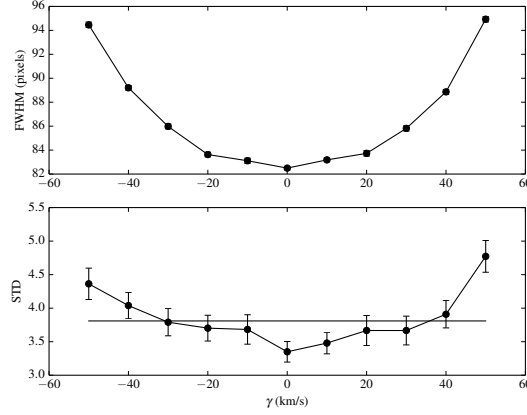


Figure 2.16: FWHM of the secondary star and STD versus value of systemic velocity γ .

Primary Velocity with Centre of Symmetry

In the Doppler map of an ideal Keplerian disc, the position of the WD should be in the centre of the map $(V_x, V_y) = (0, -K_1)$ (Figure 2.13). To extract the value of K_1 from the Doppler map, we assumed a symmetric disc and subtracted a symmetrical component of the map, centred on a range of velocities (V_x, V_y) . We then inspected the resulting maps looking for any residual signal. Figure 2.17 shows an example of K_1 versus residual level for a disc centred at $(0, -60)$ km/s. We can see in this Figure how the residual level decreases monotonically while approaching the optimal K_1 velocity. We focused on symmetric parts of the disc to avoid contamination from any asymmetries in emission (donor star - bright spot) and measured the residuals of a square region as big as the symmetry allowed us. We will call this region a “box”. This technique must be performed on relatively smooth Doppler maps, namely, before these have reach their lowest χ^2 , to avoid breaking the disc into divided spots. The centre of symmetry technique has been successfully used to find values of K_1 for Her X-1 (Still et al., 1997), Sco X-1 (Steehgs & Casares, 2002) and GW lib (van Spaandonk et al., 2010).

To test the behaviour of the method depending of the line and box, we tried five different boxes. We assumed that in any doppler map, the most asymmetric part of the disc would be the location of the bright spot which is in the 4th quadrant $(-V_x, +V_y)$. To avoid the bright spot, we used a box on the bottom left quadrant $(-V_x, -V_y)$ and the top right quadrant $(+V_x, +V_y)$ (named boxes 2 and 3, respectively). We also covered a more extended area including the bottom right quadrant that showed slight asymmetries in some lines, using boxes covering the right half and the bottom half of the map (boxes 4 and 5). The last box used, covered the whole Doppler map, as an equivalent of the analysis performed by the diagnostic diagram (box 1). Except for boxes 1 and 3, there was a small shift of 100-200 km/s in each box to avoid the secondary star.

To find the best value of K_1 that should be in the centre of symmetry of the map, for each

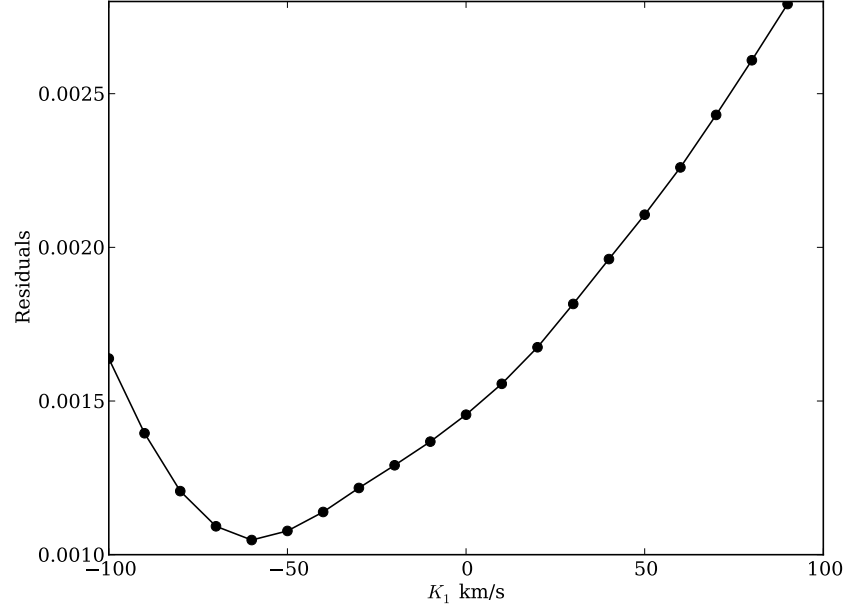


Figure 2.17: Residuals level against K_1 . The optimal value of K_1 will correspond to the lowest level of residuals.

line, we assumed centre locations (x, y) . We first varied the position of y between -200 and 0 km/s in steps of 10 km/s, leaving x fixed to 0 km/s. We picked the best centre position as the one returning the lowest residual levels (Figure 2.17). Then, we varied the position of x between -200 and 200 km/s in steps of 10 km/s, fixing y to the results given by the previous step. We repeated the residuals inspection to select the x centre position. Finally, we varied again the position of y in the same range as the first time, but this time with the x coordinate fixed to the results of the previous step.

After establishing the optimal line/region combinations, we then repeated the analysis using 500 bootstrap data samples and performed a symmetry search for each reconstructed map. We used the values of K_x and K_y , to calculate the centre of the map (K_1). The mean value was adopted as our best estimate for K_1 , using the standard deviation as its error.

2.4.8 Secondary star and Phase zero from K_{em}

In the cases where the secondary star emission is easily identifiable in the Doppler tomograms, we can calculate the velocity of the secondary star emission. We call this velocity K_{em} since it is emitted from the irradiated face of the donor star. We will discuss how to derive K_2 from K_{em} later in this Chapter.

From the geometry of the Doppler tomogram, we use the fact that the secondary star

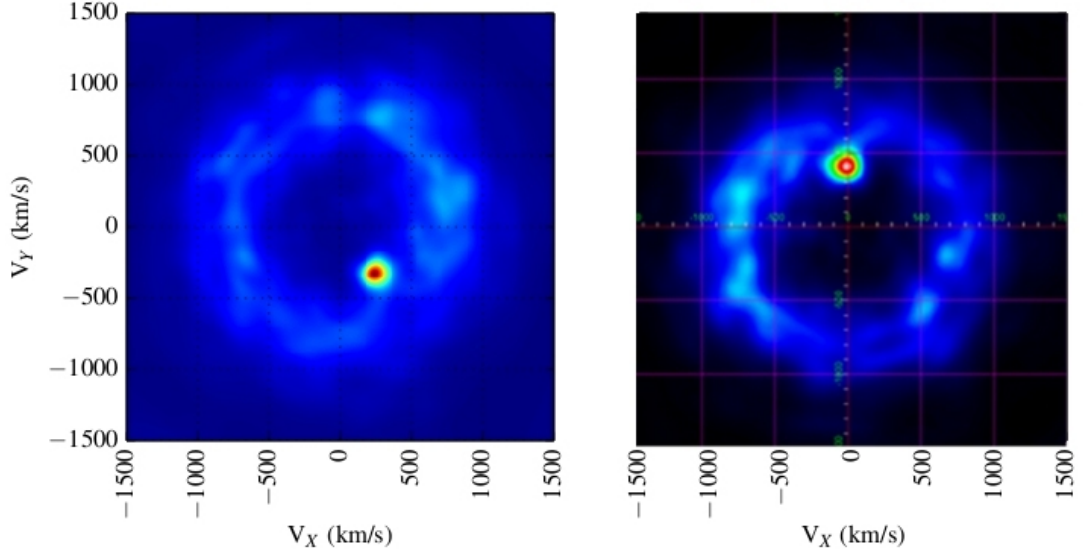


Figure 2.18: Doppler map of CaII 8662 Å of CC Scl. Same data set with unknown phase zero (left) and after rotating to the correct phase zero (right).

velocity is projected in a Doppler map at $(V_x, V_y) = (0, +K_2)$ to rotate our tomograms with a secondary detection and find the correct ephemeris for the conjunction. Figure 2.18 shows two Doppler maps of CaII 8662 Å for CC Scl. This figure illustrates how Doppler tomography can be used to set up a new ephemeris. The left hand map was made using as phase zero the HJD of the first spectrum of the data set, it can be made with any random phase, but using the HJD of the observation makes it easier to calculate a phase zero coherent with the date of our observations. Knowing the position of the secondary, it is easy to rotate the map to position the secondary at $(0 + K_2)$, right side of Figure 2.18), calculate the phase shift and translate it to HJD to report the new phase zero.

We calculated this phase correction by measuring the position of the secondary star in 500 bootstrap samples. The reported position is the average of the 500 positions. Again, we took the STD of the data as our estimate of the uncertainties.

K-correction

As mentioned previously, our detection of the donor star in emission requires a correction before it can be used to determine the donor star's orbital velocity (K_2) which, when combined with our K_1 constraint, should deliver the binary mass ratio - an important parameter for establishing the evolutionary state of a CV. The emission from the donor is clearly phase-dependent in strength, peaking at phases where we look at its inner-hemisphere, consistent with emission powered via irradiation. Since this side of the Roche lobe orbits at lower radial velocities than its centre of

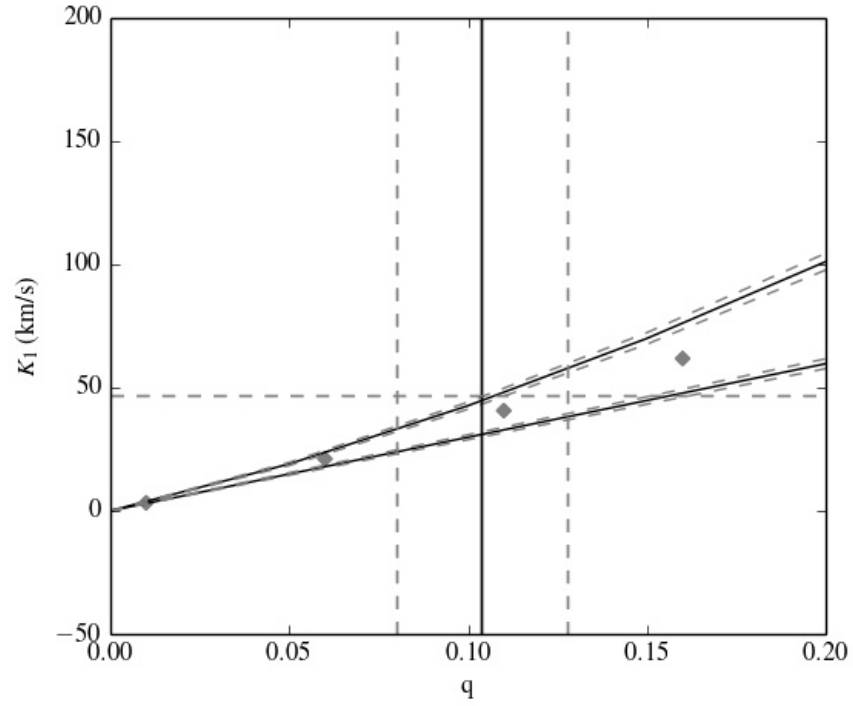


Figure 2.19: K_1 - q plane. $K_{em} > K_{L_1}$ is the top diagonal solid black line with dashed errors. $K_{em} < K_2$ is the bottom diagonal line with dashed errors. The vertical solid line with dashed errors represents the maximum value of q for a given system. The horizontal line represents the estimates of K_1 found for the Balmer lines in this case a grey dashed line. The grey diamonds are the solutions from our model.

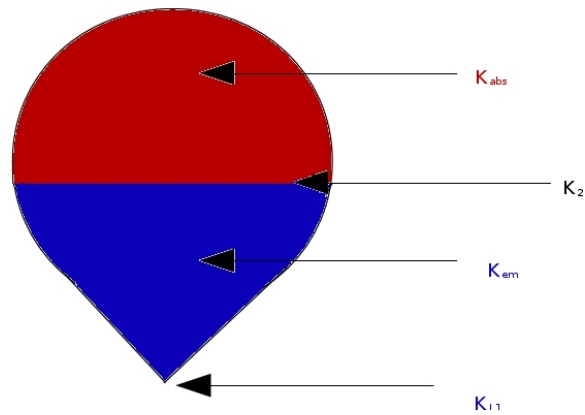


Figure 2.20: Location of different velocities on the donor surface. $K_{ab} > K_2$ and $K_{L_1} < K_{em} < K_2$.

mass, a positive correction is required to estimate the true K_2 ; $K_2 = K_{em} + \Delta K$. In the extreme case that the emission is centred on the L1 point of the donor, this deviation would be maximal. The other extreme is no correction at all. Either scenario is very unlikely and thus we have to determine an appropriate ΔK with $K_{L1} < K_{em} < K_2$.

We used the *lprofile* code from the *lcurve2*² package that calculates synthetic line profiles for an irradiated secondary. Synthetic phase-resolved data were generated for a range of models and fitted to derive the equivalent K_{em} that one would measure if this was the correct model for the secondary. For a given system, only models that are consistent with the observed K_{em} are viable, and the true K_2 is then known from the model. The key input parameters in these models is the assumed binary mass ratio, the inclination and any shielding of the secondary star due to the presence of a vertically extended and optically thick disc.

Figure 2.19 shows the K_1 - q plane to help us visualise the constraints. We represent the constraint $K_{L1} < K_{em} < K_2$ as diagonal black solid lines with dashed grey error bars. A hard upper limit on the mass ratio is provided by $q_{max} = \frac{K_{disc}}{K_{em}}$ since $K_1 < K_{disc}$ and $K_2 > K_{em}$ (Figure 2.20). This constraint is represented by the black vertical solid line with dashed errors. The horizontal dashed lines indicate the full range of K_1 values (see section 2.4.7). The absolute values of these quantities do not depend on the inclination.

Tests with model data confirm that the assumed inclination has little impact, delivering K_2 to within a few percent over the full inclination range. Figure 2.21 shows the dependence of the model and the K-correction to the inclination angle for different values of q . We fixed the inclination of the model to the system's value when known, otherwise, we fixed the model inclination to 45° . Figure 2.22 presents the $K_1 - q$ plane with models calculated for two inclination angles (cyan and grey diamonds) and solutions for these same angles (blue and black full circles). We can see that the effect of the inclination in our final solution is negligible in comparison with the error in K_1 .

As expected, the disc height, h , has a more significant effect on the correction. If we were to consider a system with no accretion disc, hence no shielding, K_{em} will still be larger than the velocity of the L_1 point. If we increase the disc height, it will start to shield the lower velocities nearest to the L_1 point, increasing our detected K_{em} . No matter how thick the disc is, K_{em} , arising from the blue area on the donor in Figure 1.1, will always be smaller than K_2 . We can see that this is well represented by the outcome of our models in the top panel of Figure 2.23. Thus, despite the fact that the K-correction is significant, we can estimate it well, and our precision on K_2 is usually the same as our error in K_{em} .

Figure 2.24, shows the difference between values of q given two values of K_1 only 20 km/s apart, showing the dominance of K_1 over the K-correction. Our findings are thus consistent

²Courtesy of Tom Marsh: <https://github.com/tmrsh/cpp-lcurve>

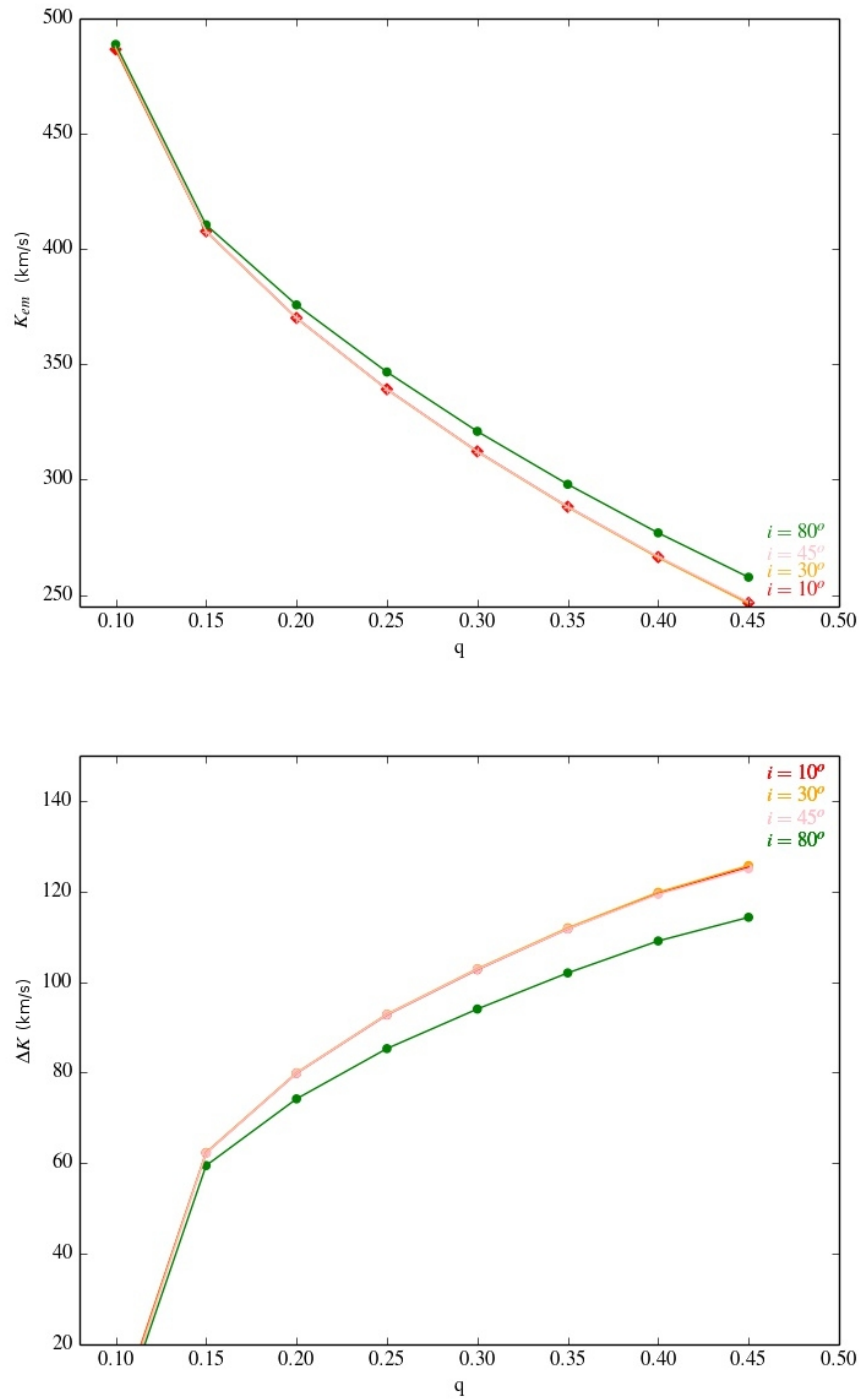


Figure 2.21: Dependence of K_{em} and K-correction upon the inclination angle assumed in the model. Values from $i = 10^\circ$ to $i = 45^\circ$ are indistinguishable.

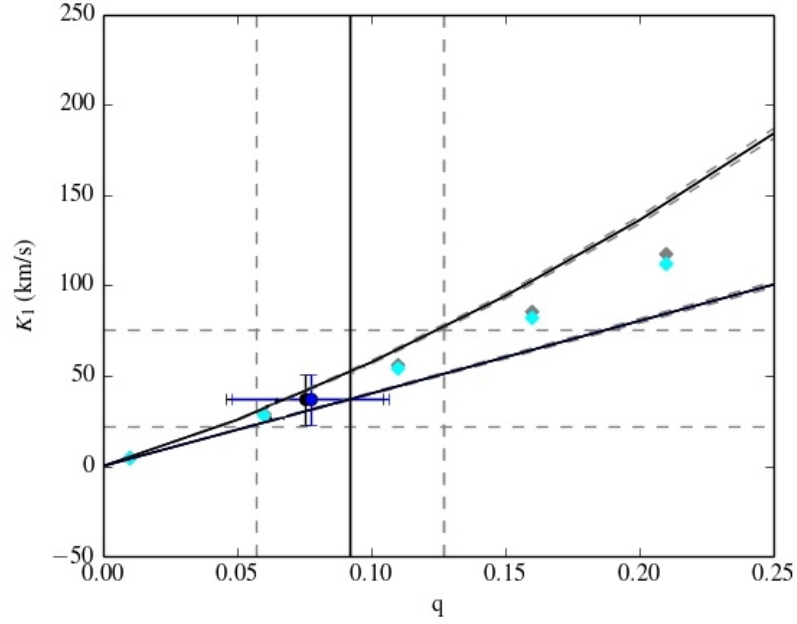


Figure 2.22: K_1 , q plane for two inclinations. Same as Figure 2.19. The grey diamonds are the solutions from our model at an inclination of 45° and the cyan diamonds are the same for an inclination of 80° . The black circle with error bars represents our best solution for the value of K_1 found from the centre of symmetry for $i = 45^\circ$ and the blue circle with error bars is the best solution calculated for $i = 80^\circ$. The grey dashed lines are the maximum and minimum estimates for K_1 derived from other emission lines.

with what was previously reported by Muñoz-Darias et al. (2005) in their extensive study of the K-correction using a different code.

Our irradiation models allow us to make a good estimate for the K-correction as a function of mass ratio, as illustrated by the grid diamonds in Figure 2.19. We consider the preferred solution to be the model that reproduces the observed K_{em} , while being consistent with the other constraints. It is the error on K_{em} and K_1 that then defines the allowed parameter range for the binary mass ratio, but the dominant source of uncertainties is still the determination of K_1 .

Synthetic Secondary Detections

Since, after our K-correction, the method can deliver good estimates of the mass ratio for observationally challenging targets, it seems important to establish the nature of the detection of the secondary star. This is especially important in low signal to noise ratio systems, such as the X-ray binary 4U1957+11 that we will discuss in Chapter 4. To quantify the nature of the detection, we generated a set of synthetic spectra with a Gaussian spot representing the secondary star at different signal to noise ratios and FWHMs. We also added the presence of an accretion disc at

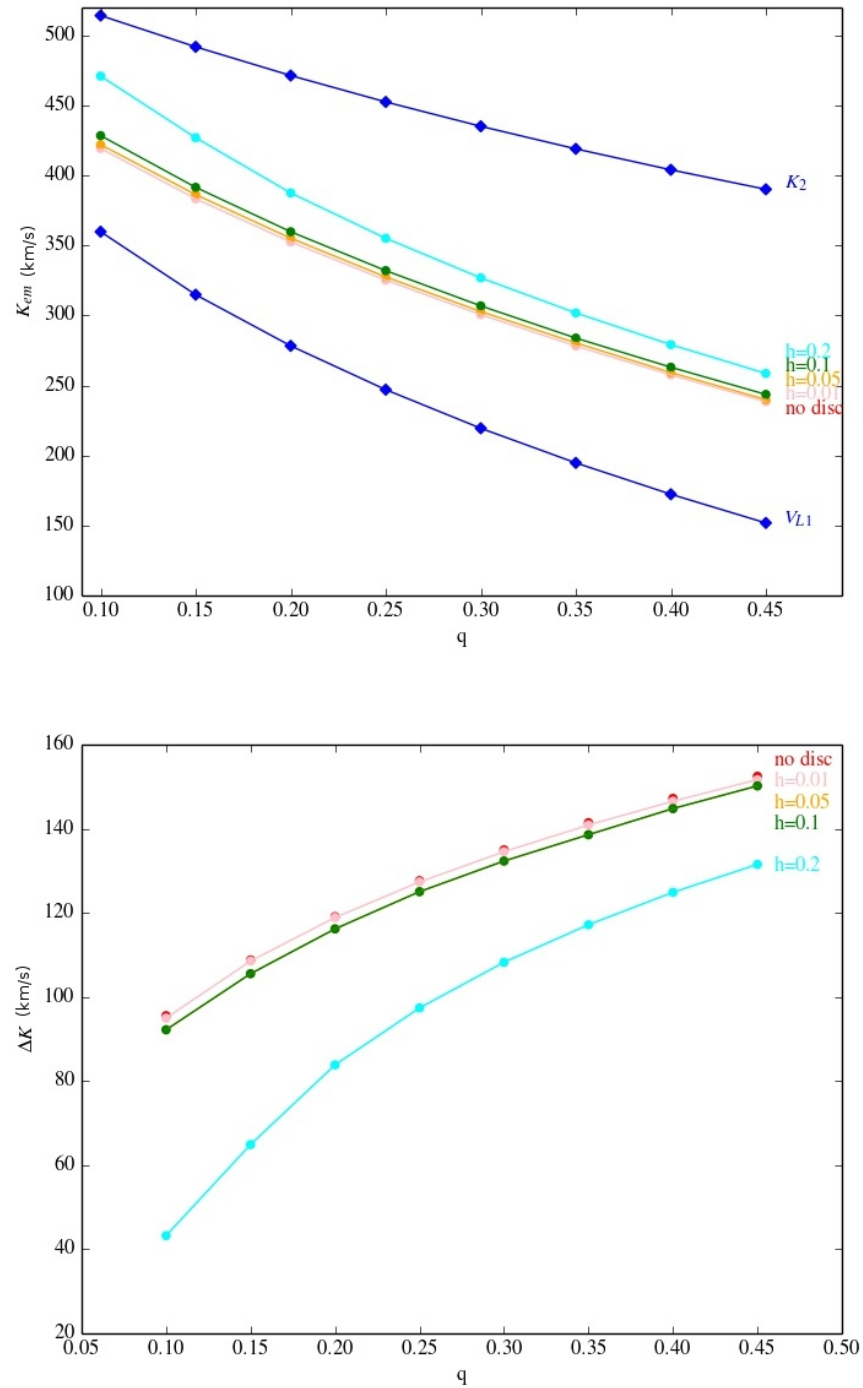


Figure 2.23: Dependence of K_{em} and K-correction upon the disc height. The solutions for $h=0.05$ and 0.1 are indistinguishable.

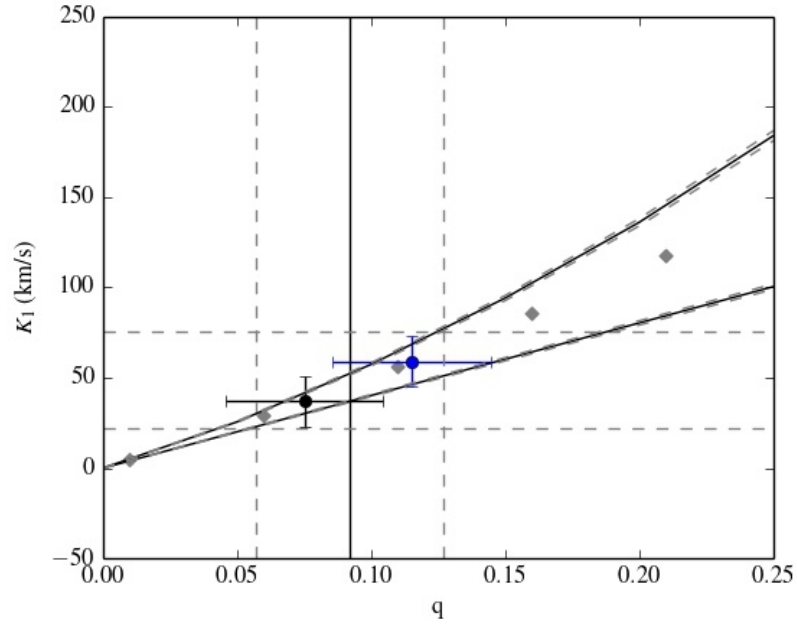


Figure 2.24: K_1 , q plane for two values of K_1 . Same as Figure 2.19 but gray and black are with a disc height angle of 0.01 and cyan and blue with a large disc thickness, 0.1.

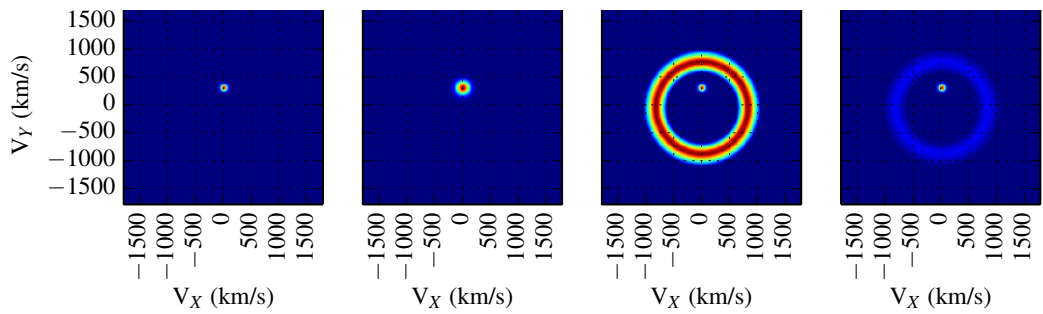


Figure 2.25: Synthetic data from left to right: Gaussian spot of FWHM=40 km/s, Gaussian spot of FWHM=80 km/s, Gaussian spot of FWHM=40 km/s plus accretion disc at the same intensity level and Gaussian spot of FWHM=40 km/s plus accretion disc at an intensity 5 times lower than the spot. Signal strength is represented from darker shades of blue (weak) to darker shades of red (strong).

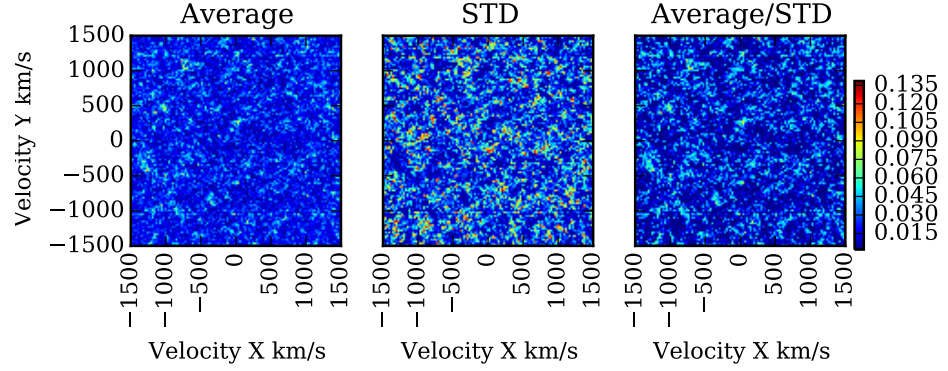


Figure 2.26: Gaussian spot of FWHM=40 km/s with a signal to noise ratio $S/N=2$. The colour scale represents the intensity of the hottest pixel.

different intensities.

Figure 2.25 shows examples of some of the original synthetic data with no added noise. The Gaussian spots are of FWHM=40 km/s and FWHM=80 km/s, located at $V_x, V_y = (0, 250)$ km/s. The accretion discs are centred at $(0, -50)$ with a width of 50 km/s. We introduced different levels of noise into these data-sets and reconstructed Doppler maps from each one. We generated 500 bootstrap samples from each reconstructed data-set and averaged these bootstrap samples in a single unbinned map, labelled “Average” on top of figures 2.26 to 2.32. We expect that a real signal would have a more consistently high signal level and therefore a lower STD on the signal of the same pixel amongst each bootstrap sample. For each data-set, we calculated the normalised STD of the signal of each pixel of the 500 samples and plotted it as the central panel map of Figures 2.26 to 2.32 (labelled “STD”). Finally, we divided the average map by the STD map (right panel of figures 2.26 to 2.32) with the idea that the smaller STD of a real signal would enhance the signal and reduce the random noise.

Figures 2.26 and 2.27 are versions of the data set showed in the first panel of Figure 2.25 with $S/N=2$ and $S/N=25$, respectively. We can see that in the extreme low S/N case of Figure 2.26 the signal of the Gaussian spot gets lost in the noise and that even though we know the signal is real, we can not differentiate it from the noise level. However, at $S/N=25$ the Doppler map (Figure 2.27) shows a strong signal at the position of the real Gaussian spot. This signal gets further enhanced after divide it by its STD. 25 is the lowest S/N that allows the indubitable determination of our simulated spot with FWHM=40 km/s. Figure 2.28 shows the results of a Gaussian spot of FWHM=80 km/s (second panel Figure 2.25) with a $S/N=2$, same as Figure 2.26. In this case, despite the extremely low S/N the Gaussian spot is easily identified as a real feature from the binned and unbinned maps, given that the signal is now over a larger number of pixels. It is also clear the very low STD of the pixels around the real signal, confirming our previous

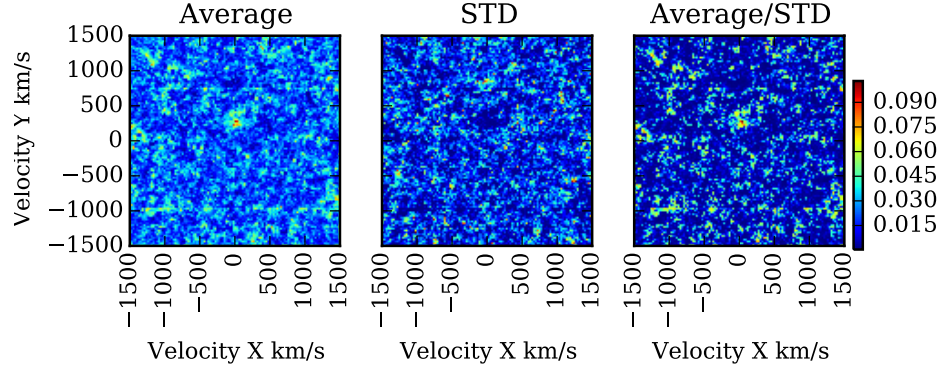


Figure 2.27: Gaussian spot of FWHM=40 km/s with a signal to noise ratio $S/N=25$. The colour scale represents the intensity of the hottest pixel.

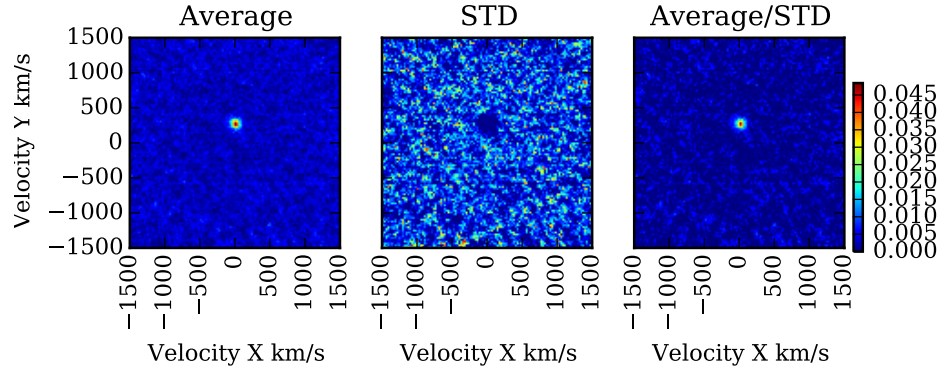


Figure 2.28: Gaussian spot of FWHM=80 km/s with a signal to noise ratio $S/N=2$. The colour scale represents the intensity of the hottest pixel.

assumption that the pixels of the real signal would have on average an equally strong signal. The fact that at the same S/N , the Gaussian spot of Figure 2.26 can not be identified is due to the properties of the fitting of the Doppler map algorithm. A spot of FWHM=80 km/s will span twice as many pixels than one of FWHM=40 km/s. As the Doppler mapping technique uses all the data simultaneously to create the final map, a broad low signal S-wave, spanning several pixels in wavelength, will be traced more easily than a narrow S-wave, with only a couple of pixels in the wavelength direction so any set of hot pixels will deviate the fit from the real S-wave and will generate a map dominated by noise such as the ones in Figure 2.26.

Figures 2.29 and 2.30 were generated with the data-set shown on the third panel of Figure 2.25 at $S/N=2$ and $S/N=25$, respectively. It can be seen that the dominant feature in both Figures is the accretion disc. The Gaussian spot is blurred in Figure 2.30 and missing in Figure 2.29.

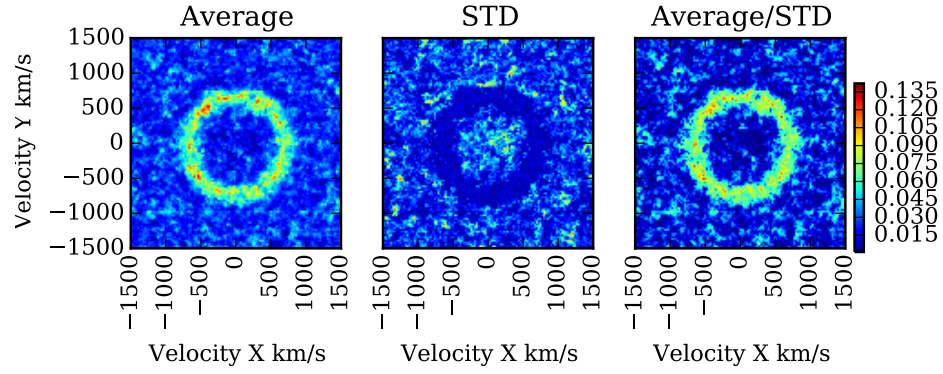


Figure 2.29: Gaussian spot of FWHM=40 km/s plus accretion disc at the same intensity level with S/N=2. The colour scale represents the intensity of the hottest pixel.

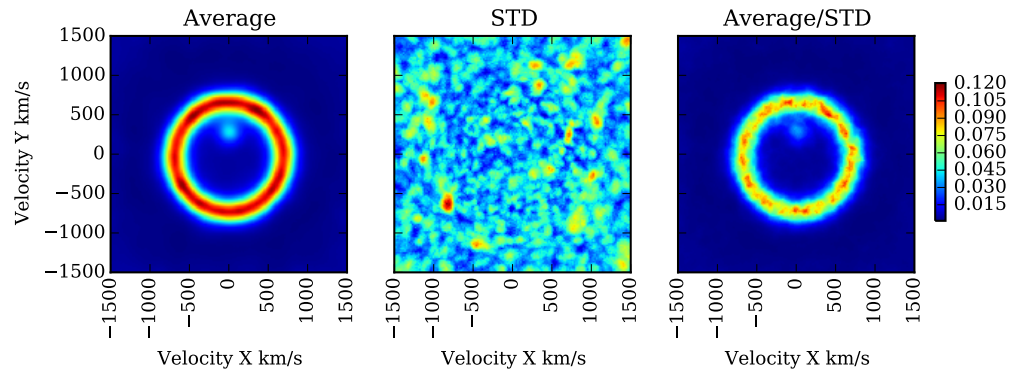


Figure 2.30: Gaussian spot of FWHM=40 km/s plus accretion disc at the same intensity level with S/N=25. The colour scale represents the intensity of the hottest pixel.

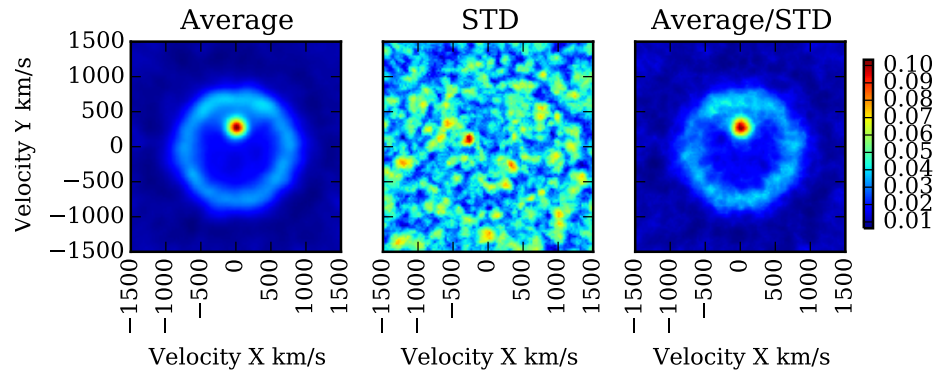


Figure 2.31: Gaussian spot of FWHM=40 km/s plus accretion disc at intensity 5 times lower than the spot with S/N=25.

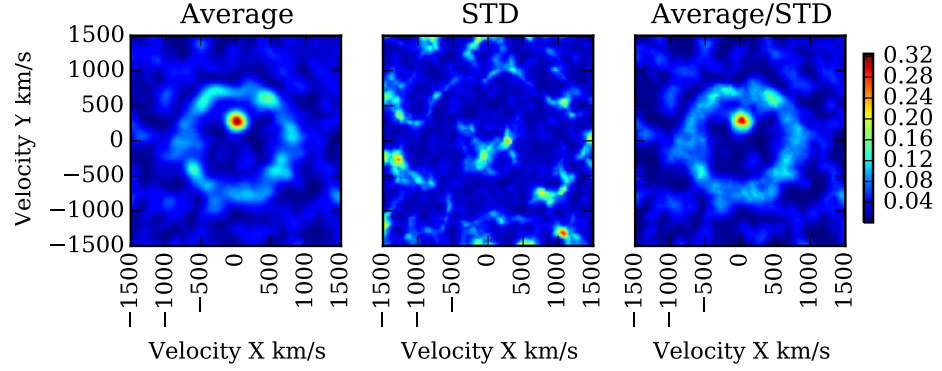


Figure 2.32: Gaussian spot of FWHM=40 km/s plus accretion disc at intensity 5 times lower than the spot with S/N=2. The colour scale represent the intensity of the hottest pixel.

The Doppler algorithm focuses on the clear disc feature in these cases, trying to best fit the disc dominated pixels, making a poor job on the spot in both cases, more dramatically at extremely low S/N.

Figures 2.31 and 2.32 show the results for the data plotted in the last panel of Figure 2.25 with S/N=2 and S/N=25, respectively. These data were generated with the same specifications of disc position, width, Gaussian spot position, and FWHM as the previous ones, but with the signal strength level of the disc five times lower than the spot. This allowed the Doppler algorithm to focus on the spot, highlighting its presence at the expense of somewhat neglecting the sharpness of the accretion disc. It can also be seen that the spot on the averaged map is reconstructed with a higher FWHM than the original synthetic feature. Nevertheless, the accretion disc and the Gaussian spot detections are evident, and the velocity of the spot feature is the same than the original noise free map. In the cases of extremely low S/N, the dominant feature is the broadened Gaussian spot, the disc is present, but blurred. In smoothed maps (before reaching optimal χ^2) the disc can be appreciated at the expense of broadening the Gaussian spot even more. Still, the centre of symmetry technique can be used on the broadened disc given that it is symmetric enough.

These tests show that the ability to recover an emission spot depends not only on S/N, but also the width of the feature and the relative strength of other emission sources. In any case, these simulations show that even at low S/N a Gaussian spot can be reliably detected, and that bootstrapping offers a mean of verifying the significance of low S/N features.

2.5 Summary

In this Chapter, we outlined the tools needed to reduce and analyse spectroscopic data, with special emphasis in the MagE spectrograph. We have shown the benefits of using the indirect imaging technique, Doppler tomography, and presented new methods to exploit these advantages to dynamically constraint CBs parameters. We have also presented a review of more classic methods and introduced the bootstrap as a reliable method to estimate uncertainties.

Three

Emission Line Tomography of the Short Period Cataclysmic Variables CC Scl and V2051 Oph

This Chapter is based on:

“Emission line tomography of the short period cataclysmic variables CC Scl and V2051 Oph”

P. Longa-Pena; D. Steeghs; T. Marsh

Monthly Notices of the Royal Astronomical Society 2014, 447 (3): p149-159

CC Scl and V2051 Oph were the first test subjects of the methods described in Chapter 2. In this Chapter, we present time resolved spectra of CC Scl and V2051 Oph obtained with MagE. In Section 3.3.3 we derive dynamical constraints on the radial velocities of the system components to estimate the mass ratio (q) of these two short period CVs. We present the first results of our method to estimate the value of the phase zero Φ_0 , K_1 , K_{em} and hence to constrain the value of q by calculating a K-correction. Furthermore, we used a variation from the Doppler tomography secondary emission method, to constrain the value of the systemic velocity γ (Section 2.4). We also use the traditional methods of radial velocity determination, double Gaussian fit and diagnostic diagrams of the disc lines (Section 3.3.2) and present the performance of these methods for different lines against the Doppler map-based techniques.

3.1 Introduction

CC Scl was independently discovered as the ROSAT source 1RXS J231553.2-304855 (Schwope et al., 2000) and in the Edinburgh-Cape Blue Object Survey as EC 23128-3105 (Chen et al. (2001)). From time resolved spectroscopy, Chen et al. derived an orbital period of 0.0584(2)d, $K_1 = 35 \pm$

10 km/s and $0.06 < q < 0.09$. They also reported a possibly transient feature resembling an eclipse present in some of their photometric light curves. This feature was also reported by Tappert, Augusteijn, & Maza (2004).

Ishioka et al. (2001a) presented a significant amount of photometry covering a six-month baseline, finding superhumps and classifying CC Scl as a SU UMa type dwarf nova. They detected a super hump period of 0.078 d, which is 30% larger than the orbital period. This would be the largest fractional superhump excess in a SU UMa type followed by the 7.7% excess observed in TU Men. During an outburst in November 2011, Woudt et al. (2012) attempted to refine the orbital period photometrically, proposing $P_{orb} = 0.00450801(6)$ d. They also identified a periodicity of 389.49 s that was associated with the WD spin period and would classify CC Scl as a super-humping intermediate polar below the period gap.

Recently, Kato (2014) have confirmed CC Scl as an eclipsing system. They presented a light curve showing a brief and shallow eclipse that was used to further refine the ephemeris and determine an accurate orbital period of the system $(BJD) = 2456668.00638(9) + 0.058567233(8)E$. The period proposed by Woudt et al. (2012) is inconsistent with the eclipse period. The periodicity detected by Woudt et al. (2012) was most likely not the orbital period, since they observed the system during outburst.

V2051 Oph was discovered by Sanduleak (1972). It is classified as an eclipsing SU Uma type CV. Kiyota & Kato (1998) confirmed this classification, using the photometric detection of superhumps in the light curve of V2051 Oph during outburst.

Baptista et al. (1998) used ground-based high-speed eclipse photometry and HST spectroscopy to derive the binary geometry and to estimate the masses. They reported a mass ratio of $q = 0.19 \pm 0.03$, an inclination of $i = 83^\circ \pm 2^\circ$ and the respective masses to be $M_1 = 0.78 \pm 0.06 M_\odot$ and $M_2 = 0.15 \pm 0.03 M_\odot$. Their photometric model would result in a projected radial velocity for the white dwarf of $K_1 = 83 \pm 12$ km/s while the secondary would move with $K_2 = 436 \pm 11$ km/s. This K_1 value is in excellent agreement with radial velocity analysis by Papadaki et al. (2008), who find $K_1 = 84.89 \pm 12.22$ km/s.

Another remark about V2051 Oph is its accretion disc asymmetry, as suggested by the eclipse mapping from Saito & Baptista (2006) and Baptista et al. (2007). This asymmetry is also found in the spectra of Steeghs et al. (2001).

Without a detection of the secondary star or a fortuitous inclination that leads to eclipses, it is difficult to derive robust binary parameters for many short period CVs. Nearly all the constraints of orbital parameters of non eclipsing systems are limited to the study of the Balmer emission lines. The, until recently neglected, Ca II triplet, however, has proven to be an auspicious candidate for orbital parameter constraints as shown by van Spaandonk et al. (2010). Despite the relative weakness of the Ca II triplet with respect to the Balmer lines, it is commonly found in short period CVs and can be used to track the secondary star better than the Balmer

lines due to its lower ionisation energy (van Spaandonk, 2011).

3.2 Observations and Reduction

The observations were taken on June 2010, using the MagE spectrograph (see Section 2.1.2). We obtained 26 spectra of CC Scl on the 8th of June and 43 of V2051 Oph on the 9th of June with 180 s exposure time, respectively. The MagE CCD is a 2048x1024 pixel E2V with 35 micron pixels and was readout unbinned in slow read out mode.

The spectra were reduced with the Python based pipeline written by Dan Kelson¹ which performs typical calibrations: flat-fielding, sky background subtraction, optimal extraction and wavelength calibration. The wavelength calibrations were derived from Thorium-Argon lamp exposures taken during the respective nights. These provide suitable lines over the entire wavelength range. The pipeline selects the closest lamp exposures in time to each science spectrum.

Raw spectra were flux calibrated using the spectrum of the flux standard Feige 110, observed at the end of each night using both a wide slit and the same slit width used for the target exposures. The wide-slit observation was used for determining the wavelength dependent flux calibration. The spectra were then divided by the ratio between the narrow and wide slit spectra in order to apply a 1st-order slit loss correction.

Due to the poor signal to noise ratio of the first ($\sim 9400 - 11200 \text{ \AA}$) and last orders ($\sim 3100 - 3500 \text{ \AA}$), these were not included in the analysis. We did not attempt to remove telluric features from the spectra.

3.3 Results

3.3.1 Spectrum

The average spectra of our targets are shown in Figures 3.1 and 3.2. We averaged all flux-calibrated exposures, giving equal weighting to each spectrum. Key spectral features are labelled. Telluric lines are not subtracted, but marked with the symbol \oplus . No correction for orbital motion has been made in constructing these average spectra. These were derived from 26 exposures spanning 1.1 orbits for CC Scl and 43 exposures covering 2.3 orbits in the case of V2051 Oph. All lines are in emission and double-peaked. The spectra are dominated by the Balmer lines that are clearly resolved up to H10 as well as broader lines from the Paschen series from P ζ to P16. They also show numerous He I and He II lines in emission. Some Fe II and Ca II lines, particularly the Ca II triplet 8498.02 \AA , 8542.09 \AA and 8662.14 \AA are also present in emission. All Balmer and He lines are asymmetric, showing a stronger blue peak in the spectrum of CC Scl. In the case of

¹ Carnegie Observatories Software Repository: <http://code.obs.carnegiescience.edu/mage-pipeline>

V2051 Oph, the red peak is stronger than the blue, differing from previously published spectra that show a stronger blue peak (Papadaki et al. 2008, Steeghs et al. 2001 and Watts et al. 1986). No orbital sampling effects are believed to be causing this behaviour, since we observed more than one full orbit. In comparison with previous published spectra of CC Scl in quiescence, (e.g. Chen et al. 2001; Tappert et al. 2004), our higher resolution spectra undoubtedly show the presence of He II 4685.75 Å. Furthermore, even though there is no evidence for the C III-N III blend in its blue wing, as reported during outburst by Hellier et al. (1997) there is a sign of He I 4713.20 Å in its red wing, previously unresolved. We also see weak He II 5411.55 Å, which we would expect to be stronger than it is in the case of an IP. A narrow absorption feature consistent with 4920 Å, potentially Fe I is blended with He I. We constructed light curves from our spectra, but no eclipse features were detected. Based on the short eclipse time suggested by Kato's light curve, our time resolution is of the order of half of the total eclipse duration. By covering only one orbital period, and adding the fact that the eclipse is not always visible, it is not surprising that we could not resolve it.

In the case of V2051 Oph, we found features unnoticed until now, such as the blend between N III 4640.64 Å, HeI 4713.20 Å and He II 4686.75 Å. N III 4640.64 Å is part of the Bowen blend, which also includes some C III components. In X-ray binaries, this blend often contains strong components from the irradiated face of the donor (Bowen blend fluorescence, see for example Steeghs & Casares 2002, Casares et al. 2006 and Casares et al. 2003). Despite our high resolution, the S/N of the blend was too low to attempt to find the secondary by this method. Si II and O II in emission, and O I in absorption are also present in our spectra.

3.3.2 Radial velocities analysis

We performed the double Gaussian analysis, as implemented by Schneider & Young (1980), to obtain the radial velocities of several lines. The measured radial velocities were then fitted with a sinusoidal curve of the form:

$$v_r(\Phi) = \gamma - K \sin(2\pi(\Phi - \Phi_0)) \quad (3.1)$$

where γ is the systemic velocity, K is the radial velocity semi-amplitude of the emission line, Φ_0 is the time of the conjunction and Φ is the orbital phase (See Chapter 2). We let K , γ and Φ_0 vary. We employed a Gaussian FWHM of 500 km/s and Gaussian separations of $a = 500 - 4000$ km/s in steps of 50 km/s and constructed diagnostic diagrams (Shafter, Szkody, & Thorstensen, 1986) for each line. We show an example diagnostic diagram in Figure 3.3, constructed with the results derived from H β for both systems. We compare the two strongest Balmer lines with Ca II 8662.14 Å in order to assess how stable the inferred parameters are against the choice of line. The results

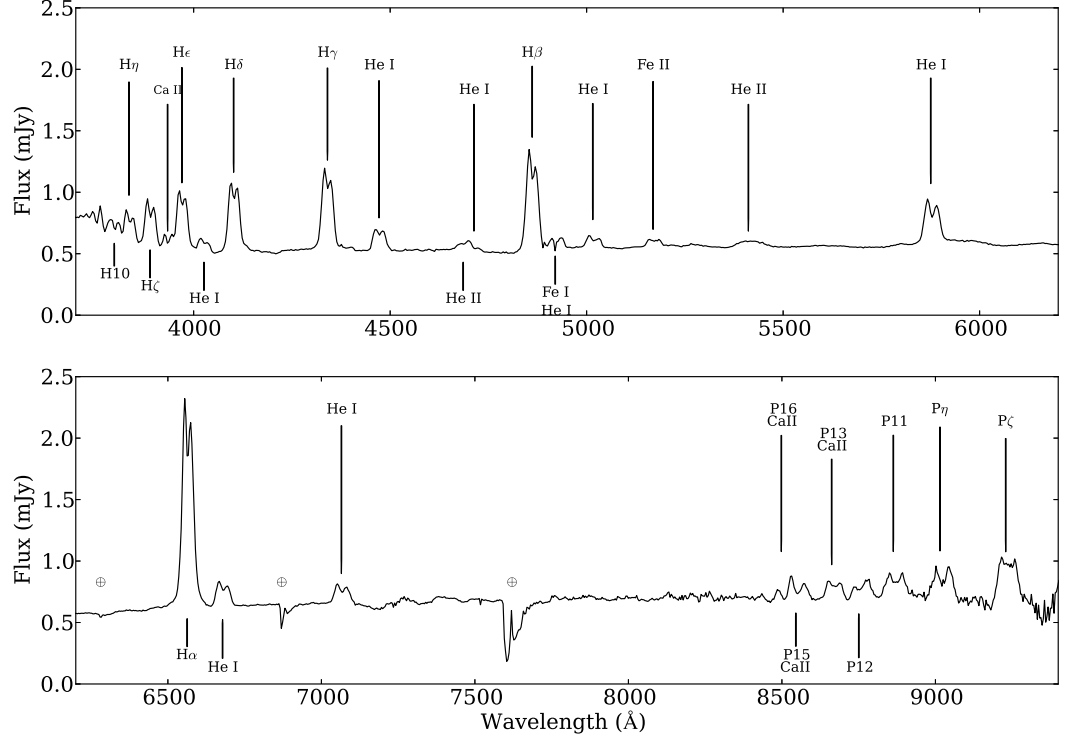


Figure 3.1: Average spectrum of CC Scl. Each of the 26 spectra were given equal weighting and no correction for orbital motion has been made.

Line	CC Scl			V2051 Oph		
	γ [km/s]	K_1 [km/s]	Φ_0	γ [km/s]	K_1 [km/s]	Φ_0
H α	117 ± 20	53 ± 5	0.1 ± 0.04	175 ± 100	110 ± 16	0.07 ± 0.02
H β	55 ± 5	59 ± 7	0.1 ± 0.03	-38 ± 40	129 ± 20	0.02 ± 0.02
CaII	193 ± 19	52 ± 11	0.1 ± 0.03	-36 ± 22	158 ± 28	-0.1 ± 0.05

Table 3.1: Orbital parameters derived from the diagnostic diagrams of CC Scl and V2051 Oph. The reported errors are the dispersion between the smallest and largest values for each parameter of the averaged plateau range. The results for Ca II in the case of V2051 Oph are not reliable, see the bottom panel of Figure 3.5.

can be found in Table 3.1. The adopted values are the average of all fits between the stable values of a , using the full range of the parameters over that range to derive an uncertainty estimate.

In the case of CC Scl, diagnostic diagrams of the lines showed a consistent shape with stable values of a between 2000 – 2500 km/s. For V2051 Oph, H α and H β diagnostic diagrams converged between 2500 – 3100 km/s, but the narrower CaII line converged between 1600 – 1800 km/s.

Some representative fits for the reported lines are shown in Figure 3.4. The radial veloc-

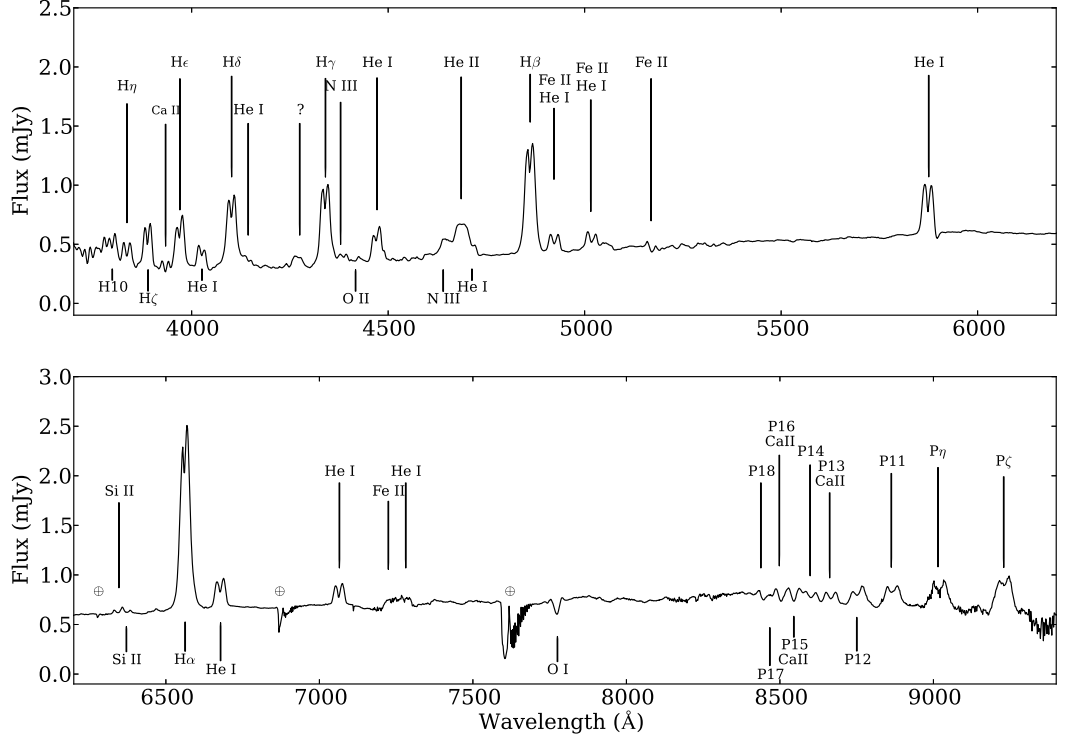


Figure 3.2: Average spectrum of V2051 Oph. Each of the 43 spectra were given equal weighting and no correction for orbital motion has been made.

ity curve of Ca II has a similar behaviour than H α and H β in the case of CC Scl. These show similar amplitude and phase shifts but significantly different values for the systemic velocity γ . It is noticeable in the fits for V2051 Oph (Figure 3.5), that the Ca II line results of the diagnostic diagram are particularly poor, suggesting the method is not reliable for this line in the case of V2051 Oph. This is at least partially due to the fact that Ca II is weaker in V2051 Oph compared to CC Scl. The discrepant results for γ depending on the line are not rare among CVs, in the case of V2051 Oph, see for example Watts et al. (1986), Papadaki et al. (2008) and references therein. This behaviour is normally associated with blending of nearby lines or asymmetries between the red and blue wings, both of which are applicable to our targets. The asymmetry in the average line profiles, as well as the fact that some of our RV fits are poor due to a distorted RV curve, suggest that these parameters may be skewed by an asymmetry in the disc emission, such as caused by a bright spot. This is a notorious issue with the double-Gaussian method, even when a diagnostic diagram is considered.

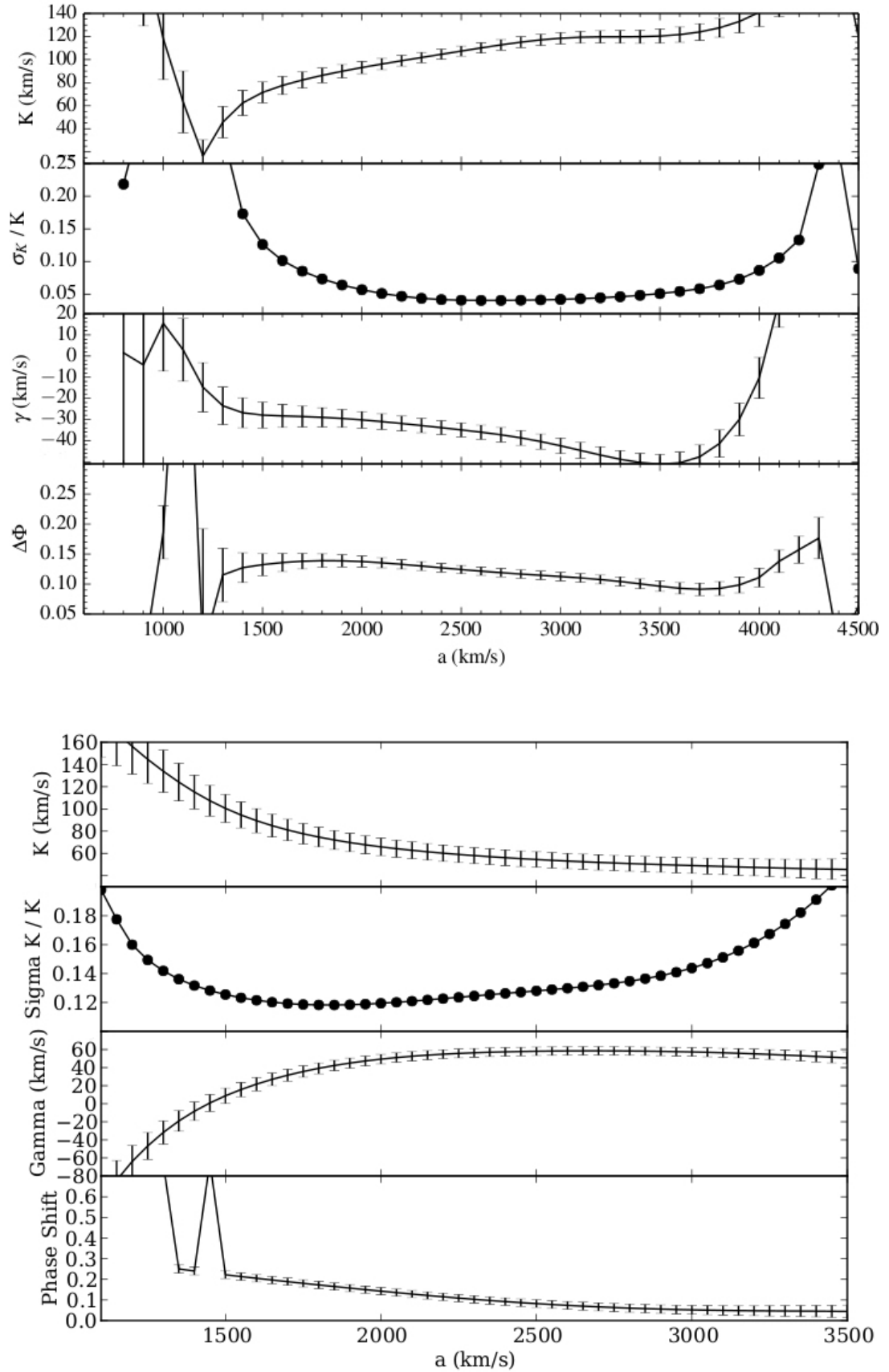


Figure 3.3: Diagnostic diagram of H β for V2051 Oph, top and CC Scl, bottom. Panels are labelled on the right side. See Chapter 2 for details on how to read this plots.

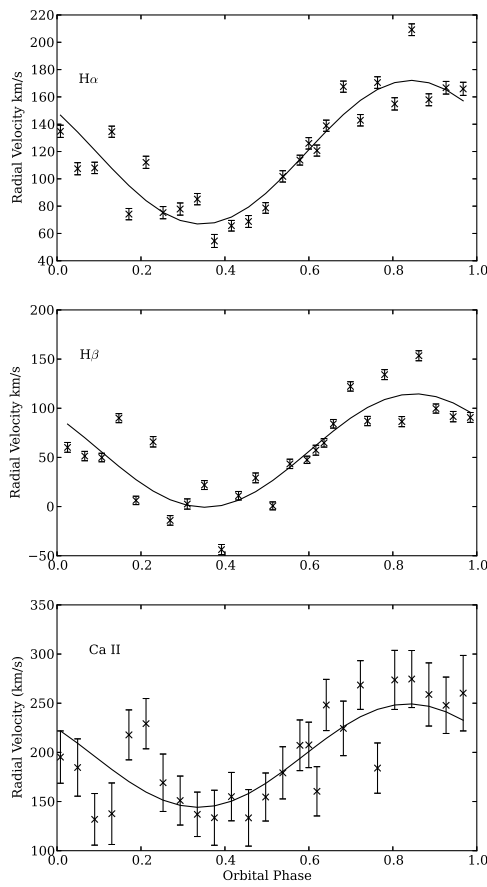


Figure 3.4: $H\alpha$, $H\beta$ and CaII radial velocity curves of CC Scl, for a Gaussian separation of 2500 km/s, folded on the orbital period.

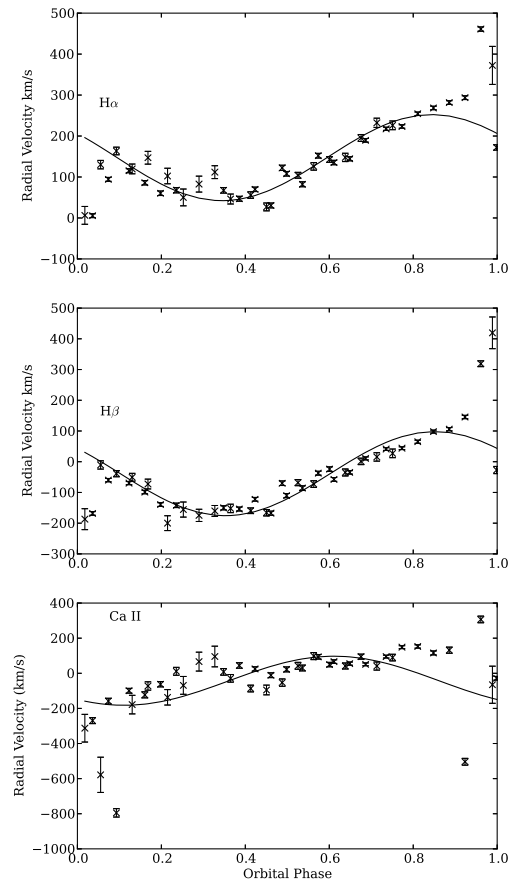


Figure 3.5: $H\alpha$, $H\beta$ and CaII radial velocity curves of V2051 Oph, folded on the orbital period, for a Gaussian separation of 3200 km/s for the Balmer lines and 1800 km/s for CaII.

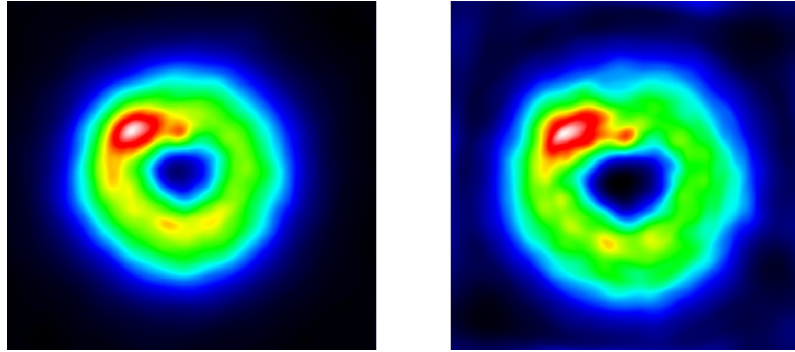


Figure 3.6: Two Doppler maps of $H\beta$ for CC Scl generated with the same value of χ^2 but with the eclipse derived period (left) and Woudt et al. (2012) period (right).

3.3.3 Doppler tomography

We used the indirect imaging technique, Doppler tomography (Marsh & Horne 1988, see Chapter 2), to resolve the origin and kinematics of the various emission components. The Doppler maps were generated for the lines with the strongest S/N. The eclipse phases were removed before calculating these Doppler maps. Due to the extensive wavelength coverage, a large number of lines were accessible for tomography, however we only show the most representative lines for each system. All the individual spectra were normalised to the continuum using low-order polynomial fits and the maps were allowed to reach low values of χ^2 . Figure 3.6 shows a comparison between two Doppler maps of CC Scl for $H\beta$ made with the spectroscopic period (Chen et al., 2001) and with the photometric period of Woudt et al. (2012). Both maps were made with the same value of χ^2 . We can see that an incorrect period will introduce structure into the map at higher values of χ^2 , confirming the claim by Kato (2014) that the photometric period reported by Woudt et al. is not correct. In Figures 3.7 and 3.8, we compare the observed data in trailed spectrogram format with the reconstructed Doppler maps as well as the predicted data in order to visually assess goodness of fit. All trailed spectra show clear evidence for a strong disc component, responsible for the double-peaked line profiles and clearly visible in all the reconstructed maps. In addition to the accretion disc, most lines show enhanced emission in the fourth quadrant, identified as the bright spot. The bright spot seems to be consistent with the trajectory of the gas stream if we consider the expected binary parameters. In addition to disc and bright spot contributions, the maps of V2051 Oph show additional regions of enhanced emission in the disc. In many lines, the right side of the disc is even brighter than the bright spot region. This enhanced emission has been reported before for this system while coming out of superoutburst by Papadaki et al. (2008) and it was believed to be the equivalent of the superhump light source. It is noticeable that this emission is located in the same place as it was when previously reported by Papadaki et al.. We reconstructed Doppler maps for the six stronger He I lines. They all showed

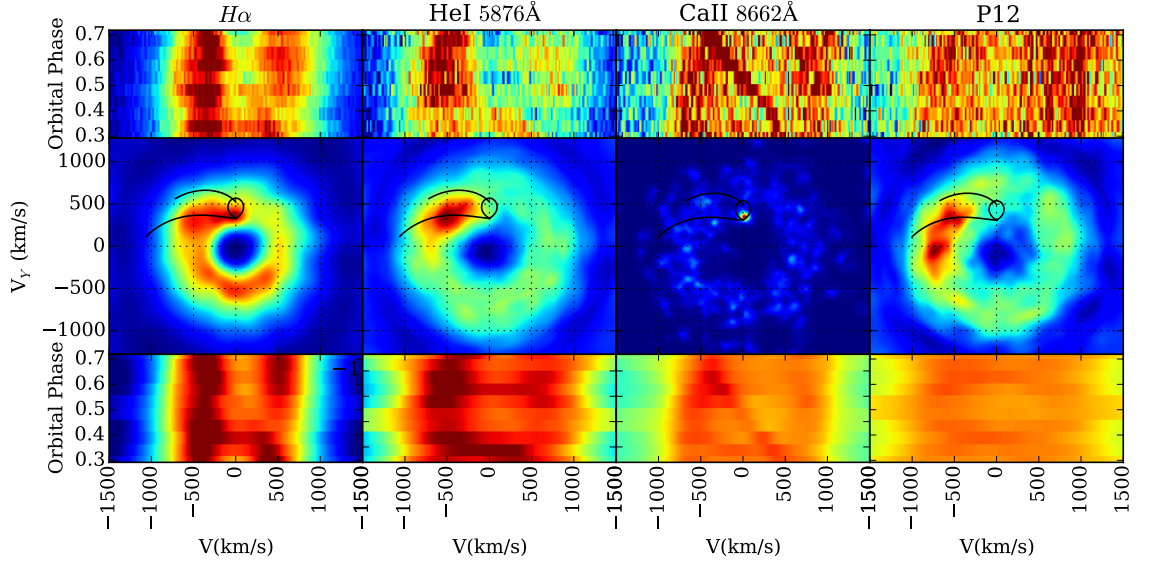


Figure 3.7: Doppler maps for CC Scl. Top, observed data, middle, Doppler map. Bottom, reconstructed data. From right to left: $H\alpha$, HeI 5876 Å, CaII 8662 Å and Paschen 12. The x and y axes are V_x and V_y , respectively. The Roche lobes model for the best orbital solution and gas stream are plotted with a solid line over the Doppler maps. The CaII map was led toward low values of χ^2 to enhance the secondary detection.

the same features and show the brightest line, HeI 5876 Å for both systems.

Noticeable in the trailed spectra of Ca II is a sharp S-wave moving in between the disc peaks. This feature is the secondary star, clearly visible in the Doppler map of Ca II of CC Scl (third panel of Figure 3.7). This Doppler map was pushed toward low χ^2 values in order to enhance the secondary star feature. Traces of the secondary emission are also visible in the maps of the Balmer lines from $H\alpha$ to $H\delta$, at velocities $(V_x, V_y) = (0, 410)$ km/s in the case of CC Scl. The emission is strongest and sharpest in the Ca II lines, as shown in the third panel of Figure 3.7. The disadvantage with the Ca II triplet is its close proximity to the Paschen lines P13, P15 and P16, respectively. This makes the Ca II profiles blend with the Paschen lines mentioned before. We have measured the contribution of each Paschen line to the respective Ca II lines by estimating a trend from Paschen 10 to 12. We considered the ratio between the blends and reconstructed simultaneous Doppler maps of both Ca II and Paschen to ensure this blending did not affect our Ca II maps. The maps shown in the third and fourth panels of Figure 3.7 are the corresponding de-blended maps.

Systemic velocity γ

As the measurements of γ from the diagnostic diagram did not yield consistent results, we determined the systemic velocity using the Doppler maps of CaII 8662.14 Å. We used the method described in Section 2.4. We choose Ca II over the Balmer lines given that it contains a sharp

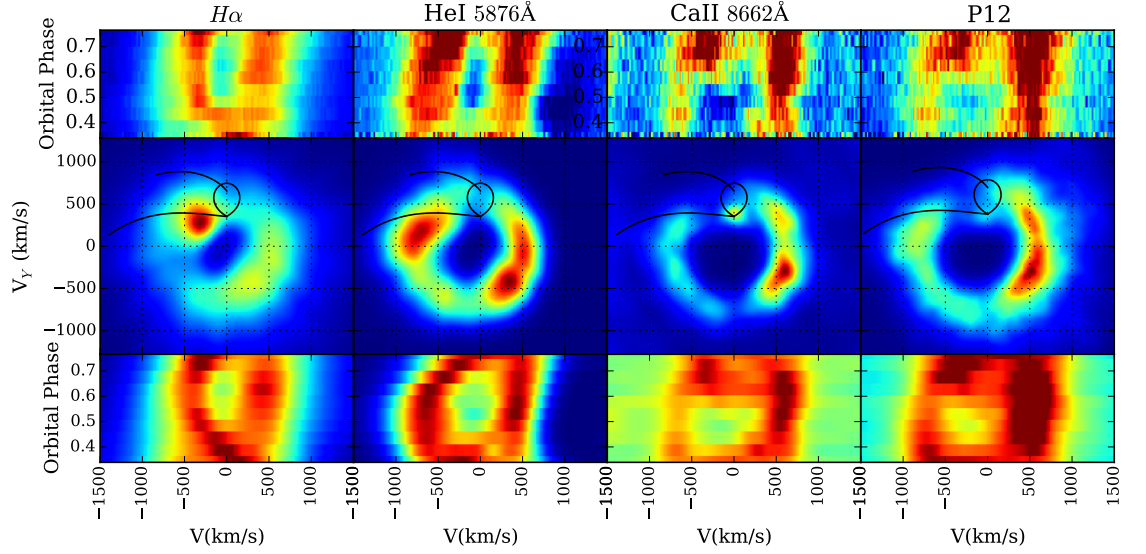


Figure 3.8: Doppler maps for V2051 Oph. Top, observed data, middle, Doppler map. Bottom, reconstructed data. From right to left: $H\alpha$, HeI 5876 Å, CaII 8662 Å and Paschen 12. The x and y axes are V_x and V_y respectively. The Roche lobes model for the best orbital solution and gas stream are plotted with a solid line over the Doppler maps.

S-wave from the donor that should map to a sharp spot in the maps.

Figure 3.9 shows two examples of our histograms, comparing $\gamma = 0$ km/s and 50 km/s. We can see that the average value of the FWHM is smaller for the $\gamma = 0$ km/s case, but also the width of the distribution is narrower than for $\gamma = 50$ km/s. This is expected if $\gamma = 0$ km/s is closer to the true value than $\gamma = 50$ km/s, as the latter would lead to distorted and broader emission spots in the reconstructions. Thus when considering these two parameters as a function of assumed γ , we would expect to be able to pick the preferred value for the systemic velocity. In Figure 3.10 and 3.11 we show how these parameters evolve as a function of γ .

To estimate an uncertainty on this optimal γ , we consider the error derived on the standard deviation of the distributions and consider all the values of the systemic velocity whose sigma values are less than three times than the standard distribution away from the optimal γ (horizontal line cutting the lower panel of Figures 3.10 and 3.11, see Section 2.4).

Using this recipe, we find a value of $\gamma = 30^{+33}_{-22}$ km/s for CC Scl and $\gamma = 0^{+12}_{-17}$ km/s for V2051 Oph. These are the values that we adopted to generate all the Doppler maps shown in this Chapter.

Primary velocity K_1

After optimising the value of the systemic velocity, we performed a centre of symmetry search of the disc feature as described in Section 2.4.7.

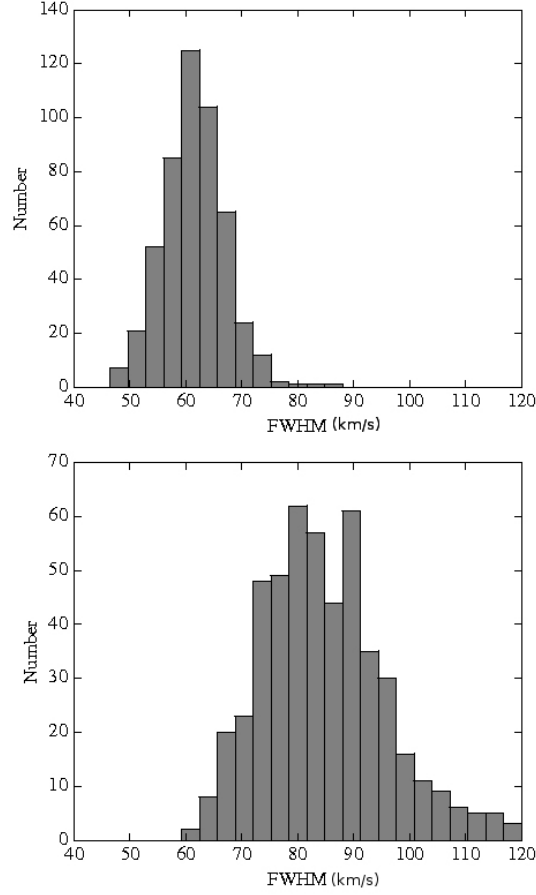


Figure 3.9: Histograms for two values of γ : our best value, $\gamma = 0$ km/s and $\gamma = 50$ km/s.

To test the behaviour of the method depending on the chosen line, box size and box location, we considered different box regions and explored the five strongest Balmer lines and Ca II 8662Å. We show the position of the so called boxes in Figure 3.12. An obvious region to exclude is the quadrant containing the bright-spot, as well as the region near any donor star emission. Good regions are the bottom left quadrant ($-V_x, -V_y$), box 2 and the top right quadrant ($+V_x, +V_y$), box 3. We also trialled a more extended area including the bottom right quadrant (despite seeing slight asymmetries in some lines) and rectangular boxes covering the bottom half and the right half of the map, boxes 4 and 5. We also ran the analysis on a box that effectively uses the whole map, to further quantify the impact of the chosen region on the inferred K_1 , box 1.

We expect that a box containing more asymmetries will deliver, on average, a larger value of K_1 . This is the case for example, shown in box 1, Figure 3.13. Box 1 is the box covering the entire doppler map, so it is comparable to the double Gaussian technique and its average K_1 value

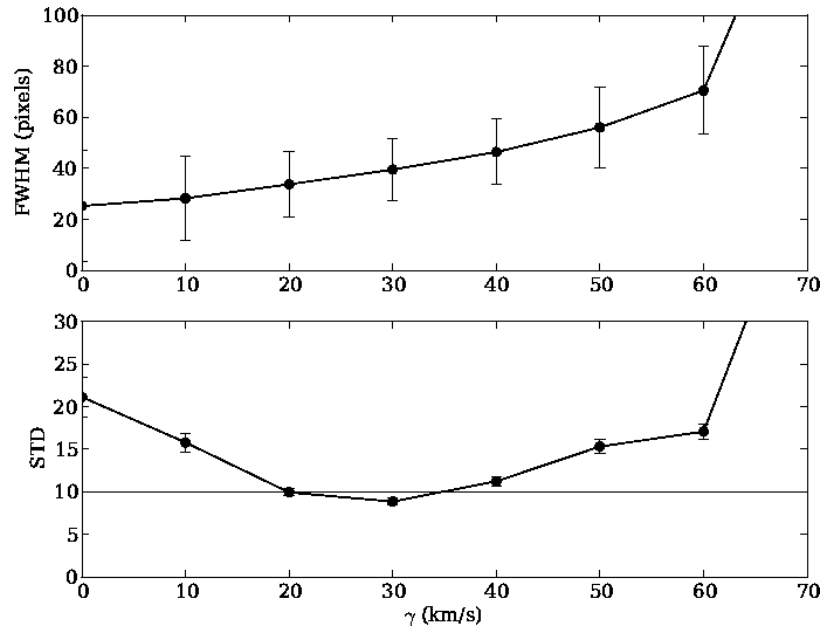


Figure 3.10: FWHM of the secondary star and STD versus value of systemic velocity, γ , for CC Scl. The error bars are sometimes smaller than the symbol.

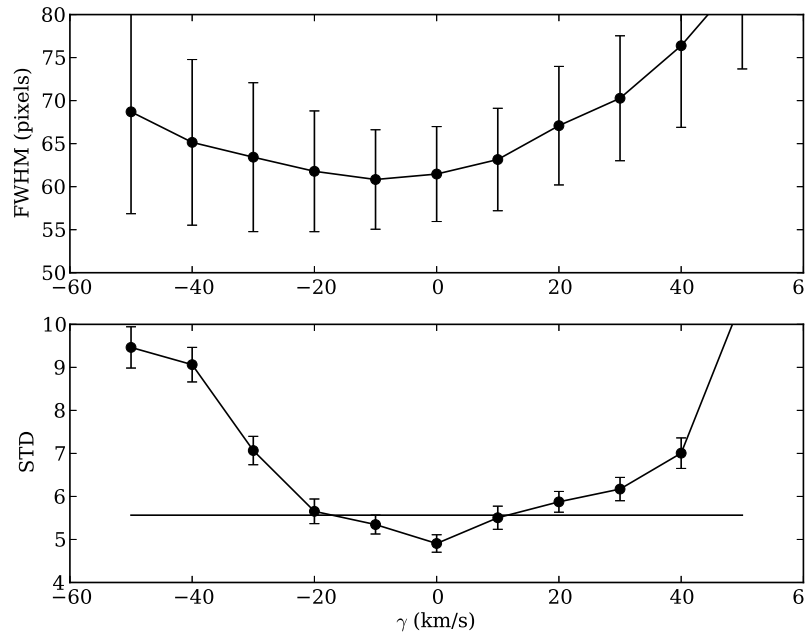


Figure 3.11: FWHM of the secondary star and STD versus value of systemic velocity, γ , for V2051 Oph.

is indeed the highest among the five boxes. In this particular case, the second largest average value was delivered by box 3 since it contained a small focus of asymmetry and the lowest values by box 2 that was, on average, the most symmetric (see Figure 3.12). As our goal was to standardise a method that delivers the best possible solution in any case, boxes 2 and 3 proved to be too strongly dependant of the morphology of the individual Doppler map to be constant. That leaves us with boxes 4 (right half) and 5 (bottom half). Despite that in our example box 5 showed on average slightly lower values than box 4, in some cases the bright spot feature would extend all the way to the 3rd quadrant introducing asymmetries in the disc inside box 5. Depending on the geometry of the disc, one should choose the best box. In the case of removing all interaction to find the optimal box (box 4 in our example) and automatically going for the least likely asymmetric box (box 5), as can be seen in Figure 3.13, we are only around 5 km/s away from what could be the optimal value and ~ 15 km/s below the value delivered by the whole box. So if automating the process, our method still delivers better results than the double Gaussian technique. Rather than do this blindly, to perform the centre of symmetry search and report a value for K_1 , we used box 4 or 5 -depending of the symmetry of the particular disc- preferring the CaII 8662 Å Doppler maps when possible.

The lines that showed the most stable behaviour were Ca II 8662 Å and H β . Variations between them for the same box are ~ 20 km/s, variation between different boxes are ~ 20 km/s in the half quadrant boxes, and up to ~ 50 km/s in the rest. The higher Balmer lines showed slightly larger variations, while H α did not deliver consistent values. We believe that the lack of consistency of H α could be due to the strength of the bright spot feature in this line.

With this technique, there is a compromise between the size of the box and the impact of asymmetries. A larger region uses more of the data, but has a higher chance of including asymmetries and non-disc components that impact the apparent centre of symmetry. We found that using a box covering around a half of the Doppler map, trying to avoid the most asymmetric parts of the disc, gives the best results for all the studied lines.

In the case of CC Scl, Ca II Doppler maps show a well-defined accretion disc, permitting a more accurate estimate for K_1 . In the case of V2051 Oph, even the Ca II Doppler map was very asymmetric (Figure 3.8). We re-examined the maps and found that the H δ map was not as sharp as Ca II but featured a relatively symmetric disc (see Figure 3.17). After this careful comparison of different lines and regions, we finally settled on using the right half of the Ca II map for CC Scl and the bottom half of the H δ map for V2051 Oph. Having established these optimal line/region combinations, we then repeated the analysis using 500 bootstrap data samples and performed a symmetry search for each reconstructed map. We did this for each box in the Doppler maps of each studied line and using K_x and K_y , we calculated the centre of the map (K_1). Depending on the symmetry of each map, the value of K_x would rarely be the theoretical one (zero) going from 2 km/s up to 10 km/s, but was always smaller than K_y . The mean value was adopted as our

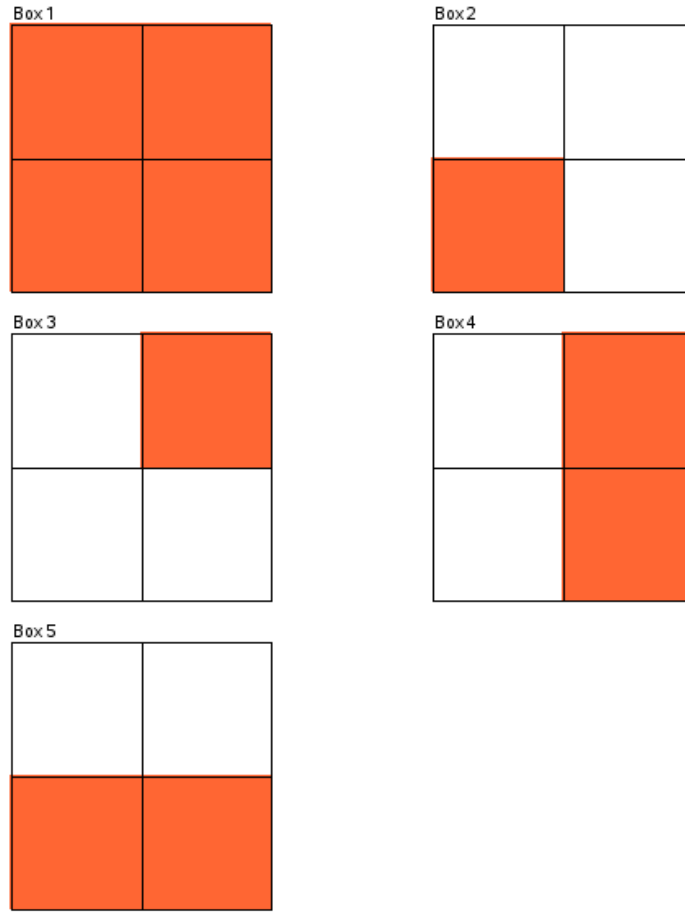


Figure 3.12: Scheme indicating the five boxes position. See text for description of the boxes.

best estimate for K_1 , using the standard deviation as its error. This delivered $K_1 = 37 \pm 14$ km/s for CC Scl and $K_1 = 97 \pm 10$ km/s for V2051 Oph. The former is consistent with the results from the diagnostic diagram, while the latter is in between the expected value from the eclipse solution ($K_1 = 83 \pm 12$ km/s) and that derived from the diagnostic diagram ($K_1 = 110 \pm 16$ km/s). It is consistent with the eclipse solution given the uncertainties and appears to be a better estimate than we were able to derive from the diagnostic diagram. This puts some confidence in the method and suggests it is a useful tool for constraining K_1 , with some clear advantages over the traditional double Gaussian approach, including the ability to deal with obvious asymmetries in a straightforward manner and, provides a more robust uncertainty by using bootstrapped reconstructions.

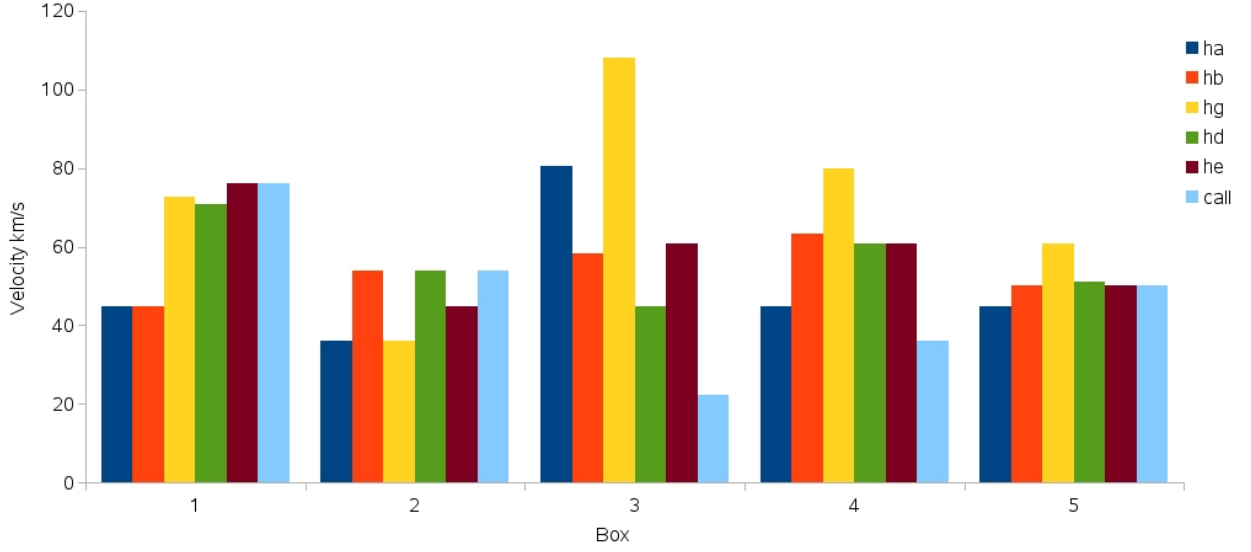


Figure 3.13: Example of K_1 velocity for five different boxes and six different lines. This plot was generated while making the final K_1 calculation for the CV CC Scl.

Secondary star and phase zero

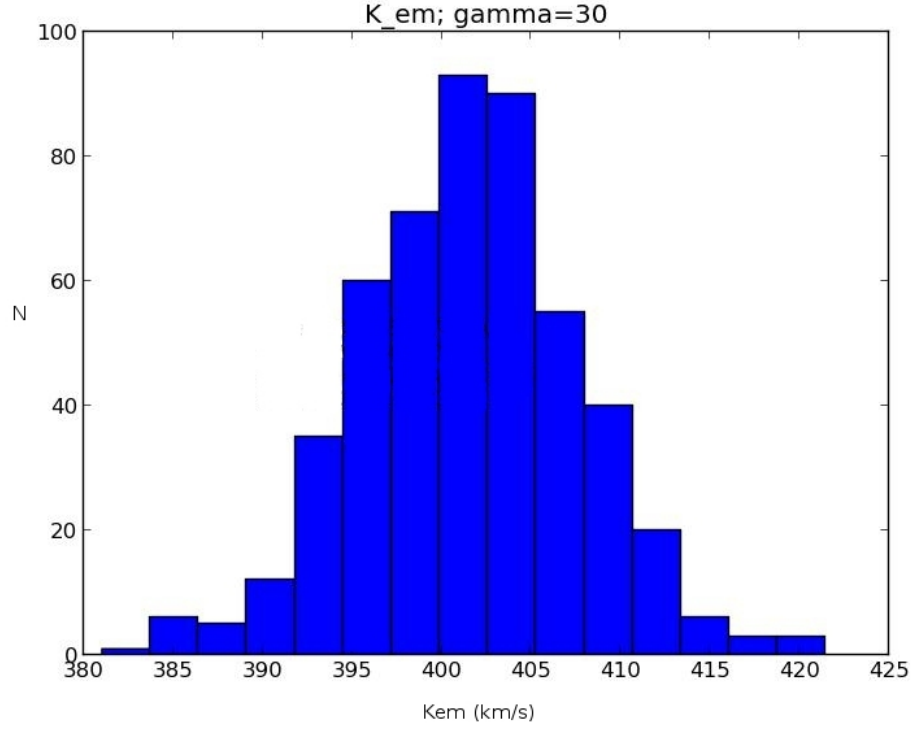
As noted above, emission from the donor star is easily identified in the Doppler tomograms and best seen in the Ca II lines (Figure 3.7 and 3.8). This was first demonstrated for GW Lib in van Spaandonk et al. (2010), and in both of our targets the donor star emission is both stronger and sharper in the Ca II triplet compared to other lines. We fitted 2-dimensional Gaussian profiles to all our donor emission spots in order to determine its (V_x, V_y) position in Doppler coordinates and thus determine the corresponding radial velocity semi-amplitude K_{em} as detailed in Chapter 2. Figure 3.14 shows the histogram of K_{em} values for CC Scl, using the optimal value of γ . The detected emission give us: $K_{em} = 402 \pm 6$ km/s for CC Scl and $K_{em} = 389 \pm 6$ km/s in the case of V2051 Oph. The errors were derived using a bootstrap method as described in the previous section. The distribution of K_{em} values across our 500 bootstraps is well described with a Gaussian distribution, with our errors corresponding to the 1-sigma equivalent.

From the geometry of the Doppler tomography, as shown in Chapter 2, we use the fact that the secondary star velocity is projected in a Doppler map at $(V_x, V_y) = (0, K_2)$ to find the ephemeris for the conjunction as follows:

HJD= 2455384.9869 ± 0.0003 for CC Scl, and

HJD= 2455384.0124 ± 0.004 for V2051 Oph.

Since there is a well established eclipse ephemeris for V2051 Oph, we compared our values with the ephemeris of Baptista et al. (1998) and find that they indeed agree within 3-sigma.

Figure 3.14: Histogram of K_{em} for CC Scl.

This confirms that the emission spot we used to set phase zero does indeed track the donor star. Recently, (Kato, 2014) reported an ephemeris for CC Scl on the basis of eclipse features seen in outburst light-curves, and again we find good agreement. This does suggest that CC Scl is a high-inclination system even though we do not see obvious evidence for an eclipse in our data.

The binary mass ratio

We used the method described in Section 2.4.8 to perform a K-correction and estimate the mass ratio of both systems.

We fixed the inclination of the model to the system's value in the case of V2051 Oph, while for CC Scl (unknown inclination, but shallow eclipses) we fixed the model inclination to 80° . It should be noted that the correction is strongly dependent on the, to be determined, mass ratio and the unknown accretion disc thickness can be a significant effect, but in our case the mass ratio is the dominant parameter.

We visualise our dynamical constraints in Figures 3.15 and 3.16 where we show the K_1 - q plane for CC Scl and V2051 Oph. We represent the constraint $K_{L_1} < K_{em} < K_2$ as diagonal black solid lines with dashed grey error bars. A hard upper limit on the mass ratio is provided by $q_{\max} = \frac{K_{\text{disc}}}{K_{\text{em}}}$ since $K_1 < K_{\text{disc}}$ and $K_2 > K_{\text{em}}$. This constraint is represented by the black vertical

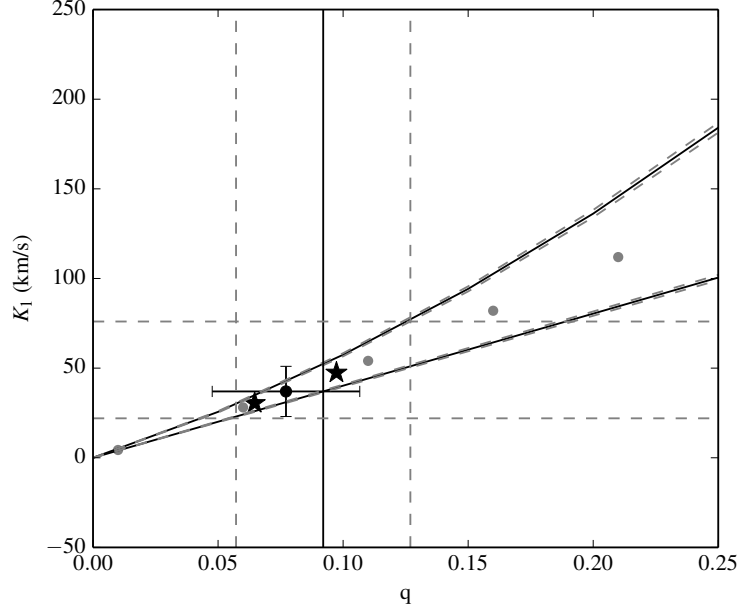


Figure 3.15: K_1, q plane for CC Scl. $K_{em} = 402 \pm 6$ km/s, $K_{em} > K_{L_1}$ is the top diagonal solid black line with dashed errors. $K_{em} < K_2$ is the bottom diagonal line with dashed errors. The vertical solid line represents the maximum value of q . The grey dots are the solutions from our model. The black point with error bars represents our best solution for the value of K_1 found from the centre of symmetry ($K_1 = 32 \pm 16$ km/s). The black stars are the solutions to the pre-bounce and post-bounce orbital periods (derived from Knigge et al. (2011), see Section 3.4)

solid line with dashed errors. The horizontal dashed lines indicate the full range of K_1 values (see Section 2.4.7). Our irradiation models allow us to make a good estimate for the K-correction as a function of mass ratio, as illustrated by the linear grey grid in Figures 3.15 and 3.16. We consider the preferred solution to be the model that reproduces the observed K_{em} , while being consistent with the other constraints. It is the error on K_{em} and K_1 that then defines the allowed parameter range for the binary mass ratio.

In the case of CC Scl, we found that for values of $K_{em} = 402 \pm 6$ km/s and $K_1 = 37 \pm 14$ km/s our best solution is $q = 0.08 \pm 0.03$. These values are in good agreement with the findings of Chen et al. (2001) (Section 3.1).

V2051 Oph has a full binary solution in the literature, since it is eclipsing, and can thus be used as a benchmark for our method. Given $K_{em} = 389 \pm 11$ km/s and $K_1 = 97 \pm 10$ km/s we find $q = 0.18 \pm 0.05$. Had we adopted the K_1 implied by the eclipse solution, we would obtain $q = 0.16 \pm 0.03$. Thus both our K_1 and q are consistent with the reported eclipse solution, giving us confidence in our methodology. While an eclipse solution might be preferred, only a few eclipsing CVs are known at short periods, whereas our method has the promise to deliver dynamical mass ratio estimates for a much larger sample of systems.

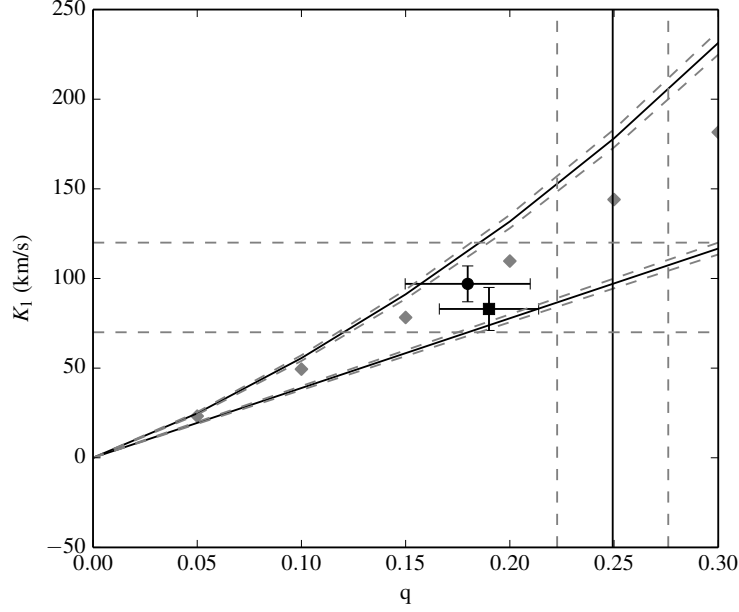


Figure 3.16: K_1, q plane for V2051 Oph. $K_{em} = 389 \pm 6$ km/s, $K_{em} > K_{L_1}$ is the top diagonal solid black line with dashed errors. $K_{em} < K_2$ is the bottom diagonal line with dashed errors. The vertical solid line represents the maximum value of q . The grey diamonds are the solutions from our model. The black point with error bars represents our best solution for the value of K_1 found from the centre of symmetry ($K_1 = 97 \pm 10$). The black square is the eclipse solution.

3.4 Discussion and Conclusions

Our analysis has demonstrated that the Ca II triplet lines offer significant advantages over the more commonly used Balmer and Helium lines. Despite being weaker than these lines, the triplet offers a superior view of the accretion disc and appears to be very sensitive to irradiated donor stars. Computational power now permits the use of bootstrap Monte-Carlo methods in Doppler tomography whereby a large number of maximum-entropy regularised reconstructions can be performed in a manageable time. As each bootstrap reconstruction is completely independent, it can also very easily be parallelized across multiple cores or cluster nodes. The bootstrap samples allow for a more robust evaluation of the significance of features in Doppler maps and we show how they can be used to perform quantitative analysis on Doppler maps including errors estimation. For example, the determination of the radial velocity of the donor star emission that can be seen in maps can be robustly determined by fitting a 2D Gaussian to each reconstruction and then considering the fit parameter distributions across the bootstrap samples in order to derive the optimal velocity and its error. We also developed an (automated) algorithm that optimises for the systemic velocity of the binary γ , one of the few input parameters to Doppler tomography. Sharp emission sources, such as the donor star, can be used to test

for the optimal value of γ for which the sharpest and most stable spot reconstruction is expected (see also Casares et al. 2003). Finally, we showed how a centre of symmetry search focusing on the disc component in Doppler maps can provide robust constraints on the white dwarf radial velocity (K_1). It offers several advantages over the traditional double-Gaussian method given its ability to mask and ignore large asymmetries that typically distort such measurements. It also profits from the bootstrap technique in terms of assigning an uncertainty on the derived K_1 .

When these techniques are combined, robust constraints on the binary mass ratio can be derived. However, we must bear in mind that both our tracer of the donor through its emission as well as the tracer of the white dwarf using the disc are not direct measurements of their centre of mass motion. In the case of the donor, we demonstrate that an irradiation model can provide good estimates for the expected K-correction that needs to be added to the observed emission velocity in order to estimate K_2 . We find that the more difficult parameter is K_1 through disc emission. Although we believe our centre of symmetry method to be better at handling disc asymmetries and distortions compared to the traditional double-Gaussian methods, these can never be fully excluded and thus our uncertainty on the binary mass ratios are set by our knowledge of K_1 . We do find that all of these methods profit from using the Ca II triplet lines which offer sharp donor star features as well as sharp disc features.

3.4.1 CC Scl

Generally speaking, our mass ratio ($q=0.08 \pm 0.03$) is in agreement with the values of Chen et al. (2001). Using M_2 derived by the $M_2 - P_{orb}$ empirical relation derived by Warner (1995), Chen et al. calculated a WD mass of $M_1 > 1.1 M_\odot$. If we instead use the more current empirical CVs donor sequence proposed by Knigge et al. (2011), given a $M_1 = 0.75 M_\odot$, we obtain two values for the mass ratio $q_{pre} = 0.097$ and $q_{post} = 0.065$. Both values are in agreement within error bars with our derived mass ratio. These solutions correspond to the pre-bounce and post-bounce orbital periods M_2 (derived from Knigge et al. (2011), table 4). We plotted these solutions in Figure 3.15 as black stars. The pre-bounce solution is located over the maximum limit of q and predicts a value of K_1 higher than our calculated value although consistent with the error bars. Given the tendency of our method to overestimate K_1 , we favoured CC Scl as a post-bounce system. According Knigge et al., the pre-bounce solution favours a M7 type and the post-bounce a T type donor star. Both presumed donor spectral types should be visible in the L band. To further clarify the donor's nature, we suggest infrared time-resolved spectroscopy of the target to attempt a direct measurement of the velocity of the donor. In the overall, CC Scl is an interesting target and future observations could confirm its potential post-bounce nature.

3.4.2 V2051 Oph

As can be seen in Figure 3.8 in section 3.3.3, there is an enhanced emission area in the second quadrant ($+V_x, -V_y$) of the Doppler maps of V2051 Oph. This feature is not consistent with the bright spot and has been noticed in previous Doppler maps by Papadaki et al. (2008) in the Balmer lines and HeI. Nevertheless, the two sets of Doppler maps show very different features, as the average spectra had highlighted (Section 3.3.1). The maps from Papadaki et al., showed an increase in the bright spot strength when moving to shorter wavelengths and as the bright spot strength decreased, the second quadrant feature increased. In our case, the reversed relation between the strength of the bright spot and the second quadrant emission is maintained, however, the intensity of the bright spot decreases when moving towards shorter wavelengths in both Balmer lines and HeI (Figure 3.17). This fact, combined with the discrepancies between the values of γ of different epochs, makes us believe that the system might be experiencing a non-orbital scale precession. This precession would account for the different values of γ found with the double Gaussian method by Watts et al. (1986), using 2.1 orbits of the system, Papadaki et al. (2008), using 2.7 orbits and this paper, with 2.3 orbits of the system, indicating that more than two orbital cycles should be necessary to get a reliable value for γ . We believe that for the time that our data were taken there was a difference of half a precession cycle with respect to the data of Papadaki et al., explaining for the contrasted lines behaviour. The value of γ derived by our method is independent from the disc and hence not affected by its variation.

Papadaki et al. report that their Doppler maps of the Fe II triplet do not show either bright spot or the second quadrant emission mentioned above. They explain this featureless disc by proposing the existence of a gas region above it where the triplet might be originated via fluorescence. We made Doppler maps of Fe II 5169 Å, the only line of the triplet that is not blended with HeI. The Doppler map of Fe II 5169 Å (the only line of the triplet that is not blended with He I), displayed a disc with no signs of the second quadrant emission, but with a notorious bright spot. The presence of the bright spot in our maps contradicts this theory of the origin of the Fe II triplet.

As seen in Figure 3.16, where the highly asymmetric disc of V2051 Oph led us towards a value of K_1 slightly higher than the eclipse solution, the obtained value of the mass ratio was $q = 0.18 \pm 0.05$. When using the eclipse solution for $K_1 = 83 \pm 12$ km/s we obtained $q = 0.16 \pm 0.03$ and $K_2 = 519 \pm 84$ km/s. Both estimated values of q agree with the eclipse solution, $q = 0.19 \pm 0.03$, building up confidence on the performance of our K-correction method.

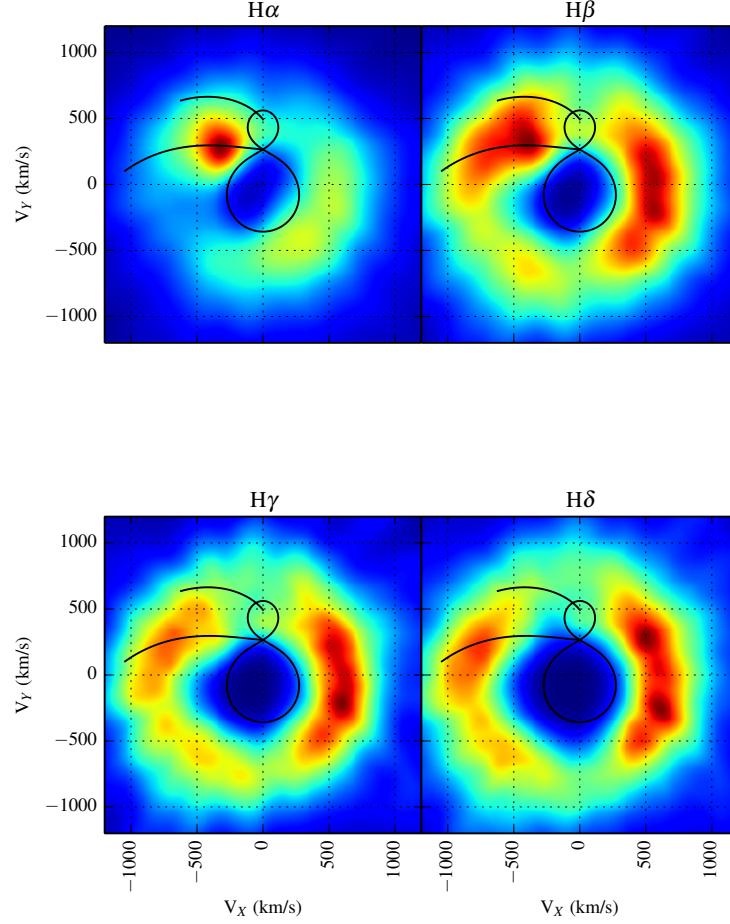


Figure 3.17: Doppler maps of the most prominent Balmer lines of V2051 Oph.

3.5 Summary

Using the methods described in Section 2.4 we have derived a full orbital solution for the short period CVs CC Scl and V2051 Oph (Our best solutions are found in Table 3.2). Our best solutions are in agreement with the eclipse solutions. We showed the potential of CC Scl as a post-period bounce system and propose further infrared observations to either confirm or deny its evolutionary state. In the case of V2051 Oph, we proposed a non-orbital scale precession to explain the conflicting values of γ and the variable behaviour of its spectral features.

We found that Doppler map-based methods can provide strong and robust constraints for the orbital parameters of short period CVs. We compare these methods against classic double Gaussian methods finding advantages from the former over the later ones. Our methods give

CC Scl			V2051 Oph		
γ [km/s]	K_1 [km/s]	Mass ratio	γ [km/s]	K_1 [km/s]	Mass ratio
30^{+33}_{-22}	37 ± 14	0.08 ± 0.03	0^{+12}_{-17}	97 ± 10	0.18 ± 0.05

Table 3.2: Summary of the orbital parameters derived with our methods.

good estimates for the values of γ , Φ_0 , K_1 and K_2 , but our optimal value of q will still depend of the accuracy of K_1 which is prone to distortions in the disc.

In Chapter 2 we used synthetic data to demonstrate that our methods should recover reliable parameters. Here we see that this is also the case using real data.

Four

Dynamical Constraints for the Low Mass Black Hole Candidate 4U 1957+111

4.1 Introduction

In this chapter, we use some of the techniques described in Chapter 2 to study the low mass black hole candidate 4U 1957+111. Using spectroscopic data of several observing runs, we constructed Doppler tomograms from emission lines, including the Bowen blend, and derived several orbital parameters of this system. We present spectroscopic confirmation of the orbital period, confirm the presence of an accretion disc structure and show the first dynamical evidence of the elusive secondary star, allowing us to constrain the mass of the compact object.

4.2 4U 1957+111

Thus far, all of the confirmed black hole binaries are either X-ray transients or high mass X-ray binaries, while most of the persistently bright LMXBs are known to be neutron star systems (see Section 1.1.5). The main criterion to classify a system as a black hole binary is through dynamical evidence that the mass is $\geq 3M_{\odot}$, beyond the maximum NS mass (see for example: Remillard & McClintock 2006). This criterion led to ~ 20 confirmed black hole systems and a comparable number of black hole candidates, based on a similar X-ray timing and spectral behaviour (Casares & Jonker, 2014). 4U 1957+111 (hereafter 4U 1957) was classified as a black hole candidate by White & Marshall (1983) mainly based on its ultra soft-X-ray spectra. This classification has been questioned by several groups, such as Yaqoob et al. (1993) and Barret et al. (1996). The main argument is that the spectral behaviour of 4U 1957 better fits with the one from neutron stars. Until now, there is no dynamical confirmation that proves either position. 4U 1957 has proved to be a very challenging target with complex orbital modulation and a highly variable light curve. The first proposed value for the orbital period came from Thorstensen (1987) finding a period of 9.33 h based on photometric observations of the optical counterpart. This period was only confirmed more than 20 years later, by Bayless et al. (2011) after an intensive photometric campaign. They also proposed an ephemeris that, regretfully, was only valid for the season

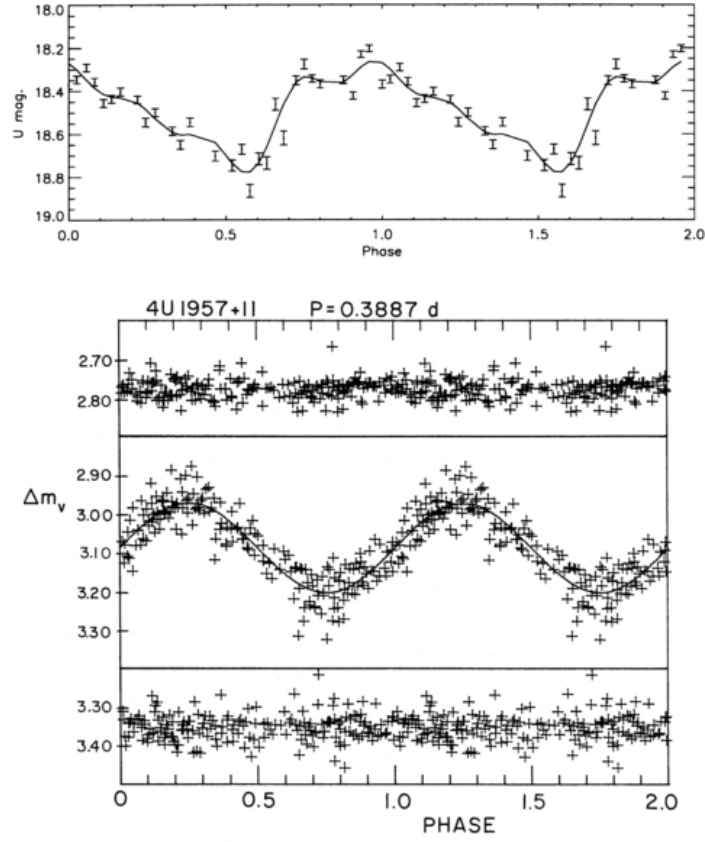


Figure 4.1: Light curves of 4U 1957. Top: Non sinusoidal light curve shown by Hakala et al. (1999). Bottom, sinusoidal light curve from Thorstensen (1987).

they observed due to its limited precision. In addition, Hakala et al. (1999) found some complex behaviour in the photometric light curve. Unlike the essentially sinusoidal profile observed by Thorstensen (1987) and Bayless et al. (2011), their light curve was not-sinusoidal, a feature interpreted as an evolving accretion disc (Figure 4.1). This theory was further supported by the X-ray observations of Nowak & Wilms (1999). After three years of optical monitoring, Russell et al. (2010) were unable to find the previously reported orbital modulation, even though they do not rule out the period found by Thorstensen (1987). Russell et al. claimed that the X-ray flux during their observations could have been stable over the time-scale that they observed, revealing the sinusoidal variations from the heated face of the secondary. Recently, Mason et al. (2012) measured the orbital period, photometrically, well enough to derive an accurate ephemeris. This allowed us to merge data from different spectroscopic observing campaigns and to find the first dynamical evidence of the compact object, using the Bowen fluorescence technique, as shown in the following sections.

The optical counterpart of 4U 1957 was first observed by Margon et al. (1978) but no sig-

Instrument	S/N_1	S/N_1 per \AA per pixel	photons ₁ /s/ \AA	S/N_2	S/N_2 per \AA per pixel	photons ₂ /s/ \AA
IMACS	24.9	0.037	0.93	6.3	0.0094	0.84
FORS	47.6	0.063	2.97	20	0.026	1.83
Blue Chanel	22.9	0.032	0.73	23.25	0.032	0.64
MagE	53.8	0.13	6.82	26.8	0.063	2.52

Table 4.1: Instruments performance comparison for the Bowen lines range.

nature of the secondary was visible in the optical spectra as shown later by Shahbaz et al. (1996). Recently, Hakala et al. (2014) showed their results of a simultaneous NIR and optical photometric campaign, proposing an extreme mass ratio and favouring a massive ($> 15M_{\odot}$) black hole primary, but found no signal of the secondary to prove their model either way. My collaborators have investigated this target for a decade looking for the donor star of 4U 1957. When I first started to work on this target, several observing campaigns to find the donor had been futile. We started our search by determining the instrument with which we had the most chances to succeed in the hunt for the elusive secondary. We show our results in the following Section.

4.3 Instrument Performance on the Bowen blend

From the first data set obtained for this research, bad weather reduced our originally five half-nights, granted with MagE, to only 2.5 hours. These data were insufficient to apply any technique that would allow us to constrain the mass of the compact object with the precision required to clarify its nature. And not having an accurate ephemeris, the merging of data from other campaigns was impossible, leaving us the only option to apply for more telescope time.

To select the best-suited instrument to resolve the Bowen blend, we performed a comparison amongst different archival data and our MagE data. We analysed the performance of each instrument between -4000 to 4000 km/s around 4640 \AA . We had existing data in the Bowen blend region from: IMACS spectrograph in Las Campanas, FORS spectrograph on the VLT and from the Blue Channel spectrograph of the MMT observatory. We took the highest flux spectrum of each of the data sets to remove the effects of weather conditions. The results are shown in table 4.1. We calculated the signal to noise ratio (S/N) in two ways: first the best estimation as $S/N_1 = N_{\text{source}}/\sqrt{N_{\text{source}}}$, a simplification of the S/N formula that does not consider the instruments background losses. Second, the error based S/N as $S/N_2 = C/\delta C$ where C is counts per pixels and δC is the counts mean error including propagated background and extraction contribution. The number of photons was calculated in two different ways: photons₁ are the average of 100 \AA around 4600 \AA (~ 4000 km/s) and photons₂ are average number of photons per pixel in the same range.

Figure 4.3 shows the spectra used to derive the results presented in Table 4.1. These figures illustrate the challenge in studying 4U 1957, a rather faint target with a weak, variable Bowen blend. It is noticeable that the results show a superior performance of the MagE spectrograph over the other considered instruments, so we focused on obtaining time with the instrument which delivered the best S/N for the Bowen blend. This performance comparison was crucial for following observing proposals that granted us observation time with MagE, reported in Table 4.2 from August 2011 onwards (Section 4.4).

4.4 Observation and Data Reduction

The following Chapter is based on observations obtained with the MagE spectrograph (see Section 2.1.2). We obtained 75 spectra with 1200 s exposure time. The observation dates are shown in Table 4.2.

The spectra were reduced with the Python based pipeline written by Dan Kelson which performs typical calibrations (see 2.1.3). Raw spectra were flux calibrated using the spectrum of the flux standard Feige 110, observed at the end of each night. Observations of a comparison star were not available or were of poor quality on some of the nights. For consistency, we performed the analysis on normalised spectra. Also, due to poor S/N and bad sky subtraction, the first ($\sim 8200 - 11200 \text{ \AA}$) and last three orders ($\sim 3100 - 4000 \text{ \AA}$) were not included in the analysis.

During this research, we had access to an unpublished analysis, by our collaborators, with a data set from the Inamori-Magellan Areal Camera & Spectrograph (IMACS), mounted in the Magellan telescope in Las Campanas. We re-analysed 72 spectra taken during June 2006, details in table 4.3. These spectra were de-biased, flat-fielded and extracted using optimal extraction techniques, see Horne (1986). Since no observations of a standard star was available to flux calibrate, the spectra were normalised.

Date	Exp time [s]	n
7/6/2010	1200	6
8/6/2010	1200	8
28/6/2011	1200	14
6/8/2011	1200	14
6/9/2011	1200	9
14/9/2011	1200	8
15/9/2011	1200	8
16/9/2011	1200	8

Table 4.2: 4U 1957 MagE observations. n is the number of spectra taken during the given date.

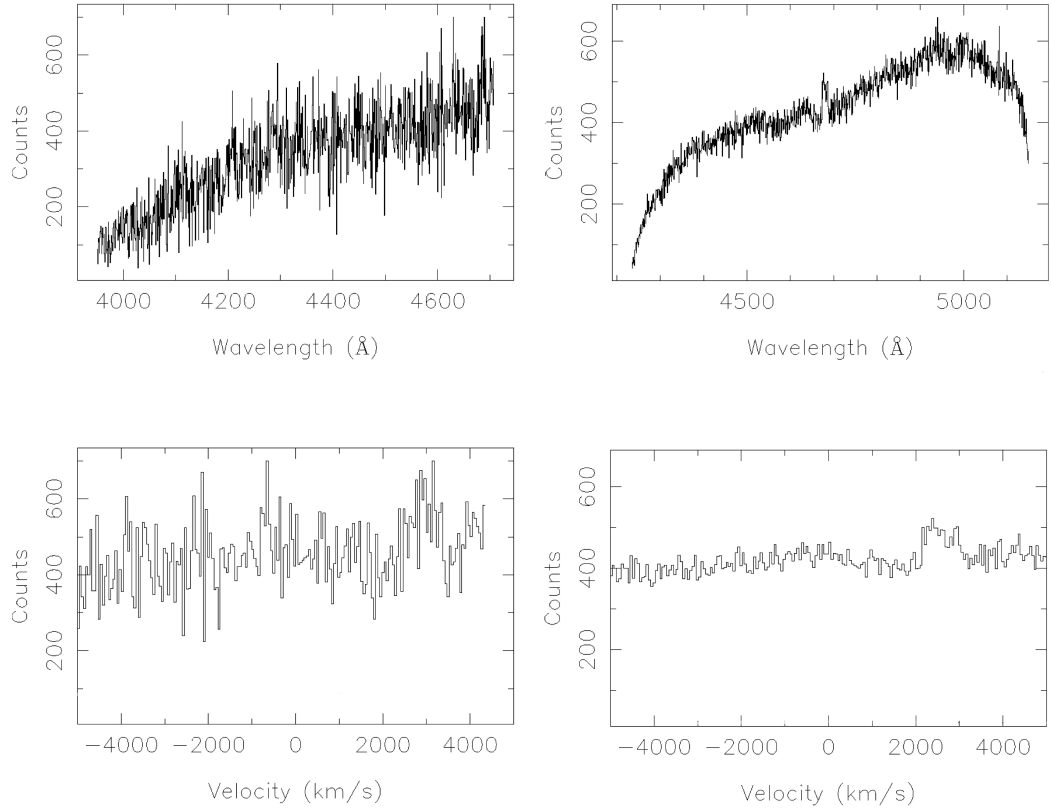


Figure 4.2: *Top:* Complete spectrum. *Bottom:* Binned spectrum spanning 4000 km/s around the Bowen blend. Left: IMACS, right: Blue Channel.

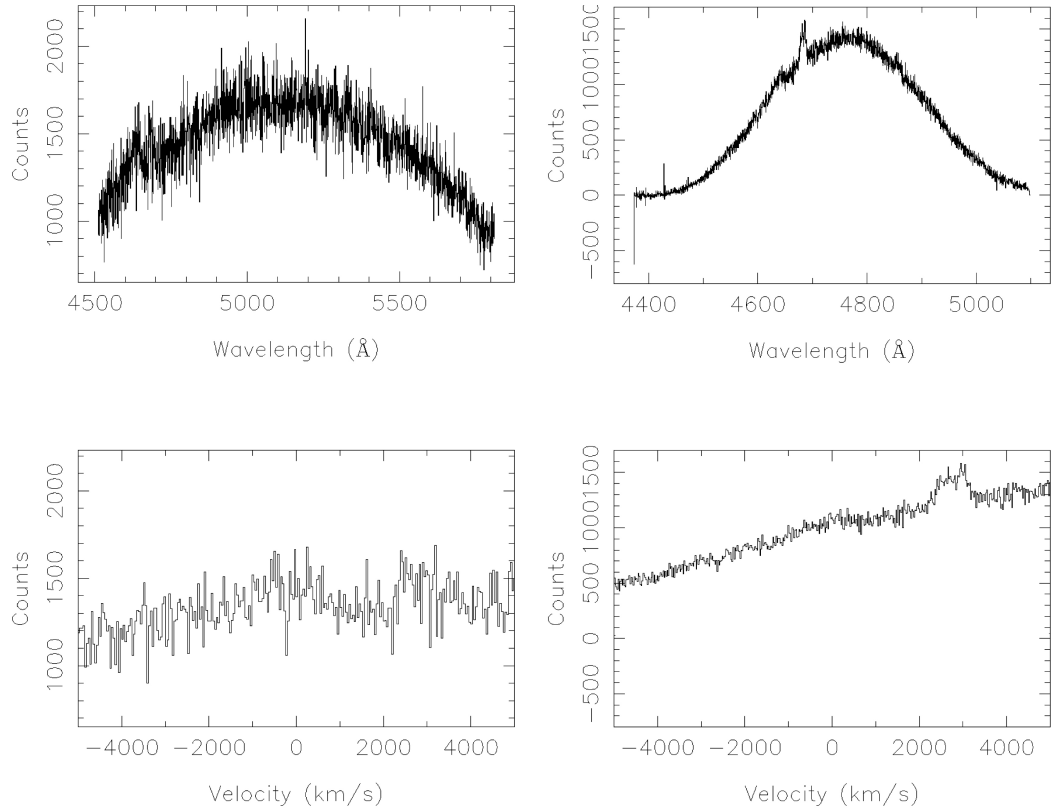


Figure 4.3: *Top:* Complete spectrum. *Bottom:* Binned spectrum spanning 4000 km/s around the Bowen blend. Left: FORS, right: MagE.

Date	Exp time[s]	n
15/6/2006	900	19
16/6/2006	900	16
17/6/2006	900	20
18/6/2006	900	17

Table 4.3: 4U 1957 IMACS observations. n is the number of spectra taken during the given date.

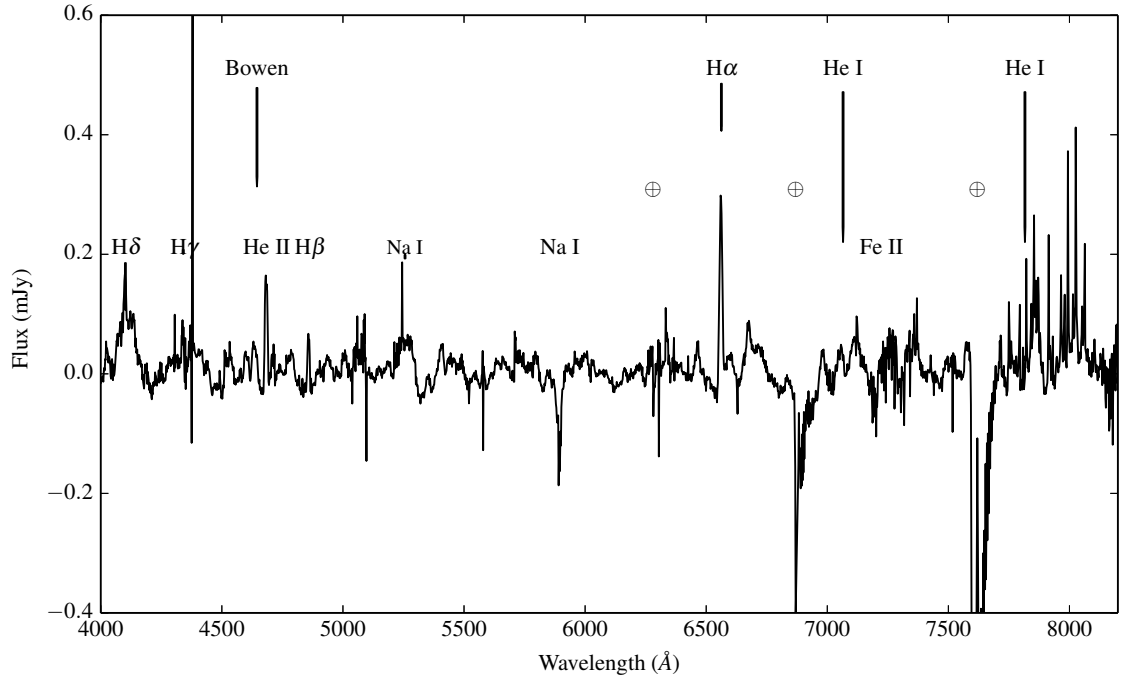


Figure 4.4: Average normalised spectrum of 4U 1957. MagE data. No orbital correction was applied.

4.5 Results

4.5.1 Averaged Spectrum

We averaged the 75 MagE spectra, giving equal weighting to each. Figure 4.4 shows the normalised average spectra of 4U 1957. We did not remove telluric features. These are marked with the symbol \oplus . No correction for orbital motion has been made.

He I and He II and the Balmer lines in emission are identified in the spectrum, although H γ is not clearly detected. We can also resolve, in emission, O III, Ca V and Fe II. The most relevant feature in the search for the secondary star is the Bowen blend (C III, N III and O II). The Na I doublet is present in absorption. This feature is a common indicator of interstellar absorption.

Date	He II [Å]	H β [Å]	H α [Å]	Bowen blend [Å]
7/6/ 2010	2.69 ± 0.13	0.8 ± 0.14	2.61 ± 0.27	1.77 ± 0.15
8/6/2010	2.49 ± 0.06	0.88 ± 0.06	2.89 ± 0.11	1.43 ± 0.07
28/6/2011	1.88 ± 0.06	1.89 ± 0.07	10.05 ± 0.1	1.1 ± 0.07
6/8/2011	2.216 ± 0.06	1.83 ± 0.07	6.98 ± 0.12	1.14 ± 0.07
6/9/2011	3.47 ± 0.17	1.18 ± 0.19	7.72 ± 0.28	0.75 ± 0.17
14/9/2011	1.42 ± 0.09	-0.31 ± 0.1	-0.29 ± 0.14	0.8 ± 0.1
15/9/2011	1.25 ± 0.07	-0.25 ± 0.08	-0.05 ± 0.12	1.23 ± 0.08
16/9/2011	1.44 ± 0.07	-0.47 ± 0.076	-0.74 ± 0.12	0.96 ± 0.07

Table 4.4: 4U 1957 average equivalent width per night. These were calculated with the normalised spectra of the MagE data.

Date	HeII [Å]	H β [Å]	H α [Å]
15/6/2006	2.00 ± 0.25	0.15 ± 0.13	0.03 ± 0.19
16/6/2006	0.97 ± 0.22	0.14 ± 0.12	-0.24 ± 0.17
17/6/2006	2.27 ± 0.28	1.02 ± 0.14	4.07 ± 0.20
18/6/2006	1.92 ± 0.19	0.56 ± 0.09	2.12 ± 0.15

Table 4.5: 4U 1957 average equivalent width per night. IMACS data.

Equivalent Width

Some extreme equivalent width (EW) variations from night to night were observed in the IMACS data. We calculated the EW of He II, the Balmer lines and the Bowen blend from night to night and show the results in Table 4.4. We averaged the data by night to calculate the EW of each night's average spectrum. Table 4.5 shows the values found with the IMACS data during 2006 for comparison. The EW of each line varies considerably from night to night in both data-sets. For the IMACS data, H α and H β are hardly visible during the first two nights, becoming prominent during the second half of the observation run. A similar behaviour of the Balmer lines is seen in the MagE data, where they are prominent in June, August and the first September night of 2011 to almost disappear a week after. The changes of He II are much smaller than those of the Balmer lines, but are still present. There is no correlation between the variation of the strength of the Balmer lines and He II, which is unsurprising since they are likely generated by different mechanisms (Section 1.3). The Bowen blend also shows a variable EW (Table 4.5). As expected, these variations follow the trend of He II for the first five nights, and become somewhat erratic on the last three nights of September, when the Balmer lines disappeared.

We calculated the EW for phase folded data in search of any periodic variations. There were no consistent correlations, which implies non periodic variations.

Instrument	Line	γ [km/s]	K_1 [km/s]	Φ_0
MagE	He II	-222 ± 20	100 ± 9	0.18 ± 0.05
IMACS	He II	-180 ± 18	106 ± 25	0.19 ± 0.03

Table 4.6: 4U 1957 orbital parameters derived from the diagnostic diagram of He II with MagE and IMACS data.

4.5.2 Radial Velocities

Figure 4.5 shows the diagnostic diagram of He II with Gaussian FWHM=200 km/s (See section 2.2.1). The same diagnostics, using $H\alpha$ and $H\beta$ proved inconclusive, possibly because of low S/N or asymmetric lines (See Figure 4.7). The diagnostic diagram of He II shows a flat plateau between $a = 600$ km/s and 900 km/s, consistent with the wings velocity (see bottom of Figure 4.5). The parameters derived from He II, as well as the results from IMACS data, are shown in Table 4.6. The values are an average of the results between $a = 600$ km/s and $a = 900$ km/s. The errors are the maximum dispersion of the results. The values derived with the IMACS data are in good agreement with our MagE-data based findings.

4.5.3 Spectroscopic Period

After an extensive unsuccessful search for the donor star with individual data sets we could combine all our MagE data with an uncertainty < 0.1 orbital phases using the ephemeris presented by Mason et al. (2012). We attempted to combine our data with the IMACS data, taken four years before, by smoothing the MagE data with a Gaussian to match IMACS resolution. The results were not conclusive, most likely because of the low resolution of the IMACS data, so we used only the superior MagE data for the following analysis.

Mason et al. (2012) also presented a refined orbital period for the system, so after folding our data we attempted to confirm the reported photometric period. We constructed a periodogram from our He II radial velocity curves, using only the MagE data. We present the resulting periodogram in Figure 4.6. Several frequencies with similar power were found at 2.5-2.6 cycles per day. Of the four strongest candidate frequencies (labelled A, B, C and D) shown at the bottom Figure 4.6, B, C and D were identified as aliases of either 1 day, 1-3 months and 1 year. The peak labelled A at 0.3889(4) days was regarded as real, and is in good agreement with the photometric period found by Mason et al., at 0.388879(5)d.

Despite the fact that our data did not allow us to further refine the orbital period, we present here the FIRST spectroscopic confirmation of the photometric period for 4U 1957, settling the debate on the correct orbital period of the binary.

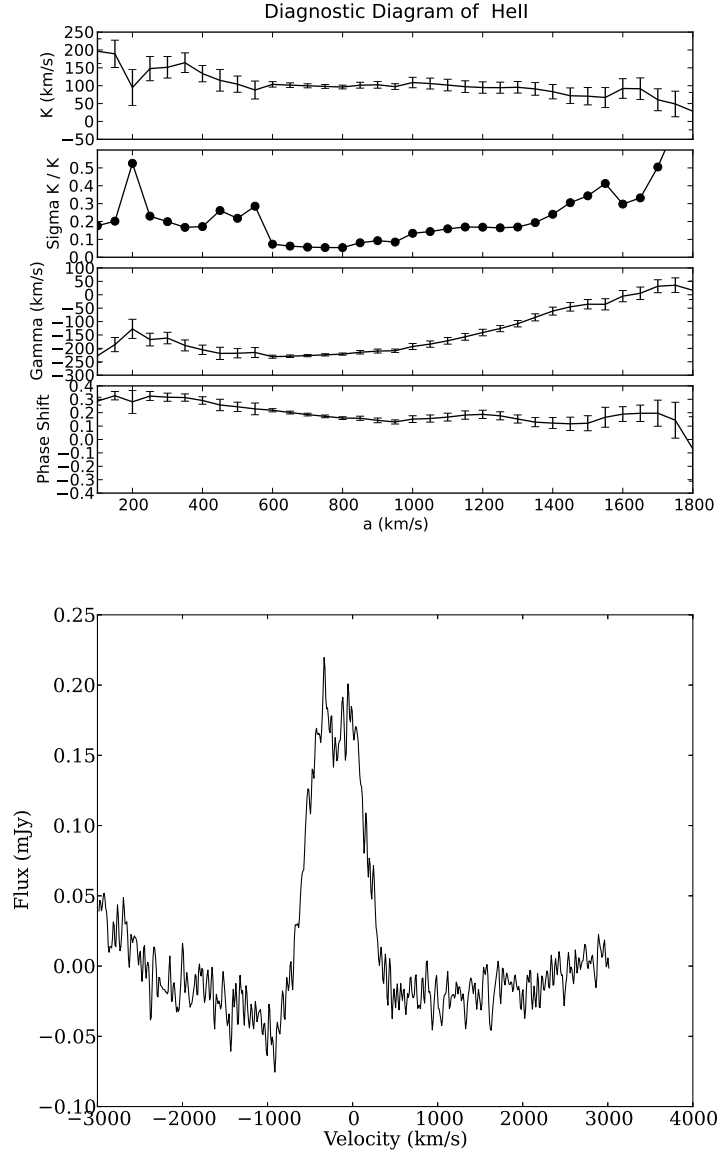


Figure 4.5: Diagnostic diagram of He II (top). Average spectrum of He II (bottom).

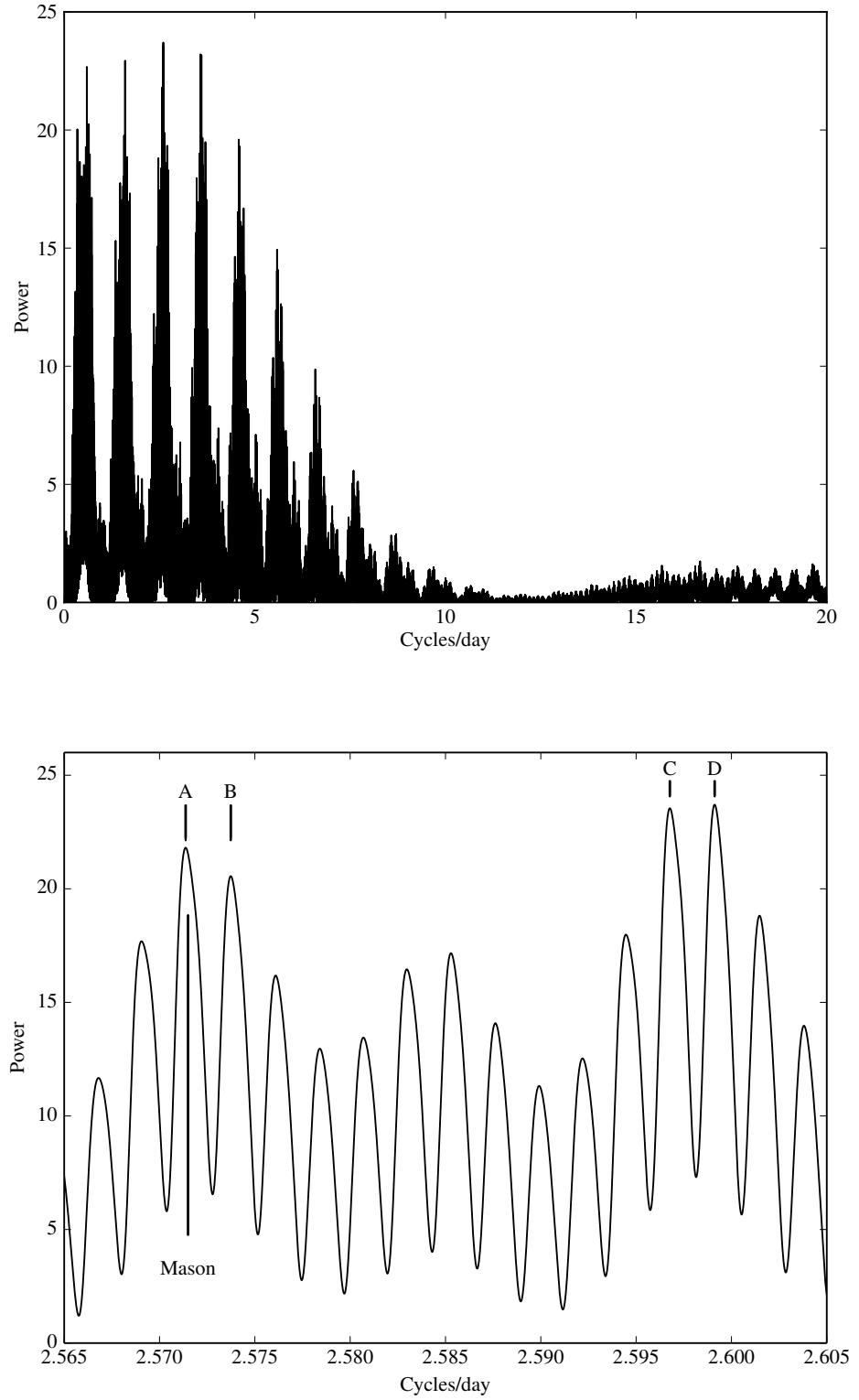


Figure 4.6: Top: 4U 1957 periodogram with MagE data. Bottom: Zoom of the vicinity of the largest peak. Peak A is in reasonable agreement with the period from Mason et al., marked on the figure. Peaks B, D and D are consistent with one month, one day and one year aliases, respectively. There where no significant periodicities after 8 cycles/day.

4.5.4 Doppler Tomography

As we mention before, Mason et al. (2012) defined an accurate ephemeris by fitting a sine curve to their photometric data, that allowed us to merge our data sets. They defined Φ_0 as the time of maximum flux, opposite to the classical definition for binaries. We recalculate the phase for it to agree with the standard properties of Doppler tomograms by adding half a period to it, obtaining: $\Phi_0 = 2452621.63456(\text{d})$. This new phase zero, based on the one from Mason et al. was used to plot all the maps in this Section.

Figure 4.7 shows the Doppler maps of the most prominent lines of the system. All these maps were constructed with MagE data. A non axis-symmetric ring-like shape is seen in the maps of $H\alpha$ and He II, confirming the presence of an accretion disc. Both maps show enhanced emission in the third quadrant ($-V_x, -V_y$), reported before for other LMXBs (XTE J2123–058 (Hynes et al., 2001), GX 9+9 (Cornelisse et al., 2007) and GR Mus (Barnes et al., 2007)). The map of $H\alpha$ also shows enhanced emission in the first quadrant ($+V_x, +V_y$). This emission is also present in the maps of $H\beta$, confirming that it is not an artifact. Because of the high EW variations of the system, we also constructed Doppler maps with data normalised by the EW. The resulting maps had the same features of the ones presented here, reassuring us that the features are real.

Secondary Detection

Our first attempt at mapping the secondary with the Bowen fluorescence technique (Steeeghs & Casares, 2002) was similar to the map shown at the bottom-right panel of Figure 4.8. This spot near the position of the secondary was encouraging, but not centred at the position of the secondary. Calculating the uncertainties of the ephemeris derived by Mason et al. (2012) used to construct these maps, the phase error corresponds to a map rotation tolerance of $\sim 20^\circ$ from the y axis. The spot is located at 16° , inside the range to be the secondary, but still surrounded by features of a comparable level. To analyse the significance of each feature, first we separated the data-set in five sub-sets, from rounds 1 to 5: 7-8 June 2010, 28 June 2011, 6 August 2011, 6 September 2011 and, 14-16 September 2011. Some of the resulting maps are shown in Figure 4.8. After this analysis, it was clear that the strong feature in the first quadrant was strongest in round one (top panels of Figure 4.8), and the potential secondary star was strongest in round 2 (bottom left and bottom middle panels of Figure 4.8). The bottom right panel of Figure 4.8 shows an average of the maps made with the six possible combinations of our sub-sets. The rightmost panel of Figure 4.7 shows the Doppler map of N III 4640.64 Å, the strongest feature of the bowen blend, after masking a few hot pixels present in round 1. After doing so, the spot near the position of the secondary star is remarkably clear. To have an undeniable detection, we aimed to generate a map with no masking of data. Knowing that some of the strongest signals were not present in all the observation dates, we generated 500 bootstrap samples of the complete, unmasked data set.

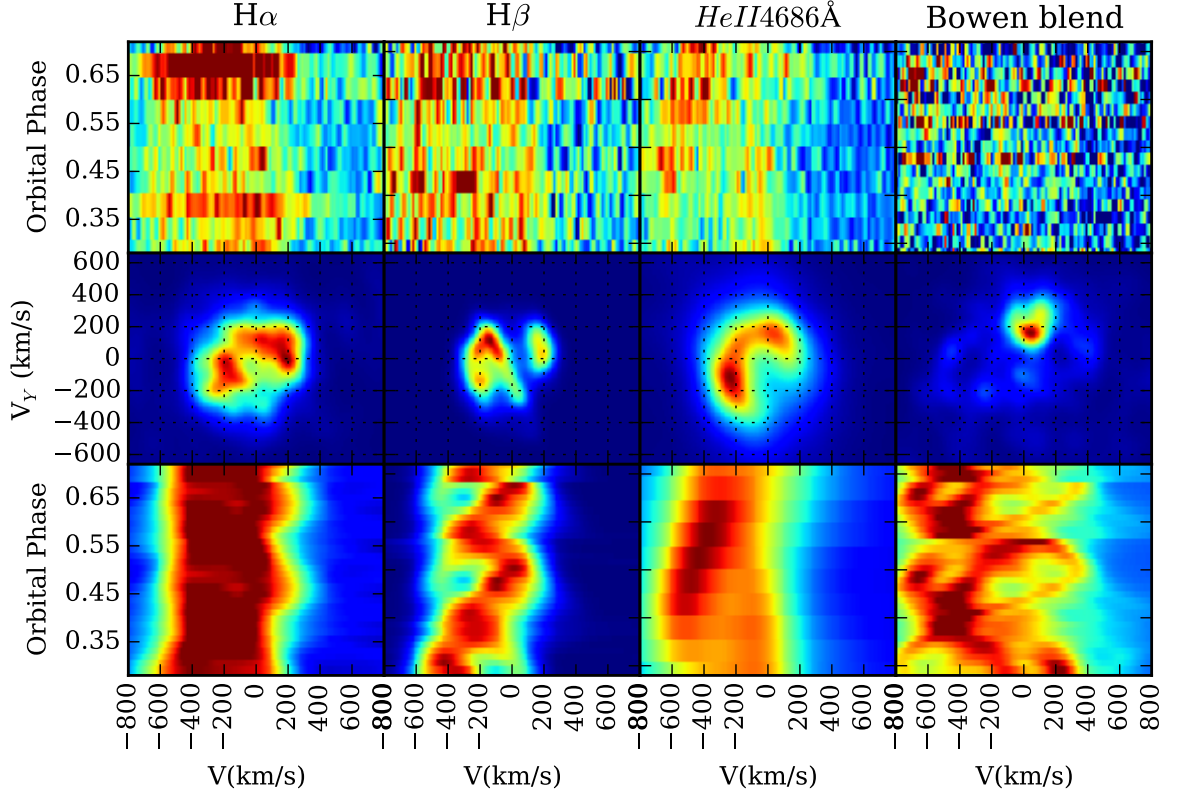


Figure 4.7: Doppler maps of the most prominent lines of 4U 1957. From top to bottom: phase-binned trailed spectra, Doppler map and reconstructed data. The corresponding emission line is indicated on the top of each map.

We analysed the resulting bootstraps as explained in Section 2.4.8. The resulting average/STD plot is presented in Figure 4.9. As seen from the synthetic spectra, the secondary feature is detectable at low S/N and it gets enhanced when it is divided by the STD, a process that suppresses the role of the random noise. The clean spot found at $V_x, V_y = (9, 150)$ km/s in 500 bootstrap samples of the Doppler map of the Bowen blend ($K_{em} = 214 \pm 26$ km/s) is the final proof of the first dynamical evidence of the secondary, with the error derived from the STD as explained in Section 2.4.8.

Systemic Velocity

Having detected the secondary star, we constrained the value of the systemic velocity as detailed in Section 2.4.7. The smallest FWHM and the lowest histogram STD was found for $\gamma = -180 \pm_{-38}^{+30}$ km/s (see Figure 4.10). This is in good agreement with the systemic velocity obtained with the diagnostic diagrams of He II. All the Doppler maps presented in this Chapter were con-

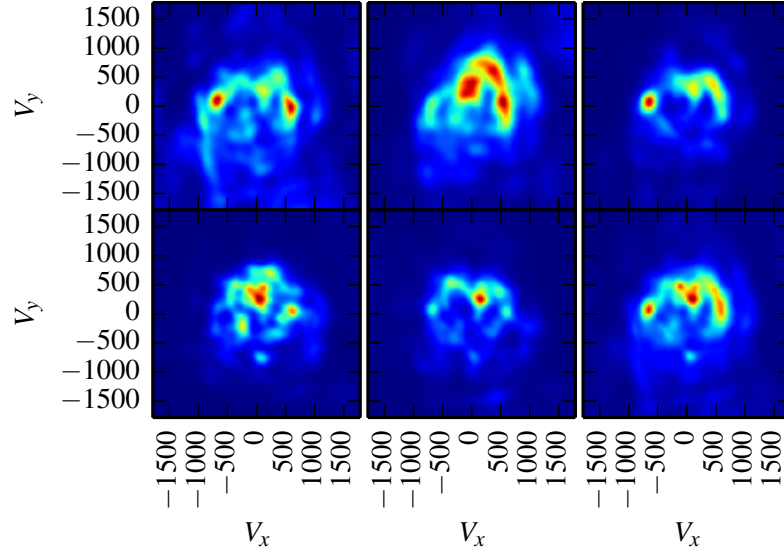


Figure 4.8: Example Doppler maps of the Bowen blend, sub-set combinations: top-left: Rounds 1 and 2, op-centre: rounds 1 and 3, top-right: rounds 1 and 4, bottom-left: rounds 2 and 3, bottom-centre: rounds 2 and 4 and bottom-right: all data sets combined. The velocities V_x and V_y are in km/s.

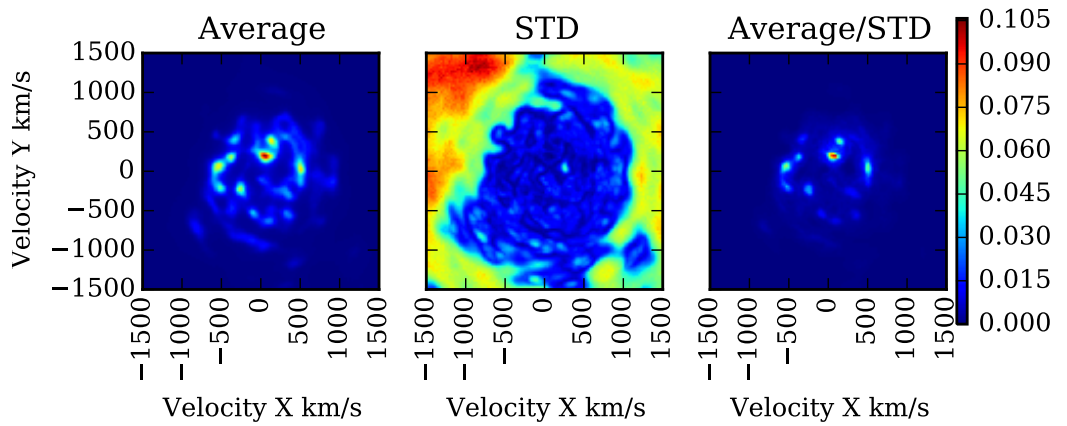


Figure 4.9: STD and average/STD from 500 bootstrap samples of the Doppler map of the Bowen blend. The colour scale represent the intensity of the hottest pixel.

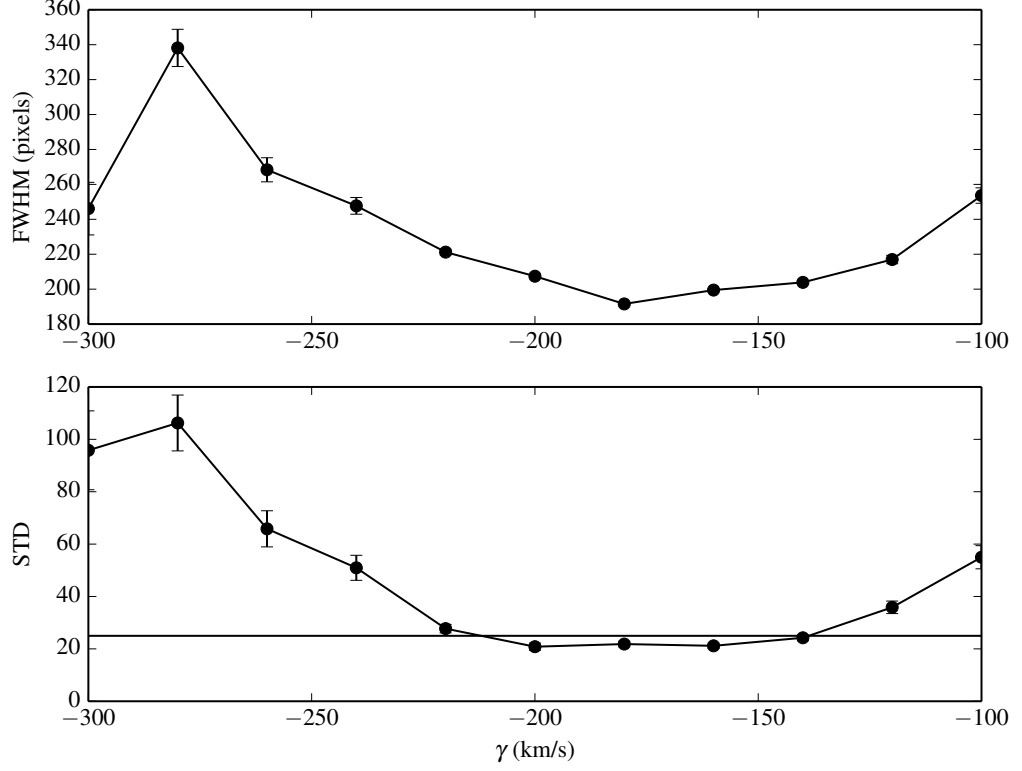


Figure 4.10: FWHM of the secondary star and STD versus value of systemic velocity γ for 4U 1957.

structured with this value of γ .

Looking for K_1

We used the Doppler map of He II 4685.75 Å to constrain the velocity of the compact object with the centre of symmetry method, used as described in Section 2.4.7. As is evident from the Doppler map of He II, Figure 4.7, the disc is very asymmetric. This leads to poor estimation of the radial velocity of the primary star using the double Gaussian method. To avoid the asymmetries of the disc, we did our search on the first quadrant ($+V_x, +V_y$) of the map, the one containing the most symmetric part of the disc. We found the centre of symmetry at 74 ± 38 km/s, significantly lower than the velocity found by the diagnostic diagram technique. Avoiding the asymmetries of the disc allows us to find a better constraint for the compact object radial velocity, although the uncertainty associated with it is still significant.

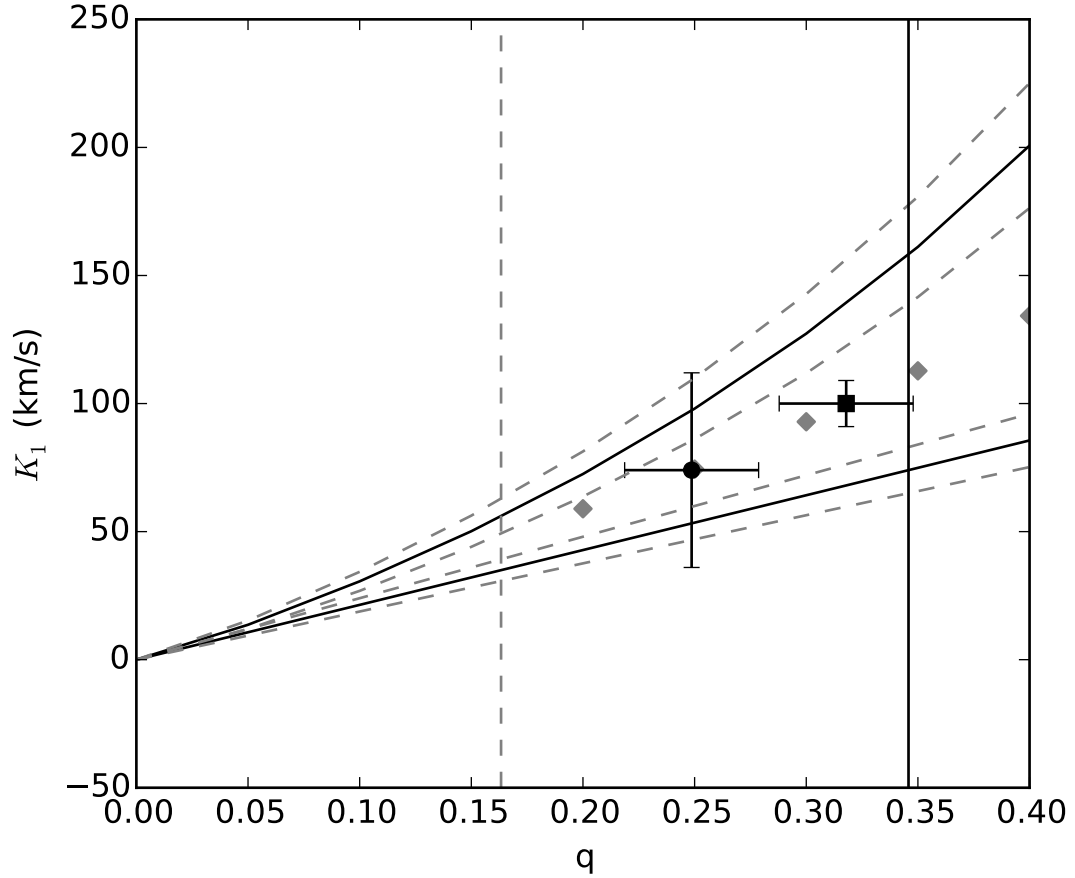


Figure 4.11: As in Figure 2.19 but for 4U 1957. The black circle is the result from the centre of symmetry technique and the black square is the result from the diagnostic diagram. There is no higher and lower limits for K_1 , since it was only calculated for He II.

Constraining the Mass Ratio

We used the method described in Section 2.4.8 to find an estimate of the mass ratio q and the radial velocity of the secondary star K_2 . As the system's inclination is unknown, we fixed the inclination of the model to 45° . We present the results in Figure 4.11. We used the value of the primary velocity, $K_1 = 74 \pm 38$ km/s derived from the centre of symmetry technique, represented in Figure 4.11 as a black circle. This velocity resulted in values of $q = 0.25 \pm 0.14$ and $K_2 = 298 \pm 15$ km/s. The black square is the resulting value for the mass ratio using the higher radial velocity obtained with the diagnostic diagram, $K_1 = 100 \pm 9$ km/s. This resulted in a mass ratio of $q = 0.32 \pm 0.03$ and a secondary radial velocity of $K_2 = 315 \pm 15$ km/s.

4.6 Discussions and Conclusions

Though our observations were not enough to refine the system's orbital period, we were able to give spectroscopic confirmation to the photometric period derived by Mason et al. (2012). This is important given the complex photometric variability of the source.

From the EW variations to the variable light curve reported by Hakala et al. (1999) 4U 1957 tells a story of strong, non-periodic variability. We know from McClintock et al. (1975) that the Bowen blend and He II are illuminated by the same mechanism. So why is He II visible in all our observed epochs and the Bowen blend is not? We believe that the disc presents variations in its thickness, randomly shielding the donor star from being irradiated. The variable accretion disc geometry would explain the evolution of the EW, the difficulty in refining the orbital period, the highly variable light curves, including the epoch in which it was non-sinusoidal and the selective presence of irradiation of the donor star. The complexity of the system indicates that the S/N was not necessarily the determinant reason why the secondary star has passed undetected for so long, but rather the variability of the system itself, shielding the real signal of the donor until, provided with the right value of γ and a refined period, we were able to find out that it has been present in the spectra all along, requiring an accurate ephemeris to emerge from the noise.

If we use our estimates of q and K_2 derived with the value of K_1 from the centre of symmetry search, we obtain a mass function of $f(M_x) = M_1 \sin^3 i \geq 0.8 M_\odot$. If we use the parameters derived from the diagnostic diagram, we obtain $f(M_x) \geq 1.1 M_\odot$. This lower limit on the mass function does not allow us to distinguish between a neutron star or a black hole. We plotted the solutions for different inclination angles in the M_1 / M_2 plane (Figure 4.12). The red dots are calculated from the centre of symmetry results and the blue dots from the diagnostic diagram. Marked are the solutions for 10° , 40° , 90° and 73° , the inclination suggested by Hakala et al. (2014). We can see from the plot that all the calculated solutions that are consistent with the proposed inclination of the system favour a relatively low mass for the compact object, pointing to a neutron star. According to our dynamical solution, even with an inclination $i \sim 10^\circ$ the highest mass for the compact object that we can obtain is $\sim 6 M_\odot$, not even half of the solution proposed by Hakala et al. (2014) for $i = 73^\circ$. If the inclination were close $i = 0^\circ$, our solution gives masses of up to $M_1 \sim 12 M_\odot$, but as the presence of the accretion disc in the Doppler maps of He II rules out a face on system, we still favour a low mass compact object primary. We use the relation between the line widths of the detected disc emission and M_1 to estimate the projected disc velocity that we would observe at low inclinations i (Warner, 1995):

$$M_1 = \frac{(0.95 \pm 0.05)^2 r_d v_D^2(I_{max})}{G \sin(i)^2}$$

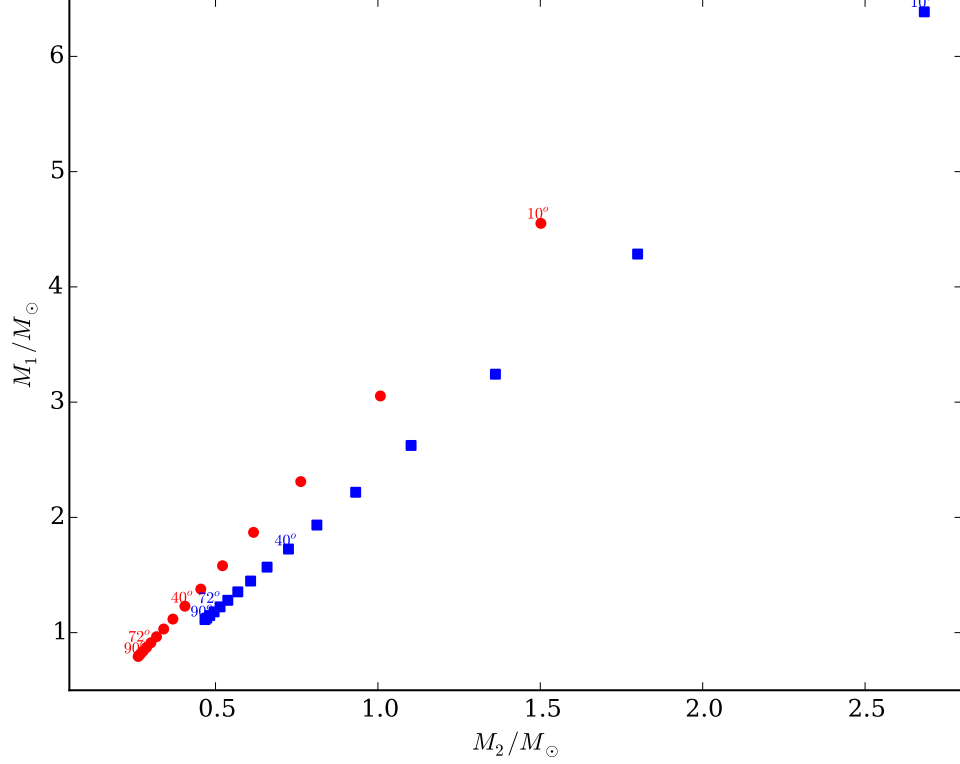


Figure 4.12: $M_1 - M_2$ plane for 4U 1957. Plotted are the results for different inclinations calculated from the centre of symmetry results (red) and the diagnostic diagram results (blue).

where r_d is the disc radius and $v_D(I_{max})$ is the velocity of the disc at maximum intensity. For our data, using He II, we find $v_D(I_{max}) \sin i = 400 \pm 50$ km/s. We plot the constraints provided by this equation with dashed lines, allowing for the uncertainty in q (and thus M_1) and v_D . We can see from Fig. 4.12 that both the constraints from the donor as those from the disc are consistent with each other. This offers further evidence that the compact emission source we see in the Doppler maps is indeed associated with the donor star.

4.7 Summary

This Chapter was devoted to the LMXB 4U 1957. 4U 1957 is a challenging target, showing a high variability that led to a wait of more than 20 years to obtain an accurate orbital period and more than 40 years to detect its donor star.

We have confirmed the system's orbital period spectroscopically (0.388879(5)d). Thanks to Doppler tomography, we presented the first dynamical evidence of the presence of the secondary star of 4U 1957 by the Bowen fluorescence technique. We have constrained the binary

mass ratio to be $q = 0.32 \pm 0.03$. Our result favours a neutron star nature, but independent information about the inclination of the system is necessary to determine the true nature of the compact object.

Five

Orbital Parameters of Four Superhumping Cataclysmic Variables

This Chapter is based on data reduced by Chris Copperwheat.

5.1 Introduction

SU UMa-type CVs have a unique characteristic among CVs: superhumps (Section 1.1.5), which can be used to derive the mass ratio of the system by the empirical relation between the superhump excess and the mass ratio q (Figure 1.6). We have mentioned before that the low mass-short period end of this relation is poorly calibrated, consisting of only one eclipsing system and a CV with poorly constrained parameters, WZ Sge.

We aim to establish more rigorous calibrators to this relation, since it is currently the only means through which we can compare the short period CV population with binary evolution models. The four systems presented in this Chapter are relatively recently discovered CVs with no previous dynamical studies, that have both short orbital periods and exhibit superhumps, indicators of low values of q . This offers the chance to use these systems as crucial calibrators for CV population studies.

AQ Eri is a SU UMa-type CV with an orbital period of 0.06094(6) days (Patterson et al., 2005). It has a low outburst frequency, so it is believed to be of an intermediate class, between SU UMa and WZ Sge (Nogami et al. 1996, Kato & Matsumoto 1999). Thorstensen et al. (1996) reported a superhump period of 0.06225(2) days. Patterson et al. (2005) derived some orbital parameters using his version of the superhump excess-mass ratio relation ($\epsilon = 0.18q + 0.29q^2$). These parameters were recalculated by Pearson (2006), using a more up to date relation ($\epsilon = 3.5 \times 10^{-4} + 0.24q - 0.12q^2$), reporting for AQ Eri: the binary mass ratio $q_{sh} = 0.129(11)$ and $M_2 = 0.069M_\odot$. We call the mass ratio derived from the relation between q and the superhump period q_{sh} to differentiate it from our derived optimal values of q that are based on dynamical con-

straints. Pearson (2006) derived M_2 using the relation between M_2 and P_{orb} for a main sequence secondary star:

$$M_2 = (0.038 \pm 0.003) P_{orb}^{1.58 \pm 0.09} \quad (5.1)$$

The SU UMa type CV, QZ Vir, is historically also known as T Leo, one of the 38 variable stars named out of their proper constellations because of erroneous coordinates or change in the constellation boundaries. It possesses one of the shortest orbital period amongst CVs with $P_{orb} = 0.0588190(5)$ days. Pearson (2006) reported for QZ Vir: $q_{sh} = 0.108(5)$ and $M_2 = 0.066 M_\odot$. Spectroscopic observations from Shafter & Szkody (1984), indicate an inclination of about 60° and a stream component located on the opposite side of the accretion disc in comparison with a normal stream impact point, proposing a magnetic WD. Our observations were taken during quiescence, but only a month after its January 2011 outburst.

SDSS J013701.06-091234.9, hereafter SDSS0137, was first identified as a Sloan Digital Sky Survey CV by Szkody et al. (2003). Its spectra show TiO bands and absorption around the Balmer lines, indicators of an M dwarf secondary (Ishioka et al., 2007). Ishioka et al. (2007) also reported weak hydrogen lines and strong helium lines in its infrared spectrum. Pretorius et al. (2004) reported an orbital period of 0.054937(7) days and a superhump period of 0.056736(5) days, while Imada et al. (2006) reported a superhump period of 0.056686(12) days. Imada et al. (2006) also reported that SDSS0137 possessed colours that are very different to other SU UMa type CVs, but consistent with late M or L-type stars. Pearson (2006) also reported parameters for SDSS0137 as: $q_{sh} = 0.113(7)$ and $M_2 = 0.060 M_\odot$.

RZ Leo was first identified as a SU UMa type CV by Ishioka et al. (2001b) during its super-outburst. Two types of superhumps were then identified: normal superhumps and the so called “early superhumps”. Early superhumps are characteristic of WZ Sge stars, a type of SU UMa that present very long outburst cycles (years-decades) with very few or no normal outbursts between super-outbursts. Only five of these systems are known and it is believed RZ Leo is one of them (Ishioka et al. (2001b), Richter (1985)). The orbital period is 0.0760383(7) days (Patterson et al., 2003). Mennickent & Tappert (2001) report an anomalous bright spot location, as the source of continuum and line emission variation in the system. Pearson (2006) reports for RZ Leo: $q_{sh} = 0.150(10)$ and $M_2 = 0.098 M_\odot$.

5.2 Observations and Data Reduction

These CVs were observed in service mode with the X-Shooter instrument on four nights during 2010 and 2011 (see Table 5.1 for detailed dates). X-Shooter is an echelle spectrograph operating at the Cassegrain focus of Unit Telescope 2 (Kueyen) on the Very Large Telescope, Antofagasta, Chile. In a single exposure the instrument covers the spectral range from the UV to the near-infra red (NIR) band in 3 arms (see Vernet et al. 2011 for details). The ultraviolet-blue (UVB)

Target	Date	K Mag.	Exp time UVB [s]	Exp. time visual [s]	Exp. time NIR [s]
AQ Eri	22/12/2010	15.3	200	215	110
QZ Vir	15/2/2011	13.8	60	75	50
SDSS0137	19/10/2010	15.3	200	215	110
RZ Leo	23/3/2011	15.4	300	310	110

Table 5.1: X-shooter observation dates.

arm covers 3000-5595 Å with a resolution of 5100 for a 1" slit width. The visual arm covers the range 5595- 10240 Å with a resolution of 8800 for a 0.9" slit width and the near-infrared arm covers 10240-24800 Å with a resolution of 5300 for a 0.9" slit width. The data was reduced by Chris Copperwheath, using the standard X-Shooter reduction pipeline version 1.5.0 (Modigliani et al., 2010), which implemented Esorex version 3.9.6. The pipeline performs all the standard calibrations: flat-fielding, sky background subtraction, optimal extraction and wavelength calibration.

5.3 Average Spectra

Figures from 5.1 to 5.12 show the average spectra of each of the targets. We show for each system the normalised UVB and visual arms. As the normalisation-flux calibration of the NIR spectra is very challenging and overall, not rewarding, we show the average spectra and only normalised the segments of the spectra relevant for this work. Tellurics are not subtracted but marked with the symbol \oplus in each spectra.

All four CVs show double-peaked Balmer lines in emission, resolved up to H10 in SDSS0137, up to H12 in AQ Eri and up to H13 in QZ Vir and RZ Leo. He I and weak He II are also present in emission, except for RZ Leo that shows no traces of He II. Some Fe I and Fe II lines are also visible in emission, albeit rather weak in some cases. The Ca II triplet is present in all four systems and Paschen lines, resolved up to Pa 18 are in emission in all but SDSS0137.

The spectra of AQ Eri presented by Szkody (1987) shows all peaks to be asymmetric, with a blue peak more prominent than the red, except for H β that shows a larger red peak. In our spectra, all double lines showed a more prominent red peak.

The high resolution spectra of QZ Vir allowed us to identify features, such as the weak Ca II 5307Å and O I double-peaked in emission, that were unnoticed until now.

SDSS0137 is the only CV in our sample with no traces of the Paschen lines and is in general, the one with the lowest EW in all lines. It was reported by Ishioka et al. (2007) that the system showed a weakness of hydrogen lines in the IR, this led them to link the system to El Psc, an unusual CV with a very evolved secondary (Uemura et al., 2002). Remarkably, we can see strong Na I 8190 Å in absorption, in anti-phase with the emission lines, tracing the movement of the secondary star. TiO bands are not evident even before normalisation, but we do see the broad

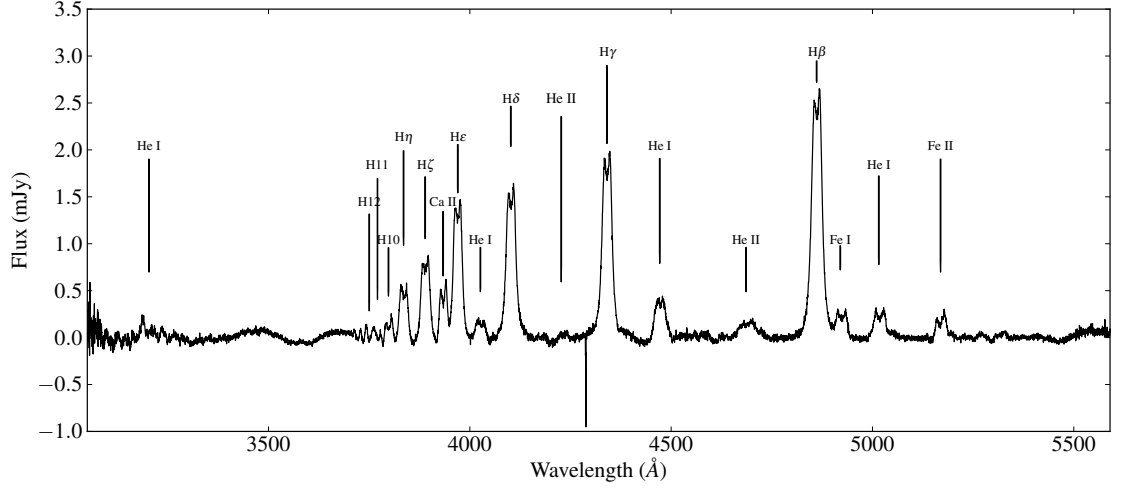


Figure 5.1: Average of 20 spectra of AQ Eri UVB arm.

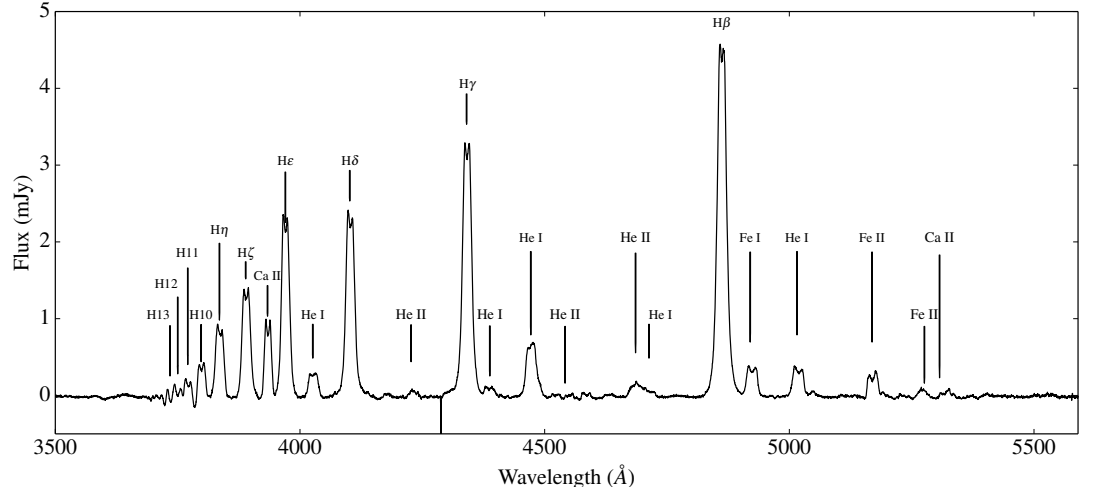


Figure 5.2: Average 40 spectra of QZ Vir UVB arm.

absorption around the Balmer lines from the WD, as reported in previous spectroscopic analysis (Ishioka et al., 2007).

Our averaged spectra of RZ Leo presents well defined, strong and symmetric double peaks similar to the ones reported by Mennickent & Tappert (2001) and Patterson et al. (2003) while the system remained in quiescence. Our extensive wavelength coverage allow us to confirm that this strong double peaks feature is present in all the Balmer series, as well as all the other emission lines, indicating a fairly high inclination.

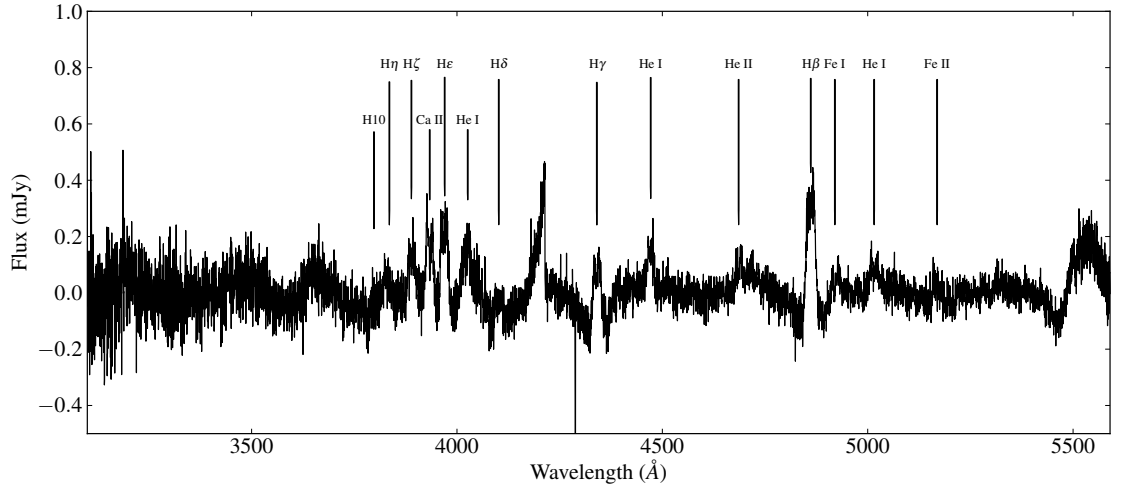


Figure 5.3: Average of 21 spectra of SDSS0137, UVB arm. The emission feature between 4000 and 4500 Å is a side effect from the order merging in the reduction of the spectra.

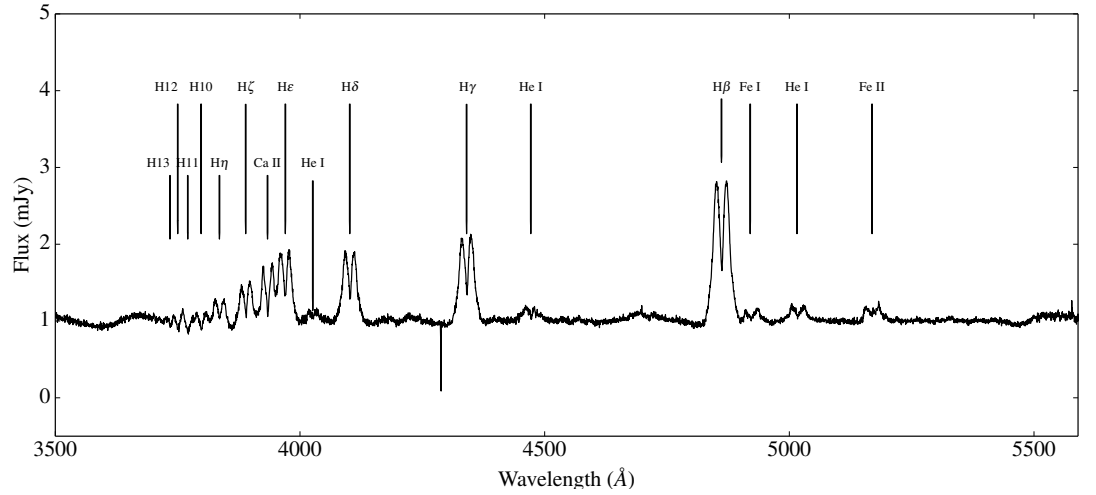


Figure 5.4: Average of 21 spectra of RZ Leo, UVB arm.

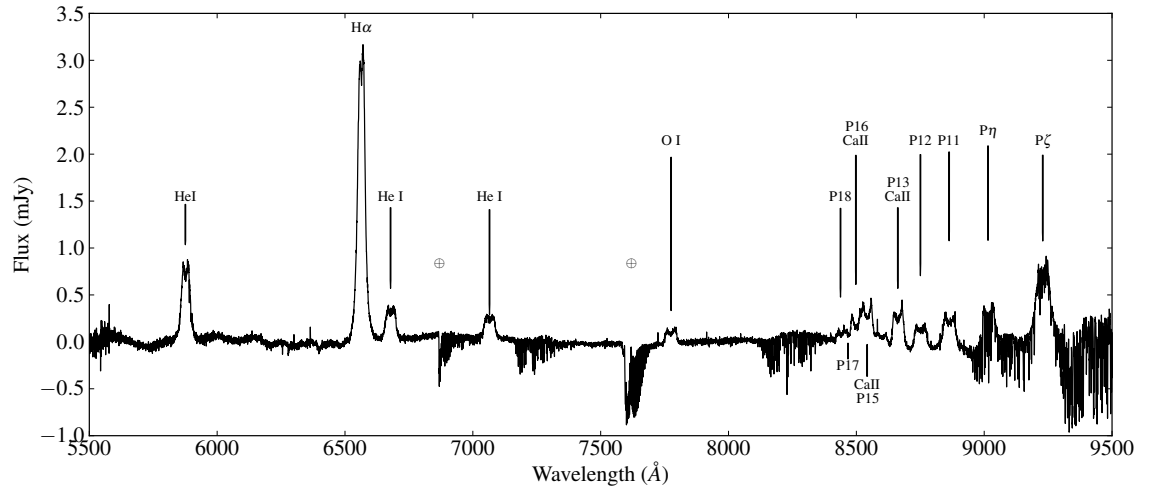


Figure 5.5: Average of 20 spectra of AQ Eri visual arm.

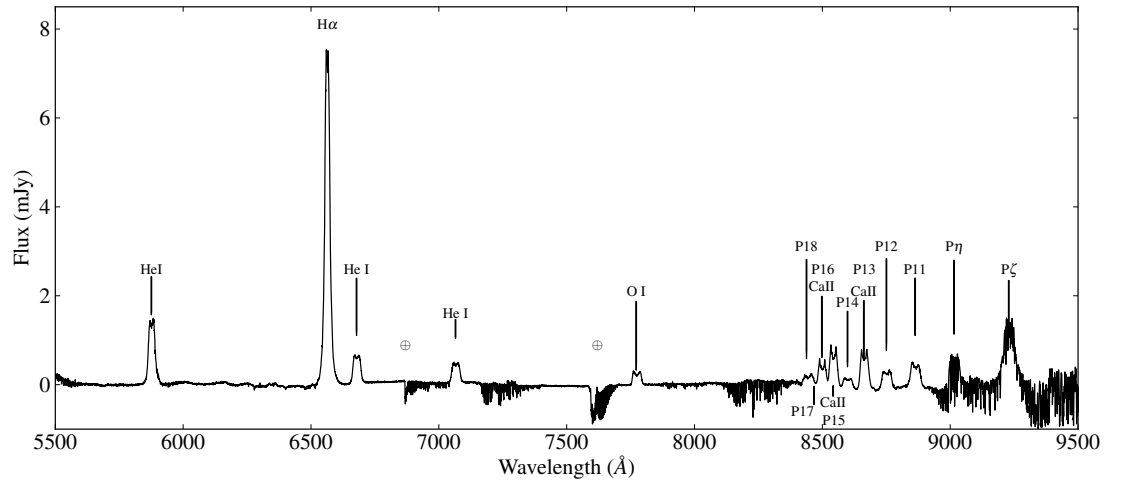


Figure 5.6: Average 40 spectra of QZ Vir visual arm.

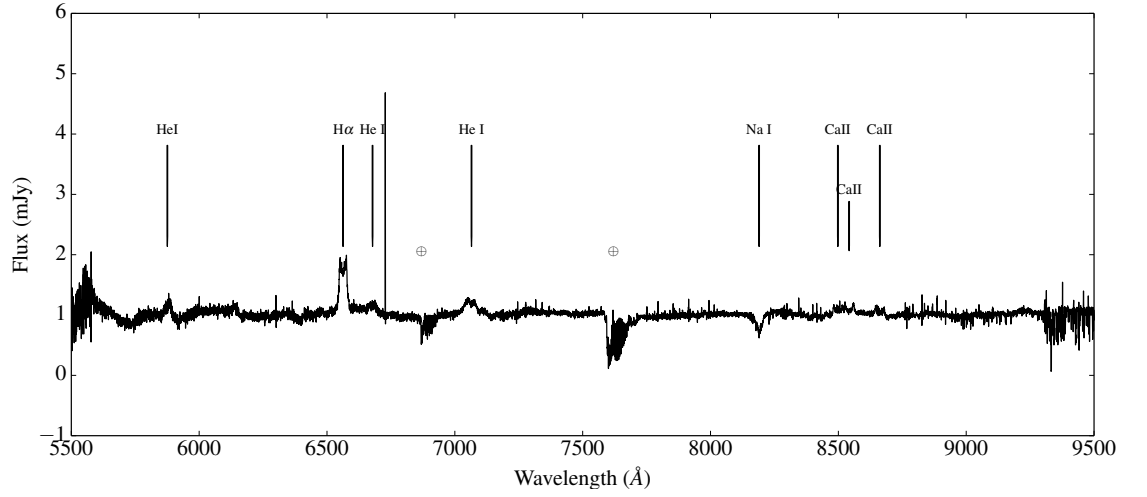


Figure 5.7: Average of 21 spectra of SDSS0137, visual arm.

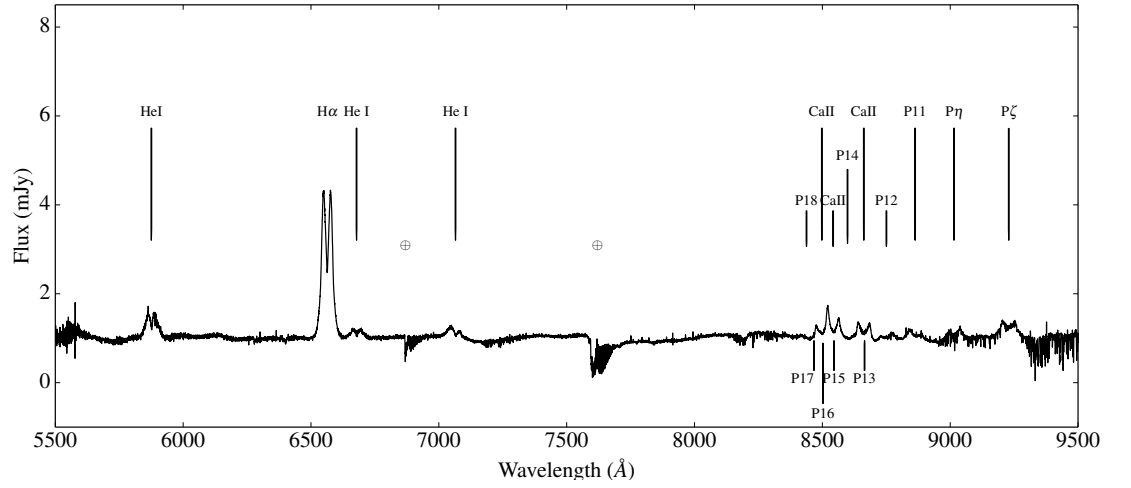


Figure 5.8: Average of 21 spectra of RZ Leo, visual arm.

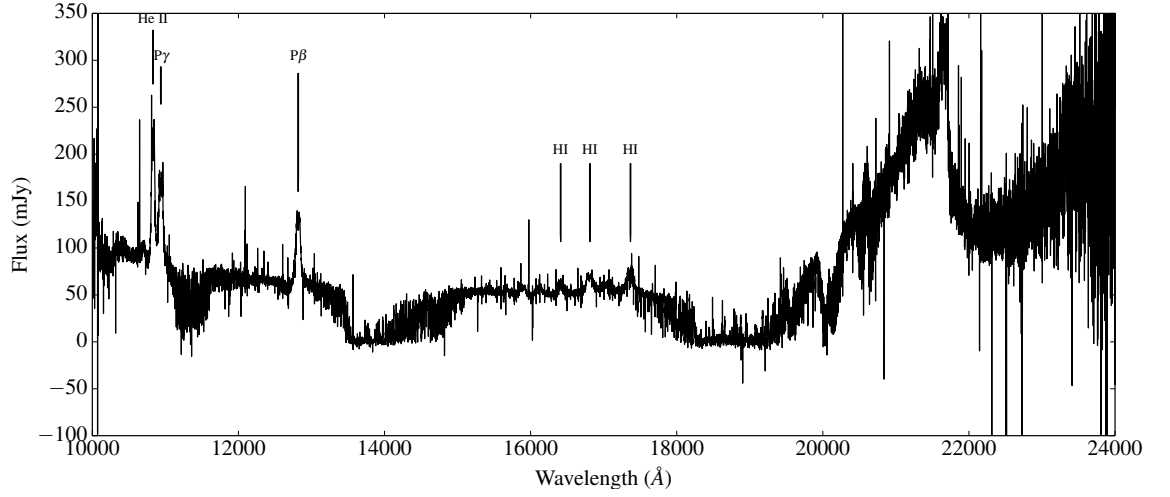


Figure 5.9: Average 10 spectra of AQ Eri NIR arm.

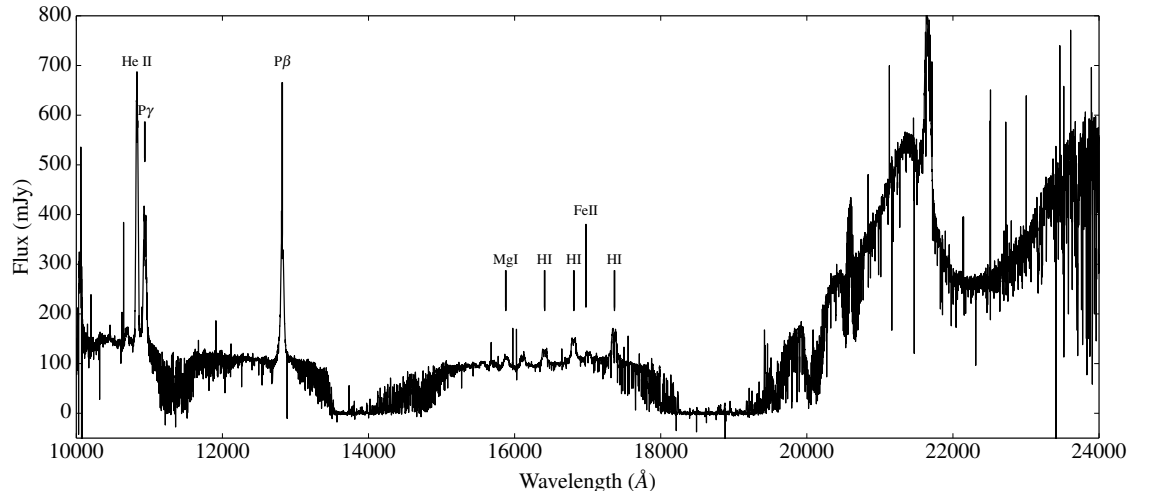


Figure 5.10: Average of 20 spectra of QZ Vir NIR arm.

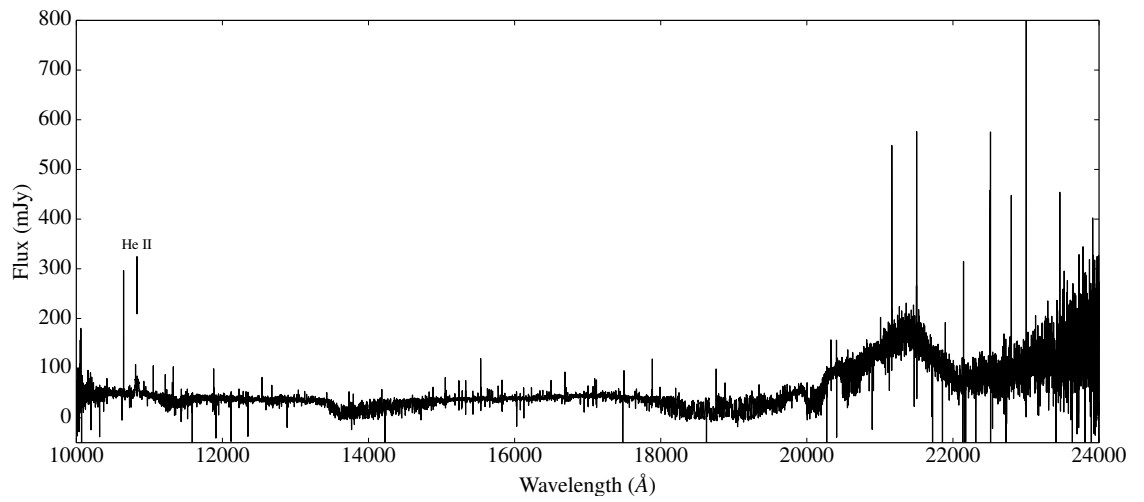


Figure 5.11: Average of 10 spectra of SDSS 0137, NIR arm.

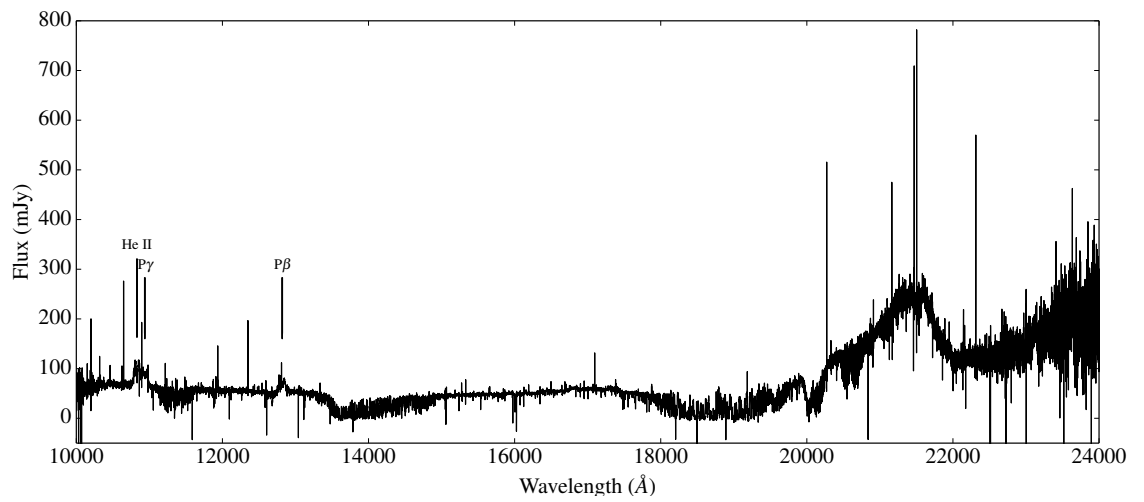


Figure 5.12: Average of 10 spectra of RZ Leo, NIR arm.

AQ Eri				QZ Vir		
Line	γ [km/s]	K_1 [km/s]	Φ_0	γ [km/s]	K_1 km/s	Φ_0
H α	45 ± 11	42 ± 18	0.1 ± 0.05	78 ± 6	52 ± 9	0.08 ± 0.03
H β	23 ± 13	41 ± 20	0.1 ± 0.06	68 ± 7	43 ± 10	0.05 ± 0.03
CaII	48 ± 13	47 ± 20	0.1 ± 0.06	148 ± 14	28 ± 20	0.04 ± 0.1

SDSS0137				RZ Leo		
Line	γ [km/s]	K_1 [km/s]	Φ_0	γ [km/s]	K_1 [km/s]	Φ_0
H α	23 ± 9	37 ± 15	0.03 ± 0.06	7 ± 8	74 ± 15	0.1 ± 0.02
H β	44 ± 24	103 ± 48	0.09 ± 0.05	13 ± 18	76 ± 32	0.2 ± 0.04
Ca II	-260 ± 22	63 ± 33	0.13 ± 0.07	-23 ± 8	50 ± 16	0.1 ± 0.01

Table 5.2: Orbital parameters derived from the diagnostic diagrams of AQ Eri, QZ Vir, SDSS0137 and RZ Leo. Φ_0 is relative to our ephemeris (Section 5.5).

5.4 Radial Velocities

We analysed our four systems with the classical double Gaussian technique as described in Section 2.2. We constructed diagnostic diagrams of the strongest Balmer lines and Ca II 8662.14 Å. We show as an example, in Figures 5.13 and 5.14, the diagnostic diagrams constructed for AQ Eri and RZ Leo. In the case of AQ Eri, the diagnostic diagrams of H α and H β converge in the range 1300-2400 km/s and the narrower Ca II converges between 1300-2000 km/s. For RZ Leo, the diagnostic diagrams converge in the range 2000-3000 km/s for the Balmer lines and between 1700-2200 km/s for Ca II. The reported values are the average of the parameter in the convergence range and the reported errors are the propagated errors of each parameter in the given range.

We present the parameter results for the diagnostic diagrams of the most representative Balmer lines and Ca II for each system in Table 5.2. As we have seen before in Chapter 3, different lines tend to agree with the value of K_1 , but show very different values for the systemic velocity γ .

We can see that the values of γ are spread and vary strongly depending on the observed line. This result is not surprising and we have discussed it before as products of asymmetries and blending. It should be noticed the result of γ for CaII in SDSS0137. We have previously attributed higher γ values of Ca II to the blending with the Paschen lines before, but the spectra of SDSS0137 shows no traces of the Paschen lines and the systemic velocity of the line is ~ 300 km/s lower than the Balmer lines.

The values of K_1 are generally consistent considering the errors. We will investigate the values of K_1 again in Section 5.5 using the centre of symmetry technique.

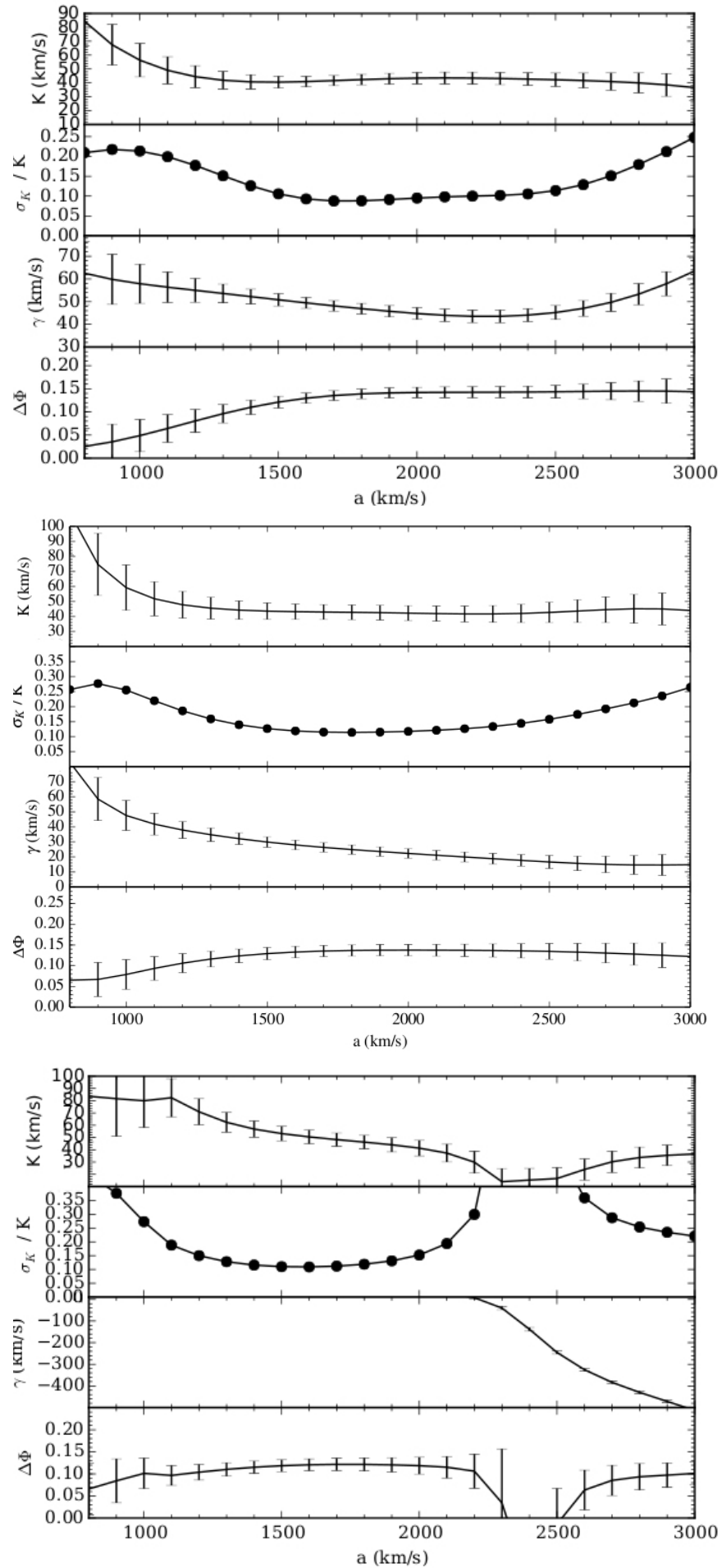
We also performed a single Gaussian fit to the Na I doublet present in absorption in the spectra of SDSS0137. We used the first peak of the doublet, since the second one presents con-

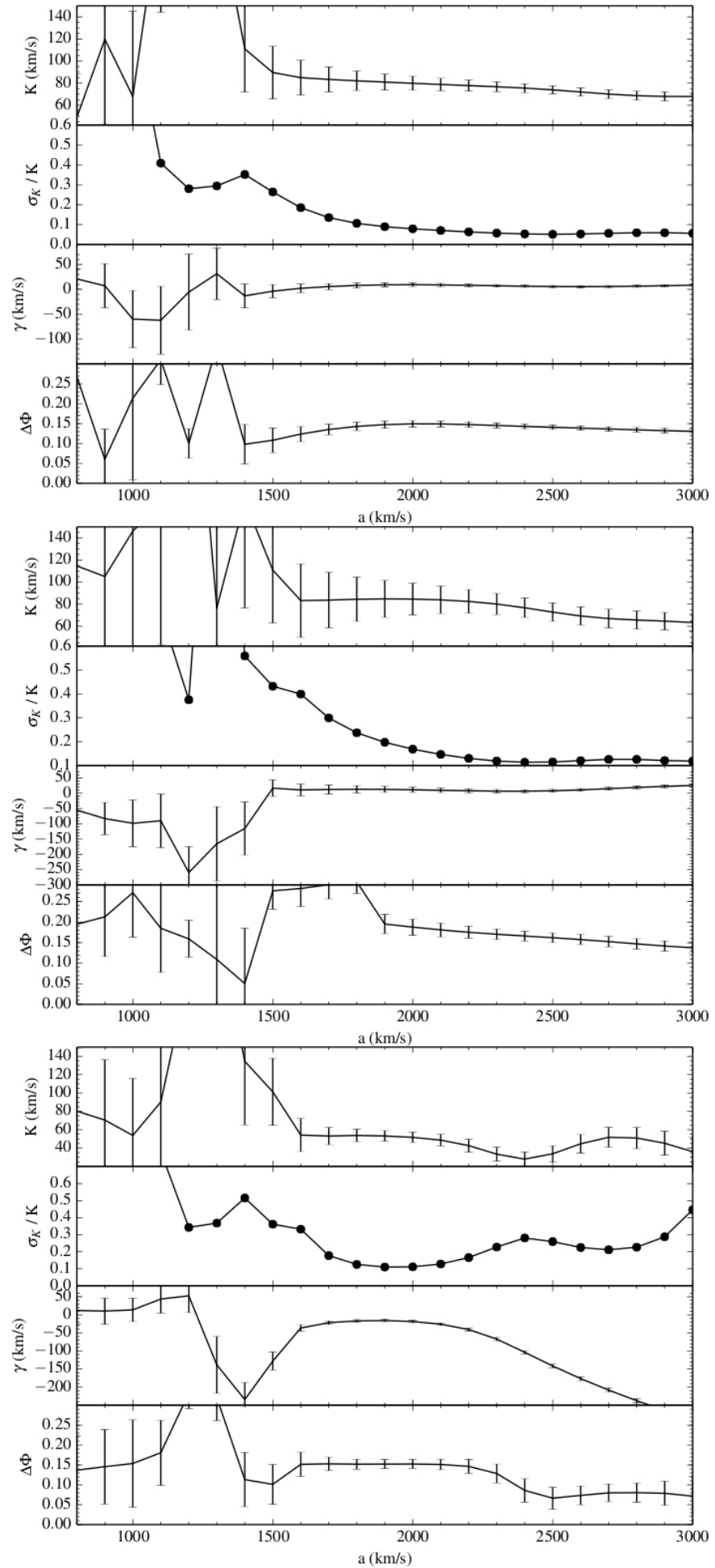
tamination, likely from another line, that makes difficult to quantify the limits of the wings. We obtained a value of $K_{ab} = 337 \pm 8 \text{ km/s}$. We call this value K_{ab} to differentiate it from K_{em} , the radial velocity of the irradiated face of the secondary and from the value of K_2 derived from the K-correction.

5.5 Doppler Tomography

We present the Doppler maps of a selection of the strongest emission lines from our spectra in Figures 5.15 to 5.18. The secondary roche lobe, calculated from our best q (Section 5.5.4) are plotted on top of the maps. We will discuss specific features of each system individually.

Figure 5.15 shows the Doppler maps of AQ Eri. All maps show the ring-shape associated with the accretion disc. We can see that the disc in $H\alpha$ has lower velocities compared to the other lines. It is smaller than the other Balmer lines and we include the map of $H\beta$ as a comparison. This might be either an effect due the optical thickness of the line or a real temperature gradient in the disc permitting selective ionisation. The He I lines behave as He I 5876, with smooth discs, strong bright spots and no traces of the secondary star. It was not possible to construct reliable maps of He II. We show the Doppler maps for Fe I and Fe II, both dominated by the disc. A remarkable feature present in all maps except the ones from He I is an enhanced emission region in the second quadrant ($+V_x, -V_y$), sometimes extending all the way to the third quadrant ($-V_x, -V_y$). We have encountered such enhanced emission before in V2051 Oph. It was proposed by Papadaki et al. (2008) that this emission could be the equivalent to the superhump light source, but the last superoutburst of AQ Eri before our observation date was in January 2010, almost a year before our data was taken. The secondary star is visible in $H\alpha$ (and shows traces in the Balmer lines Doppler maps up to $H\delta$) and in Ca II. We show the Doppler map of Ca II 8662.14 Å next to its neighbouring Paschen line, Pa 13. These maps were made simultaneously by weighting for the contribution of each line which were given independent maps. At the bottom left of Figure 5.15 we show the Doppler map of Ca II 3933.37 Å. Since Ca II 3933 is blended with the stronger He, the map is full of artifacts and the size of the disc is not reliable. We show it only to remark that signal from the irradiated face of the secondary star was only visible in the Ca II NIR triplet, despite the superior strength of Ca II 3933.37 Å in this system. Tappert et al. (2003) have constructed Doppler maps of AQ Eri, using $H\alpha$. They separated the data in three subsets, each containing one full orbit. They found significant differences between the maps from one orbit to the next, with an enhanced emission zone moving to a position in the third quadrant ($-V_x, -V_y$). They proposed this enhanced feature as arising from the secondary star. Our superior resolution map of $H\alpha$ shows indeed the donor star, but given that Tappert et al. (2003) reports no velocity estimates from this feature, we are unable to confirm their detection. Concerning the short period variations, having only one full orbit of the system, we cannot construct

Figure 5.13: Diagnostic diagram for AQ Eri. From top to bottom: H α , H β and CaII 8662.14 Å.

Figure 5.14: Diagnostic diagrams of RZ Leo. From top to bottom: H α , H β and CaII 8662.14 Å.

reliable independent maps to test their claims.

Figure 5.16 shows the Doppler maps for QZ Vir. All maps show the ring shape consistent with the accretion disc. We generated Doppler maps of the Balmer lines up to H10, the secondary star was resolvable in all of these. There are also traces of the secondary in the maps of the Paschen lines. The secondary feature is also resolvable in He I maps, we show He I 5876 in the second panel of Figure 5.16. The secondary feature allows us to get a reliable phase for the system. We also present Fe II and O I, maps, both showing the presence of the accretion disc. Szkody et al. (2001) presented Doppler maps for $H\alpha$, $H\beta$, $H\gamma$ and HeI 4471Å. Their $H\gamma$ Doppler map presented a very strong low velocity emission near the centre of mass, which is not present in our $H\gamma$ map or any other Balmer line. Szkody et al. (2001) also proposed a stream component located on the opposite side of the accretion disc from the normal stream impact. We can see that this is true for $H\alpha$, where the bright spot appears to be in the second quadrant ($+V_x, -V_y$) but the rest of the emission lines show an enhanced emission on the x axis, almost on top of the secondary star. We currently have no explanation for this odd feature.

Figure 5.17 shows the Doppler maps generated for SDSS0137. The Balmer lines showed a consistent presence of the accretion disc, and presence of the secondary star. All the maps of He I were similar to the one showed in the second panel of Figure 5.17 with only the bright spot present and no signal from the rest of the accretion disc. This is an indication that the He I emission is generated close to where the stream of material impacts the accretion disc. In the case of SDSS0137, the Ca II lines show the opposite behaviour than AQ Eri: there is no presence of the secondary star in Ca II 8662.14 Å or any of the Ca II triplet, but there is a clear secondary emission from the stronger Ca II 3933.67 Å. Given that the ionisation energy necessary to excite Ca II 3933.67 Å is higher than the Ca II triplet (3.15 eV versus 1.43 eV necessary for the CaII triplet), and that the opposite case occurs for AQ Eri, we believe that the absence of secondary emission in the Ca II triplet is due to an image reconstruction effect due to the low S/N of the Ca II triplet.

RZ Leo, Figure 5.18 shows no signal from the secondary star in any emission line. The HJD of the first observation was used as the zero phase. The hydrogen lines and Ca II lines showed the usual disc shape, with what we could identify as the bright spot. All the generated Doppler maps of He I though, showed only the bright spot, as the map of He I 6678 Å presented in Figure 5.18. This strong S-wave was also seen by Patterson et al. (2003) in their He I trails. This bright spot is the only feature visible in the maps, as there is no presence of the disc. This bright spot is present in all the other maps, though the hydrogen and calcium maps also show a second enhanced emission region in the lower right quadrant.

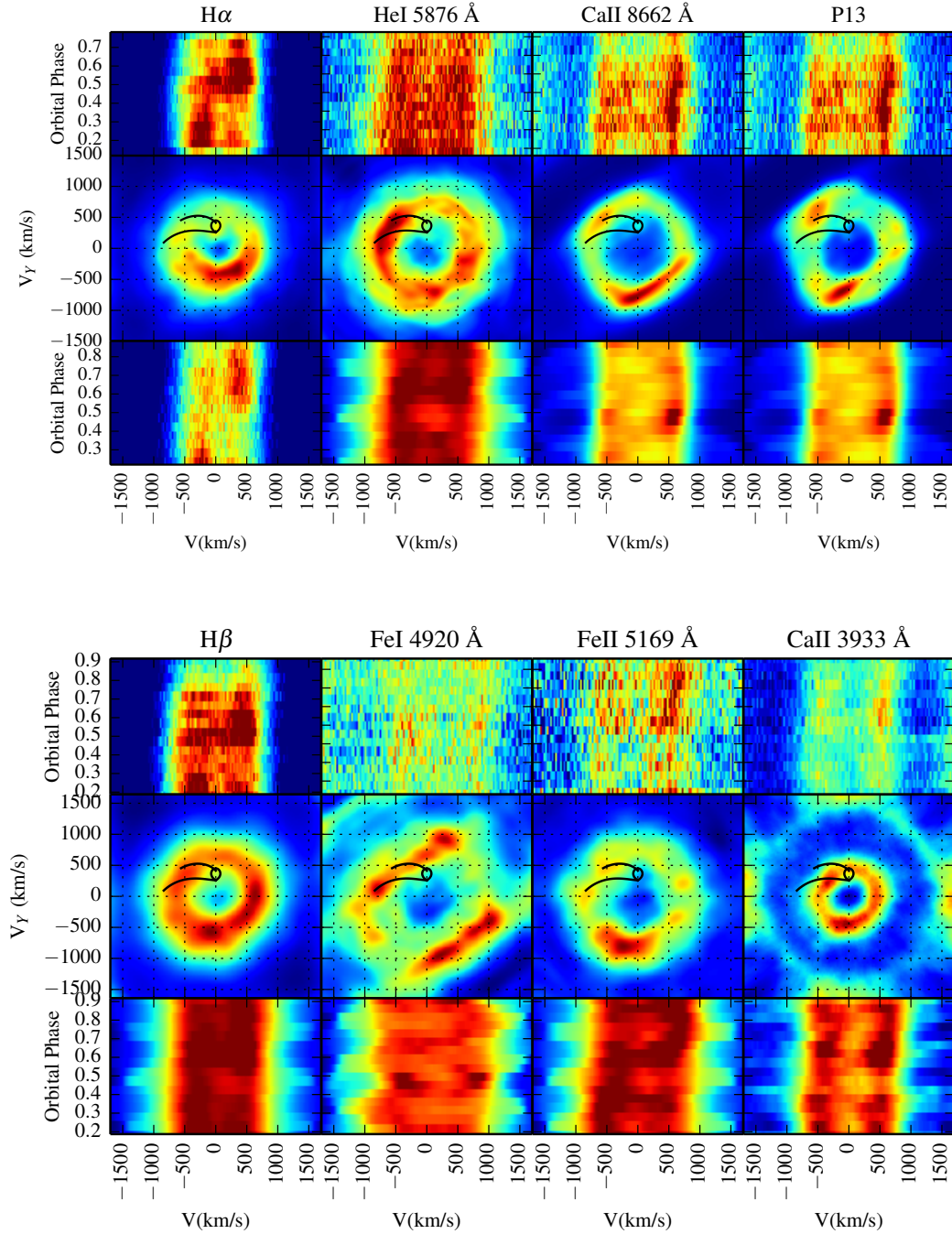


Figure 5.15: Doppler maps of AQ Eri. Lines are labelled on top of each panel. The x and y axes are V_x and V_y , respectively. The Roche lobe model for the best orbital solution and gas stream are plotted with a solid line over the Doppler maps.

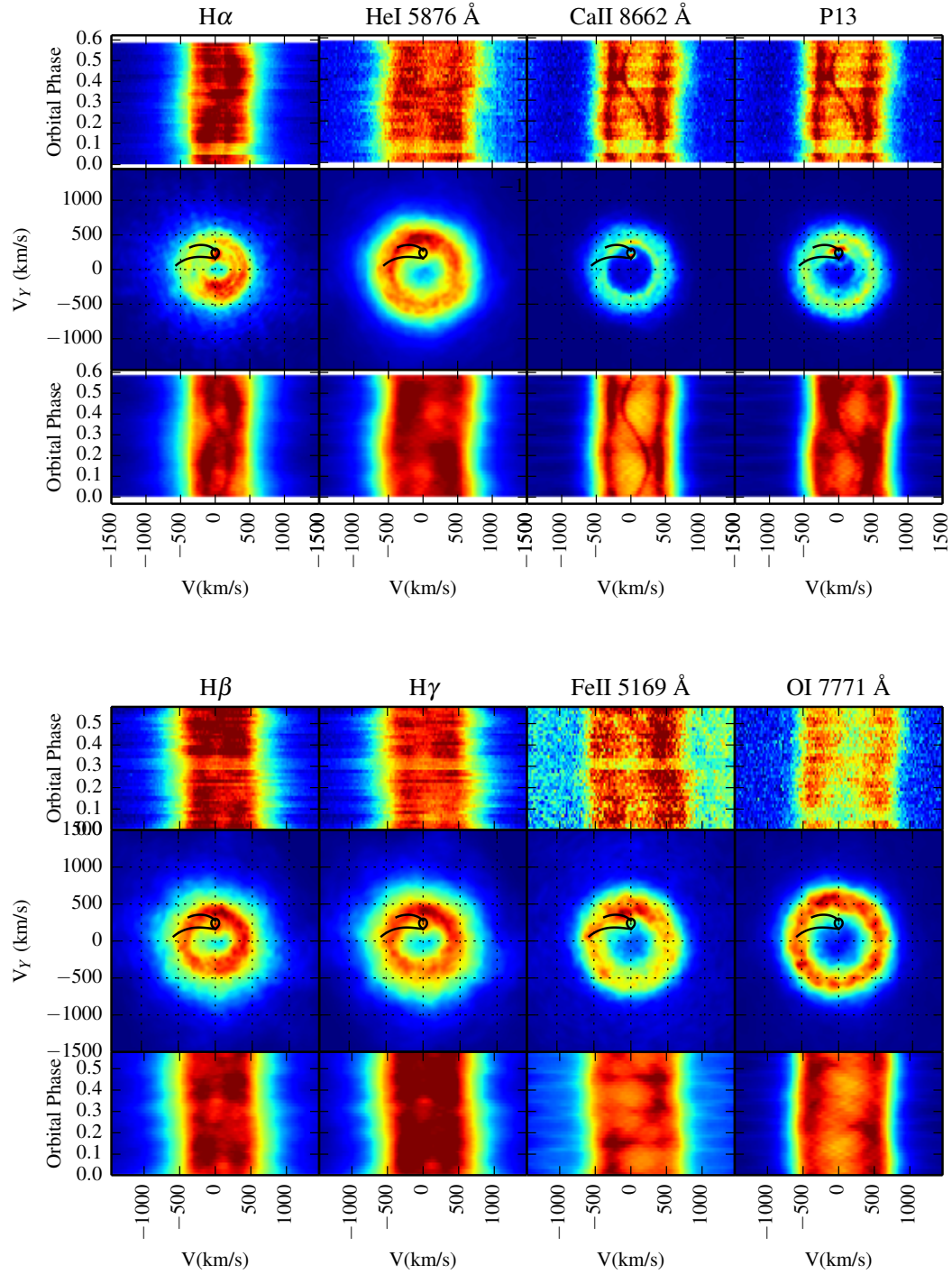


Figure 5.16: Doppler maps of QZ Vir. Lines are labelled on top of each panel. The x and y axes are V_x and V_y , respectively. The Roche lobe model for the best orbital solution and gas stream are plotted with a solid line over the Doppler maps.

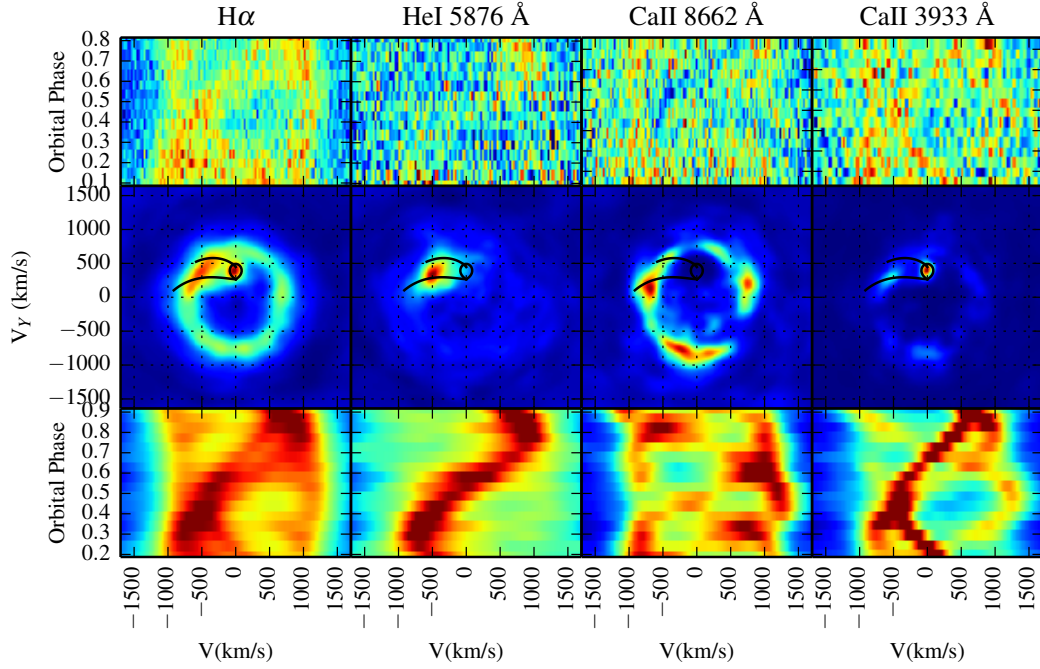


Figure 5.17: Doppler maps of SDSS0137. Lines are labelled on top of each panel. The x and y axes are V_x and V_y , respectively. The Roche lobe model for the best orbital solution and gas stream are plotted with a solid line over the Doppler maps.

System	T_0 (HJD)	K_{em} (km/s)
AQ Eri	2455552.702 ± 0.014	280 ± 10
QZ Vir	2455607.794 ± 0.014	186 ± 27
SDSS0137	2455488.597 ± 0.013	317 ± 20

Table 5.3: Ephemeris and K_{em} of the systems with a visible donor.

5.5.1 Secondary Star and Phase Zero

As no secondary star feature was present in RZ Leo, it was not possible to determine a new ephemeris. Using the secondary star emission, we calculated ephemerides for the other three systems, and the Doppler maps presented in this chapter were generated using these ephemerides. In the systems with a secondary star feature, we also determined the velocity of the irradiated face of the donor star, K_{em} , by generating 500 bootstrap samples of each map and fitting a 2-D Gaussian to each sample, as explained in Section 2.4.8. We present the results in Table 5.3

We have shown that the ephemeris derived from the position of the secondary star are reliable, using eclipsing systems in the previous Chapter.

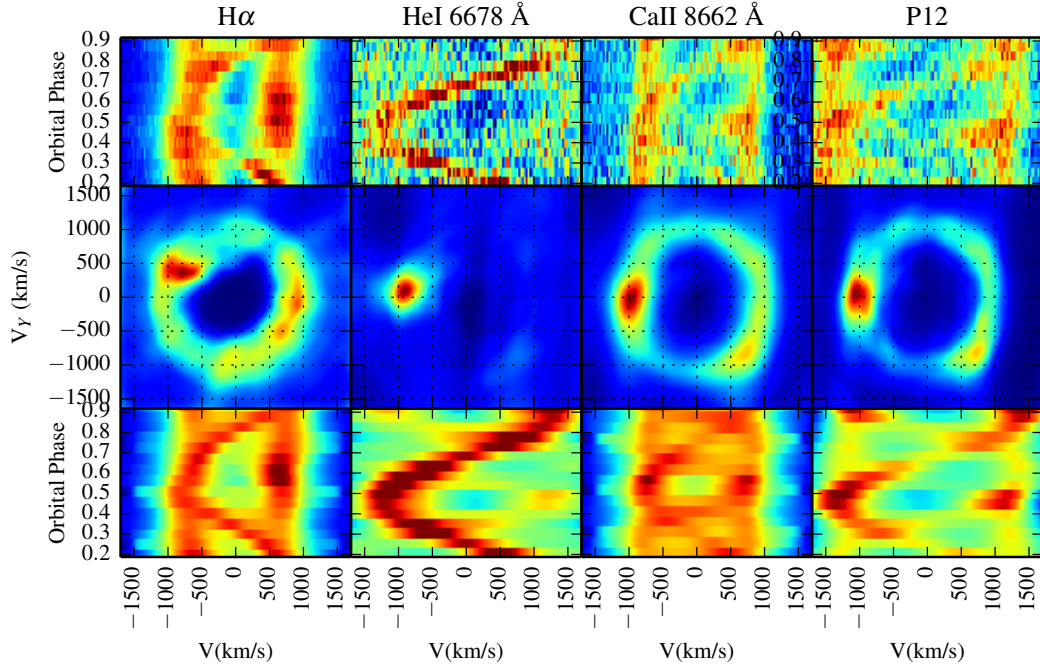


Figure 5.18: Doppler maps of RZ Leo. Lines are labelled on top of each panel. The x and y axes are V_x and V_y , respectively.

5.5.2 Systemic Velocity γ

Using the method described in Section 2.4.7 and 3.3.3, we constrain the systemic velocity for the CVs with a visible secondary star. In the case of AQ Eri and QZ Vir, we used the Doppler maps of Ca II 8662.14 Å to construct the diagrams of Figures 5.19 and 5.20, obtaining $\gamma = 50^{+12}_{-11}$ km/s for AQ Eri and $\gamma = 60^{+20}_{-20}$ km/s for QZ Vir. There is an obvious spike at $\gamma = 65$ km/s in the diagram of QZ Vir. This spike was produced by the script picking up random noise features instead of the secondary star. Despite that it is unlikely that the noise dominates over the secondary signal, if it happens, with our method -which explores a wide range of values of γ - we get a warning that lets us deal with it (in this case, by increasing the uncertainty of the determination of γ). SDSS0137 showed no traces of the secondary in Ca II 8662.14 Å, but it did appear in H α and Ca II 3933.37 Å. We used these to constrain the value of γ with the results plotted in Figures 5.21 and 5.22, obtaining $\gamma = 50^{+6}_{-10}$ km/s and 30^{+16}_{-11} km/s. Assessing these results with the plot, we can see that for Ca II there isn't a well defined minimum for the STD and that the lowest FWHM happens for $\gamma = 50$ km/s, so we used $\gamma = 50^{+6}_{-10}$ km/s for making the Doppler maps in this chapter.

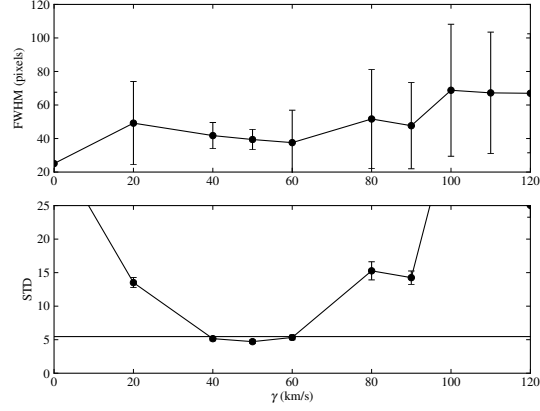


Figure 5.19: FWHM of the secondary star and STD versus systemic velocity for AQ Eri. The error bars are sometimes smaller than the symbol.

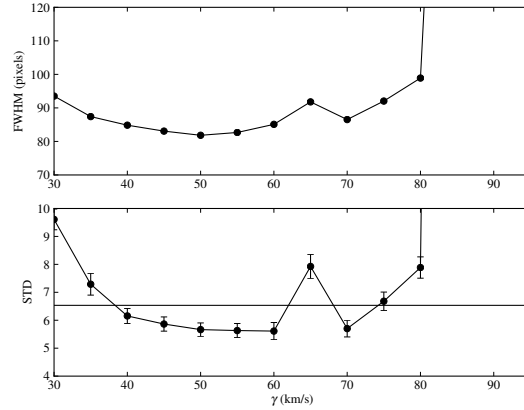


Figure 5.20: FWHM of the secondary star and STD versus value of systemic velocity, γ , for QZ Vir.

5.5.3 Radial Velocity of the Primary Star

After constraining the value of the systemic velocity, we performed a centre of symmetry search of the disc feature on the four systems, as described in Section 2.4.7. We used box 5 (lower half) in AQ Eri and QZ Vir and box 4 (right half) for SDSS0137 and RZ Leo. We prefer Ca II over the Balmer lines since, as we showed in the previous Chapter, it was on average the line that delivered the lowest and most stable values of K_1 . We used Ca II 8662.14 Å in all except for SDSS0137 in which H α showed a less asymmetric disc and we used it instead. For each system, we constructed 500 bootstrap samples, subtracted the symmetric part at different velocities and measured the level of residuals. Figure 5.23 shows an example of histograms of the velocity at which the lowest level of the residuals was found for each of the 500 bootstrap samples of the Ca II Doppler map of AQ Eri. As in the case of γ , outliers as the one found in $K_x = -80$ km/s are due to the fitting script

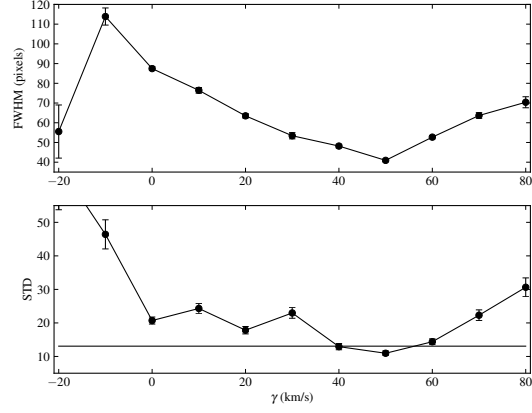


Figure 5.21: FWHM of the secondary star and STD versus value of systemic velocity, γ , for SDSS0137. We used H α to perform this analysis.

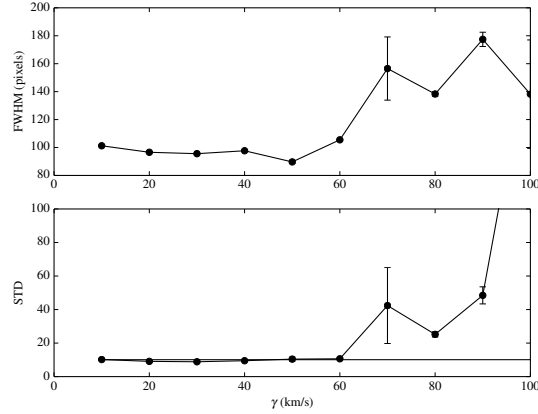


Figure 5.22: FWHM of the secondary star and STD versus value of systemic velocity, γ , for SDSS0137. We used Ca II 3933Å for this analysis.

selecting a noise feature instead of the secondary signal. After making sure that it is the case in a particular outlier, these can be removed from the final calculations. Our results are summarised in table 5.4.

5.5.4 Mass Ratio

We used the method described in Section 2.4.8 to perform a K-correction and estimate the mass ratio of the systems. For the models, we used $i = 60^\circ$ for QZ Vir and $i = 45^\circ$ for the ones with no known inclination constraints. Figures 5.24 to 5.26 show the derived dynamical constraints for each system. The full black circle represents our best solution while the full square represents the superhump solution. The other constraints are the same as in Figure 3.15.

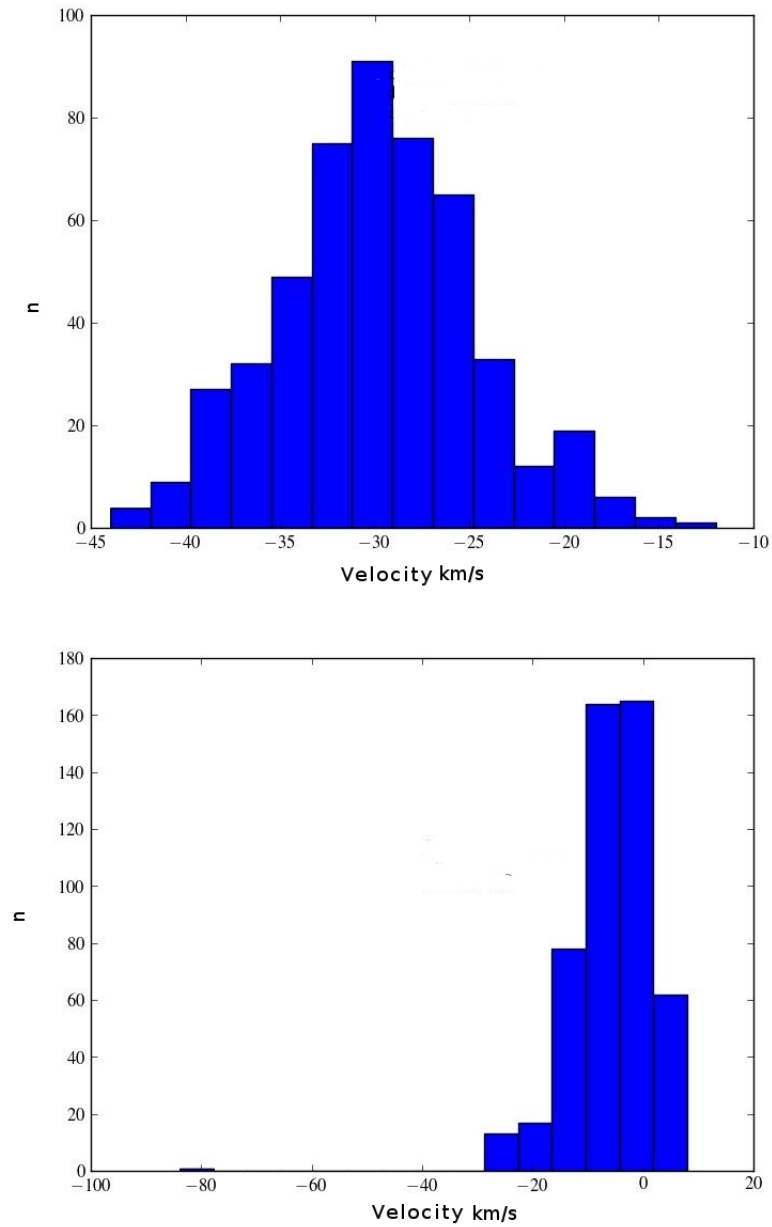


Figure 5.23: Histograms of K_y (top) and K_x (bottom) at which the lowest residual values were found for the 500 bootstrap samples. The average of both components is used to estimate K_1 . The uncertainty is the STD of the histograms.

System	K_1 [km/s]	Line
AQ Eri	$K_1 = 31 \pm 7$	Ca II
QZ Vir	$K_1 = 26 \pm 3$	Ca II
SDSS0137	$K_1 = 43 \pm 19$	H α
RZ Leo	$K_1 = 68 \pm 24$	H α

Table 5.4: Primary velocity of the four systems calculated using the centre of symmetry technique.

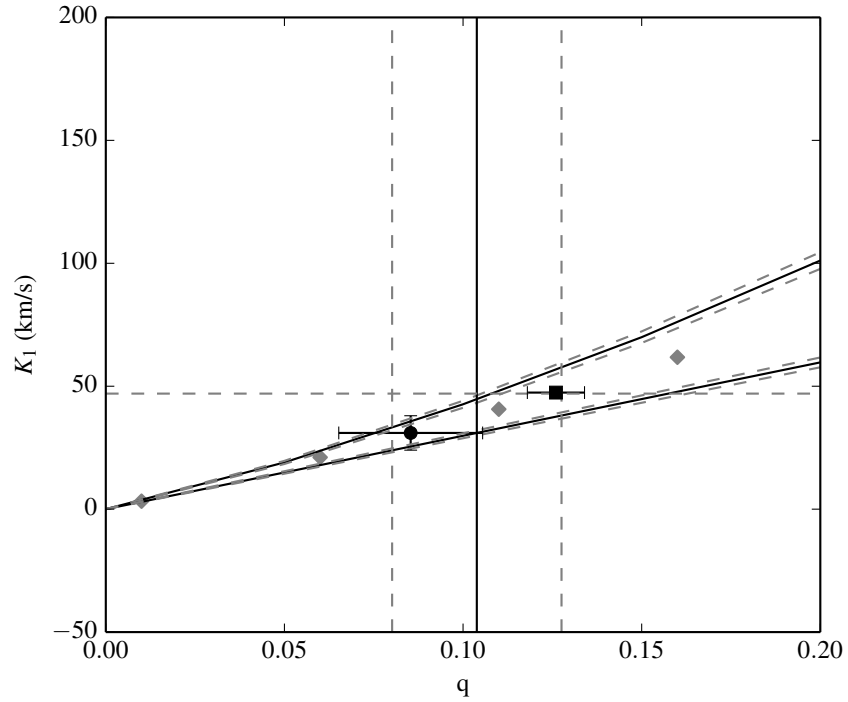


Figure 5.24: K_1, q plane for AQ Eri. $K_{em} > K_{L_1}$ is the top diagonal solid black line with dashed errors. $K_{em} < K_2$ is the bottom diagonal line with dashed errors. The vertical solid line represents the maximum value of q . The grey diamonds are the solutions from our model. The black point with error bars represents our best solution for the value of K_1 found from the centre of symmetry technique ($K_1 = 31 \pm 7$ km/s). The black square is the superhump solution.

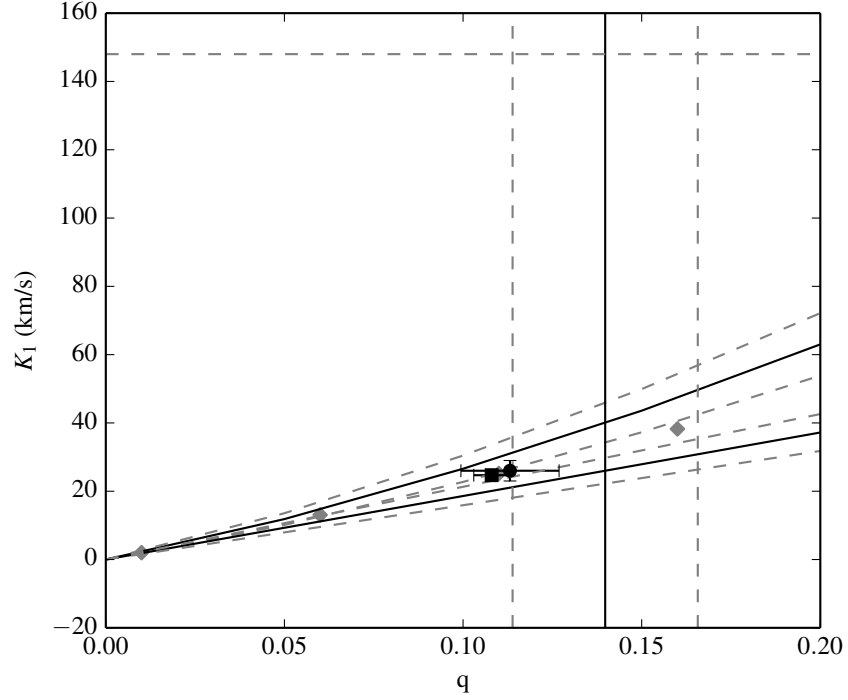


Figure 5.25: K_1 - q plane for QZ Vir, all markers as indicated in Figure 5.24.

For AQ Eri, the superhump solution is $q_{sh} = 0.126 \pm 0.08$, giving $K_{1sh} = 47 \pm 1.6$ km/s, $K_{2sh} = 376$ km/s. Our best solution is $q = 0.085 \pm 0.02$, $K_1 = 31 \pm 7$ km/s and $K_2 = 363 \pm 41$ km/s, only marginally consistent with the superhump solution.

The superhump solution for QZ Vir: $q_{sh} = 0.108 \pm 0.005$, leads to component velocities of $K_{1sh} = 24.7 \pm 0.9$ km/s, $K_{2sh} = 229 \pm 1$ km/s. Using our best estimates of K_1 and K_{em} , we obtained: $q = 0.11 \pm 0.01$, $K_1 = 26 \pm 3$ km/s, $K_2 = 230 \pm 25$ km/s. These solutions are in very good agreement.

As for SDSS0137, the superhump solution: $q = 0.116 \pm 0.010$, $K_{1sh} = 46 \pm 4$ km/s and $K_{2sh} = 396 \pm 37$ km/s is also in agreement with our best solution: $q = 0.109 \pm 0.049$, $K_1 = 43 \pm 19$ km/s and $K_2 = 393 \pm 41$ km/s. Considering that the correction from K_{ab} to K_2 is negligible, we calculated the value of q from K_{ab} , plotted with the black diamond in Figure 5.26, obtaining $q_{ab} = 0.13 \pm 0.06$, in agreement with the previous solutions.

5.6 Discussions and Conclusions

SDSS0137 is the only CV in our sample with a detectable absorption line from the secondary star, which is likely a late type star. A M-dwarf star would present not only Na I absorption lines, but, at least K I. The absence of any other features in the spectrum of SDSS0137 and the very broad nature of the Na I doublet (300 km/s) might be indicative of a secondary later and cooler than a

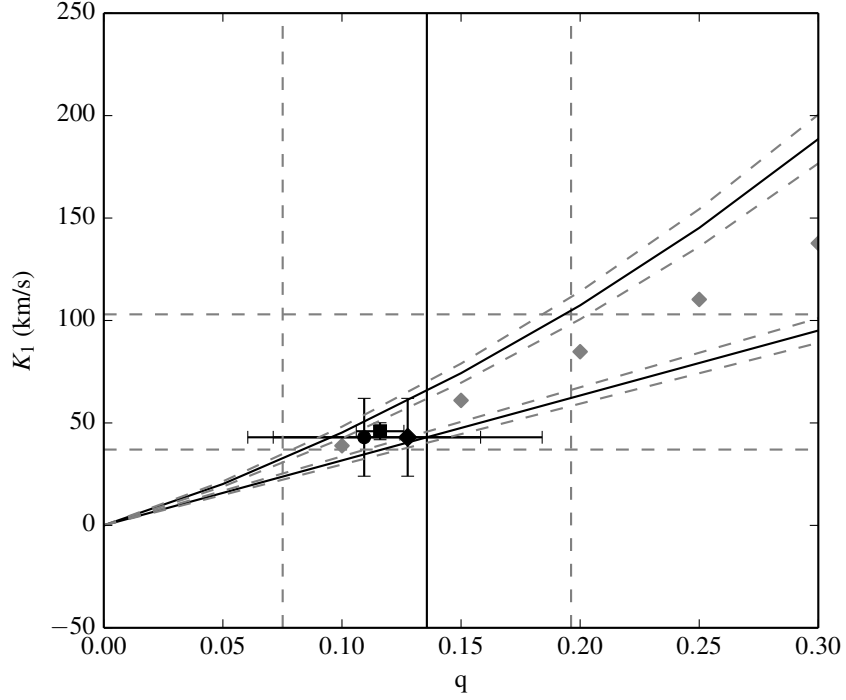


Figure 5.26: K_1 - q plane for SDSS0137, markers as indicated in Figure 5.24. Black diamond with error bars is the K_{ab} solution.

M type star. Despite that measuring the radial velocity lines of the secondary's absorption lines has proven to be a reliable way to find K_2 and q (e.g. Steeghs & Jonker 2007), we find that our radial velocity measurements ($K_{ab} = 337 \pm 8$ km/s) seem low in comparison with $K_{em} = 317 \pm 20$ (if we consider that a typical correction for K_{em} is around $\Delta K \sim 80$ km/s and that $K_{ab} > K_2$). To better understand this, we calculated the projected rotational velocity of the secondary, using the expression $v \sin(i) / K_2 = 0.46[(1 + q)^2 q]^{1/3}$ (Wade & Horne, 1988), finding that it is of the order of 85 km/s. This value is not comparable to the line widths, which further indicates another source of broadening like the one found in latter type (Díaz et al., 2007) and cooler (Tripicchio et al., 1997) stars. We will investigate this issue and its implications on the calculation of v and K_{ab} in a future paper, although discrepancies between velocities calculated from de Na I doublet has been reported before (see (Bleach et al., 2002) and references within).

One of the most notorious features of these four systems is the presence of enhanced features in the Doppler maps that are not in the location of the bright spot. We have seen this kind of emission before in the second quadrant of the Doppler maps of V2051 Oph. At the time, these features were identified by Papadaki et al. (2008) as the superhump light source. We found the same feature in our quiescence-spectra Doppler maps for V2051 Oph. The Doppler maps of the four systems studied in this chapter presented notorious emission in “anomalous locations”.

Despite having been observed during quiescence, AQ Eri and QZ Vir were observed ~ 15 days after superoutburst, but in the case of RZ Leo and SDSS0137, the observations were \sim a year from any superoutburst before or after. As the four systems are in different stages of quiescence -hence their discs are not elliptical- we cannot support the superhump light source hypothesis of Papadaki et al. (2008) to explain all of these.

In the particular case of QZ Vir, Szkody et al. (2001) reported an enhanced emission in $H\alpha$ at the same position where we encountered it. Given that the anomalous located bright spots were indeed the superhump bright source, one would expect them to move with the precession of the elliptical disc. It is also noticeable that $H\alpha$ does not present any sign of a bright spot in the “normal” position, and is the only line in which we find this feature.

Independently of the origin of these anomalously located bright spots, our method to estimate the radial velocity of the primary star, K_1 , can successfully avoid most asymmetries of the accretion disc. We believe that the value of K_1 would not be affected by these anomalously located bright spots, hence the lower velocities derived from our method in comparison with the average solution of the diagnostic diagram.

If we revise the case presented by Wolf et al. (1998) with the CV IP Peg in quiescence, an enhanced emission in an “anomalous” position (centre-right of the Doppler map) is identified as evidence of spiral structure in the accretion disc, found by Steeghs et al. (1997) in the system during outburst. As in the case of the quiescence maps of IP Peg by Wolf et al. (1998), neither of the Doppler maps of our four targets seem to present clear signs of spiral shocks, other than double bright spots. Despite that no evidence of spiral structure has been found in short period SU Uma stars in outburst (see Harlaftis et al. (1999) and references within), Baba et al. (2002) present evidence of spiral-like structure in WZ Sge in superoutburst. WZ Sge is a sub class of SU Uma type CVs, with a period below the period gap, opening the possibility that spiral shocks could occur during superoutburst in other short period systems. However, we would not expect such tidally excited features in quiescence. Furthermore, if we look the Doppler maps of other short period CVs, like SDSS 123813.73-033933.0 in figure 4 of Aviles et al. (2010), we can clearly see an extended bright region opposite to the bright spot. We find the same features in the Doppler maps of SDSS J080434.20+510349.2 if we look at figure 9 of Zharikov et al. (2013). Also, for SDSS J103533.02+055158.3, presented in figure 11 of Southworth et al. (2006), looking at the constructed map (left side) no anomalous bright spot is detected, but after subtracting the symmetric part (right hand), the familiar asymmetry is revealed. Zharikov et al. (2013) proposed the following: In low mass ratio ($q \lesssim 0.06$) systems, given that the WD is massive enough, we can assume that it will have a huge primary Roche lobe. If this is the case, the accretion disc could extend to the 2:1 resonance radius, as proposed by Kunze & Speith (2005). Reaching this resonance, a two arms pattern would appear at the disc rim, which (according to the model proposed by Zharikov et al. 2013) will be seen as the enhanced double emission in the Doppler maps of the

short period CVs in quiescence and it could be a signal of a bounce back CV.

To try and set our systems on the pre- or post-bounce sequence, we used the parameters derived for the CVs donor sequence given a typical $M_1 = 0.75M_\odot$, presented in table 4 of Knigge et al. (2011), to estimate the solutions for our systems.

For AQ Eri, the pre-bounce solution is $q = 0.112$ and the post-bounce solution is $q = 0.057$. Given that our best solution for AQ Eri, $q = 0.085 \pm 0.02$, is between both values, we can not use it to further clarify its nature. Nevertheless, the superhump solution $q_{sh} = 0.126 \pm 0.08$ would be indicative of a pre-bounce system. For QZ Vir, the results are: for pre-bounce $q = 0.102$ and for the post-bounce case $q = 0.064$. Our best solution is $q = 0.11 \pm 0.01$, also favouring a pre-bounce system. The superhump solution, $q_{sh} = 0.108 \pm 0.005$, agrees with this conclusion. In the case of SDSS0137, Knigge et al. (2011) derived solutions for systems with orbital periods down to 82 minutes, so it is not included in their models. We did calculate both $K_{em} = 317 \pm 20$ km/s with the $H\alpha$ emission line and $K_{ab} = 337 \pm 8$ km/s for the Na I absorption line. As $K_{em} < K_{ab}$, and given that the absorption line showed a broad profile in comparison with the emission lines, we believe that the absorption lines could be generated from a large area on the back side of the secondary star, farther away from the centre of mass, while it is believed that Ca II emission lines are generated on the inner face of the donor near the L_1 point. As the true value of K_2 should be between K_{em} and K_{ab} , our estimated value $K_2 = 393 \pm 41$ km/s is rather large in comparison. This could be indicative of our method overestimating the value of K_2 , but we should consider that in the case of SDSS0137, we calculated the values of K_{em} using the secondary feature in $H\alpha$ and not the optimal feature Ca II. The intrinsic broadening of the Balmer lines, as proposed by Marsh & Dhillon (1997), could have led to a saturated secondary signal, filling the theoretical Roche lobe and hence increasing the measured radial velocity K_{em} . Another possibility is the one mentioned above, given that the Na I profile is too broad to be explained solely by rotational broadening, the absorption may come from another source. This would imply an incorrect K_{ab} , since the absorption lines would not be coming from the donor's surface.

We have derived solutions for the mass ratio of three super-humping short period CVs, independent from the superhump relation. In general, our independent results agree with the superhump solution. Given the reduced number of calibrators for the superhump period-mass ratio relation on the short-period systems end, studies such as the one presented here, can improve the current model.

5.7 Summary

In this chapter, we have used the techniques tested with eclipsing systems in Chapter 3, to derive dynamical solutions for a selection of short period CVs with known superhump periods, but otherwise poorly constrained parameters. We have compared our best solutions against the mass

ratio calculated with the observationally derived relation between superhump period and mass ratio. We found our best solutions to be in agreement with the superhump-derived solution. We found that the Doppler maps for these systems share similar features, namely, enhanced emission at the location of the bright spot and on the opposite side of the disc. These features have been found before in several post-bounce candidate systems and it is believed to be a sign of outer disc structure caused by tidal interactions in systems with evolved secondary stars. We used the empirical relation between secondary mass and orbital period to determine the position of the systems in the evolutionary track, finding a favourable pre-bounce solution for two systems. Better constraints on K_1 would be required to reduce our uncertainty on q before we can rule out a post-bounce scenario.

Six

Discussions and Conclusions

6.1 Dynamic constraints with Doppler tomography

Doppler map based methods can provide strong constraints on the orbital parameters of short period CVs and LMXB. We compared these methods against classic double Gaussian methods finding advantages from the former over the classic ones.

Our method to constrain the value of γ , although following the same logic as Casares et al. (2003), has the advantage of being able to determine the optimal value with uncertainties lower than 50 km/s, significantly smaller than the error derived from the difference between the FWHM of the secondary for different γ , which is often only detected for values $\gtrsim 30$ km/s apart. Using Doppler tomography instead of other radial velocities techniques also has advantage over the uncertainties induced by disc asymmetries, giving more reliable results.

We have shown that using the donor emission in Doppler tomography is an easy and reliable way to measure K_{em} and to determine the phase zero point. As the emission of the donor originates from the inner Lagrangian point, we need to apply a K-correction to our measured K_{em} to find the true radial velocity of the secondary, K_2 , which we have done using model spectra to find the best solution for a given set of parameters. We found that this K-correction is quite well constrained and is not the limiting factor in any of the data sets we considered.

We have automatised the centre of symmetry technique to find the optimal value of K_1 , giving it meaningful uncertainties with the bootstrap method while avoiding obvious asymmetries.

Our Doppler tomography based methods give good estimates for the values of K_1 and K_2 , but our relatively large error on the small K_1 , expected in low q systems, sets the accuracy of our derived mass ratios. We have showed the advantages of the method, delivering individual systems with spectroscopic parameters and provided calibrators to vindicate the reliability of superhump inferred mass ratios.

6.2 Ca II emission

We have found that the Ca II 8662.14Å line consistently shows better results than the Balmer lines when using Doppler map-based techniques. The lower ionization energy in comparison with the Balmer lines makes it ideal to trace the secondary star emission as well as sharp features from the accretion disc.

In the case of SDSS0137, we found that even though the Ca II NIR triplet showed no emission from the secondary star, Ca II 3933.67 had a strong and sharp secondary emission. Given that the ionization energy of Ca II 3933.67 is higher than the Ca II infrared triplet, and that the secondary emission was also present in $H\alpha$, we believe that the absence of the secondary emission is a reconstruction artefact, like the case showed with simulated data in Figure 2.26, Section 2.4.8, where the low signal to noise of the data, combined with a narrow secondary emission, result in the absence of the secondary signal from the reconstructed maps.

6.3 4U 1957 and the Bowen blend

We found that the bootstrap technique is a valuable tool to test the authenticity of a detection, in this particular case with rewarding results: using the donor emission from the Bowen blend, we have shown dynamical evidence of the secondary star for the first time and estimated the mass ratio of the system. Our solution favours a low mass compact object, most likely a neutron star.

The stellar black hole mass distribution predicts a narrow distribution of BH with a lack of BHs systems with masses $< 5M_{\odot}$ that is not accounted for in population models. Özel et al. (2010) argue that this is not due to a selection effect. With increasing numbers of known parameters of LMXBs, the persistent absence of low mass BHs becomes more evident that the continuous distributions of BH masses are not accurate and that the lack of BH with masses $< 5M_{\odot}$ can be due a physical effect not accounted for.

6.4 Implications for the $\epsilon - q$ relation

The main objective of Chapter 5 was to find new calibrators for the empirical relation between the superhump excess, ϵ , and the mass ratio q . We have seen in the previous Chapter that our independent results for 4 short period CVs agree with the superhump solution, now we will attempt to add these results to the most current model.

We excluded CC Scl from this analysis, since, as we have mentioned before, it has an anomalously large superhump excess, casting doubts on the veracity of the detection and any implied ϵ .

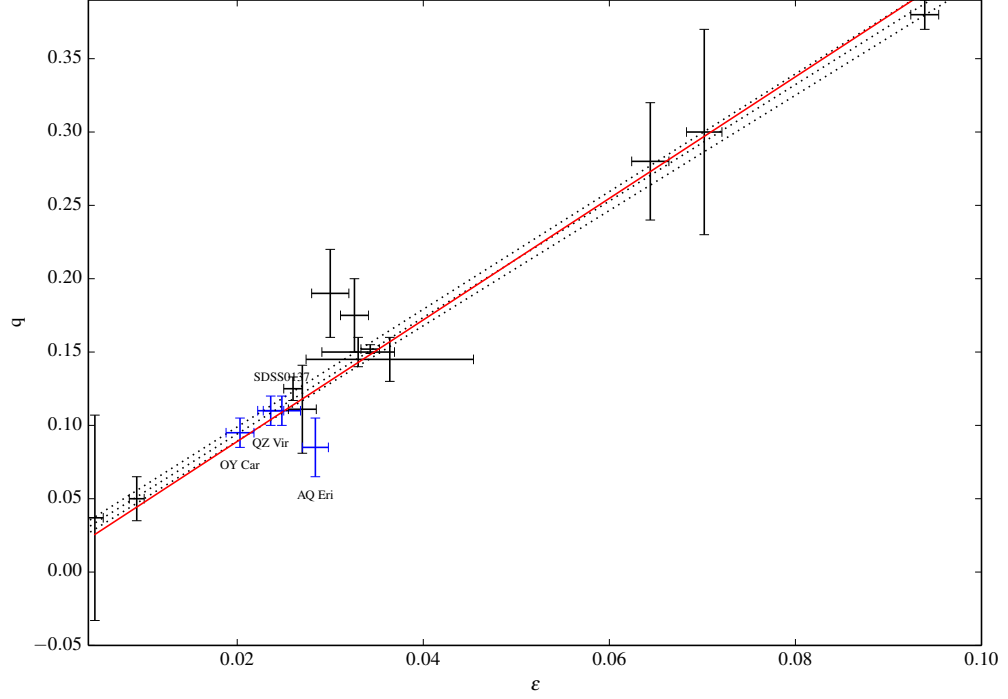


Figure 6.1: $\epsilon - q$ plane. Knigge solution is the dotted line with dotted error bars, this work's solution, considering the new calibrators, is plotted in red.

Knigge (2006) proposed a relation $q(\epsilon) = (0.114 \pm 0.005) + (3.97 \pm 0.41)x(\epsilon - 0.025)$ using a 0.025 shift to ϵ to ensure that the fit parameters are reasonably uncorrelated. They also treated q (instead of ϵ) as the independent variable, since the ultimate goal is to estimate q from our measured ϵ . As these are good logic, we chose to use the same treatment.

We added the four systems' mass ratio to the calibrators used by Knigge and attempted a fit. We found that the best fit for the data is indeed a linear fit of the form : $q = a + b\epsilon$, confirming the model proposed by Knigge.

Using the same treatment as Knigge and including the new calibrators to the fit, we obtain the relation: $q = (0.109 \pm 0.001) + (4.14 \pm 0.13)x(\epsilon - 0.025)$. We show our solution as a red solid line in Figure 6.1. The dotted line with dotted error bars in Figure 6.1 is the solution computed by Knigge. Both solutions are in good agreement, thus we have confirmed the validity of the $\epsilon - q$ relation and provided new calibrators to improve its accuracy.

6.5 Conclusions

We have presented dynamical constraints for 7 CVs and one LMXB, mass ratios for 7 of these and for 4 systems this is the first time they have had their orbital parameters constrained. We have used the Ca II triplet and Bowen blend to detect the emission of the donor star in observationally challenging systems. We intentionally included a few systems with known parameters to test our methods. Our best estimates of q for eclipsing systems are in good agreement with the eclipse solutions, giving confidence in the validity of the mass ratio estimation method for the non-eclipsing systems.

6.6 Future Research

6.6.1 Ca II

Armed with a working method to find orbital parameters via Ca II, we can look for these features in CVs with existing data from the VLT obtained by the University's WD group. As our science scopes are different, our research will not overlap.

GAIA, with a strong scientific goal on variable stars and WDs and its high resolution spectrometer centred on the Ca II triplet was a promising player for the exploitation of the CaII triplet. Unfortunately, problems after its launch meant that the spectrograph is now limited to < 15 Mag objects, making it less likely to target any new-interesting CV. But it is not the end of the world: with large samples of CVs from different surveys like the Catalina Real-time Transient Survey (Breidt et al., 2014), we have a broad selection of potential new targets and with our high-rate of Ca II detections from a WHT survey (Steeghs et al., in preparation), and a working method to constrain orbital parameters, we have a solid scientific rationale to ask for further telescope time.

6.6.2 Short Period CVs

Given the faint donor stars in short period CVs, the validation of the $\epsilon - q$ relation via dynamical constraints presents a great indicator of the mass ratio of the systems, given the easy to measure superhump period, and hence superhump excess.

It would be interesting to survey systems with very-low superhump excesses looking for donor emission and add some accuracy to the lowest end of the $\epsilon - q$ plane. To do this, we will need to find a sample with a broader range of q : enter the surveys CV sample and more reasons for telescope time on new targets.

6.6.3 Extending the method

Classical novae (CNe) are hot CVs that have only shown one observed outburst of 6-19 magnitudes. We call this outburst a nova eruption as they are very different from DNe outbursts. CNe are thought to undergo a thermonuclear runaway on the surface of the WD due to the accreted mass (Starrfield et al. 1976). Despite the ejected material, the binary is not destroyed and mass transfer is reestablished after a couple of years (e.g. Retter et al. 1998).

It is believed that nova eruptions are recurrent events but on long time scales. The recurrence time is estimated to be $t_{rec} > 10^3 \text{ yr}$ (Shara et al. 2012). It has been shown that the most important factors that determine t_{rec} are the internal temperature of the WD, the mass transfer ratio and the mass of the WD. The main discussion between the Supernova community about these targets is about the mass of the WD. The WD mass increases with the accretion process, but it is unproven if, over long timescales the novae eruptions make it on average lose all that excess mass and more, decreasing the WD mass over time. This will mean that CNe could not be Type Ia supernovae progenitors. Otherwise, if during nova eruptions the WD should lose less mass than it accreted, it could be a strong candidate for Type Ia supernovae progenitors. There are theoretical models supporting both views, although the newest studies point to the latter possibility (Zorotovic et al., 2011).

It is thought that 50% of CNe should have orbital periods between 3-4 hours (Townsley & Gänsicke 2009, Townsley & Bildsten 2005). As with the DNe, comparing theoretical prediction and actual data generates problems. Only 31 % of the population with known orbital periods are in the 3-4 hours range (see figure 6.2). In the case of CNe it is not only the lack of constrained orbital parameters that obscures our understanding of their evolution, but also that these are still significantly under sampled. To be able to understand nova eruptions and their long term consequences (the gain or loss of mass of the WD), it is necessary to build up CNe orbital parameters to a statistically significant size and compare them as a group to the rest of the population.

In several CNe the presence of the Bowen blend has been reported (e.g. Tappert et al. 2014, Tappert et al. 2013, Ribeiro & Diaz 2006, Zwitter & Munari 1996, Ringwald et al. 1996). The presence of the Bowen blend in CVs with high mass transfer rate opens the possibility of using our method to constrain orbital parameters of the under sampled CNe.

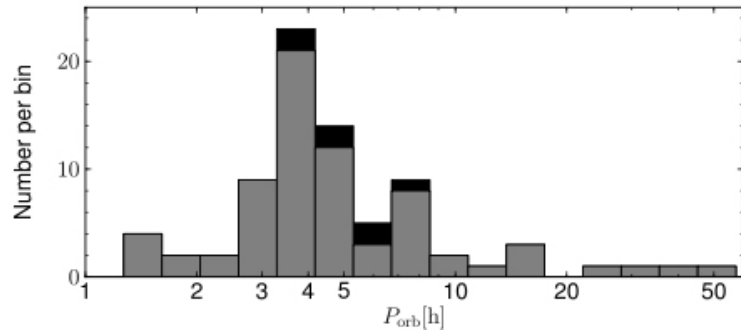


Figure 6.2: Observed period distribution of CNe. The grey data are from Ritter & Kolb (2003) and black data from Tappert et al. (2013). The addition of the 2013 data represent an increase of about 10 percent, emphasising the under-sampling of the distribution (from Tappert et al. (2013)).

Bibliography

- Aviles, A., et al., 2010, ApJ, 711, 389
- Baba, H., et al., 2002, PASJ, 54, L7
- Baptista, R., Catalan, M. S., Horne, K., Zilli, D., 1998, MNRAS, 300, 233
- Baptista, R., Santos, R. F., Faúndez-Abans, M., Bortoletto, A., 2007, AJ, 134, 867
- Barnes, A. D., Casares, J., Cornelisse, R., Charles, P. A., Steeghs, D., Hynes, R. I., O'Brien, K., 2007, MNRAS, 380, 1182
- Barret, D., McClintock, J. E., Grindlay, J. E., 1996, ApJ, 473, 963
- Bayless, A. J., Robinson, E. L., Mason, P. A., Robertson, P., 2011, ApJ, 730, 43
- Benson, R. S., 1970, in Bulletin of the American Astronomical Society, vol. 2 of *Bulletin of the American Astronomical Society*, p. 295
- Berger, E., et al., 2005, Nature, 438, 988
- Bleach, J. N., Wood, J. H., Smalley, B., Catalán, M. S., 2002, MNRAS, 336, 611
- Breidt, E., et al., 2014, MNRAS, 443, 3174
- Carrol, B. W., Ostlie, D. A., 2007, An Introduction to Modern Astrophysics, Pearson Education Inc.
- Casares, J., Jonker, P. G., 2014, Space Sci. Rev., 183, 223
- Casares, J., Charles, P. A., Naylor, T., 1992, Nature, 355, 614
- Casares, J., Steeghs, D., Hynes, R. I., Charles, P. A., O'Brien, K., 2003, ApJ, 590, 1041
- Casares, J., Cornelisse, R., Steeghs, D., Charles, P. A., Hynes, R. I., O'Brien, K., Strohmayer, T. E., 2006, MNRAS, 373, 1235
- Chen, A., O'Donoghue, D., Stobie, R. S., Kilkenney, D., Warner, B., 2001, MNRAS, 325, 89

- Cornelisse, R., Steeghs, D., Casares, J., Charles, P. A., Barnes, A. D., Hynes, R. I., O'Brien, K., 2007, MNRAS, 380, 1219
- de Loore, C. W. H., 1992, Structure and Evolution of Single and Binary Stars, Kluwer Academic Publishers
- Díaz, R. F., Cincunegui, C., Mauas, P. J. D., 2007, MNRAS, 378, 1007
- Efron, B., 1979, Ann. Statist., 7, 1
- Efron, B., Tibshirani, R. J., 1993, An introduction to the Bootstrap, Chapman Hall/CRC Monographs on Statistics Applied Probability
- Frank, J. King, A. R., Raine, D., 2002, Accretion power in astrophysics, 3rd edition, Cambridge University Press
- Gänsicke, B. T., et al., 2009, MNRAS, 397, 2170
- Gehrels, N., et al., 2005, Nature, 437, 851
- Hakala, P., Muhli, P., Charles, P., 2014, MNRAS, 444, 3802
- Hakala, P. J., Muhli, P., Dubus, G., 1999, MNRAS, 306, 701
- Harlaftis, E. T., Steeghs, D., Horne, K., Martín, E., Magazzú, A., 1999, MNRAS, 306, 348
- Haswell, C. A., King, A. R., Murray, J. R., Charles, P. A., 2001, MNRAS, 321, 475
- Hellier, C., 2001, Cataclysmic Variable Stars, how and why they vary, Springer
- Hellier, C., Mukai, K., Beardmore, A. P., 1997, MNRAS, 292, 397
- Hirose, M., Osaki, Y., 1990, PASJ, 42, 135
- Horne, K., 1985, MNRAS, 213, 129
- Horne, K., 1986, PASP, 98, 609
- Horne, K., Marsh, T. R., 1986, MNRAS, 218, 761
- Hynes, R. I., Charles, P. A., Haswell, C. A., Casares, J., Zurita, C., Serra-Ricart, M., 2001, MNRAS, 324, 180
- Imada, A., et al., 2006, PASJ, 58, 143
- Ishioka, R., Kato, T., Matsumoto, K., Uemura, M., Iwamatsu, H., Stubbings, R., 2001a, Information Bulletin on Variable Stars, 5023, 1

- Ishioka, R., Sekiguchi, K., Maehara, H., 2007, PASJ, 59, 929
- Ishioka, R., et al., 2001b, PASJ, 53, 905
- Kato, T., 2014, CC Scl: eclipsing SU UMa-type dwarf nova Time-resolved spectroscopic survey of short period CVs, vsnet-alert 17622
- Kato, T., Matsumoto, K., 1999, Information Bulletin on Variable Stars, 4767, 1
- Kirchhoff, G., 1860, Annalen der Physik, 185, 275
- Kiyota, S., Kato, T., 1998, Information Bulletin on Variable Stars, 4644, 1
- Knigge, C., 2006, MNRAS, 373, 484
- Knigge, C., Baraffe, I., Patterson, J., 2011, ApJS, 194, 28
- Kolb, U., Baraffe, I., 1999, MNRAS, 309, 1034
- Kunze, S., Speith, R., 2005, in Hameury, J.-M., Lasota, J.-P., eds., The Astrophysics of Cataclysmic Variables and Related Objects, vol. 330 of *Astronomical Society of the Pacific Conference Series*, p. 389
- Landau, L. D., Lifshitz, E. M., 1969, A Course of Theoretical Physics, Pergamon Press, Oxford
- Lubow, S. H., 1991, ApJ, 381, 268
- Margon, B., Thorstensen, J. R., Bowyer, S., 1978, ApJ, 221, 907
- Marsh, T. R., 2001, in Boffin, H. M. J., Steeghs, D., Cuypers, J., eds., Astrotomography, Indirect Imaging Methods in Observational Astronomy, vol. 573 of *Lecture Notes in Physics, Berlin Springer Verlag*, p. 1
- Marsh, T. R., Dhillon, V. S., 1997, MNRAS, 292, 385
- Marsh, T. R., Horne, K., 1988, MNRAS, 235, 269
- Marshall, J. L., et al., 2008, in Society of Photo-Optical Instrumentation Engineers (SPIE) Conference Series, vol. 7014 of *Society of Photo-Optical Instrumentation Engineers (SPIE) Conference Series*
- Mason, P. A., Robinson, E. L., Bayless, A. J., Hakala, P. J., 2012, AJ, 144, 108
- Massey, P., Hanson, M. M., 2013, Astronomical Spectroscopy, p. 35
- McClintock, J. E., Canizares, C. R., Tarter, C. B., 1975, ApJ, 198, 641

- Mennickent, R. E., Tappert, C., 2001, A&A, 372, 563
- Mennickent, R. E., Unda-Sanzana, E., Tappert, C., 2006, A&A, 451, 613
- Modigliani, A., et al., 2010, in Society of Photo-Optical Instrumentation Engineers (SPIE) Conference Series, vol. 7737 of *Society of Photo-Optical Instrumentation Engineers (SPIE) Conference Series*
- Muñoz-Darias, T., Casares, J., Martínez-Pais, I. G., 2005, ApJ, 635, 502
- Narayan, R., Nityananda, R., 1986, ARA&A, 24, 127
- Neilsen, J., Steeghs, D., Vrtillek, S. D., 2008, MNRAS, 384, 849
- Neo, S., Miyaji, S., Nomoto, K., Sugimoto, D., 1977, PASJ, 29, 249
- Nogami, D., Kato, T., Hirata, R., 1996, PASJ, 48, 607
- Nomoto, K., Nariai, K., Sugimoto, D., 1979, PASJ, 31, 287
- Nowak, M. A., Wilms, J., 1999, ApJ, 522, 476
- Osaki, Y., 1974, PASJ, 26, 429
- Özel, F., Psaltis, D., Narayan, R., McClintock, J. E., 2010, ApJ, 725, 1918
- Paczynski, B., 1986, ApJ, 308, L43
- Paczynski, B., Sienkiewicz, R., 1981, ApJ, 248, L27
- Paczynski, B., Zytkow, A. N., 1978, ApJ, 222, 604
- Papadaki, C., Boffin, H. M. J., Steeghs, D., Schmidtbreick, L., 2008, A&A, 487, 611
- Patterson, J., et al., 2003, PASP, 115, 1308
- Patterson, J., et al., 2005, PASP, 117, 1204
- Pearson, K. J., 2006, MNRAS, 371, 235
- Perlmutter, S., et al., 1999, ApJ, 517, 565
- Postnov, K. A., Yungelson, L. R., 2014, Living Reviews in Relativity, 17, 3
- Pretorius, M. L., Woudt, P. A., Warner, B., Bolt, G., Patterson, J., Armstrong, E., 2004, MNRAS, 352, 1056
- Prialnik, D., Livio, M., 1985, MNRAS, 216, 37

- Rappaport, S., Verbunt, F., Joss, P. C., 1983, *ApJ*, 275, 713
- Remillard, R. A., McClintock, J. E., 2006, *ARA&A*, 44, 49
- Retter, A., Leibowitz, E. M., Kovo-Kariti, O., 1998, *MNRAS*, 293, 145
- Ribeiro, F. M. A., Diaz, M. P., 2006, *PASP*, 118, 84
- Richter, G. A., 1985, *Information Bulletin on Variable Stars*, 2714, 1
- Riess, A. G., et al., 1998, *AJ*, 116, 1009
- Ringwald, F. A., Naylor, T., Mukai, K., 1996, *MNRAS*, 281, 192
- Ritter, H., Kolb, U., 2003, *A&A*, 404, 301
- Ruiz-Lapuente, P., et al., 2004, *Nature*, 431, 1069
- Russell, D. M., Lewis, F., Roche, P., Clark, J. S., Breedt, E., Fender, R. P., 2010, *MNRAS*, 402, 2671
- Saito, R. K., Baptista, R., 2006, *AJ*, 131, 2185
- Sanduleak, N., 1972, *Information Bulletin on Variable Stars*, 663, 1
- Scargle, J. D., 1982, *ApJ*, 263, 835
- Schmidt, B. P., et al., 1998, *ApJ*, 507, 46
- Schneider, D. P., Young, P., 1980, *ApJ*, 238, 946
- Schwöpe, A., et al., 2000, *Astronomische Nachrichten*, 321, 1
- Shafter, A. W., Szkody, P., 1984, *ApJ*, 276, 305
- Shafter, A. W., Szkody, P., Thorstensen, J. R., 1986, *ApJ*, 308, 765
- Shahbaz, T., Smale, A. P., Naylor, T., Charles, P. A., van Paradijs, J., Hassall, B. J. M., Callanan, P., 1996, *MNRAS*, 282, 1437
- Shakura, N. I., Sunyaev, R. A., 1973, *A&A*, 24, 337
- Shara, M. M., Mizusawa, T., Zurek, D., Martin, C. D., Neill, J. D., Seibert, M., 2012, *ApJ*, 756, 107
- Skumanich, A., 1972, *ApJ*, 171, 565
- Smith, M. A., 1979, *PASP*, 91, 737
- Southworth, J., Gänsicke, B. T., Marsh, T. R., de Martino, D., Hakala, P., Littlefair, S., Rodríguez-Gil, P., Szkody, P., 2006, *MNRAS*, 373, 687

- Southworth, J., Marsh, T. R., Gänsicke, B. T., Aungwerojwit, A., Hakala, P., de Martino, D., Lehto, H., 2007, *MNRAS*, 382, 1145
- Southworth, J., Hickman, R. D. G., Marsh, T. R., Rebassa-Mansergas, A., Gänsicke, B. T., Copperwheat, C. M., Rodríguez-Gil, P., 2009, *A&A*, 507, 929
- Sparks, W. M., Stecher, T. P., 1974, *ApJ*, 188, 149
- Starrfield, S., Sparks, W. M., Truran, J. W., 1974, *ApJS*, 28, 247
- Starrfield, S., Sparks, W. M., Truran, J. W., 1976, in Eggleton, P., Mitton, S., Whelan, J., eds., *Structure and Evolution of Close Binary Systems*, vol. 73 of *IAU Symposium*, p. 155
- Steeghs, D., 2003, *MNRAS*, 344, 448
- Steeghs, D., Casares, J., 2002, *ApJ*, 568, 273
- Steeghs, D., Jonker, P. G., 2007, *ApJ*, 669, L85
- Steeghs, D., Harlaftis, E. T., Horne, K., 1997, *MNRAS*, 290, L28
- Steeghs, D., O'Brien, K., Horne, K., Gomer, R., Oke, J. B., 2001, *MNRAS*, 323, 484
- Steeghs, D., Longa-Peña, P., van Spaandonk, L., T.R., M., in preparation, Time-resolved spectroscopic survey of short period CVs, in preparation
- Still, M. D., Quaintrell, H., Roche, P. D., Reynolds, A. P., 1997, *MNRAS*, 292, 52
- Szkody, P., 1987, *ApJS*, 63, 685
- Szkody, P., Nishikida, K., Long, K. S., Fried, R., 2001, *AJ*, 121, 2761
- Szkody, P., et al., 2003, *AJ*, 126, 1499
- Tappert, C., Mennickent, R. E., Arenas, J., Matsumoto, K., Hanuschik, R. W., 2003, *A&A*, 408, 651
- Tappert, C., Augusteijn, T., Maza, J., 2004, *MNRAS*, 354, 321
- Tappert, C., Schmidtbreick, L., Vogt, N., Ederoclite, A., 2013, *MNRAS*, 436, 2412
- Tappert, C., Vogt, N., Della Valle, M., Schmidtbreick, L., Ederoclite, A., 2014, *ArXiv e-prints*
- Thorne, K. S., Hawking, S. W., Israel, W., 1987, *Gravitational radiation*
- Thorstensen, J. R., 1987, *ApJ*, 312, 739
- Thorstensen, J. R., Patterson, J. O., Shambrook, A., Thomas, G., 1996, *PASP*, 108, 73

- Townsley, D. M., Bildsten, L., 2005, *ApJ*, 628, 395
- Townsley, D. M., Gänsicke, B. T., 2009, *ApJ*, 693, 1007
- Tripicchio, A., Severino, G., Covino, E., Terranegra, L., Garcia Lopez, R. J., 1997, *A&A*, 327, 681
- Uemura, M., et al., 2002, *PASJ*, 54, L15
- van Spaandonk, L., 2011, Exploring new emission line diagnostics for accreting compact objects, Ph.D. thesis, University of Warwick
- van Spaandonk, L., Steeghs, D., Marsh, T. R., Torres, M. A. P., 2010, *MNRAS*, 401, 1857
- Verbunt, F., 1982, *Space Sci. Rev.*, 32, 379
- Verbunt, F., Zwaan, C., 1981, *A&A*, 100, L7
- Vernet, J., et al., 2011, *A&A*, 536, A105
- Wade, R. A., Horne, K., 1988, *ApJ*, 324, 411
- Warner, B., 1995, *Cataclysmic Variable Stars*, Cambridge University Press
- Watts, D. J., Bailey, J., Hill, P. W., Greenhill, J. G., McCowage, C., Carty, T., 1986, *A&A*, 154, 197
- Webbink, R. F., 1977, *ApJ*, 211, 881
- Whelan, J., Iben, Jr., I., 1973, *ApJ*, 186, 1007
- White, N. E., Marshall, F. E., 1983, *IAU Circ*, 3806, 2
- Whitehurst, R., 1988, *MNRAS*, 232, 35
- Wolf, S., Barwig, H., Bobinger, A., Mantel, K.-H., Simic, D., 1998, *A&A*, 332, 984
- Woosley, S. E., Taam, R. E., Weaver, T. A., 1986, *ApJ*, 301, 601
- Woudt, P. A., et al., 2012, *MNRAS*, 427, 1004
- Yaqoob, T., Ebisawa, K., Mitsuda, K., 1993, *MNRAS*, 264, 411
- Zharikov, S., Tovmassian, G., Aviles, A., Michel, R., Gonzalez-Buitrago, D., García-Díaz, M. T., 2013, *A&A*, 549, A77
- Zorotovic, M., Schreiber, M. R., Gänsicke, B. T., 2011, *A&A*, 536, A42
- Zwitter, T., Munari, U., 1996, *A&AS*, 117, 449